TOTAL LIGHTNING OBSERVATIONS OF SEVERE CONVECTION OVER NORTH TEXAS

A Thesis

by

CHRISTOPHER MICHAEL MCKINNEY

Submitted to the Office of Graduate Studies of
Texas A&M University
in partial fulfillment of the requirements for the degree of

MASTER OF SCIENCE

August 2008

Major Subject: Atmospheric Sciences

TOTAL LIGHTNING OBSERVATIONS OF SEVERE CONVECTION OVER NORTH TEXAS

A Thesis

by

CHRISTOPHER MICHAEL MCKINNEY

Submitted to the Office of Graduate Studies of
Texas A&M University
in partial fulfillment of the requirements for the degree of

MASTER OF SCIENCE

Approved by:

Co-Chairs of Committee,	Lawrence D. Carey
	Richard E. Orville
Committee Members,	Courtney Schumacher
	Thomas Wehrly
Head of Department,	Kenneth Bowman

August 2008

Major Subject: Atmospheric Sciences

ABSTRACT

Total Lightning Observations of Severe Convection Over North Texas. (August 2008)

Christopher Michael McKinney, B.S., Texas A&M University

Co-Chairs of Advisory Committee: Dr. Lawrence D. Carey
Dr. Richard E. Orville

Five severe convective cells over North Texas from three separate dates were examined to determine what three dimensional, or "total" lightning data can add to the understanding of a convective cell's intensity, propagation, and severe weather potential. Total lightning data were obtained from Vaisala Inc.'s Dallas/Fort Worth (D/FW) Lightning Detection and Ranging (LDAR) network. Radar data from two Weather Surveillance Radar – 1988 Doppler (WSR-88D) sites were used for position data and information regarding the intensity and kinematic properties of each cell.

Total lightning products used by the National Weather Service Forecast Office in Fort Worth, Texas were compared to total lightning flash rate; a quantity that has been shown to be correlated to changes in cell intensity inferred from other sources, such as radar and satellite data. These products, specifically flash extent density (FED) were also compared to CG flash rate and radar derived measures from the WSR-88D sites.

The results of this work show that FED and total flash rate are well correlated, with an average Pearson correlation value of 0.73, indicating that previous total flash rate results may also apply to FED. Lightning hooks, holes, and notches in FED displays indicated likely updraft regions, while appendages were observed to develop prior to

deviant motion with two supercells. These results, combined with a greater update frequency provided a useful complement to radar data in the warning decision process. FED jumps were observed prior to several severe weather reports, indicating that total lightning activity may be related to updraft strength as found in past studies. However, FED jumps were sometimes observed without any associated severe event. More work is clearly needed to define what FED changes are of most importance in the short-term prediction of storm severity. The usefulness of the total lightning data on these dates was dependant upon LDAR network status and distance of the cell from the network center.

The results of this study suggest that combining total flash rate trends with visual displays of FED provides the greatest added benefit to forecasters in maintaining situational awareness during warning operations.

ACKNOWLEDGEMENTS

I would like to thank my committee members Dr. Schumacher and Dr. Wehrly for their support of my research, as well as my Co-Chairs, Dr. Carey and Dr. Orville. Without their many suggestions, corrections, and ideas, I would not have been able to complete this work. I would also like to thank Dr. Nielsen-Gammon for providing additional comments on this thesis. Special thanks go to Dr. Carey, who reviewed multiple revisions of this text making suggestions for improvement. The final page count is my fault, not his.

I would also like to thank Greg Patrick from WFO FWD who provided much of his time to assist in the setup of WES at TAMU, along with information on using the AWIPS system. Thanks also to Bill Bunting, for allowing me to hang out at the office over the past few years, both as a volunteer student and SCEP intern. Many thanks are also owed to Dr. Martin Murphy and Nick Demetriades of Vaisala, who provided the majority of the data this research is based upon as well as many helpful suggestions and insights into the D/FW LDAR network.

I would not have been able to finish this work without the support of my friends here in the department, both as an undergrad and graduate student. I would specifically like to mention Joe Jurecka, Ian Boedeker, and Cameron Homeyer, who provided a sounding board for research ideas and also helped to maintain my sanity during this process.

Finally, I would like to thank my family. They have been a source of support and encouragement throughout my academic career. I would especially like to thank my wife for her support during the course of my graduate work, including putting up with the many late nights I spent writing this thesis.

NOMENCLATURE

AvFED	Average Flash Extent Density
AvFIDT	Average Flash Initiation Density Total
AvGSD	Average Gridded Source Density
CG	Cloud-to-ground
D2D	Display Two Dimensions
dBZ	Decibels of reflectivity
FED	Flash Extent Density
FIDT	Flash Initiation Density Total
GrFED	Grid boxes of Flash Extent Density
GrFIDT	Grid boxes of Flash Initiation Density Total
GrGSD	Grid boxes of Gridded Source Density
GSD	Gridded Source Density
LDAR	Lightning Detection and Ranging
MCS	Mesoscale Convective System
MSI	Mesocyclone Strength Index
MxFED	Maximum Flash Extent Density
MxFIDT	Maximum Flash Initiation Density Total
MxGSD	Maximum Gridded Source Density
NLDN	National Lightning Detection Network
SCIT	Storm Cell Identification and Tracking

SHI	Severe Hail Index
TOA	Time-of-Arrival
UTC	Universal Coordinated Time
VIL	Vertically Integrated Liquid
WDSS-II	Warning Decision Support System – Integrated Information
WSR-88D	Weather Surveillance Radar -1988 Doppler

TABLE OF CONTENTS

Page

LIST OF FIGURES

FIGURE Page

FIGURE Page

FIGURE Page

FIGURE Page

LIST OF TABLES

1. INTRODUCTION AND BACKGROUND

1.1 Introduction

The mission of the National Weather Service (NWS) is to issue weather forecasts and warnings for the United States "for the protection of life and property" (NWS 2005). During severe weather operations, NWS meteorologists use a warning decision process (e.g., Andra et al. 1994) combining information from surface observations, satellite, computer models, and Doppler weather radar. While the Weather Surveillance Radar – 1988 Doppler (WSR-88D) is heavily relied upon for information on the structure and evolution of severe convective cells; information on the electrical structure of the thunderstorm may also aid forecasters in the prediction of severe weather events.

Two sources of lightning information are available to forecasters at the National Weather Service Forecast Office in Fort Worth, Texas (WFO FWD). The first is the National Lightning Detection Network (NLDN), a low-frequency (LF) network that detects CG lightning strikes. The network, owned by Vaisala, Inc. of Tucson, Arizona provides data on CG strike location, polarity (positive or negative), multiplicity, and peak current (e.g., Cummins et al. 1998). While this information is of value to forecasters, previous studies have shown that intra-cloud (IC) flash rates can be much greater than CG flash rates, even up to 30 times greater (Lang et al. 2000). Wiens et al. (2005) found that for any given one minute period, IC lightning accounted for over 95%

This thesis follows the style of *Journal of the Atmospheric Sciences.*

of the total flash rate of a tornadic supercell. Boccippio et al. (2001) calculated the average ratio of IC:CG flashes over the contiguous United States for a four-year period. They found that value was regionally dependent, with an average value of 2.5 IC flashes per each CG flash. To aid in the detection of IC flashes, forecasters at WFO FWD have access to information from the Dallas / Fort Worth Lightning Detection and Ranging II (LDAR) network, also owned and operated by Vaisala, Inc. This system, covering a limited geographic area around the D/FW metroplex, detects very high frequency (VHF) energy sources, which emit radiation in the lightning breakdown process. These sources can be compiled to provide information on the three dimensional electrical activity within a cell, comprised of both IC and CG flashes. It is this ability to detect both types of flashes that has led to VHF networks being called "total" lightning networks.

Previous observations of total lightning associated with severe convection have focused on the use of total flash rate as a predictor of severe weather associated with a cell (e.g., Williams et al. 1999; Goodman et al. 2005). These studies have found that lightning "jumps", or sharp increases in total flash rate, preceded many occurrences of severe weather at the surface. It is hypothesized that the amount of electrical activity within a convective cell is highly correlated with the strength of the cell updraft, and hence, severe potential. As the updraft strengthens, more material is lofted into the mixed phase region above the environmental freezing level, and the cell is able to produce ice particles of greater size, and in greater amounts. This results in greater charging within the cell, as collisions between graupel and smaller ice crystals increase, depositing charges of opposing signs on the two particles. Increases in this collisional

charging in turn lead to increases in storm scale charge separation and lightning activity within the cell (Williams 2001). Carey and Rutledge (1996, 2000) found that the total flash rate was well correlated with graupel volume and mass in the mixed phase region of convective cells, a quantity that increases with increasing updraft strength (Williams 2001). Wiens et al. (2005) showed that total flash rate was well correlated with both inferred graupel echo and measured updraft velocity within a tornadic supercell observed during the STEPS project in 2004 (Lang et al. 2004).

While these results are encouraging with regards to the link between total lightning activity and updraft strength, total flash rate is not in use operationally at WFO FWD. At this time, there is no known work that examines the relationship between total flash rate and flash extent density (FED), the product most often used in operational situations at WFO FWD (Gregory Patrick, personal communication). FED is a gridded measure of total lightning activity that is created by counting the number of lightning flashes that cross through 1 square kilometer in a give time interval (Lojou and Cummins 2005). FED data are displayed in plan view and color-coded in a manner similar to radar reflectivity. More information on FED will be provided in the data and methodology section of this text. While it would stand to reason that the total flash rate and FED values for a cell would be related, it is uncertain how well correlated the two products are, especially in their temporal variation. Any systematic lag or lead in lightning "jumps" between the two products has serious implications in the nowcasting and warning decision process. Additionally, contoured displays of FED have shown features that may be related to the structure and strength of the cell. Features such as lightning

holes, hooks, and appendages (Demetriades et al. 2002, Lang et al. 2004, Murphy and Demetriades 2005) have been observed that may correspond to the updraft region of the cell and the bounded weak echo region (BWER) aloft (Krehbiel et al. 2000; MacGorman et al. 2005). While these qualitative features show promise as an additional source of information on the convective strength of the cell at a given moment, more analysis is needed to tie these features to the timing and location of severe convective reports, cell structure and kinematics, as well as the radar derived signatures of cell strength observable with the Weather Surveillance Radar – 1988 Doppler (WSR-88D). Particular emphasis will be placed on examining FED appendages and lightning hook "echoes", as there are relatively few examples of these features in the peer-reviewed literature as compared to lightning holes.

1.2 Background

1.2.1 Cloud Electrification and Electrical Structure of Thunderstorms

Experiments to determine the electrical nature of clouds date back to observations taken by Ben Franklin and even earlier. The first modern hypotheses of cloud electrification were the inductive method of collisions between polarized particles, proposed by Elster and Geitel, and the ion-capture method proposed by C.T.R. Wilson. Many subsequent theories have been proposed (see Saunders (1993) or MacGorman and Rust (1998) for greater discussion of these and other theories), however the one most

widely accepted at this time is the theory of non-inductive graupel-ice collisions, as first proposed by Reynolds et al. (1957).

Non-inductive charging does not require a preexisting electrical field to polarize the colliding particle, as is the case with the inductive charging hypothesis. In the non-inductive collision method, the ice particles become charged due to their rebounding collisions with each other. Under normal cloud conditions of temperature, liquid water content, and droplet size distribution, the larger graupel particles will tend to acquire a negative charge while the smaller ice crystals will become positively charged (e.g., Takahashi (1978); Jayaratne et al. (1983)). Once this particle-scale charge separation occurs, the differences in terminal velocity between the two hydrometeors lead to cloud-scale charge separation, as the larger graupel particles sediment towards the bottom of the cloud while the lighter ice crystals are more easily held aloft by the cell updraft (Williams 2001). Once this separation occurs, we are left with the simple positive dipole model (an area of positive charge above a negative charge region) of the thunderstorm, first proposed by C.T.R. Wilson.

Several factors have been shown to affect the amount of charge transferred and the polarity of the rebounding particles. Takahashi (1978) found that the sign of the charge deposited on each particle depended on the surrounding temperature. At temperatures colder than -10 C, graupel particles were charged negatively, as discussed above. However, at warmer temperatures, the graupel charged positive, and the smaller ice crystals became negatively charged. This boundary is known as the reversal temperature. It has also been shown that the reversal temperature is dependent upon the

amount of supercooled liquid present, with warmer reversal temperatures for lower amounts of liquid water (Jayaratne et al. 1983).

The simple model of an electrified cloud, mentioned above, is that of a region of positive charge above a negative charge region (referred to as a positive dipole). In-situ measurements of electrified clouds have shown that, in addition to these two main layers, a smaller region of positive charge often exists in the lowest part of the cloud, forming a tripole model (e.g. Marshall and Rust (1991)) (Fig. 1.1). Another layer of charge has also been observed to occur at the upper boundary of the thunderstorm, as the charge region within the upper level of the cell attracts opposing charge to the cloud edge. This "screening layer" has been observed in several observational studies (e.g., Vonnegut et al. (1962); Marshall and Rust (1991)). While the model of a dipole/tripole structure with an upper screening layer at the cloud top is sufficient for the discussion of electrical structure within this work, it should be pointed out that the actual observed electrical structures within thunderstorms are often quite complex, with several more layers of charge present (Stolzenburg 1998). A list of thunderstorm charge characteristics observed with most cells can be found on page 52 of MacGorman and Rust (1998).

1.2.2 Lightning

Lightning is an electrical discharge that results from the accumulation of charges of opposite sign, either within a cloud or between the cloud and the earth's surface. As the amount of charge increases, so does the electric field, leading to the breakdown, or

breakeven process (Marshall et al. 1995), which results in a lightning flash. There are two types of lightning, intra-cloud (IC) flashes, and cloud-to-ground (CG) flashes. IC flashes occur between regions of opposite charge within a cloud, and are typically the first flashes to occur with a thunderstorm (Krehbiel 1986). CG flashes occur between the cloud and the earth's surface, and may be either positive or negative, depending upon the polarity of the charge lowered to the ground.

The entire sequence of events within a lightning flash is outside of the scope of this study, however a few key processes must be discussed as they relate to the lightning detection methods used by instruments in this study. The following descriptions of CG and IC flash processes are adapted from Uman and Krider (1982) and Uman (1987). For CG flashes, once the electric field strength reaches breakdown field strength the initial breakdown within the cloud leads to the formation of a stepped leader (Fig. 1.2). This leader propagates downwards in a series of short "steps", which are tens of meters in length and last approximately 1μs, with an interval of 50 μs between steps. The stepped leader follows a branched path towards the ground, until the electric field near the surface becomes sufficient to initiate the attachment process, and an upward moving leader, called a streamer, propagates upward from the surface (or a tall object such as a tree or building). Once this streamer and the stepped leader connect, a return stroke propagates up the lightning channel. If sufficient charge exists within the cloud, a dart leader may propagate down the channel leading to successive return strokes. IC cloud flashes originate in the same manner as CG flashes, although they occur between regions

of opposite charge within a cloud. The IC flash leader leads to a series of weak return strokes, referred to as K-changes.

Lightning flashes are broadband electromagnetic radiators (MacGorman and Rust 1998). Uman and Krider (1982) found that the processes in IC and CG flashes caused similar electric field frequency spectra at frequencies below 1 kHz and above 100 kHz. Between these values, CG flashes radiate much stronger due to the return strokes, which have a peak frequency around 10 kHz, in the low frequency (LF) range (MacGorman and Rust 1998). Thus, low frequency (LF) lightning detection networks are well suited for the identification of CG lightning flashes, while very high frequency (VHF) networks are used to detect IC flashes, and the intracloud portion of CG flashes, which are observed to radiate similar to IC flashes (Proctor 1981; Uman and Krider 1982).

1.2.3 Low Frequency Lightning Detection Networks

The use of magnetic direction finding (DF) for the purpose of lightning location dates back to the early 1920s. These early networks used narrow band (tuned) direction finding, a technique that led to significant position errors for lightning occurring within a few hundred kilometers of the sensor (see Rakov and Uman (2003) for further discussion and references). Current DF lightning detection sensors use a Low Frequency (LF) (30-300 kHz) gated, wideband magnetic direction finder to reduce these errors, a technique described in Krider et al. (1976).

Magnetic direction finders use two orthogonal loop antennas that detect the magnetic field signal of a CG lightning strike. The detected signal from the two loops (usually oriented N-S and E-W) can be compared to determine a direction vector to the strike location (Krider et al. 1980). The signal received by the loop oriented E-W varies as the sine of the angle between the strike and north, and the N-S signal varies as the cosine of that angle (Rakov and Uman 2003). The actual ground strike location can be determined by comparing direction vectors from multiple known sensor locations (Fig. 1.3). This triangulation technique is still employed by the NLDN, although the current sensors combine this with time of arrival (TOA) methods employing global positioning system (GPS) technology, which will be discussed in a later section (Cummins et al. 2006). Location errors from narrow band detectors are overcome using wideband detectors that only consider the first few microseconds of a return stroke waveform, ensuring that the lightning channel being measured is relatively vertical and close to the surface. This allows for the magnetic field to be as close to horizontal as possible, as the electric field is assumed to be vertical (Krider et al. 1976, 1980).

Large-scale DF networks for the location of CG lightning strikes in the United States were first installed in the late 1970s (Krider et al. 1980). These networks, owned by the Bureau of Land Management (BLM) were installed in the western United States and Alaska to aid in the detection of forest fires. Subsequent networks were installed in other regions of the country, including one operated by the National Severe Storms Laboratory (NSSL) and the East Coast Lightning Detection network (Orville et al. 1983), operated by SUNY Albany. Over time, the number of networks and their

coverage expanded to contain the entire contiguous United States. The combined network, known as the National Lightning Detection Network (NLDN) is owned and operated by Vaisala, Inc. of Tucson Arizona (a more detailed history of the NLDN can be found in Orville 2008).

Data from the NLDN has been used to study the electrical activity of many thunderstorms, including both isolated supercells and mesoscale convective systems (MCS), in an effort to relate trends in cloud to ground lightning with the occurrence of severe weather at the surface. Results of these studies with regards to operational forecasting vary widely (e.g., MacGorman et al. 1989; MacGorman and Nielsen 1991; Bluestein and MacGorman 1998). Perez et al. (1997) investigated thunderstorms producing violent (F4 or F5) tornadoes and found that there was no clear correlation between trends in CG lightning activity and tornadogenesis. MacGorman and Nielsen (1991) observed that negative CG flash rate was well correlated with low-level cyclonic shear with a tornadic supercell near Edmond, OK, contrary to the observations of the Binger tornadic supercell studied in MacGorman et al. (1989), which exhibited considerably less CG lightning activity. They suggested that the relatively high ratio of IC to CG flashes for the Binger supercell was a result of a strong updraft that lifted the lower negative charge layer closer to the main layer of positive charge. The effect of this shift was to reduce the amount of charge necessary to produce IC lightning, while suppressing CG lightning production. In their studies, Carey and Rutledge (1996, 1998) observed some non-severe thunderstorms produce higher CG flash rates than nearby severe cells. Also, Carey and Rutledge (2003) showed that CG lightning properties (e.g.,

flash density and polarity and magnitude of peak current) for severe and non-severe were different between cells in the northern and southern Great Plains, a result supported by the regional differences in the IC:CG flash ratios found in Boccippio et al. (2001). Further discussion on the results of CG lightning studies can be found in MacGorman and Rust (1998) and Williams (2001).

1.2.4 Very High Frequency Lightning Detection Networks

While the LF lightning detection networks were being deployed, similar research was progressing on the development of Very High Frequency (VHF) (30-300 MHz) lightning detection networks. These networks use the Time Of Arrival (TOA) technique first proposed for VHF lightning detection by Oetzel and Pierce (1969). TOA networks compare the time that a particular VHF radiation source arrives at several receivers within the network to determine the exact source location. A VHF source that occurs at time t and location (x,y,z) arrives at a sensor located at (x_i,y_i,z_i) at time t_i, according to the following equation:

$$(1) \qquad c(t-t_i) = \sqrt{(x-x_i)^2 + (y-y_i)^2 + (z-z_i)^2}$$

If 4 or more sites within the network detect this source the above equation produces a series of four equations in four unknowns (x,y,z,t) that can be solved to determine the exact source location (Thomas et al. 2004) (Fig. 1.4). In reality, although four sensors is the minimum number to detect a source, this would result in large position errors. Operational VHF detection networks usually require 6 sensors to detect a source to

reduce location errors and detection of random noise sources (e.g., Rison et al. 1999; Koshak and Solakiewicz 1996; Koshak et al. 2004). In addition to its use in VHF source detection, the TOA principle can also be applied in LF detection networks, and is used in the sensors that make up the NLDN (Cummins et al. 1998, 2006).

The first VHF detection network was deployed in South Africa in the late 1960's. Operating in the 250 MHz range, this network consisted of five VHF TOA sensors with baselines between 10 and 30 km. The data from each sensor was combined on a cathode ray tube monitor that was photographed by 35 mm drum cameras for later analysis (Proctor 1971). A similar short baseline network, the Lightning Detection and Ranging (LDAR) network, was installed at NASA's Kennedy Space Center (KSC) in the early 1970's (Lennon 1975). An updated LDAR network was installed at KSC in the early 1990's (see Lennon and Maier 1991 and Maier et al. 1995 for further description of this network). A system similar to LDAR, the Lightning Mapping Array (LMA) was developed by researchers at New Mexico Tech (Rison et al. 1999; Krehbiel et al. 2000). The development of the LMA was a significant improvement upon the original LDAR network, incorporating GPS timing to allow for the calculation of arrival times at each station independently, rather than at a central site as was done in the original LDAR system (Krehbiel et al. 2000). The current generation LDAR-II network (referred to in the rest of the text simply as "LDAR") benefits from many of the improvements made in the LMA design, including the use of GPS timing at each independent sensor. LMA networks have been deployed in central Oklahoma (National Severe Storms Laboratory (NSSL); Mach et al. 1986), northern Alabama (NASA; Goodman et al. 2005), and

Washington, D.C. (NASA; Krehbiel et al. 2006). Additionally, an LMA network was deployed temporarily in eastern Colorado and western Kansas to support the Severe Thunderstorm Electrification and Precipitation Study (STEPS) in 2000, a field campaign aimed at studying lightning production in severe thunderstorms, including both supercell thunderstorms and mesoscale convective systems (MCSs) (Lang et al. 2004). LDAR networks are currently in operation in Houston, Texas (Texas A&M University; Ely et al. 2008) and Dallas/Fort Worth, Texas (Vaisala, Inc.; Carey et al. 2005), in addition to the previously mentioned network at KSC. The Dallas/Fort Worth (D/FW) network has been operational since March 2001, with real time data becoming available to the local NWS weather forecast office in the fall of 2004. Specifics on the D/FW LDAR network will be discussed further in the Data and Methodology section of this text.

1.2.5 Supercell Thunderstorms

Supercell thunderstorms are intense convective cells that retain a quasi-steady structure and persist for a period of time much longer than the lifetime of an ordinary convective cell (Browning 1964). They are marked by the presence of a mesocyclone, a broad region of rotation within the thunderstorm updraft, which is usually between 2 and 10 miles wide (Browning 1977; Lemon and Doswell 1979; Doswell and Burgess 1993). Supercells generally produce some form of severe weather during their lifetime, and are responsible for a majority of tornadoes, and nearly all of the strong to violent (EF-2 to EF-5) tornadoes (Johns and Doswell 1992).

Supercells initially develop as ordinary convective cells within regions of strong wind shear (rapid changes in wind speed and direction with height). Under normal shear conditions, wind shear can cause the thunderstorm precipitation to fall into the region of warm inflow winds that feeds the storm, effectively killing it. However, if environmental wind shear is strong enough, the precipitation is displaced downshear of the updraft, and the cell is able to sustain itself (Browning 1964; Klemp 1987). In regions of strong wind shear, the thunderstorm updraft can lift and tilt the horizontal rotation present in the environment, producing a pair of counter-rotating vortices (Fig. 1.5). Under conditions of unidirectional shear, new updrafts will form on both flanks of the original updraft, and two rotating updrafts (one cyclonic and one anticyclonic) will be formed (Rotunno 1981). However, shear in the atmosphere is rarely unidirectional and often changes direction rapidly at lower levels. Under these conditions, dynamical forces produce a region of downward motion on either the right or left flank of the original updraft, suppressing growth on that side (Klemp 1987). Usually environmental winds will turn anticyclonically (clockwise) with increasing height in the atmosphere. This condition favors growth on the right flank of the original updraft, and suppresses it on the left flank (Klemp and Wilhelmson 1978; Rotunno and Klemp 1985) (Fig. 1.6). Thus, most supercells observed will move to the right of the mean mid-atmosphere flow (Browning 1964), leading to the terms “right deviant” or “right moving” supercell. However, when the vertical shear is cyclonic, left moving supercells are the preferred supercell type. For a more thorough discussion of the dynamical processes related to supercell formation and motion, see Weisman and Klemp (1986) or Klemp (1987).

Supercell thunderstorms have several characteristics and features that distinguish them from ordinary convective cells. The first is the tendency for cell propagation either to the right or left of the mean flow, as discussed above. Another is the presence of a rotating updraft (mesocyclone) that can be detected using Doppler weather radar (Browning 1977). The presence of a mesocyclone within a cell is a strong indicator that the cell will produce at least some severe weather, as 90% of cells with an observed mesocyclone produce reported severe weather during the Joint Doppler Operational Project, conducted in Oklahoma in 1977 and 1978 (Stumpf et al. 1998). During testing of the WSR-88D in Norman, Oklahoma, 30% of cells with a detected mesocyclone produced a tornado (Burgess and Lemon 1991). Supercells often display a tight gradient of radar reflectivity factor (hereafter reflectivity) near the updraft region of the cell. This gradient is a result of larger hail and graupel falling out of the storm close to the updraft as they move out of the strongest upward winds. Another common feature, although not always present, is the radar "hook echo" (Fig. 1.7). This is a radar reflectivity signature of the mesocyclone wrapping precipitation from the core of the thunderstorm around the updraft region. The updraft region is marked by an absence of precipitation, leading to a radar reflectivity weak echo region (WER) at the surface, and a bounded weak echo region (BWER) (Browning 1964) aloft (Fig. 1.8). Further discussion of supercell characteristics can be found in Doswell and Burgess (1993), and Bluestein (1993).

1.2.6 Mesoscale Convective Systems

Mesoscale convective systems (MCS) are large cloud complexes containing both convective and stratiform precipitation. The most common type of MCS is a leading line of convective precipitation with a trailing stratiform region (Houze et al. 1990). The convective line is made up of numerous individual convective cells (Fig. 1.9), and may include embedded supercells.

Although they are not typically linked with violent (EF-4 or EF-5) tornadoes, MCSs do produce a variety of severe weather, including weaker tornadoes, large hail, and strong straight-line winds. A particularly severe MCS structure is a "bow echo" (Fujita 1981) (Fig. 1.10). A bow echo is a section of the convective line that has surged ahead of adjacent cells within the line. Within the bow echo, small notches known as rear inflow notches (RIN) may be present. These indicate the presence of strong winds flowing into the rear of the convective line at mid levels, often referred to as a rear inflow jet (RIJ). If the RIJ winds descend to the surface in the convective line, they can produce narrow swaths of damaging winds, often in excess of 100 mph (Pryzbylinski 1995).

1.2.7 Results from Prior VHF Network Research

Past studies on the use of total lightning data in the warning decision process have focused on the use of VHF source data to infer information about the potential for severe weather associated with a given convective cell (Williams et al. 1999; Goodman et al. 2005). Several studies have noted large changes in total flash rate prior to occurrences of severe weather. It is hypothesized that the amount of electrical activity within a convective cell is highly correlated with the strength of the cell updraft, and hence, severe potential. Stronger updrafts allow for increased lightning production as more hydrometeors are lofted into the mixed phase region, leading to increases in the production of ice particles and collisional charging (Williams 2001).

Several studies have documented trends in VHF sources prior to and during severe weather events. Williams et al. (1999) noted that total flash rates for severe convective cells over Florida exceeded 60 flashes per minute (fpm), with some cells reaching values of 500 fpm. They also state that these occurred as part of a lightning 'jump', where total flash rate values increased rapidly to their peak values between 5 and 20 minutes prior to the severe weather event. Goodman et al. (2005) found similar trends in total flash rates for severe thunderstorms observed by the North Alabama LMA, with peak flash rates in excess of 70 fpm for severe cells. Lightning jumps were found to occur 15-25 minutes prior to reported tornadoes, which matches with Williams's results, as well as those of Bridenstine et al. (2005) and Gatlin and Goodman (2004), who found that lightning jumps preceded tornadic activity by up to 20 minutes

for cells observed by the North Alabama LMA. Goodman also noted that while trends in CG flash rate were similar to total flash rate trends, the signal of increased activity was clearer in the total lightning data. Steiger et al. (2007a) observed that source heights dropped during a 25-minute period prior to tornadogenesis with two supercells observed using the D/FW LDAR network. This result was not observed with non-tornadic supercells in the region, suggesting that the updraft may have weakened prior to tornadogenesis, in agreement with the theory suggested by Lemon and Doswell (1979).

Features in VHF source density plots have also been linked to severe convective cells. Lightning "holes", or areas within a cell with little or no total lightning activity, have been observed in VHF source density plots of several supercell thunderstorms (e.g., Krehbiel et al. 2000; Goodman et al. 2005; MacGorman et al. 2005; Murphy and Demetriades 2005; Wiens et al. 2005). These features occur in an area of the cell co-located with the convective updraft, and Lang et al. (2004) found that a lightning hole in a supercell thunderstorm studied during STEPS was associated with the BWER, a radar indication of an updraft. Similar features such as lightning hooks and notches have also been observed with supercells (Demetriades et al. 2002). It is currently hypothesized that these total lightning features are indications of the updraft region of the convective cell, as supported by the observations of Williams et al. (1999), Goodman et al. (2005), and others. Additionally, Steiger et al. (2007b) observed notches in VHF density plots on the rear flank of bowing line segments within an MCS over the D/FW network. Features such as these rear notches may indicate the presence of a rear inflow jet and the possibility for severe straight-line winds within that line segment.

1.3. Thesis Objectives and Hypothesis

The objectives of this work are to evaluate trends in the total lightning products in use at WFO FWD and their relationship to storm structure and intensity, including reports of severe weather at the surface. This analysis will be carried out with an emphasis on determining the usefulness of FED in severe weather nowcasting, as this is the total lightning product most widely used at WFO FWD. While several studies have considered the use of total flash rate as a proxy for updraft strength (i.e., Williams et al. 1999; Goodman et al. 2005) the relationship between trends in FED and total flash rate (and updraft strength) remains to be shown.

Temporal variations of FED will be compared with trends in flash rate (CG and total) and total flash rate, a quantity that has shown some correlation with the occurrence of severe weather in previous studies (e.g. Williams et al. 1999; Goodman et al. 2005; Gatlin and Goodman 2008). Emphasis will be placed on determining if there is any systematic lag or lead between "jumps" in FED, CG flash rate, and total flash rate, a result which has implications for operational use of total lightning data by NWS forecast offices. Average and maximum FED values for a cell will both be considered to determine which value has the highest correlation to total flash rate, or the clearest signal of increasing (decreasing) electrical activity within a convective cell. In addition to these measures of electrical activity within a cell, radar derived cell parameters will also be compared to FED trends. Specifically, FED will be compared to trends in Vertically Integrated Liquid (VIL) (e.g. Kitzmiller et al. 1995), the Severe Hail Index (SHI) (Witt

et al. 1998a), and the Mesocyclone Strength Index (MSI) (Stumpf et al. 1998) to determine the relationship between trends in cell intensity based upon the two primary observing platforms (LDAR and WSR-88D) available to forecasters at WFO FWD for severe thunderstorm investigation.

In addition to investigating trends in FED and other measures of cell intensity, this work will focus on evaluating features present in FED displays and relating them to radar indicated cell features. Qualitative features in radar reflectivity, such as hook echoes (Stout and Huff 1953) and bounded weak echo regions (BWERs) (Browning 1964) have been shown to be indicators of a cell's organization and strength, and identification and analysis of these features is an important part of the warning decision process. In an effort to determine the usefulness of total lightning displays, radar reflectivity and velocity data will be compared to FED to determine the relationship between well known radar signatures of strong convective cells with corresponding features in the FED data. Particular emphasis will be placed upon investigating whether the presence of holes or notches in density plots of total lightning data are indications of the updraft region of the cell, as has been suggested in numerous other studies (e.g., Krehbiel et al. 2000; Demetriades et al. 2002; Wiens et al. 2005).

Based upon the work of previous research studies, we hypothesize that total lightning data can provide information on a convective cell's intensity, propagation, and potential for severe weather at a greater frequency than radar data from the WSR-88D network. The integration of this data into the warning decision process may increase situational awareness for warning forecasters at WFO FWD.

2. DATA AND METHODOLOGY

The following four sections describe the data sources and methodology used in this work. The first section discusses the WSR-88D radar, algorithms for storm tracking and intensity, and reports of severe weather. The second section discusses specifics of the National Lightning Detection Network (NLDN) that were not covered in the section on LF lightning detection networks in the introduction chapter. Section three will discuss the Dallas/Fort Worth (D/FW) Lightning Detection and Ranging (LDAR) network and the operational LDAR products delivered to the National Weather Service's Fort Worth/Dallas Weather Forecast Office (WFO FWD). The final section discussed the specific methodology employed in this work, with emphasis on the manipulation of data from the LDAR network.

2.1 Radar Data and Severe Weather Reports

2.1.1 Weather Surveillance Radar – 1988 Doppler

The Weather Surveillance Radar – 1988 Doppler (WSR-88D) is the result of the Next Generation Radar (NEXRAD) program that was initiated in the late 1970's (Crum and Alberty 1993). The goal of this program was to replace the non-Doppler meteorological radars in use by the Department of Commerce, Department of Transportation, and Department of Defense with a single network of radars that could

support each organization's operational requirements (Serafin and Wilson 2000). The current network consists of 155 radars operating in the contiguous United States, Alaska, Hawaii, and Puerto Rico (OFCM 2007). The WSR-88D is an S-band radar, with a wavelength of approximately 10 cm and a peak output power of 750 kW. The radar antenna is 8.5 m (28 ft) in diameter, with a 0.98-degree beamwidth that is divided into range bins of 250 m in length (OFCM 2006b).

Each WSR-88D measures radar reflectivity factor, radial velocity, and spectrum width. Radar reflectivity factor (commonly referred to as radar reflectivity) is a measure of the power returned to the radar by the backscattering of the radar pulse from hydrometeors (i.e., rain and hail). The amount of returned energy for each range bin is displayed as the color-coded images that are the radar product most familiar to the general public. Brighter colors correspond to higher returned powers, and are indications of more intense rainfall or hail. Radial velocity images are produced by measuring the shift in frequency of the returned signal, which is related to the velocity of the target relative to the radar. Each target sampled by the radar within a range bin returns a slightly different frequency, which are then averaged to produce the radial velocity value for that bin. The addition of this capability allows the WSR-88D to measure rotation within a thunderstorm, leading to more accurate tornado warnings with increased lead times over conventional non-Doppler radars (Polger et al. 1994). Red colors correspond to radial velocities away from the radar, while green colors represent velocity towards the radar. Again, brighter colors are used to display higher values.

Spectrum width is a measure of turbulence based upon the returned frequencies of targets within a range bin, and is not relevant to the work in this study.

The WSR-88D employs several scanning strategies, or Volume Coverage Patterns (VCP), in order to scan the atmosphere. There are several VCPs in use by the NWS, which are categorized into clear-air and precipitation modes. The two VCPs used in this work are VCP 11 and VCP 12, which are both precipitation-mode scanning strategies (OFCM 2006a). In VCP 11, the WSR-88D will make 16 scans covering 360 degrees of azimuth over a series of 14 elevation angles between 0.5 and 19.5 degrees, taking five minutes to complete (Fig. 2.2). VCP 12 is a newer precipitation mode strategy for the WSR-88D. VCP 12 also scans at 14 elevation angles, but reduces the number of higher elevation angles sampled in order to increase sampling at lower elevations (between 0.5 and 4.0 degrees) (Fig. 2.3). VCP 12 also runs faster than VCP 11, taking just over 4 minutes to complete. This newer scanning strategy was implemented to better sample features at lower levels inside convective cells, as well as to improve performance of the storm cell identification and tracking (SCIT) algorithm, which is discussed below (Lee and Steadham 2004).

The radar data used in this research are from the Ft. Worth/Dallas (KFWS) and Dyess Air Force Base (KDYX) WSR-88D sites and were obtained from the National Climatic Data Center (NCDC). Data from the two sites were used as input into the Warning Decision Support System – Integrated Information (WDSS-II) software package developed by researchers at the National Severe Storms Laboratory (NSSL) (Lakshmanan et al. 2007). Radar reflectivity and velocity data from KFWS were used

on all three case dates. However, a radar product generator (RPG) failure at approximately 2215 UTC on 25 April 2005 caused a loss of data necessary for input into several WDSS-II algorithms used in this study. Data from the KDYX site were substituted as input into WDSS-II for this case date. KFWS was operated using VCP 11 on each case date, while KDYX was operated using VCP 12 on 25 April 2005.

2.1.2 Warning Decision Support System – Integrated Information

Within WDSS-II, cells were identified and tracked using the Storm Cell Identification and Tracking (SCIT) algorithm (Johnson et al. 1998), which is included in the Severe Storms Analysis Package (SSAP). This algorithm was used to provide the cell center latitude and longitude for each radar volume scan, giving a radar based cell location every four to five minutes, depending upon the specific VCP used by the radar on that date. However, the operational total lightning products delivered to WFO FWD are updated every two minutes, giving forecasters approximately two images of total lightning data per each radar volume scan. To improve the accuracy of assigning lightning flashes to each convective cell, a linear interpolation was used to create intermediate cell positions between each SCIT location. This was done by creating a linear path between each of the SCIT derived cell locations and returning the latitude and longitude of the path midpoint. This midpoint was then assigned as a cell position with a time stamp halfway between the two radar position times.

Other algorithms used within the SSAP included the Hail Detection Algorithm (HDA) (Witt et al. 1998a) and Mesocyclone Detection Algorithm (MDA) (Stumpf et al. 1998). These were used to provide quantitative measures of cell intensity for comparison with lightning data. Specifically, this study focused on vertically integrated liquid (VIL) (Greene and Clark 1972, Kitzmiller et al. 1995), the severe hail index (SHI) (Witt et al. 1998a), and mesocyclone strength index (MSI) (Stumpf et al. 1998). VIL is the integration of liquid water content based upon reflectivity values from cells sampled by the WSR-88D, expressed in kilograms per meters squared (kg m^{-2}). SHI is calculated in a similar manner to VIL, but is weighted towards high reflectivity values sampled at altitudes above the environmental freezing level. Because VIL is an integration of radar reflectivity, larger VIL values imply the presence of larger hydrometeors and a stronger updraft within the cell (Greene and Clark 1972; Kitzmiller et al. 1995). Similarly, Witt et al. (1998a) found that larger SHI values corresponded to larger observed maximum hail size, an indication of a stronger updraft within a cell. MSI is determined by vertically integrating the strength of a storm scale vortex through the entire depth of the feature. Values of shear, rotational velocity, and gate-to-gate velocity difference (the difference in velocity between adjacent areas sampled within a radar scan) are integrated and then normalized over the depth of the vortex feature. The detection of a mesocyclone within a thunderstorm suggests a higher level of organization and severe weather potential with a thunderstorm, as discussed in the introduction section on supercells. Carpenter et al. (2004) found slightly higher values of MSI for tornadic vs. non-tornadic supercells. Studies using MSI have shown that values less than 2300 are

generally associated with weak mesocyclones, values between 2300 and 3600 are associated with moderate mesocyclone strength, and values in excess of 3600 are associated with strong mesocyclones (Carey et al. 2003; Carpenter et al. 2004).

2.1.3 Storm Data

Reports of severe weather events were taken from the official Storm Data publications for April 2005 and April 2007, available from NCDC. While these reports are generally in good agreement in timing and location with respect to cell locations from the KFWS radar data, the times listed may be up to 5 or 10 minutes off of the actual event time due to the nature of the reporting method, as discussed in Witt et al. (1998b).

2.2 National Lightning Detection Network

Data on cloud to ground (CG) lightning were obtained from the NLDN, owned by Vaisala, Inc. of Tucson, Arizona. The NLDN uses a network of 114 low frequency (LF) sensors to provide information on CG flash location, polarity (positive or negative), multiplicity, and peak current across the network domain (Orville and Huffines 1999) (Fig. 2.4). The network has undergone several upgrades over the past twenty years. A 1994 upgrade saw the introduction of Improved Accuracy from Combined Technology (IMPACT) sensors that combined both the magnetic direction finding (DF) and time of

arrival (TOA) methods to improve CG flash detection. This upgrade increased the location accuracy of detected strikes to within 500m, with a flash detection efficiency of 85% for flashes that had a peak current greater than 5 kA (Cummins et al 1998). Another upgrade was performed during 2002-03, during which all sensors were replaced with an improved IMPACT-ESP sensor, and 8 additional sensor locations were added. This upgrade brought the network to its current configuration of 114 sensors, with baselines of approximately 300 km between sensor locations (Cummins et al. 2006). Field campaigns aimed at measuring the improvements in network performance from this upgrade measured flash detection efficiencies of 92% in the area of North Texas covered in this study (Biagi et al. 2007). All data from the NLDN used in this study were filtered to remove positive flashes with peak currents below 15 kA, as these are believed to be misidentified IC flashes rather than CG lightning flashes (Biagi et al. 2007).

2.3 Lightning Detection and Ranging Network

VHF source data from the D/FW LDAR II network were obtained from Vaisala, Inc. The D/FW LDAR network currently consists of 9 TOA sensors with baselines of approximately 20 to 30 km between sensors. However, on the dates included in this study, only the first 7 sensors were installed and in operation (Fig. 2.5). The D/FW LDAR network detects VHF radiation emitted during the lightning breakdown process. Due to the very short duration of these emissions, they may be modeled as point sources

of radiation (e.g., Mazur et al. 1997; Carey et al. 2005). The network operates within a frequency range from 60 – 66 MHz, corresponding to TV channel 3. Each sensor reports the time of the highest amplitude signal received in a 100 μs time interval. These data are collected at a central site, where the time of arrival of a source at multiple locations can be used to determine the three dimensional location of the source. VHF detection networks detect are sensitive to both IC flashes and the intra-cloud portions of CG flashes, leading to the term "total lightning" detection network. It is believed that most sources are detected within the positive region of a thunderstorm, as lightning propagation within positive regions is noisier in the VHF frequency range than propagation through negative charge regions (Rison et al. 1999). Previous work has shown that the expected flash detection efficiency of the D/FW LDAR network is believed to be greater than 95% within the interior of the network, with a flash detection efficiency of greater than 90% out to a range of 120 km. The location accuracy of individual VHF sources is believed to be within 200m when the source is within a 30 km radius of the network center at D/FW International Airport (sensor site "A" in Fig. 2.5). Position errors for VHF sources are believed to be less than 2 km out to a range of 150 km from the network center (Demetriades et al. 2002; Carey et al. 2005). Recently, a portable LMA was deployed in tandem with the D/FW LDAR network to compare the performance of each system (information on the detection efficiency of the LMA can be found in Thomas et al. 2004). It was found that the LDAR network was noisier than the LMA network, but had good detection efficiency for IC flashes and positive CG flashes

(Krehbiel et al. 2008). A few negative CG flashes were found to be less well detected by the LDAR network, although these were only preliminary results.

2.3.1 Operational LDAR products at WFO FWD

Data from the LDAR network are sent in real time to WFO FWD through the Southern Region Headquarters of the NWS. The LDAR data, which are in network common data form (netCDF), are then ingested via the Local Data Acquisition and Dissemination system at WFO FWD. Forecasters may then access the data using the Display Two Dimensions (D2D) program that is part of the Advanced Weather Information Processing System (AWIPS) used by the NWS. Currently there are three products shipped to the office by Vaisala; gridded source density (GSD), flash extent density (FED), and flash initiation density total (FIDT). All three are density products, gridded into 1 km by 1 km horizontal bins. GSD displays the number of VHF sources detected by the LDAR network within each 1 km grid box. It is available for 7 altitudes, the first six of which are 3km vertical cuts between 0-3km, 3-6km, 6-9 km, 9-12 km, 12-15 km, and 15-18 km. The final GSD image available is the total column value, displaying all sources detected within the horizontal grid box from the surface up to an altitude of 20 km. Vaisala creates FED values after the raw VHF source data is run through a flash-grouping algorithm. This process applies a series of spatial and temporal criteria to the sources that are based upon the propagation speed of lightning processes measured by the LDAR network. By grouping sources that meet the constraints of the

flash algorithm individual lightning flashes can be reconstructed. Specific information on the Vaisala flash-grouping algorithm was not made available, although it is a modification of a flash-grouping algorithm created by NASA (McCormick 2003). Another adaptation of this NASA flash algorithm was used within this study for the purposes of creating VHF flash rates. The criteria of that algorithm are discussed below. Once individual flashes have been recreated the number of identified flashes passing through each 1 km grid box are summed to produce the FED value for that grid box (Lojou and Cummins 2005). FED is only available for the full 0-20 km column, and has units of flashes km^{-2} min^{-1}. It is important to note that each flash passing through a grid box counts only once. If a flash has multiple branches passing through the same grid box, the first one will be counted and subsequent branches will be disregarded. FIDT is a product similar to GSD, however the sources are filtered such that only those VHF sources identified by the flash algorithm as being the first source within a flash are included. Currently, FED is the preferred product for operational use of total lightning at WFO FWD (Gregory Patrick, personal communication), as it is less susceptible to range effects than the simple source density plots, which suffer from a decrease in source detection efficiency with increasing range from the network (Carey et al. 2005). This comparative advantage of FED is due to the use of flash grouping in the creation of the product. While the source detection efficiency loss results in fewer sources being detected, as long as the remaining sources meet the temporal and spatial criteria of a flash, as defined by the grouping algorithm, flashes will still be created and plotted in FED.

2.4 Methodology

Analysis of lightning data was performed using the Interactive Data Language (IDL). A flash grouping algorithm written for IDL was used to group VHF source data provided by Vaisala into individual lightning flashes. This code, based upon an algorithm used by NASA, was written by Lee Nelson and provided to the Cooperative Institute for Applied Meteorological Studies (CIAMS) at Texas A&M for research use by Dr. Gary Huffines of the University of Northern Colorado. This algorithm applies specific criteria to VHF sources in order to recreate lightning flashes in three dimensions. For a source to be included within a flash, it must be within 5 km of another source, be within 0.5 s of another source in the flash or within 0.03 s within another source in the same branch. The entire flash is constrained to a maximum duration of 3 s. These criteria are similar to those used in previous research studies (e.g., Williams et al. 1999; McCormick 2003). To avoid confusion between the two flash algorithms, Vaisala's flash algorithm (used in the creation of FED values) will be referred to as the "Vaisala flash algorithm", while the algorithm used by the author (for the creation of VHF flash rate data) will be referred to as the "IDL flash algorithm".

Once VHF source data were grouped into individual flashes using the IDL flash algorithm the dataset was filtered to return only those VHF sources identified as the first source within a flash. These sources were then assigned to individual cells based upon their location in time and space relative to the radar cell positions determined from the SCIT algorithm. Flash initiation sources were first grouped temporally to associate them

with the position (either SCIT reported or interpolated) closest in time to the flash initiation time. Then the distance between each point and the cell position was calculated, with only the flashes within a certain radius of the cell position returned. For each date in this study, radii of 10 km, 15 km, and 20 km were applied to all cells. Additional radii of 8 km and 5 km were applied to cells from 05 April 2005 and 13 April 2007 due to the less isolated nature of the convection occurring on those dates. Once all sources assigned to a cell were returned, these data were separated into two minute intervals to create a VHF flash rate for comparison with the lightning products delivered to WFO FWD by Vaisala.

CG lightning flashes were assigned to convective cells using a method similar to the VHF source data. While the time and space constraints were the same for both data, the position assigned to CG flashes was the ground strike location, as determined by the NLDN. Once all CG flashes assigned to a cell were identified, these data were also grouped into 2-minute intervals for comparison with operational total lightning products delivered to WFO FWD. Information returned for each two-minute period of CG lightning data included total number of flashes, the number of positive flashes, and the percentage of positive flashes.

Quantitative analysis of the LDAR products available at WFO FWD was also conducted using IDL. Each netCDF file containing two minutes of LDAR data was read in by IDL, with the same cell radii criteria applied to each LDAR product. For each product (FED, GSD, and FIDT) the maximum and average values associated with the cell were returned, as well as the number of 1 km grid boxes that contained data. For the

time-series comparisons between products, the 3 km vertical slices of GSD were not used. Only the total column (0-20 km) GSD values were compared along with FED and FIDT values.

Time series of all data were plotted using the Microsoft Excel spreadsheet program. Additionally, correlation coefficients between VHF flash rate, CG flash rate, and the operational total lightning products were computed to determine the linearity of the relationship between changes in VHF flash rate and the lightning products in use at WFO FWD. All of these parameters were also compared to values of VIL, SHI, and MSI obtained from WDSS-II, in order to compare trends in intensity as measured by LDAR, the NLDN, and the WSR-88D.

In addition to the quantitative analysis included in this work, qualitative analysis of FED images was performed to evaluate the usefulness of these displays in identifying significant features of storm structure and evolution. Specifically, FED features such as lightning holes, hooks, and notches (e.g., Krehbiel et al. 2000; Demetriades et al. 2002, MacGorman et al. 2005; Wiens et al. 2005) were compared to radar reflectivity and velocity images obtained from the KFWS radar. This analysis has an analog in the early research using weather radar, such as the observation that hook echoes were a signal of tornadic potential with a thunderstorm, as was first proposed by Stout and Huff (1953). All images of FED were displayed using the Warning Event Simulator (WES). WES is a version of the AWIPS system that is used for forecaster training within the NWS (Ferree and Quoetone 2001). The displays of LDAR data within WES are identical to

those presented to forecasters in real time within AWIPS (Gregory Patrick, personal communication).

3. RESULTS

Results from each of the three case dates are presented in this section. Data from each date will be presented individually, and are divided into three sections. The first section, labeled qualitative analysis, will cover observed features in the plan view displays of FED and GSD currently in use at WFO FWD. The second section, labeled quantitative analysis, will focus on analysis of time series plots of the operational total lightning products (FED, GSD, and FIDT), total flash rate, and CG flash rate. The final section for each case will show correlation coefficients between the products mentioned above, and also with radar derived values of VIL, SHI, and MSI.

The first two cases in this study are from April 2005. On 25 April 2005, a dryline located to the west of the D/FW metroplex served to initiate numerous showers and thunderstorms during the afternoon, including two tornadic supercells that moved across portions of Tarrant, Dallas, Johnson, and Ellis counties (all counties referenced in this section can be found on the LDAR network map in figure 2.5, unless otherwise noted). Earlier that same month, on 05 April 2005, a broken line of thunderstorms developed in the afternoon hours across sections of Collin, Denton, Dallas, and Ellis counties. Within this line, a supercell with left deviant motion moved across Dallas County and produced several reports of severe weather. The final case presented is from 13 April 2007, when a linear mesoscale convective system (MCS) moved across the D/FW metroplex, including an embedded supercell that crossed across northern Tarrant

and Dallas counties. This cell was responsible for several reports of tornadoes and large hail across the network domain.

3.1 25 April 2005

3.1.1 Qualitative Analysis

On this date, an eastward advancing dryline was located just to the west of the D/FW metroplex by mid afternoon. Several cells initiated along this boundary, including the two supercells discussed herein. At 2100 UTC, these two cells were located in eastern Tarrant and central Johnson County, and moved southeastward into Dallas and Ellis counties during the analysis period. By 2300 UTC, the northern cell (cell one) had begun to dissipate, and cell two (southern cell) had moved into northeastern Navarro County (not located in figure 2.5; Navarro County is immediately southeast of Ellis County, which is included in the figure).

The FED of cell one, the northern (Tarrant county) storm, exhibited a rightward shift in direction between 2112 and 2118 UTC. This shift of FED to the right of the previous storm track corresponded to a similar shift in radar reflectivity data, and is discussed in detail in Patrick and Demetriades (2005). The FED maximum of cell two, the southern (Johnson county) storm, also turned to the right, later in the study period, between 2210 and 2222 UTC (Fig. 3.1). However, this shift in FED maximum lagged behind the shift in radar reflectivity, which began around 2200 UTC (not shown).

Cell one displayed a minimum in FED and GSD in southeastern Tarrant County at 2128 UTC (Figs. 3.2 and 3.3). This lightning hole was located 5 km to the east of a well-pronounced hook shaped echo at low levels in the KFWS radar reflectivity data (Fig. 3.4). A north-south cross section of radar data through this FED minima shows that it corresponds to an area of relatively low radar reflectivity values up to an altitude of 2 to 3 km (Fig. 3.5). This vaulted shape corresponds to a radar reflectivity weak echo region (WER) (Fig. 3.4) at low elevation angles and a bounded weak echo region (BWER) aloft (not shown), which are radar indications of a strong cell updraft. Another similar area of minimum FED values occurred at 2234 UTC, corresponding to an area where no sources were present in the GSD data (Fig. 3.6). This region also corresponded to an area of weak reflectivity (25.5 - 27.5 dBZ) on the KFWS radar data at the 5.3 and 6.0-degree elevation angles, at altitudes of 7.2 km (23.7 kft) and 8.3 km (27.4 kft) above ground level (AGL) (not shown). However, this lightning minimum corresponds to relatively high values of radar reflectivity (~55 dBZ) on the 0.5 and 1.5-degree elevation at altitudes of approximately 1.1 km (3.7 kft) and 2.6 km (8.5 kft) AGL (not shown). Each minimum in lightning activity was observed on only one two-minute image of either FED or GSD. However each minimum was followed by a notch in the FED and GSD data that persisted for several images, corresponding to the updraft region of the cell as inferred from KFWS imagery. Examples of these notches are indicated with white arrows in figure 3.7.

Another interesting observation was the presence of lightning appendages on cell one that appeared in displays of both FED and GSD at several points in the evolution of

the storm. They were present at 2116 UTC (Fig. 7c in Patrick and Demetriades 2005), and again between 2132 and 2144 UTC (Fig. 3.7). No similar features were observed in the FED or GSD images of the second cell. At 2158 UTC, another appendage was observed to form on the southern edge of the FED maximum from cell one (Fig. 3.8). This appendage evolved over the next five FED images into a separate area of relatively high FED values separate from cell one. During this time, the maximum FED value observed with this new feature was between 14 and 16 flashes km^{-2} min^{-1}. Cell one displayed a decrease in both the value and extent of the FED maxima during this ten-minute period. At 2210 UTC, the two FED maxima merged on the D2D display into one feature. FED values associated with the merged feature began to increase at 2216 UTC on the southwest side of the cell, with FED values approaching 9 flashes min^{-1} km^{-2}. This intensification continued until a maximum of over 17 flashes min^{-1} km^{-2} was observed at 2226 UTC. Trends in GSD for this event were similar to those displayed by the FED (not shown), however an area of relatively high GSD was apparent at 2154 UTC (Fig. 3.9) four minutes prior to being a prominent feature in the FED display. The two GSD maxima remained distinct until 2216 UTC when they were observed to merge. GSD values peaked just over 30 sources min^{-1} km^{-2} at 2226 UTC, corresponding to the time of highest FED values.

While FED values for both cells were variable throughout the study period, several large changes in maximum FED values were readily observed in the D2D display. Cell one displayed increasing FED values between 2124 and 2140 UTC, reaching values in excess of 30 flashes min^{-1} km^{-2} (Fig. 3.10). A drop in FED values

then followed at 2142 UTC, where the maximum value was just over 20 flashes min^{-1} km^{-2} (image not shown, see Fig. 3.13 for a time series of maximum FED values). FED values quickly increased after this drop, with maximum values again above 30 flashes min^{-1} km^{2} by 2146 UTC (image not shown, see Fig. 3.13 for time series). Storm reports indicate that a tornado was spotted on the ground at 2135 UTC in Cedar Hill (NCDC 2005). Another "jump" in FED for cell one occurred just after 2200 UTC. FED values increased between 2200 and 2204 UTC, reaching a maximum value in excess of 20 flashes min^{-1} km^{-2} (not shown). The maximum FED value dropped below 10 flashes min^{-1} km^{-2} at 2206, and continued to drop as a second FED maximum (discussed previously) approached from the southwest. No severe weather was reported, despite the cell being located in a well-populated region just to the south of the Dallas metro area. The FED increased again between 2216 and 2226 UTC after the apparent merger of these two features. Maximum values reached just over 17 flashes min^{-1} km^{-2} before dropping to below 11 flashes min^{-1} km^{-2} by 2230 UTC. A report of 2.50 cm (1.00 in) hail was reported in Ferris in far northern Ellis County at 2221 UTC (NCDC 2005), corresponding roughly to a slight drop in FED values observed at 2220 UTC.

The time evolution of FED values in cell two exhibited similar behavior as in cell one. At 2128 UTC, FED values for cell two reached a maximum between 14 and 16 flashes min^{-1} km^{-2} just to the east of Alvarado (image not shown, see Fig. 3.18 for time series). At 2130 the maximum FED value dropped to between 5 and 6 flashes min^{-1} km^{-2} before increasing again at 2132 UTC (image not shown, see Fig. 3.18 for time series). Storm reports show that large hail reaching 7.0 cm (2.75 in) was observed in Keene at

2120 UTC (NCDC 2005). A tornado was reported 1 mile west of Alvarado at 2125 UTC, and 2.50 cm (1.00 in) hail was reported in Alvarado at 2130 UTC (NCDC 2005). Another strong increase in FED occurred with this cell in western Ellis County between 2142 and 2148 UTC with values reaching a maximum value of 14-16 flashes min^{-1} km^{-2} at 2148 UTC (Fig. 3.11). On the 2150 UTC image, FED values were observed to drop significantly, with maximum FED values of only 6 to 7 flashes min^{-1} km^{-2} (Fig. 3.12). A tornado was reported near the community of Maypearl at 2156 UTC (NCDC 2005).

3.1.2 Quantitative Analysis

Maximum values of FED (referred to in quantitative sections as MxFED) associated with cell one during the study period are plotted in Fig. 3.13. This time series plot displays the maximum value of FED within a specified radius around the radar derived cell location, which for the cells on this date was 15 km. A sharp drop in MxFED was observed at 2108 UTC, with the value dropping from 16.5 flashes min^{-1} km^{-2} at 2104 UTC to a minimum value of 8.5 flashes min^{-1} km^{-2} at 2108 UTC. MxFED values increased over the next two time intervals, reaching 17.5 flashes min^{-1} km^{-2} at 2112 UTC. The drop in MxFED at 2108 UTC occurred 6 minutes prior to a tornado reported with this cell along Interstate 35 in south Ft. Worth at 2114 UTC. MxFED values increased during the period from 2114 through 2130, reaching a value of 24.5 flashes min^{-1} km^{-2} at 2130. A dip in MxFED values occurred at 2132, with a value of 23 flashes min^{-1} km^{-2}, before quickly increasing to 31.5 flashes min^{-1} km^{-2} at 21:36. A

tornado was reported in the town of Mansfield, in southeast Tarrant County, at 2130 UTC, during the time of increasing MxFED values. MxFED values remained above 30 flashes min^{-1} km^{-2} until 2146, with the exception of a sharp drop in value at 2142 UTC to 22.5 flashes min^{-1} km^{-2}. Another tornado was reported with this cell south of Cedar Hill, in southwestern Dallas County, at 2135 UTC. MxFED values decreased between 2142 and 2152 UTC, to a value of 13 flashes min^{-1} km^{-2}, although no severe weather was reported with this cell during this time. MxFED values increased again during the next two images, reaching a value of 25.5 flashes min^{-1} km^{-2} at 2156 UTC before decreased to 6.5 flashes min^{-1} km^{-2} at 2214 UTC. Another period of increasing MxFED values occurred between 2214 and 2226 UTC, with the exception of a short dip in values at 2220 UTC, roughly at the same time the report of severe hail in the community of Ferris mentioned previously. After 2226 UTC, values of MxFED begin to decrease as the cell started to weaken considerably on radar reflectivity images from KFWS.

Trends in average FED (AvFED) followed closely with those of MxFED, and are also shown in Fig. 3.13. This curve is similar to MxFED, with the exception that the values plotted represent the average of all non-zero FED values contained within a particular radius of the radar derived cell center (15 km for this cell), rather than the single maximum value. While the values were considerably smaller than those for MxFED, a decrease in AvFED was visible before the tornado reported at 2114 UTC, as was a slight decrease in AvFED that occurred at 2130 UTC, concurrent with the reported tornado in Mansfield. The drop in MxFED values that was noticed prior to the severe hail report near the town of Ferris is not easily visible in the plot of AvFED values.

Similarly, trends in maximum and average GSD (Fig. 3.14) followed with those of the FED values, although a peak in maximum GSD values seen at 2108 UTC was a local minimum value for all other time series examined. Values of maximum and minimum flash initiation density totals (MxFIDT and AvFIDT) are displayed in Figure 3.15. These are the maximum and average values of source density for flash initiation sources, which are the first sources of each new flash identified by the flash grouping algorithm (in this case, the Vaisala flash grouping algorithm, as opposed to the IDL flash algorithm used by the author). Values for FIDT were considerably lower than those for GSD, due to the much fewer number of flash initiation sources compared to the total number of sources for each flash, and the MxFIDT time series was noisier than those of MxFED and MxGSD.

Trends of VHF flash rate (calculated using the IDL flash algorithm) were comparable to those of MxFED (Fig. 3.16). However, after a peak value of 69 flashes per minute between 2126 and 2128 UTC values of VHF flash rate then decreased through 2150 UTC. This peak at 2128 UTC occurred just before the drop in AvFED and GSD values that occurred at 2130 UTC. Similarly, a local minima of VHF flash rate values occurred at 2144 UTC, two minutes after the minima in the FED and GSD values at 2142 UTC. CG flash rates increased during the period from 2100 to 2138 UTC, reaching a maximum of 19 flashes per minute at that time (Fig. 3.16). CG flashes generally decreased in frequency after this time through when the SCIT algorithm stopped tracking the cell at 2238 UTC, although the relative fraction of positive CG flashes increased, with early values of 20 to 40 % positive CGs reaching 66 % at 2216

UTC and again at 2222 UTC. The average ratio of IC to CG flashes (IC flashes defined as the number of VHF flashes detected minus the number of CG strikes detected, divided by the number of CG strikes detected) for cell one was 13.85 IC flashes to each CG flash.

The total number of grid boxes that contained FED data during each two-minute period are plotted in Fig. 3.17. Values for this dataset, labeled as GrFED, increased to a maximum of 504 grid boxes at 2114 UTC. After a brief decrease in values, the highest value of GrFED observed with this cell occurred at 2122 UTC, reaching 519 grid boxes. Local minima occurred with this dataset at 2130, 2144, and 2216 UTC. Again, these minima occurred near the reported times of the three tornadoes associated with this cell. The total number of active GSD grid boxes, labeled GrGSD is also plotted in Fig. 3.17. The GrGSD data trends were nearly identical to those for GrFED for the entire case, although the values were lower than those for GrFED, usually by 20 to 100 grid boxes. The number of grid boxes containing flash initiation points identified by Vaisala's flash grouping algorithm is labeled GrFIDT in Fig. 3.17. Trends in values of GrFIDT were observed to follow closely to those of the VHF flash rate discussed above.

Cell two MxFED values were much lower than those for cell one throughout the lifetime of the cell, with an absolute maximum value of 18 flashes min^{-1} $km^{-2,}$ which occurred at 2216 UTC, when the cell was located in central Ellis County (Fig. 3.18). A peak in MxFED of 17 flashes min^{-1} km^{-2} occurred with this cell at 2118 UTC. Values quickly dropped off from this time to 6 flashes min^{-1} km^{-2} at 2130 UTC. This peak in MxFED and subsequent drop in values is during the time that two occurrences of severe

hail and a brief tornado touchdown were reported with this cell in central and eastern Johnson County. Another peak in MxFED values was observed at 2148 UTC, with a maximum value of 16.5 flashes min^{-1} km^{-2}. Again, MxFED values dropped off quickly after this time, to 6 flashes min^{-1} km^{-2} at 2152 UTC. Severe hail reaching 4.5 cm (1.75 in) in diameter was reported in Venus at 2140 UTC, and 2.50 cm (1.00 in) hail was reported in the town of Alvarado at 2145 UTC. Additionally, another tornado was observed to touchdown near the town of Maypearl in western Ellis County, at 2156 UTC, as mentioned previously. After reaching a minimum value of 4.5 flashes min^{-1} km^{-2} at 2202 UTC, MxFED values began a large increase over the next 8 time intervals, reaching a maximum value of 18 flashes min^{-1} km^{-2} at 2216 UTC, as discussed previously. While MxFED values dropped off rapidly after this time and remained low through the end of radar tracking for this cell, two more reports of severe hail were made, with 4.5 cm (1.75 in) hail observed roughly 5 miles to the south of Waxahachie, in central Ellis County, at 2230 UTC, and 2.5 cm (1.00 in) hail reported in Ennis at 2235 UTC. A brief increase in MxFED occurred between 2224 and 2228 UTC, with values reaching 6 flashes min^{-1} km^{-2}.

Values of AvFED for cell two are displayed in Fig. 3.18. Trends in AvFED were roughly similar to those for MxFED, with dips in the AvFED value occurring at 2130, 2150 and 2202 UTC, concurrent with large decreases seen in the MxFED value. The largest value of AvFED observed occurred at 2218 UTC, two minutes after the highest MxFED value. AvFED values dropped off after this time as well, although the increase in values of MxFED between 2224 and 2228 UTC was also present in AvFED data.

Figure 3.19 shows values of MxGSD and AvGSD for cell two. While values of MxGSD for cell one reached nearly 100 sources min^{-1} km^{-2} at one point, and frequently had values in excess of 60 sources min^{-1} km^{-2}, values of MxGSD for cell two reached a maximum value of only 30.5 sources min^{-1} km^{-2}, which occurred at 2110 UTC. This time was during a period of increasing values of MxFED for cell two, leading to the peak at 2118 UTC discussed previously. Values of AvGSD and AvFED also showed peaks at 2110 UTC. Another maximum of MxGSD values occurred at 2204 UTC, with a value of 27 sources per min^{-1} per km^2. This peak occurred just after a local minimum in MxFED values that was observed at 2202 UTC. The other major features discussed in the MxFED plot were present on the MxGSD plot, although the timing of the peak values was frequently shifted 2 minutes either before or after the MxFED maximum. Trends in AvGSD were much smoother, and closely followed those of the AvFED plot. MxFIDT and AvFIDT values for cell two are plotted in Fig. 3.20. The MxFIDT plot was quite noisy, although the decrease in the other variables noted at 2152 UTC also occurred in the MxFIDT time series.

Trends in the VHF and CG flash rates for cell two are displayed in figure 3.21. The peak in MxGSD observed at 2110 UTC also occurred with the VHF flash rate data. Another local maximum of VHF flash rate values occurred at 2124 UTC, concurrent with a small increase in MxFED values. A third peak in VHF flash rate, with the second highest VHF flash rate values for this cell, occurred at 2154 UTC. This peak, of 73 flashes per minute, was close to the reported time of the Maypearl tornado at 2156 UTC. This peak in VHF flash rate was during a local minimum in the FED and GSD plots.

Values decreased after this peak to a minimum of 45.5 flashes per minute during the two minutes preceding 2202 UTC, which corresponds to the time of local minimum values seen in the values of FED and GSD. CG lightning rates increased during the period 2202 to 2210 UTC, corresponding to a similar increase in both MxFED and VHF flash rate (Fig. 3.18). CG lightning values showed another large increase in values between 2240 and 2256 UTC. This increase, during the latter part of the time the cell was tracked by SCIT from the KDYX radar, corresponds to a period of much reduced activity in the FED, GSD, and VHF flash rate plots when compared to earlier cell times. This increase in CG lightning rates occurred during the time of the last two hail reports for this cell, which occurred at 2245 and 2250 UTC (NCDC 2005). The average ratio of IC to CG flashes for cell two was 5.75 IC flashes for every CG flash.

GrFED, the total number of grid boxes containing FED data for cell two, are shown in Fig. 3.22. These values increased to a local maximum of 370 grid boxes at 2108 UTC, before dropping to 325 grid boxes at 2110 UTC. The largest value of GrFED observed with cell two was at 2216 UTC, with 471 grid boxes containing data. The local minima that occurred with other variables at 2130 and 2142 UTC were also visible in the GrFED data. A minima of GrFED values occurred at 2150 UTC, just prior to the minima in FED and GSD values discussed previously. Trends for GrGSD were similar to those of GrFED, although as will cell one, values of GrGSD were less than those of GrFED, usually by 30 to 90 grid boxes. Cell two GrFIDT trends were observed to follow closely the changes of VHF flash rate, similar to the analysis found for cell one (Fig. 3.22).

3.1.3 Correlation Analysis

The results of a correlation analysis between the operational total lightning products (FED, GSD, and FIDT), VHF total flash rate, CG flash rate, and radar derived variables (VIL, SHI, and MSI) for cell one are summarized in Table 3.1. Due to the availability of radar data for this cell, the correlations with VIL, SHI, and MSI occurred over shorter time periods than those between the lightning network products. Correlations with VIL were calculated for the period between 2100 and 2238 UTC. SHI correlations were calculated between 2100 and 2156 UTC, while MSI correlations were calculated over the period between 2048 and 2142 UTC.

The highest correlation value was observed between VHF total flash rate and GrFIDT values. Correlation values between VHF total flash rate and the operational lightning products ranged from 0.62 to 0.89. Correlation values between CG flash rate and the operational total lightning products ranged from 0.19 to 0.77. The correlation coefficient for VHF total flash rate and CG flash rate was 0.42. Correlation values between the lightning and radar products were much lower, with VIL correlation coefficients between 0.11 and 0.51. SHI correlation values were between 0.18 and 0.59, while correlation coefficients were negative between MSI and all lightning parameters. Total flash rate, GrFED, and GrGSD had the strongest observed relationship with MSI, with correlation coefficients of -0.86 for all three variables.

Correlation coefficients for cell two variables are shown in Table 3.2. VIL values for this cell were correlated over the period between 2100 and 2312 UTC, SHI values

were correlated between 2100 and 2218 UTC, and MSI values were from the period between 2128 and 2212 UTC. The highest value for this cell was 0.96, between VHF total flash rate and GrFIDT. Correlation coefficient values between VHF total flash rate and the operational total lightning products ranged between 0.78 and 0.96. Correlation coefficient values between CG flash rate and the operational total lightning products were between 0.34 and 0.72. The correlation coefficient value between VHF total flash rate and CG flash rate was 0.46. Correlation coefficient values between the operational lightning products and VIL were between 0.10 and 0.60, while for SHI those values were between -0.34 and 0.71. Correlation coefficient values for MSI and the operational lightning products were low, with values ranging between -0.35 and 0.10.

3.2 05 April 2005

3.2.1 Qualitative Analysis

At 2200 UTC on 05 April 2005, a solid line of convection extended from southern Oklahoma down through Collin County. This line extended further south and west as a broken line of cells from Collin to Bosque County (located to the southwest of Johnson County in Fig. 2.5). The primary cell of interest on this date formed at approximately 2254 UTC on the tri-county border between Tarrant, Dallas and Ellis counties. This cell began to split at 2309 UTC on the KFWS imagery with the left

moving cell rapidly moving northeast across Dallas county before merging with another cell in far eastern Collin county at approximately 2348 UTC (Fig. 3.23).

This left moving cell exhibited updraft signatures in FED and GSD images that were similar to those of the northern supercell from 25 April. Several "FED notches" were noted with this cell, corresponding to tight reflectivity gradients on the northwestern side of this cell (Figs. 3.24 and 3.25). FED values with this cell were much lower than those from the 25 April northern supercell, but two distinct peaks in FED activity were noted. The first peak occurred at 2314 UTC with a value between 9 and 10.5 flashes min^{-1} km^{-2} (Fig. 3.24). FED values peaked with this cell again at 2326 UTC, with a maximum value between 9 and 10.5 flashes min^{-1} km^{-2} over northeastern Dallas County (Fig. 3.25). At 2322 UTC 2.50 cm (1.00 in) hail was reported 5 miles northeast of Dallas, and 3.75 cm (1.50 in) hail was reported two miles north of Garland (northeast of Dallas) at 2336 UTC. A report of 2.50 cm (1.00 in) hail was reported in Blue Ridge, in eastern Collin County at 2350 UTC, immediately after the merger of the left moving cell with another cell in the line.

While there was some increase in FED values associated with this new cell prior to this severe weather event, an apparent loss of FED data at 2338 UTC (manifested as a significant drop in FED values across all cells in the LDAR II network domain for one image) makes it difficult to make an accurate statement on the lightning activity leading to the severe hail report at 2350 UTC. A third, smaller cell began to develop northeast of Desoto in Dallas County at approximately 2334 UTC. This cell had a peak in FED between 13.5 and 18 flashes min^{-1} km^{-1} just to the west of the town of Mesquite at 2340

UTC, but no severe weather was reported at the time. Again, data from this cell is also hampered by the apparent data loss mentioned previously, but after dropping off from 2340 UTC, FED values on the northeast side of this cell begin to rise again at 2358 UTC in northeastern Rockwall County. The values peaked between 13.5 and 18 flashes min^{-1} km^{-2} (the highest values seen on this date) at 0002 UTC (not shown). FED values began to decline on the 0004 UTC image, which was the last image of FED data available for this study. Although this cell showed higher values of FED than the supercell in this case, no severe weather was reported with this cell.

The left moving supercell in this case displayed lightning appendages on the left flank of the cell similar to those seen on the right flank of the northern cell from April 25. The first appendage developed at 2314 UTC and became more pronounced on the 2316 UTC image (Fig. 3.24). The output from the SCIT algorithm shows that the cell track shifted to the left between 2319 and 2324 UTC, just after the development of this feature (Fig. 3.25). A second appendage and an associated FED notch developed at 2328 UTC (Fig. 3.26). After each of these appendages developed the FED values appeared to turn towards them and the higher values of FED shifted farther to the left.

3.2.2 Quantitative Analysis

Values of MxFED for this cell were increasing during the time that the cell formed immediately after 2254 UTC (Fig. 3.27). The 2300 UTC value peaked at 5.5 flashes min^{-1} km^{-2} before dropping off to 2.5 flashes min^{-1} km^{-2} at 2302 UTC. Another peak in MxFED values was observed at 2314 UTC, reaching 10.5 flashes min^{-1} km^{-2}, the highest value recorded on this date. MxFED values decreased slowly after this peak, reaching a minimum of 6 flashes min^{-1} km^{-2} for the 2322 and 2324 UTC images. During this period of decreasing MxFED values, the cell shifted to the left of its previous track, as noted from radar reflectivity images from the KFWS radar (not shown). Large hail of 2.50 cm (1.00 in) diameter was reported 5 miles to the northeast of Dallas (NCDC 2005) during this time. MxFED values peaked again at 2326 UTC, reaching 10.5 flashes min^{-1} km^{-2}, the same value recorded at 2314 UTC. Relatively high values of MxFED persisted in the 2328 UTC image, before dropping to 6 flashes min^{-1} km^{-2} on the 2330 and 2332 UTC images. Another increase in MxFED began after this time, reaching 8 flashes min^{-1} km^{-2} by 2336 UTC. The apparent loss of data at 2338 UTC (mentioned previously) was manifested in the MxFED value by a drop to only 1 flash min^{-1} km^{-2} before quickly returning to 6.5 flashes min^{-1} km^{-2} by 2340 UTC. A report of ping-pong ball sized hail (3.75 cm, 1.50 in) 2 miles north of Garland, in northeast Dallas County, was made at 2336 UTC (NCDC 2005). The MxFED value dropped off after this time, to a minimum of 1.5 flashes min^{-1} km^{-2} at 2344 UTC. MxFED values remained low for the remainder of the cell lifetime, peaking at 3.5 flashes min^{-1} km^{-2} on the 2352 and 0004 UTC images.

A report of 2.5 cm (1.00 in) hail was recorded in Blue Ridge, in eastern Collin County, at 2350 UTC, after the merger of this cell with another cell in the convective line (NCDC 2005).

Average FED values remained fairly steady for this case, and as with the MxFED values, were much lower than those observed with the two cells on 25 April 2005 (Fig. 3.27). The highest value of AvFED recorded for this cell was 1.97 flashes min^{-1} km^{-2}, recorded at 2336 UTC. The peak in FED values noted at 2314 UTC in the MxFED data occurred at 2316 UTC for the AvFED data. The sudden drop in MxFED value at 2338 UTC was also noted in the AvFED data, with a value of 0.53 flashes min^{-1} km^{-2}, while the two data points to either side of it had values of 1.97 and 1.57 flashes min^{-1} km^{-2}. MxGSD values increased during the initial cell times, with a series of three peaks occurring at 2300, 2308, and 2314 UTC (Fig. 3.28). The initial peak persisted across both the 2300 and 2302 UTC images, with a value of 16 sources min^{-1} km^{-2}. The MxGSD value for 2308 UTC reached 24 sources min^{-1} km^{-2}, while the 2314 UTC peak was 40 sources min^{-1} km^{-2}, the highest GSD value recorded for this cell. These three peaks all occurred simultaneously with peaks in the MxFED data discussed above. Values of MxGSD decreased after 2314 UTC, with the exception of a large increase between the 2314 and 2316 UTC images, where the value increased from 16.5 to 25.5 sources min^{-1} km^{-2}. Again, as with the MxFED and AvFED data, a large decrease in the MxGSD value occurred at 2338 UTC, with the value dropping to 3 sources min^{-1} km^{-2} although it quickly returned to 9.5 sources min^{-1} km^{-2} at 2340 UTC. Values of AvGSD were more variable than those of AvFED, and displayed similar peaks to those of the

MxFED and MxGSD data (Fig. 3.28). The two largest peaks in AvGSD data occurred at 2300 UTC, with a value of 3.97 sources min^{-1} km^{-2}, and at 2316 UTC, with a value of 5.72 sources min^{-1} km^{-2}, the largest AvGSD value from this cell. There was a sharp decrease in value for AvGSD at 2338 UTC, although as with the other datasets the value at 2340 UTC returned to a value similar to those observed before 2338 UTC. The MxFIDT data had several spikes, occurring at 2308, 2314, 2328 and 2336 UTC (Fig. 3.29). The highest MxFIDT value was 3 flash initiation sources min^{-1} km^{-2}, which occurred at both 2328 and 2336 UTC. The spike in MxFIDT at 2336 corresponds to the reported time of the severe hail in Garland (NCDC 2005). The MxFIDT value decreased to 0.5 flash initiation sources min^{-1} km^{-2}, corresponding to the drop in all other datasets. Trends for AvFIDT followed closely to those of MxFIDT, with peaks at all of the times mentioned above (Fig. 3.29). There was a decrease in AvFIDT at 2338 UTC, although it was not as pronounced as those in the other data sets, as the value at 2340 UTC was not much larger than that at 2338 UTC, 0.57 flash initiation sources min^{-1} km^{-2} vs. the 0.5 flash initiation sources min^{-1} km^{-2} observed at 2338 UTC.

The VHF flash rate for this supercell is displayed in Figure 3.29. There were a series of sharp peaks in VHF flash rate leading up to 2336 UTC, where 45.5 flashes per minute were recorded. The timing of these peaks was similar to those in the FED and GSD plots, with maxima at 2300, 2308, 2314, 2316, and 2326 UTC before the largest peak at 2336 UTC. The report of severe hail 5 miles northeast of Dallas at 2322 UTC occurred during a relative minimum in the VHF total flash rate, with 17 flashes per minute reported for the two minute period from 2320-2322 UTC (NCDC 2005). CG

flash rates remained low during most of the lifetime of this cell, with only three significant peaks at 2308, 2322, and 2326 UTC with values of 5.5, 4.5, and 6 flashes per each minute (Fig. 3.30). A smaller peak in the CG flash rate occurred at 2338 UTC, a time where every other data set showed a sharp decrease in values. The CG flash rate began to increase after 2346 UTC, reaching a maximum value for this cell at 0006 UTC, with 17 flashes per minute recorded between 0004-0006 UTC. It should be noted that this increase in CG flash rate coincides with the merger of this cell and another cell within the convective line that occurred at approximately 2348 UTC in the KFWS radar reflectivity data. The percentage of positive CG flashes for this cell varied considerably throughout the lifetime of the cell, with the two-minute positive flash percentage reaching 100 % twice, for the periods 2332-2334 UTC and 2344-2346 UTC. There were relatively few CG flashes during these periods, with four flashes in the first interval and only two recorded during the second. The average percentage of positive CG flashes for this cell was 22.4%; with an average ratio of IC:CG flashes of 12.06 IC flashes to each CG flash.

GrFED data for this cell show a period of rapid increase in values from the time the cell formed up to a value of 338 grid boxes at 2304 UTC (Fig. 3.31). A series of 3 small peaks in the data led to the largest value of GrFED observed for this case, 346 grid boxes, at 2322 UTC. This peak corresponds to the severe hail report 5 miles northeast of Dallas (NCDC 2005). GrFED values decreased to a minimum of 216 grid boxes at 2332 UTC before rapidly increasing again to 280 grid boxes at 2336 UTC. As with the other data sets, a sharp decrease occurred at 2338 UTC, with a value of only 69 grid boxes

reported. The 2340 UTC GrFED value was 332 grid boxes, which decreased to 127 grid boxes on the 2346 UTC image. Another peak occurred at 2352 UTC, two minutes after the reported time of severe hail in Blue Ridge (NCDC 2005). This peak was after the previously discussed merger of this cell with another one over eastern Collin County. Trends in GrGSD followed closely to those in GrFED, although the difference in values between the FED and GSD grid boxes was greater during the latter part of the cell's lifetime, as it moved farther from the center of the LDAR network (Fig. 3.31). GrFIDT values were much smaller than those for GrFED and GrGSD, and appeared to follow closely to changes in the VHF total flash rate discussed above (Fig. 3.31).

3.2.3 Correlation Analysis

The correlation coefficients between the operational total lightning products, VHF total flash rate, CG flash rate, and radar derived variables for this cell are displayed in Table 3.3. Radar correlations for this cell are over the period between 2300 to 2324 UTC for VIL, 2350 to 0008 UTC for SHI, and 2310 to 2324 UTC for MSI. The highest correlation value was 0.85, between MxFED and VHF total flash rate. Values for VHF total flash rate and the operational total lightning products were between 0.55 and 0.85, while the correlation between the CG flash rate and the VHF total flash rate was -0.27. Correlation values between CG flash rate and the operational total lightning products were all negative, between -0.44 and -0.13. Correlation coefficients between VIL and the operational total lightning products were between 0.02 and 0.81, except for AvFIDT,

which had a correlation coefficient with VIL of -0.17. AvFED had the strongest positive relationship to VIL. The correlation coefficient for VIL and VHF total flash rate was 0.49. Correlation coefficients between MSI and the operational total lightning products were varied: the strongest relationship was between MSI and AvFED, with a correlation coefficient of -0.80. The weakest linear relationships with MSI were found for GrFIDT and total flash rate, with correlation coefficients of -0.02 and 0.02.

3.3 13 April 2007

3.3.1 Qualitative Analysis

On this date, a dryline across North Central Texas served as a triggering mechanism for the formation of a broken line of isolated cells to the west of the Dallas/Fort Worth metroplex that soon formed into a solid linear MCS. At the center of this line, an embedded supercell developed and moved across Tarrant and Dallas counties, producing several reports of tornadoes and hail up to 7.50 cm (3.00 in). Due to concerns with network communications, only data after 2300 UTC were considered in this study. Additionally, at 2336 UTC, values of FED began to decrease for all cells, until all VHF data across the network were lost after 23:40 UTC (not shown). After this image, FED values began to slowly climb through the 2354 UTC image where values returned to their magnitudes before this data loss. This loss in data occurred as areas of strong convection crossed several of the sensor sites.

The first feature of interest from this date occurs at 2316 UTC in southern Denton County. A large "hook" appendage developed on the southern edge of a large FED maximum (Fig. 3.32). When compared to radar data, the FED minimum encircled by this appendage was located in an area with reflectivity values between 40 and 45 dBZ (Fig. 3.33). An area of cyclonic rotation and a radar hook echo develop on the southern end of this storm by 2332 UTC (Figs. 3.34 and 3.35), signals of tornadic potential with this cell (see discussion on supercells in introduction). This feature quickly dissipated during the next two radar volume scans as the activity to the south of this cell rapidly moved eastward.

At 2324 UTC, a notch began to develop on the west side of the FED maximum located in Denton County (Fig. 3.36). This feature persisted into the network data loss period between 2336 and 2352 UTC. After this data loss, the feature became most pronounced on the 2354 UTC FED image as a sharp notch of low FED values extending into the large FED maximum that had crossed into Collin County (Fig. 3.37). At 2347 UTC, velocity data from the KFWS radar showed outbound velocities of over 80 knots in southeastern Denton County at approximately 6.4 km (21.0 kft). Outbound velocities at approximately 3.9 km (13.0 kft) and 3.0 km (10.0 kft) were 77 and 54 knots, respectively. The 4.3 and 3.4-degree tilts at this time also show a slight bow in reflectivity in this area. At 0001 UTC, the bowing reflectivity was observed on the 2.4 and 1.5-degree tilts, and outbound velocities from the 2.4-degree tilt had increased from 54 knots at 2347 UTC to greater than 64 knots. Outbound velocities in this area on the 1.5-degree scan were greater than 51 knots, at an altitude of approximately 2.1 km (7.1

kft) AGL (Fig. 3.38). A wind gust of 50 knots was reported 0.9 miles northeast of Allen in south central Collin County at 0015 UTC (NCDC 2007).

Another minimum of FED appeared in Dallas County at 2354 UTC, associated with the supercell embedded within the convective line (Fig. 3.39). This feature was located in an area of relatively low radar reflectivity values to the south of a tight radar reflectivity gradient and to the east of a radar hook echo that developed on the 2356 UTC 0.5-degree radar tilt (Fig. 3.40). A strong area of cyclonic rotation persisted in this area for several volume scans, as shown on the 2356 UTC velocity image (Fig. 3.41). At 0000 UTC on 06 April, a tornado was reported 4 miles to the east-northeast of Dallas (NCDC 2007).

3.3.2 Quantitative Analysis

As mentioned in section 3.2.1, analysis for this case began at 2300 UTC, due to data quality concerns related to network communications. Thus, total and CG flash rates are already quite high at the start of the analysis. Also, due to the positioning of the FED core relative to the SCIT derived cell location, data for cell one are from a radius of 20 km from the SCIT cell location before 2338 UTC, while the data after 2352 UTC use a 10 km radius, due to the proximity of other convective cells at that time. Thus, only relative trends, rather than absolute values, should be compared across the period of missing LDAR data for this cell.

The values of MxFED for cell one, which was located in Denton County at 2300 UTC, are shown in Figure 3.42. Three distinct periods of increased MxFED values are visible in the plot. MxFED values increase rapidly between 2310 and 2314 UTC, rising from 4 to 26 flashes min^{-1} km^{-2}. A minimum in MxFED occurred at 2322 UTC, with a reported value of 11 flashes min^{-1} km^{-2}. The second peak in MxFED values occurs at 2328 UTC, with a value of 28 flashes min^{-1} km^{-2}, the highest recorded with this cell before the loss of LDAR data beginning at approximately 2340 UTC. After this peak, the MxFED value decreases quickly to 7 flashes min^{-1} km^{-2} at 2332 UTC. One final peak occurred at 2336 UTC, before MxFED values decreased into the period when LDAR data was unavailable. After LDAR data resumed at approximately 2350 UTC, MxFED values increased to a peak of 21.5 flashes min^{-1} km^{-2} at 2358 UTC. After a decrease in MxFED at 0000 UTC, the 0002 and 0004 LDAR files were also missing. The MxFED value had decreased to 13.5 flashes min^{-1} km^{-2} when data resumed at 0006 UTC, decreasing to 7.5 flashes min^{-1} km^{-2} at 0008 UTC.

AvFED values before the data loss followed the same general pattern of increasing and decreasing values as the MxFED data, although the initial peak in MxFED values at 2314 was not reflected in the AvFED data; values increased gradually until 2320 UTC before decreasing into the missing data period (Fig. 3.42). When LDAR data resumed, AvFED increased to a peak value of 9.97 flashes min^{-1} km^{-2} at 2354 UTC, after which values decreased through the end of SCIT output for this cell. MxGSD values before the LDAR data loss showed the same three active periods as the MxFED data, with the exception of a short decrease in the MxGSD value at 2318 UTC (Fig.

3.43). After LDAR data resumed, MxGSD values climbed to a peak of 24.5 sources min^{-1} km^{-2} at 2354 UTC, a value that was much lower than the peak values before the data loss period, which were between 39 and 54.5 sources min^{-1} km^{-2}. AvGSD values for this cell also showed three periods of increased values during the first half of data for this cell, and a local maximum at 2354 UTC after LDAR data resumed (Fig. 3.43). This peak, with a value of 8.78 sources min^{-1} km^{-2}, was the highest AvGSD value for this cell. MxFIDT values for this cell varied between 1 and 2 flash initiation sources min^{-1} km^{-2} both before and after the period of missing LDAR data, while AvFIDT values showed little variation throughout the cell's lifetime, ranging from 0.5 to 0.65 flash initiation sources min^{-1} km^{-2} (Fig. 3.44).

The VHF total flash rate for this cell increased from 2304 to 2312 UTC, reaching a value of 57 flashes per minute (Fig. 3.45). After a brief decrease at 2314 UTC, the VHF total flash rate reached a peak of 72 flashes per minute at 2326 UTC, the highest total flash rate value for this cell. After decreasing into the period of LDAR data loss, the VHF total flash rate was 39.5 flashes per minute at 2352 UTC. A peak in total flash rate occurred with this cell at 0006 UTC, with a value of 41 flashes per minute before values decreased into the end of SCIT output for this cell. CG flash rates for this cell peaked at 50.5 flashes per minute at 2314 UTC before decreasing into the period of missing data from the LDAR network (Fig. 3.45). A sharp decrease in flash rate was observed at 2334 UTC, with a value of only 22 flashes per minute recorded. The CG flash rate increased from a minimum of 17 flashes per minute at 2342 UTC to 46 flashes per minute at 2352 UTC. The CG flash rate quickly dropped off, with one last peak in

flash rate at 0006 UTC. The ratio of IC flashes to CG flashes was 0.95 for this cell before the LDAR data loss, and 0.81 during the period after LDAR data resumed. The percentage of positive CG flashes was less than 20% for the entire lifetime of the cell, with an average value of 4.5% for the entire study period.

The number of active FED grid boxes is shown in figure 3.46. The pattern of three peaks seen in the other data was also present in the GrFED data. The large difference in GrFED and GrGSD values before and after the loss of LDAR data is due to the need to decrease the radius for data collection from 20 km to 10 km to avoid contamination from adjacent cells. The GrFED value was much less variable during the period after LDAR data resumed, showing only a slight increase before the second data loss period. After data resumed, the GrFED value decreased through the end of SCIT output for this cell. Values of GrGSD followed the same trends as shown in the GrFED data, although the values during the first half of the cell's lifetime were much lower than those for the GrFED data, with an average difference of 100 grid boxes for each data period (Fig. 3.46). GrFIDT values followed similar trends to the AvFED and AvGSD data sets discussed earlier, with two distinct decreases at 2322 and 2332 UTC (Fig. 3.46).

MxFED values for cell two, the embedded supercell that crossed Tarrant and Dallas counties, are shown in Fig. 3.47. MxFED values increased to an initial peak of 10 flashes min^{-1} km^{-2} at 2314 UTC. This cell produced a tornado, rated EF-1 on the enhanced Fujita scale, in Haltom City between 2309 and 2315 UTC, with one fatality reported at a lumberyard. This cell also produced several reports of severe hail during

this period, including a report of 6.35 cm (2.50 in) hail in Saginaw at 2303 UTC. Baseball sized hail (7.0 cm/2.75 in) was observed at WFO FWD, in northeast Ft. Worth, at 2306 UTC, and 4.5 cm (1.75 in) hail damaged many vehicles at North East Mall in the town of Hurst at approximately 2315 UTC. MxFED values increased to 14.5 flashes min^{-1} km^{-2} at 2326 UTC before dropping to only 3 flashes min^{-1} km^{-2} at 2332 UTC. At 2336 UTC the MxFED value reached 22.5 flashes min^{-1} km^{-2}, the highest value observed before the loss of LDAR data at approximately 2338 UTC. Hail 7.60 cm (3.00) in diameter was reported in Colleyville, in northeast Tarrant County, at 2332 UTC. After LDAR data resumed, the MxFED value at 2354 UTC was 23.5 flashes min^{-1} km^{-2}, the highest value reported with this cell. A sharp decrease in MxFED values then occurred into the second period of missing data, with the 0000 UTC MxFED value only at 12.5 flashes min^{-1} km^{-2}. This cell produced another tornado at this time, rated EF-0, four miles to the east-northeast of Dallas, which persisted for only a few minutes. After this time MxFED values decreased through the end of SCIT output for this cell.

AvFED also showed a sharp drop at 2332 UTC, before rapidly increasing to 5.85 flashes min^{-1} km^{-2} at 2336 UTC just prior to LDAR data being lost (Fig. 3.47). After LDAR data resumed at 2354 UTC, AvFED values slowly decreased until the cell dissipated, at approximately 0020 UTC. MxGSD values for this cell showed a quick drop between the first two reported values before three sharp peaks at 2314, 2326, and 2336 UTC (Fig. 3.48). These spikes, with values of 40.5, 26.5, and 57.5 sources min^{-1} km^{-2}, correspond to the peaks found in the MxFED data for this cell. After LDAR data resumed, the MxGSD values decreased through the end of the dataset, from an initial

value of 30.5 flashes min^{-1} km^{-2} at 2354 UTC. AvGSD values for this cell followed very closely to the trends seen in the AvFED data (Fig. 3.48). Values of MxFIDT showed two peaks, one at 2314 UTC and one at 2330 UTC, both with a value of 2.5 flash initiation sources min^{-1} km^{-2}. AvFIDT trends were closer to those of the other data sets, with peaks at 2314, 2326, and 2336 UTC (Fig. 3.49).

Cell two VHF total flash rates increased during the period prior to the LDAR blackout, with a small peak at 2314 UTC before reaching a value of 61.5 flashes per minute at 2328 UTC (Fig. 3.50). The VHF total flash rate decreased after this time into the period of missing LDAR data. After the LDAR data resumed, the VHF total flash rate increased from 38.5 flashes per minute to 48 flashes per minute at 0000 UTC, when the second tornado was reported with this cell. After this time the total flash rate decreased until SCIT output ended for this cell. CG flash rates for this cell also increased early on, although the CG flash rate peaked at 2336 UTC, with a value of 32 flashes per minute (Fig. 3.50). The CG flash rate decreased over the next few time intervals, before increasing to 47 flashes per minute at 2354 UTC. After this peak, the CG flash rate was quite variable, with values ranging between 16 and 32.5 flashes per minute, although the overall trend was that of a decline in CG flash rates. The IC:CG ratio from the period 2300-2338 UTC was 9.28 IC flashes for each CG flash, while in the later period from 2352-0020 UTC it had decreased to only 0.61 IC flashes for each CG lightning flash. There were relatively few positive CG lightning flashes detected with this cell, and the percent positive flashes remained below 15%, with an average value of only 1.6%.

The GrFED and GrGSD values for this cell are shown in Fig. 3.51. Both curves show a drop in the total number of grid boxes containing data at 2332 UTC, as well as a sharp downturn at 2338 UTC before LDAR data was lost. Also plotted on this figure are the GrFIDT values for the cell and the difference between GrFED and GrGSD, labeled as GrDIFF. This difference in grid box counts was most pronounced near 2300 UTC, and again after 0010 UTC, near the end of the radar tracking for this cell. Difference values were at their lowest during a period from roughly 2315 to 2330 UTC, corresponding to the time that the cell passed closest to the center of the LDAR network. Trends in GrFIDT for this cell followed closely to those displayed by the GrGSD data.

3.3.3 Correlation Analysis

Due to the periods of missing data from the LDAR network from this date, correlation coefficients for each cell were only computed for the period between 2300 and 2338 UTC. Correlation coefficients for cell one are displayed in Table 3.4, with the highest correlation between AvFED and total flash rate, a value of 0.76. The rest of the correlation values between total flash rate and the operational lightning products fell between 0.58 and 0.76, with the exception of maximum and average FIDT, which had negative correlation coefficients. Correlation coefficients between CG flash rate and MxFIDT and AvFIDT were also negative, with all other values between 0.44 and 0.72. The correlation coefficient between total flash rate and the CG flash rate was 0.68. Correlation coefficients between the radar derived parameters and the operational total

lightning products were mostly negative, with the strongest linear relationship found between AvFED and SHI, which had a correlation coefficient of -0.72.

Correlation coefficients for cell two are found in Table 3.5. Correlation coefficients between total flash rate and the operational total lightning products were lower for this cell, ranging between -0.24 and 0.51. Correlation values between CG flash rate and the operational total lightning products were also low, between -0.37 and 0.61. The correlation coefficient between the total flash rate and CG flash rate was 0.89, the highest value for this relationship among all five cells. Correlation coefficients between the lightning variables and the radar parameters for this cell were also low, although most values were positive. The highest positive correlation value was 0.43, between total flash rate and VIL, and the most negative value was -0.66, between CG flash rate and MSI.

4. DISCUSSION

Displays of FED and GSD have shown the ability of total lightning data to highlight key characteristics of supercell structure on the dates examined in this study. FED and GSD imagery successfully highlight the radar inferred updraft regions of the cells, as shown by the lightning holes present at two separate times with the northern cell on April 25. The radar reflectivity cross section through the first lightning hole on April 25th clearly shows the vaulted shape of a bounded weak echo region (BWER). Although each of these lightning holes themselves were only apparent on one image of either FED or GSD, both holes evolved into a persistent notch in the lightning data at the same location in the cell as the radar reflectivity hook echo or updraft notch, similar to the lightning notch described in Demetriades et al. (2002). The embedded supercell from April 13th also showed a minimum in FED at 2354 UTC that was clearly associated with the updraft region of this cell. Although this minimum appears to be visually similar to the lightning hole seen with the northern supercell on 25 April, this may be a consequence of its location between the FED maximums associated with the convective core of the supercell and the flanking line to the south. Regardless of whether this feature is a true lightning hole, it does bring the forecaster's attention to the updraft region associated with the main cell. Additionally, the lightning "hook echo" and associated FED minima that developed along the convective line in Denton County at 2316 UTC appears to indicate a strong updraft with the cell just to the north of the main supercell. On April 5th, similar FED updraft notches were present in FED imagery of

the left moving supercell that crossed Dallas County. In this case, the FED provides even greater benefit, as this cell tended not to have a well-defined radar hook echo around the updraft region. The presence of the updraft notch in FED in addition to the tight radar reflectivity gradient on the northwest side of this cell served to highlight it as a left moving supercell, despite the lack of the "classic" supercell shape.

As a consequence of these results and those of other studies discussed earlier it appears that forecasters can use lightning data in D2D as a secondary indication of the presence of a strong updraft associated with a particular cell, as regions within the cell with little intracloud lightning have shown a strong correlation with the thunderstorm updraft (Krehbiel et al. 2000; Goodman et al. 2005; Murphy and Demetriades 2005; Wiens et al. 2005).

In a similar fashion, the rear notch in FED associated with the cell moving across southern Denton and Collin counties on 13 April 2007 appears to highlight an apparent rear inflow jet in this part of the convective line similar to the results of Steiger et al. (2007b). This notch, which first formed at 2124 UTC, became most pronounced on the 2354 UTC FED image. The development of this feature preceded the descent of strong outbound radar velocities to low levels in the KFWS volume scans. No rear inflow notches were readily apparent in radar reflectivity data during this time period with this line. The occurrence of a severe wind gust near Allen in southern Collin County at 0015 UTC suggests that this rear notch may be an FED signature of the potential for severe straight-line wind gusts associated with a linear MCS as in Steiger et al. (2007b). This feature is not to be confused with the "updraft" notches also described in the text. The rear

notch in FED from 13 April is a much larger and more pronounced feature than the updraft notches, and not located in an area of the cell that would suggest an updraft. More cases involving linear systems with severe straight-line winds need to be investigated to determine whether this is an isolated feature or a reliable indication of severe weather potential.

Another very interesting result from the analysis of FED images in this study is the occurrence of FED appendages that appear to signal a tendency for deviant motion with a supercell. On 25 April, the northern supercell develops two appendages during its lifetime that appear to be just to the east of the updraft region of the cell. These appendages developed at 2116 UTC and again between 2132 and 2144 UTC. During both of these times the cell was in the process of shifting to the right of its previous track. Right moving supercells were favored on this day based on the veering of the low-level winds in the 1900 UTC sounding from WFO FWD (not shown). Additionally, two similar appendages were observed to develop with the left moving supercell from April 5th. Again, each of these appendages developed at approximately the same time as the cell motion became more deviant, this time to the left. After the development of each of these appendages, the highest values of FED appeared to "roll" towards these appendages, co-locating the highest FED values with the strongest reflectivity gradient with the cell. This tendency appears to follow the observation from Steiger (2007a) that the highest values of FED are found with the strongest gradients in reflectivity. These observations appear to show that FED not only indicates updraft regions of a supercell but may also indicate when a new updraft is developing on the preferred side, leading to

a shift in cell track. This ability to highlight updraft development and propagation on a timescale faster than the update time of the WSR-88D makes the LDAR data an important resource for forecasters to maintain situational awareness during warning operations.

It is worth noting that each lightning hole on 4/25/2005 was far more evident in GSD imagery than in FED, as the method by which FED is calculated tends to fill in bounded areas without VHF sources. This advantage of GSD over FED is good reason for forecasters to check both products, at least at distances close enough to the LDAR network that GSD data are not significantly degraded by decreasing detection efficiency. Carey et al. (2005) evaluated source detection efficiency with the D/FW LDAR network for one case date in 2004 and found that source detection efficiency decreased to 10% at a range of 50 kilometers from the center of the LDAR network. An example of the decrease in source density performance is shown in Fig. 3.51. The difference between the number of grid boxes containing FED data vs. GSD data, labeled as GrDIFF, shows a decreasing trend during the first half of the cell tracking period, with the lowest values coming between the period between 2320 UTC and 2335 UTC. After LDAR data resumed at 2354 UTC, this value had increased again. This period of low GrDIFF values corresponds to the time when the cell passed closest to the network center, located near D/FW International Airport (Fig. 2.1). While the cell was farther from the network center, fewer sources were detected, thus the number of grid boxes containing GSD data decreased. FED, however, is created using output from a flash algorithm, and thus is able to recreate flashes as long as the temporal and spatial criteria between sources are

still being met. This relative advantage of FED over GSD makes it the preferred product for display in AWIPS at WFO FWD.

The results of this study also appear to support the hypothesis that trends in FED intensity show promise in indicating the potential for severe weather from a cell. Several efforts have been made to correlate changes in total lightning flash rates with the occurrence of severe weather at the surface (Williams et al. 1999; Goodman et al. 2005; Bridenstine et al. 2005; Steiger et al. 2007a,b), with some interesting results in regard to spikes in total flash rate and changes in altitude of lightning activity. Although FED values cannot be considered interchangeable with flash rates they do appear to show a similar trend with respect to severe weather reports. Jumps in FED values on April 25th were visible in D2D before reports of tornadoes and large hail for each cell. FED values increased sharply for cell two 9 minutes prior to the first reported tornado, and 14 minutes before the second tornado. Lead times were lower for the northern cell, with a jump in FED values beginning at 2108 UTC, 6 minutes prior to a reported tornado at 2114 UTC in southern Tarrant County. A peak in lightning activity occurred at the same time as the reported tornado in Mansfield at 2130 UTC, although an increase in MxFED values between 2124 and 2126 UTC was noticeably greater than the overlying trend of increasing values between 2114 and 2130 UTC. Another tornado was reported south of Cedar Hill in Dallas County at 2135 UTC, although the radar data from KFWS suggests that this time might be slightly off from the actual event time. Based upon radar reflectivity and velocity data, the tornado near Cedar Hill probably occurred closer to 2145 UTC. A jump in FED values began at 2132 UTC, suggesting a possible lead time

for this event of up to 13 minutes. Reports of severe hail with these cells tended to occur either during or just after a lightning jump, as did those of the left moving supercell on April 5th, which showed two distinct spikes in lightning activity that were 8 and 10 minutes prior to each of the reports of severe hail with this cell in Dallas County. This supports the theory that total lightning activity is related to the strength of the cell's updraft, as a strengthening updraft would lead to a greater threat of severe hail.

A key objective of this work was to diagnose the relationship between total flash rate and the operational products in use at WFO FWD, specifically FED. While prior studies have worked to establish the relationship between total flash rate and convective cell intensity and severity, no known work has been done to establish a relationship between total flash rate and FED. The results of correlating total flash rate and maximum and average FED values are shown in figures 4.1 and 4.2. Each cell's lightning activity was evaluated at multiple radii from the SCIT determined cell location. Values of FED were found to have a strong positive correlation with total flash rate, with all correlation coefficients of MxFED and AvFED greater than 0.5 for all 21 samples in this study. MxFED was found to have an average correlation coefficient with total flash rate of 0.73, out of a range from 0.51 to 0.91. The lower values in this range were observed with the cells on 13 April 2007, when convection was considerably less isolated than what was observed in the other two cases. However, despite the relatively high correlation between FED values and total flash rate, time series trends of total flash rate were smoother than those of FED, which appeared to have more noise. Thus, while trends in FED are certainly useable for real time tracking of total lightning activity

within a cell, the total flash rate may produce more clear signals related to severe weather (i.e., lightning jumps).

The other operational total lightning products also had positive correlation coefficients with total flash rate, although the values were generally lower except for GrFIDT, which also showed a strongly positive correlation to total flash rate. This result makes sense, given the nature of the FIDT product. GrFIDT is the total number of 1 km grid boxes containing a flash initiation point, which, in effect, is a very coarse measurement of the total flash rate. The slightly lower correlations between total flash rate and maximum and average values for FIDT may be due to differences in how the two flash algorithms handle flashes with few detected sources. The IDL flash algorithm used to create total flash rate in this study requires at least 3 sources to produce a valid flash. Vaisala's flash algorithm that is used to create the FED product may require a higher number of detected sources per flash. The three-source threshold used for flash rate calculations is designed to eliminate "singletons", or single source flashes. Singletons were discussed in Williams et al. (1999), with their results showing that the number of single source flashes increased from 12% to 30% with increasing range from the center of the Kennedy Space Center (KSC) LDAR network.

Correlations between CG flash rate and the operational total lightning products showed a few strong positive correlations, but there was much greater spread in these values, which were both positive and negative. This suggests that the relationship between CG flash rate and FED is much weaker than that between FED and total flash rate. However, MacGorman et al. (2007) showed that convective cells in close

proximity to each other, or those displaying complex structure, tended to have enhanced CG flash rates. This may have contributed to the lower correlations seen between FED and CG flash rate for the left moving supercell on 05 April 2005 and the embedded supercell on 13 April 2007.

While this study attempted to evaluate the relationships between total lightning and radar-derived products, there were several issues present with the radar data available for this study that affected this analysis. As mentioned previously, the radar data for the April 25, 2005 cells were from the KDYX WSR-88D. This radar is located well to the west of the Dallas/Fort Worth metroplex, and as such the values sampled by the radar may be questionable. Of particular concern are the MSI values for this cell, due to the altitude limit imposed upon that product. MSI is calculated using only data from the lowest 8 km of a cell's depth. At 2100 UTC, the first time examined in this study, cell two, the closer of the two cells, was approximately 165 km from the KDYX radar. At this range, the effect of earth's curvature is such only the lowest four elevation angles used in VCP 11 are below 8 km. Thus, the vertical integration of rotational strength used in MSI is only based on at most 4 samples per radar volume scan. Other issues exist at such great range, such as the tendency to overestimate values of VIL for distant convection (Brown et al. 2000). The range issues were not as problematic on the other two case dates, although the SCIT cell tracking was much less consistent with VCP 11, which was used with the KFWS radar on both 05 April 2005 and 13 April 2007. The loss of VIL, SHI, and MSI data each time the radar lost tracking for a cell made it difficult to correlate these values to total lightning over longer periods of time. An

interesting aside to this issue is the performance of VCP 12 versus VCP 11. VCP 12 was designed with the intent to increase sampling at low levels and for more stable cell tracking and algorithm performance (Lee and Steadham 2004). This was definitely seen in this study, as the two cells that were sampled from KDYX using VCP 12 were tracked and maintained the same cell ID numbers throughout the study period, despite being located very distant from the radar.

The results of the comparison between radar and total lightning data in this study showed that values of MxFED had a very weak positive correlation with VIL, while the other total lightning products had correlation coefficients with VIL that were either widely spread or very close to zero. Similarly, the correlation between total flash rate and VIL was found to be weakly positive for most of the cells. Correlation coefficients between SHI and the total lightning products varied widely, with no consistent relationship visible. The results from this study showed a weak negative correlation between MSI and both FED and total flash rate. This result appears to be counter to those found in previous studies, such as Williams et al. (1999), which found that for tornadic thunderstorms in Florida, the time of greatest rotation aloft was concurrent to the time of greatest total flash rates. A similar result was found in Gatlin and Goodman (2004), where increases in low level shear were well correlated to jumps in total flash rate. There were several issues with the radar data used for the cases in this study, discussed previously, which could have caused improper results from this analysis. In particular, the strongest correlation values for MSI were from the cells on April 25, 2005, which were measured from the KDYX radar, located well to the west of the D/FW

metro area. Thus, this result may not be an accurate depiction of the relationship between mesocyclone strength and total flash rate or FED. The full set of correlation coefficients between total and CG flash rates, the operational lightning products (FED, GSD, and FIDT), and radar variables are located in Appendix B.

Another result of this study that has operational implications is that the usefulness of the LDAR data appears to be highly dependent upon the distance of the cell from the network and the performance ability of the network on a given day. On April 25th, the southern cell consistently displayed much lower values of FED and GSD than the northern cell, despite having higher values of radar reflectivity and more severe weather reports. Additionally, on this date, one sensor within the network stopped reporting for a 15-minute period from approximately 2045 UTC to 2100 UTC. The loss of data from this sensor led to a dramatic decrease in FED and GSD values for this time period, much greater than any of the decreases in activity associated with the lightning jumps mentioned previously (Fig. 4.3). Another example of such a situation occurs in the April 13th case, as FED and GSD data drop off and return for all cells between 2336 and 2354 UTC. While sharp decreases in FED values for one particular cell should signal a forecaster that a severe weather event might be imminent; a similar decrease with all cells is more likely a network detection issue, and not the harbinger of widespread severe weather. As detection ability can vary day to day given the status of the network sensors, forecasters should be kept aware of any situations (maintenance, communication problems, etc.) that would affect the data being sent to the WFO, so that

artificial signals are not treated as indicative of the actual convective or severe activity within a given cell.

While there is encouraging evidence that trends within the lightning data can aid in the warning decision process, the FED values with each cell varied substantially throughout the entire study. In the case of April 5, the cell with the highest FED values showed FED spikes without producing any severe weather, indicating that there are possibly other considerations beyond the maximum flash rate or FED value. More research is needed to quantify what rates of change of total flash rate or FED are significant in order to reduce the false alarm potential associated with jumps in the lightning data. Data from the North Alabama Lightning Mapping Array are being used to develop a lightning jump algorithm that may be able to predict the potential for tornadic activity based upon the total flash rate. Early results from this work have shown probabilities of detection and critical skill index values that compare favorably to the performance of the Tornado Vortex Signature (TVS) algorithm in use operationally with the WSR-88D radar (Gatlin and Goodman 2008). This is perhaps the greatest benefit of total lightning trend data on days with widespread convection, as they can be used to highlight cells that may be more likely to produce severe weather, which could then be monitored with greater emphasis from the warning forecaster (Goodman et al. 2005).

Although the results of the quantitative comparison between total lightning and radar values for these cases may be questionable, the LDAR network has two relative advantages with regard to the WSR-88D that make it an important tool in the analysis of severe convective cells. The first is the ability of the LDAR network to rapidly update

images with respect to the WSR-88D. The current two-minute display period of the LDAR data at WFO FWD produces images twice as fast as VCP 12, the faster of the WSR-88D precipitation mode scanning strategies. This update period is also not fixed; if desired, total lightning parameters could be updated with even higher frequency in situations where cells produce large amounts of total lightning. Thus, total lightning data can provide information on the location and strength of a convective scale at a much greater temporal resolution than the WSR-88D. Also, when the radar and LDAR networks are located in close proximity, as is the case for KFWS and the D/FW LDAR network, the LDAR network can be relied upon in situations where the radar cannot accurately sample cells at very close ranges. While the usefulness of the WSR-88D decreases as cells move into close proximity to the radar, the LDAR data is improving as the cells move within the network, where detection efficiency and location accuracy are highest (Carey et al. 2005). Thus, the performance of the LDAR network is increasing as the performance of the radar decreases. This relationship between the two observing systems, coupled with the ability of the LDAR data to show important information on cell structure and intensity, make the total lightning data an important compliment to the WSR-88D in the warning decision process.

The results of this study support the conclusion that FED is the preferred product for displaying total lightning information in plan view, while the total lightning flash rate is the better product for tracking values in real time. It remains to be decided if either method is superior to the other for use by the NWS during warning operations. The most obvious answer, and probably the best one, is to use both. While future work may refine

the definition of a lightning jump and the ability to diagnose them in real time, the plan view displays of FED in this study were very effective in highlighting the most active cells, as well as important information on their structure and movement. This situation has a direct analog in the use of radar data. While numerous algorithms and indices have been developed to diagnose the strength of a convective cell, meteorologists still rely heavily on displays of radar reflectivity and velocity data and their qualitative interpretation (e.g., hook echo, WER, notches, velocity couplets) during warning operations. A similar approach of balanced use between qualitative and quantitative measures of total lightning provides the greatest added benefit to forecasters in the warning decision process.

5. SUMMARY

The following points summarize the findings of this study:

1) Flash extent density (FED) values were found to be positively correlated with total flash rate. Correlation coefficient values ranged between 0.51 and 0.91 for all cells, with an average value of 0.73. Thus, although total flash rate is not delivered in real time to meteorologists at WFO FWD, results from previous severe weather research using total flash rate can be applied to warning operations at WFO FWD using the FED data provided by Vaisala, Inc. from the D/FW LDAR network. However, due to the greater noise in time series plots of FED values, total flash rate was found to be the better product for time series graphs of the cells studied in this case.

2) Qualitative displays of total lightning data, including both FED and GSD, can be used by forecasters as indicators of the presence of a strong updraft within a convective cell. Regions of little total lightning activity within a cell, including features such as lightning holes and updraft notches, have been observed to occur with strong updrafts in cells on each of the three case dates examined in this study.

3) FED appendages were observed with multiple cells prior to and during shifts in cell track in radar reflectivity images. These appendages may be an indicator of updraft redevelopment on the preferred flank, signaling the potential for deviant motion with that cell. Forecasters at WFO FWD should be aware of these features, as they may signal a change in cell motion before the next radar volume scan is available.

4) FED "jumps" or sharp increases in the maximum FED value for a cell have been shown to occur prior to tornadogenesis with several cells examined in this study. These jumps occurred up to 14 minutes before the reported time of the tornado. Additionally, FED jumps were associated with numerous reports of severe hail in both tornadic and non-tornadic thunderstorms. These jumps may be indications of a strengthening cell updraft, and forecasters should be aware of the increased potential for severe weather with that cell. However, there was significant variability in FED values throughout each cell's lifetime, and further research will be needed to evaluate which changes are FED jumps, and which ones are not important indications of cell intensity.

5) Total lightning data from the LDAR network provides a much more complete picture of a convective cell's electrical activity compared to CG lightning data. Comparison of total lightning flash rate and CG flash rate showed that the ratio of IC flashes to CG flashes was usually between 6 and 13 IC flashes for each CG lightning flash. The low IC:CG ratios observed on April 13, 2007 were likely due to the non-isolated nature of the convection on that date. Due to the close proximity of other cells, CG flash rates may have been enhanced, either physically (as suggested in MacGorman et al. 2007), or artificially, as flashes that originated outside of the cell study domain contacted the ground inside the cell domain.

6) The ability of FED displays to highlight changes in cell intensity and movement make it an important addition to the WSR-88D data used during warning operations. This is especially true in situations where the radar may not be adequately sampling a cell at very close range, or if the radar were inoperative during a severe weather event.

7) The performance of the LDAR network appears to be dependent upon both the distance of the cell from the network and the operational status of the network sensors. Forecasters must be educated on the strengths and weaknesses of the LDAR data, as well as informed of changes in the status of the network that may affect performance, otherwise warning forecasters may misinterpret network artifacts as physical changes in the electrical structure of a convective cell.

Although the results of this study have shown great promise for the ability of total lightning data to improve the warning decision process, many more cases will need to be investigated to determine how total lightning data is most useful to forecasters in real time operations. The two new sensors added to the D/FW LDAR network after the dates in this study should improve network performance, and severe weather cases from after this network upgrade need to be studied in order to evaluate its performance versus the cases in this study and other from prior to the network upgrade. Additional research is also needed to evaluate FED imagery associated with severe straight-line wind events, to determine if the FED rear notch observed in this case is an indicator of such events. Several of these events occurred in the Dallas/Fort Worth metroplex in the spring of 2008.

Additionally, future work is needed to compare FED values to radar parameters not tested in this study. While the focus of this work was to use radar indicators currently available to forecasters at WFO FWD, other measures of intensity that have shown high correlations with the total flash rate such as vertically integrated ice (VII: Motley 2006). The planned upgrade of the WSR-88D to dual polarization will allow for

the comparison of FED with graupel volume and mass within the cell, a quantity that has shown to be highly correlated with the total flash rate (Carey and Rutledge 1996, 2000; Wiens et al. 2005).

REFERENCES

Andra, D. L., E. M. Quoetone, and W.F. Bunting, 2002: Warning decision making: the relative roles of conceptual models, technology, strategy, and forecaster expertise on 3 May 1999. *Wea. Forecasting*, **17**, 559–566.

Biagi, C. J., K. L. Cummins, K. E. Kehoe, and E. P. Krider, 2007: National Lightning Detection Network (NLDN) performance in southern Arizona, Texas, and Oklahoma in 2003-2004. *J. Geophys. Res.*, **112**, D05208, doi: 10.1029/2006JD007341.

Bluestein, H. B., 1993: *Principles of Kinematics and Dynamics. Vol. II, Synoptic Dynamic Meteorology in Midlatitudes*. Oxford University Press, 594 pp.

_____, and D. R. MacGorman, 1998: Evolution of cloud-to-ground lightning characteristics and storm structure in the Spearman, Texas tornadic supercells of 31 May 1990. *Mon. Wea. Rev.*, **126**, 1451-1467.

Boccippio, D. J., K. L. Cummins, H. J. Christian, and S. J. Goodman, 2001: Combined satellite- and surface-based estimation of the intracloud–cloud-to-ground lightning ratio over the continental United States. *Mon. Wea. Rev.,* **129**, 108–122.

Bridenstine, P. V., C. B. Darden, J. Burks, and S. J. Goodman, 2005: The application of total lightning data in the warning decision making process. *Conference on Meteorological Applications of Lightning Data*, San Diego, CA, Amer. Meteor. Soc. CD preprints.

Brown, R. A., V. T. Wood, and D. Sirmans, 2000: Improved WSR-88D scanning strategies for convective storms. *Wea. Forecasting*, **15**, 208–220.

Browning, K. A., 1964: Airflow and precipitation trajectories within severe local storms which travel to the right of the winds. *J. Atmos. Sci.*, **21**, 634-39.

_____, 1977: The structure and mechanism of hailstorms. *Hail: A Review of Hail Science and Hail Suppression, Meteor. Monogr.*, No. 38, Amer. Meteor. Soc., 1-39.

Burgess, D. W., and L. R. Lemon, 1991: Characteristics of mesocyclones detected during a NEXRAD test. *25th Int. Conf. on Radar Meteorology*, Paris, France, Amer. Meteor. Soc., preprints.

Carey, L. D. and S. A. Rutledge, 1996: A multiparameter radar case study of the microphysical and kinematic evolution of a lightning producing storm. *Meteorology and Atmospheric Physics*, **59**, 33-64.

_____, and _____, 1998: Electrical and multiparameter radar observations of a severe hailstorm. *J. Geophys. Res.*, **103**, 13,979-14,000.

_____, and _____, 2000: The relationship between precipitation and lightning in tropical island convection: a C-band polarimetric radar study. *Mon. Wea. Rev.*, **128**, 2687-2710.

_____, and _____, 2003: Characteristics of cloud-to-ground lightning in severe and nonsevere storms over the central United States from 1989-1998. *J. Geophys. Res.*, **108**, doi: 10.1029/2002JD002951.

_____, W.A. Petersen, and S.A. Rutledge, 2003: Evolution of cloud-to-ground lightning and storm structure in the Spencer, South Dakota, tornadic supercell of 30 May 1998. *Mon. Wea. Rev.*, **131**, 1811–1831.

_____, M. J. Murphy, T. L. McCormick, and N. W. S. Demetriades, 2005: Lightning location relative to storm structure in a leading-line, trailing-stratiform mesoscale convective system. *J.Geophys. Res.,* **110**, D03105, doi:10.1029/2003JD00437.

Carpenter, E. E., A. E. Gerard, and E. R. Agre, 2004: An analysis of NSSL WDSS circulation parameters during 1999-2000 tornado events in the NWS Jackson, Mississippi, county warning area. *20th Conference on Severe Local Storms*, Orlando, FL, Amer. Meteor. Soc., Boston, Massachusetts.

Crum, T. D., and R. L. Alberty, 1993: The WSR-88D and the WSR-88D operational support facility. *Bull. Amer. Meteor. Soc.*, **74**, 1669–1687.

Cummins, K. L., M. J. Murphy, E. A. Bardo, W. L. Hiscox, R. B. Pyle, and A. E. Pifer, 1998: A combined TOA/MDF technology upgrade of the U. S. National Lightning Detection Network. *J. Geophys. Res.*, **103**, 9035-9044.

_____, J. A. Cramer, C. J. Biagi, E. P. Krider, J. Jerauld, M. A. Uman, and V. A. Rakov, 2006: The U.S. National Lightning Detection Network: post-upgrade status. *2nd Conf. on Meteorological Applications of Lightning Data*, Atlanta, GA, Amer. Meteor. Soc., CD preprints.

Demetriades, N., M. J. Murphy, and R. L. Holle, 2002: Lightning Detection and Ranging (LDAR) II: results from Vaisala-GAI's Dallas-Fort Worth research network and Kennedy Space Center's operational network. *International Lightning Detection Conference,* Tucson, AZ, Conference Preprint.

Doswell, C. A. III and D. W. Burgess, 1993: Tornadoes and tornadic storms: a review of conceptual models. The tornado: its structure, dynamics, prediction, and hazards (Church et al., eds). Amer. Geophys. Union, *Geophys. Monogr.* 79, 161-172.

Ferree, J.T., and E.M. Quoetone, 2001: Using the Warning Event Simulator. *Interactive Symposium on AWIPS*, Orlando, FL, Amer. Meteor. Soc., CD preprints.

Fujita, T. T., 1981: Tornadoes and downbursts in the context of generalized planetary scales. *J. Atmos. Sci.*, **38**, 1511–1534.

Gatlin, P. N., and S. J. Goodman, 2004: Signatures in lightning activity during Tennessee valley severe storms of 5-6 May 2003. *22nd Conference on Severe Local Storms,* Hyannis, MA, Amer. Meteor. Soc., CD preprints.

_____, and _____, 2008: Severe weather precursors in the lightning activity of Tennessee valley thunderstorms. *3rd Conference on Meteorological Applications of Lightning Data*, New Orleans, LA, Amer. Meteor. Soc.

Greene, D. R., and R. A. Clark, 1972: Vertically integrated liquid water—a new analysis tool. *Mon. Wea. Rev*., **100**, 548–552.

Goodman, S. J., and Coauthors, 2005: The North Alabama Lightning Mapping Array: recent severe storm observations and future prospects. *Atmos. Res*., **76**, 423-437.

Houze, R. A., M. Biggerstaff, S. Rutledge, and B. Smull, 1989: Interpretation of Doppler weather radar displays of midlatitude mesoscale convective cystems. *Bull. Amer. Meteor. Soc.*, **70**, 608–619.

_____, B. F. Smull, and P. Dodge, 1990: Mesoscale organization of springtime rainstorms in Oklahoma. *Mon. Wea. Rev*., **118**, 613–654.

Jayaratne E. R., C. P. R. Saunders, and J. Hallet, 1983: Laboratory studies of the charging of soft hail during ice crystal interactions. *Quart. J. Roy. Meteor. Soc.*, **109**, 609-630.

Johns, R. H., and C. A. Doswell, 1992: Severe local storms forecasting. *Wea. Forecasting*, **7**, 588–612.

Johnson, J. T., P. L. MacKeen, A. Witt, E. D. Mitchell, G. J. Stumpf, M.D. Eilts, and K. W. Thomas, 1998: Storm cell identification and tracking algorithm: an enhanced WSR-88D algorithm. *Wea. Forecasting,* **13**, 263-276.

Kitzmiller, D. H., W. E. McGorvern, and R. F. Saffle, 1995: The WSR-88D severe weather potential algorithm. *Wea. Forecasting*, **10**, 141-159.

Klemp, J. B., and R. B. Wilhelmson, 1978: Simulations of right- and left-moving storms produced through storm splitting. *J. Atmos. Sci.*, **35**, 1097–1110.

_____, 1987: Dynamics of tornadic thunderstorms. *Ann. Rev. Fluid Mech.*, **19**, 1-33.

Koshak, W.J., and R. J. Solakiewicz, 1996: On the retrieval of lightning radio sources from time-of-arrival data. *J. Geophys. Res.*, **101**, 26631-26640.

_____, and Coauthors, 2004: North Alabama Lightning Mapping Array (LMA): VHF source retrieval algorithm and error analysis. *J. Atmos. Oceanic Technol.,* **21**, 543-558.

Krehbiel, P. R., 1986: The electrical structure of thunderstorms. *The Earth's Electrical Environment*, National Acad. Press, 99-113.

_____, R. J. Thomas, W. Rison, T. Hamlin, and M. Davis, 2000: GPS-based mapping system reveals lightning inside storms. *EOS*, **81**, 21-22, 25.

_____, and Coauthors, 2006: The Washington DC metro area Lightning Mapping Array. American Geophysical Union, Fall Meeting 2006.

_____, W. Rison, R. Thomas, N. O'Connor, 2008: Comparison of LMA and LDAR-II observations in the Dallas-Ft. Worth LDAR-II network. *International Lightning Detection Conference*, Tucson, AZ.

Krider, E. P., R. C. Noggle, and M. A. Uman, 1976: A gated wideband magnetic direction finder for lightning return strokes. *J. Appl. Meteor.*, **15**, 301-306.

_____, R. C. Noggle, A. E. Pifer, and D. L. Vance, 1980: Lightning direction-finding systems for forest fire detection. *Bull. Amer. Meteor. Soc.*, **61**, 980-986.

Lakshmanan, V., T. Smith, G. Stumpf, and K. Hondl, 2007: The Warning Decision Support System–Integrated Information. *Wea. Forecasting*, **22**, 596–612.

Lang, T. J., S. A. Rutledge, J. E. Dye, M. Venticinque, P. Laroche, and E. Defer, 2000: Anomalously low negative cloud-to-ground lightning flash rates in intense convective storms observed during STERAO-A. *Mon. Wea. Rev.,* **128**, 160–173.

_____, and Coauthors, 2004: The Severe Thunderstorm Electrification and Precipitation Study. *Bull. Amer. Meteor. Soc.*, **85**, 1107-1125.

Lee, R. R., and R. M. Steadham, 2004: WSR-88D algorithm comparisons of VCP 11 and new VCP 12. *20th Conference on Interactive Information and Processing Systems (IIPS) for Meteorology, Oceanography, and Hydrology*, Seattle, WA, American Meteorological Society. CD Preprint.

Lemon, L. R., and C. A. Doswell III, 1979: Severe thunderstorm evolution and mesocyclone structure as related to tornadogenesis. *Mon. Wea. Rev.*, **107**, 1184-97.

Lennon, C. L., 1975: LDAR – a new lightning detection and ranging system. *Eos, Trans. AGU*, **56**, 991.

_____, and L. Maier, 1991: Lightning mapping system. *Proc. 1991 Int. Aerospace and Ground Conf. on Lightning and Static Electricity, Cocoa Beach, Florida*, vol. II, pp. 89/1-10, NASA Conf. Publ. 3106.

Lojou, J-Y. and K. L. Cummins, 2005: On the representation of two- and three-dimensional total lightning information. *Extended Abstracts, Conf. on Meteorological Applications of Lightning Data, San Diego, CA, Amer. Meteor. Soc., CD preprints.*

MacGorman, D. R., and W. D. Rust, 1998: *The Electrical Nature of Storms*. Oxford University Press, 422 pp.

_____, W. D. Rust, P. Krehbiel, W. Rison, E. Bruning, and K. Wiens, 2005: The electrical structure of two supercell storms during STEPS. *Monthly Weather Review*, **133,** 2583-2607.

_____, T. Filiaggi, R. L. Holle, and R. A. Brown, 2007: Negative cloud-to-ground lightning flash rates relative to VIL, maximum reflectivity, cell height, and cell isolation. *J. Lightning Res.*, **1**, 132-147.

Mach, D. M., D. R. MacGorman, W. D. Rust, and R. T. Arnold, 1986: Site errors and detection efficiency in a magnetic direction-finder network for locating lightning strikes to ground. *J. Atmos. Oceanic Technol.*, **3**, 6774.

Maier, L., C. Lennon, T. Britt, and S. Schaefer, 1995: LDAR system performance and analysis. *Proc. 24th Int. Conf. Cloud Physics*, Dallas, Texas, paper 8.9, American Meteorological Society, Boston, Massachusetts.

Marshall, T. C., and W. D. Rust, 1991: Electric field soundings through thunderstorms. *J.Geophys. Res.*, **96**, 22297-22306.

_____, M. P. McCarthy, and W. D. Rust, 1995: Electric field magnitudes and lightning initiation in thunderstorms. *J. Geophys. Res.*, **100**, 7097-7103

Mazur, V., E. Williams, R. Boldi, L. Maier, and D. E. Proctor, 1997: Initial comparison of lightning mapping with operational time of arrival and interferometric systems. *J. Geophys. Res.,* **102**, 11071-11085.

McCormick, T. L., 2003: Three dimensional radar and total lightning characteristics of mesoscale convective systems. M.S. thesis, Dept. of Marine, Earth and Atmospheric Sciences, North Carolina State University, 354 pp.

Motley, S. M., 2006: Total lightning characteristics of ordinary convection. M.S. thesis, Dept. of Atmospheric Sciences, Texas A&M University, 165 pp.

Murphy, M. J., and N. W. S. Demetriades, 2005: An analysis of lightning holes in a DFW supercell storm using total lightning and radar information. *Extended Abstracts*, *Conf. on Meteorological Applications of Lightning Data*, San Diego, CA, Amer. Meteor. Soc., CD preprints.

NCDC, 2005: *Storm Data*. Vol. 47, No. 4, 264 pp. [Available from National Climatic Data Center, Federal Building, 151 Patton Ave., Asheville, NC 28801.]

_____, 2007: *Storm Data*. Vol. 49, No. 4, 318 pp. [Available from National Climatic Data Center, Federal Building, 151 Patton Ave., Asheville, NC 28801.]

NWS, 2005: Working Together to Save Lives: National Weather Service strategic plan for 2005-2010. National Oceanic and Atmospheric Administration, 33 pp.

Oetzel, G. N., and E. T. Pierce, 1969: VHF technique for locating lightning. *Radio Sci*., **4**, 199-201.

OFCM, 2006a: *Federal Meteorological Handbook No. 11 Doppler radar meteorological observations Part C: WSR-88D products and algorithms*. FCM-H11C-2006, 451 pp. [Available from Office of the Federal Coordinator for Meteorology 8455 Colesville Road, Suite 1500 Silver Spring, MD 20910.]

_____, 2006b: *Federal Meteorological Handbook No. 11, Doppler radar meteorological observations Part D: WSR-88D systems description and operational applications*. FCM-H11D-2006, 169 pp. [Available from Office of the Federal Coordinator for Meteorology 8455 Colesville Road, Suite 1500 Silver Spring, MD 20910.]

OFCM, 2007: *Federal Meteorological Handbook No. 11 Doppler radar meteorological observations Part A: system concepts, responsibilities, and procedures*. FCM-H11A-2007, 15 pp. [Available from Office of the Federal Coordinator for Meteorology 8455 Colesville Road, Suite 1500 Silver Spring, MD 20910.]

Orville, R. E., R. W. Henderson, and L. F. Bosart, 1983: An East Coast lightning detection network. *Bull. Amer. Meteor. Soc*., **64**, 1029-1037.

_____, and G. R. Huffines, 1999: Lightning ground flash measurements over the contiguous United States: 1995-1997. *Mon. Wea. Rev.,* **127**, 2693-2703.

_____, 2008: Development of the National Lightning Detection Network. *Bull. Amer. Meteor. Soc.*, **89**, 180-190.

Patrick, G. R., and N. W. S. Demetriades, 2005: Using LDAR II total lightning data in an operational setting: experiences at WFO Fort Worth, TX. *21st Conference on Weather Analysis and Forecasting, 17th Conference on Numerical Weather Prediction*, Washington, D.C., Amer. Meteor. Soc.

Perez, A. H., L. J. Wicker, and R. E. Orville, 1997: Characteristics of cloud-to-ground lightning associated with violent tornadoes. *Wea. Forecasting*, **12**, 428-437.

Polger, P. D., B. S. Goldsmith, R. C. Pryzwarty, and J. R. Bocchieri, 1994: National Weather Service warning performance based on the WSR-88D. *Bull. Amer. Meteor. Soc.,* **75,** 203 -214.

Proctor, D.E., 1971: A hyperbolic system for obtaining VHF radio pictures of lightning. *J. Geophys. Res.,* **76**, 1478-1489.

_____, 1981: VHF radio pictures of cloud flashes. *J. Geophys. Res.,* **86**, 4041-4071.

Przybylinski, R. W., 1995: The bow echo: observations, numerical simulations, and severe weather detection methods. *Wea. Forecasting*, **10**, 203-218.

Rakov, V. A., and M. A. Uman, 2003: *Lightning: Physics and Effects*. Cambridge University Press, 687 pp.

Reynolds, S. E., M. Brook, and M. F. Gourley, 1957: Thunderstorm charge separation. *J. Meteor.*, **14**, 426-436.

Rison, W., R. J. Thomas, P. R. Krehbiel, T. Hamlin, and J. Harlin, 1999: A GPS-based three-dimensional lightning mapping system: initial observations in central New Mexico. *Geophys. Res. Lett.*, **26**, 3573-3576.

Rotunno, R., 1981: On the evolution of thunderstorm rotation. *Mon. Wea. Rev*., **109**, 577–586.

_____, R., and J. Klemp, 1985: On the rotation and propagation of simulated supercell thunderstorms. *J. Atmos. Sci.*, **42**, 271–292.

Saunders, C. P. R., 1993: A review of thunderstorm electrification processes. *J. Appl. Meteor.,* **32**, 642-655.

Serafin, R.J., and J.W. Wilson, 2000: Operational weather radar in the United States: progress and opportunity. *Bull. Amer. Meteor. Soc.*, **81**, 501–518.

Steiger, S. M., R. Orville, and L. Carey, 2007a: Total lightning signatures of thunderstorm intensity over North Texas. Part I: supercells. *Mon. Wea. Rev.,* **135**, 3281-3302.

_____, _____, and _____, 2007b: Total lightning signatures of thunderstorm intensity over North Texas. Part II: mesoscale convective systems. *Mon. Wea. Rev.,* **135**, 3303-3324.

Stolzenburg, M., W. D. Rust, and T. C. Marshall, 1998: Electrical structure in thunderstorm convective regions, 2. Isolated storms. *J. Geophys. Res.*, **103**, 14079-14096.

Stout, G. E., and F. A. Huff, 1953: Radar records Illinois tornadogenesis. *Bull. Amer. Meteor. Soc.*, **34**, 281-284.

Stumpf, G. J., A. Witt, E. D. Mitchell, P. L. Spencer, J. T. Johnson, M. D. Eilts, K. W. Thomas, and D. W. Burgess, 1998: The National Severe Storms Laboratory Mesocyclone Detection Algorithm for the WSR-88D. *Wea. Forecasting*, **13**, 304–326.

Takahashi, T., 1978: Riming electrification as a charge generation mechanism in thunderstorms. *J. Atmos. Sci*., **35**, 1536-48.

Thomas, R. J., P. R. Krehbiel, W. Rison, S.J. Hunyady, W.P. Winn, T. Hamlin, and J. Harlin, 2004: Accuracy of the Lightning Mapping Array. *J. Geophys. Res.*, **109**, doi:10.1029/2004JD004549.

Uman, M. A., and E. P. Krider, 1982: A review of natural lightning: experimental data and modeling. *IEEE Transactions on Electromagnetic Compatibility*, **2**, 79-112.

_____, 1987: *The Lightning Discharge*. International Geophysics Series, Vol. 39, Academic Press, 377 pp.

Vonnegut, B., C. B. Moore, R. G. Semonin, J. W. Bullock, D. W. Staggs, and W. E. Bradley, 1962: Effect of atmospheric space charge on initial electrification of cumulus clouds. *J. Geophys. Res.*, **67**, 3909-21.

Wiens, K. C., S. A. Rutledge, and S. A. Tessendorf, 2005: The 29 June 2000 supercell observed during STEPS. Part II: lightning and charge structure. *J. Atmos. Sci.*, **62**, 4151–4177.

Williams, E. R., and Coauthors, 1999: The behavior of total lightning activity in severe Florida thunderstorms. *Atmos. Res.*, **51**, 245-265.

_____, 2001: The electrification of severe storms. *Severe Convective Storms*, *Meteor. Monogr.*, No. 50, Amer. Meteor. Soc., 527–561.

Witt, A., M.D. Eilts, G.J. Stumpf, J.T. Johnson, E.D. Mitchell, and K.W. Thomas, 1998a: An enhanced hail detection algorithm for the WSR-88D. *Wea. Forecasting*, **13**, 286–303.

_____, _____, _____, E.D. Mitchell, J.T. Johnson, and K.W. Thomas, 1998b: Evaluating the performance of WSR-88D severe storm detection algorithms. *Wea. Forecasting*, **13**, 513–518.

Weisman, M. L., and Klemp, J. B., 1986: Characteristics of isolated convective storms. *Mesoscale Meteorology and Forecasting*, P. S. Ray, Ed., Amer. Meteor. Soc., 331–358.

APPENDIX A

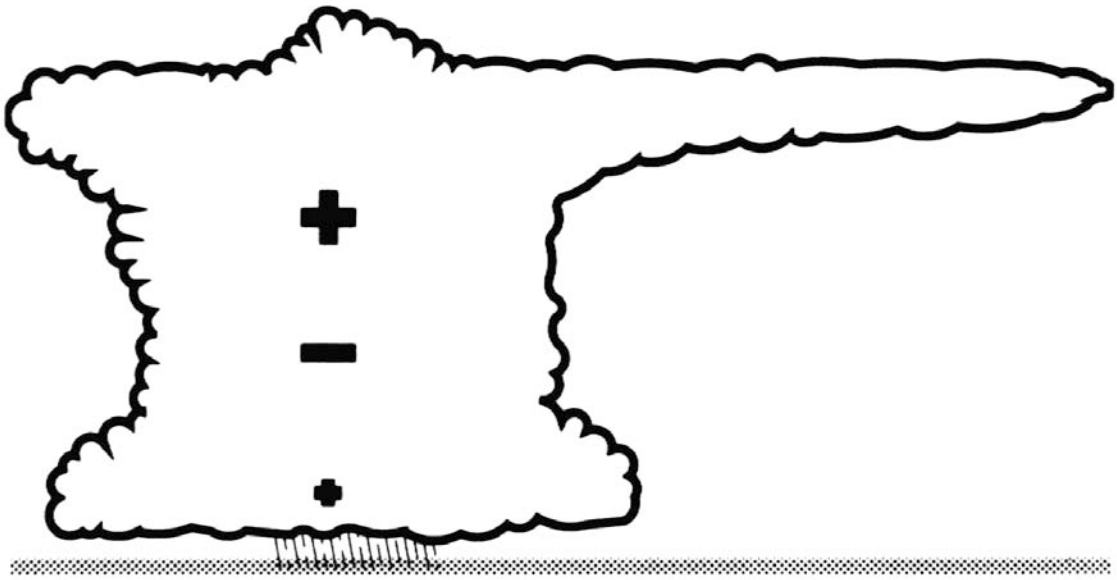

Figure 1.1. The simple dipole/tripole model of thunderstorm charge regions (From MacGorman and Rust 1998).

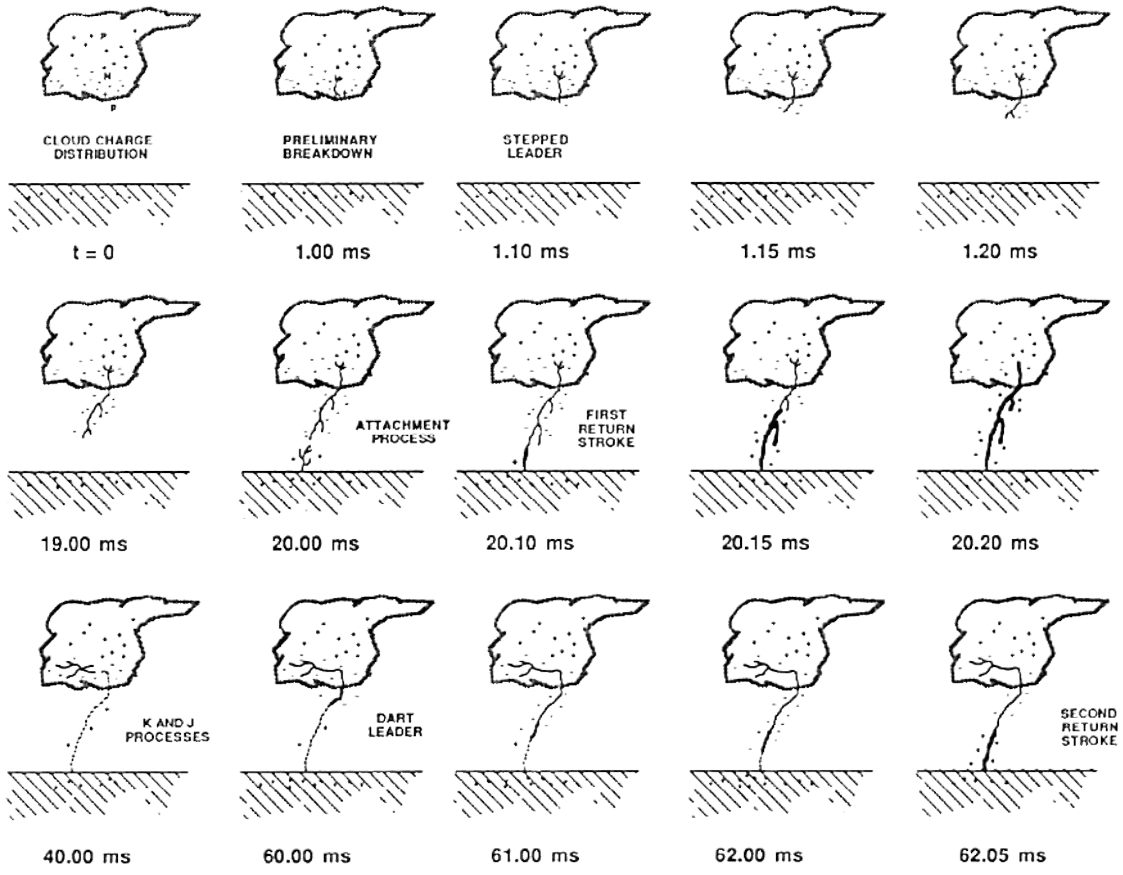

Figure 1.2. Illustration of a cloud-to-ground lightning flash (From Uman 1987).

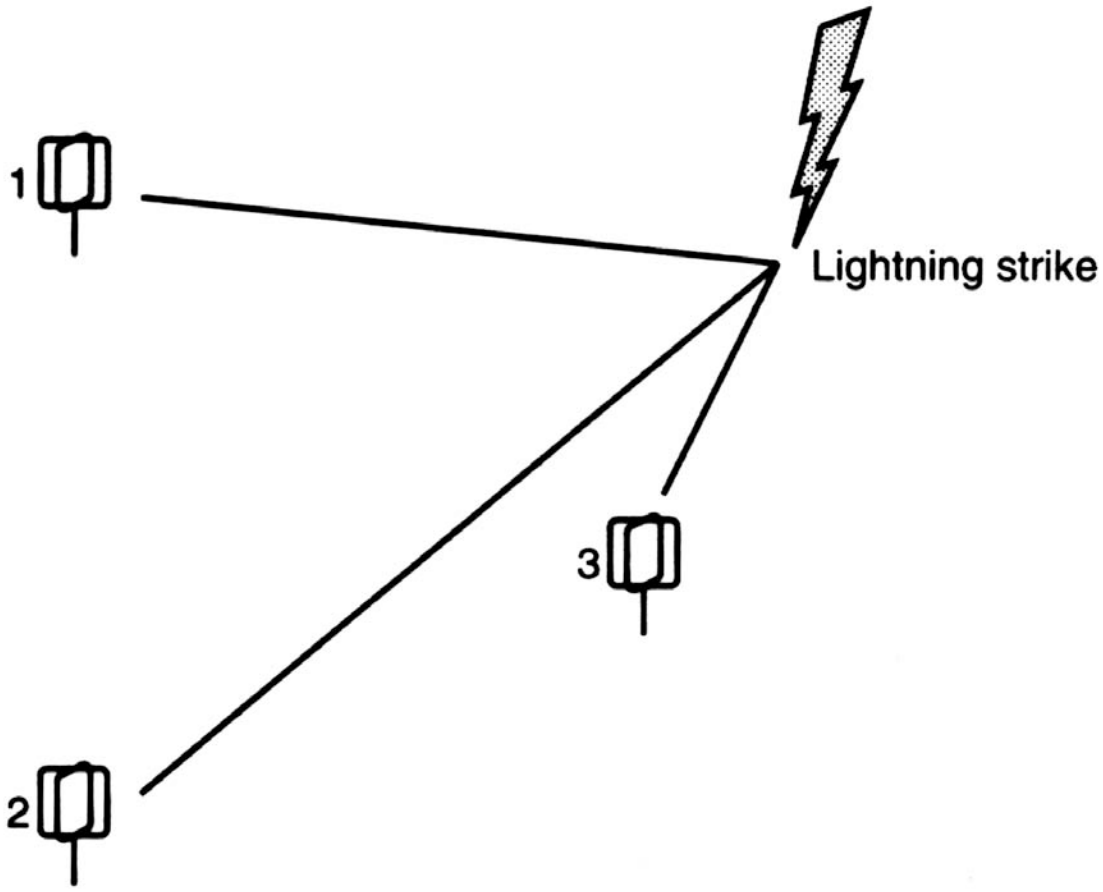

Figure 1.3. Location of CG lightning strike point using direction vectors from magnetic direction finders (From MacGorman and Rust 1998).

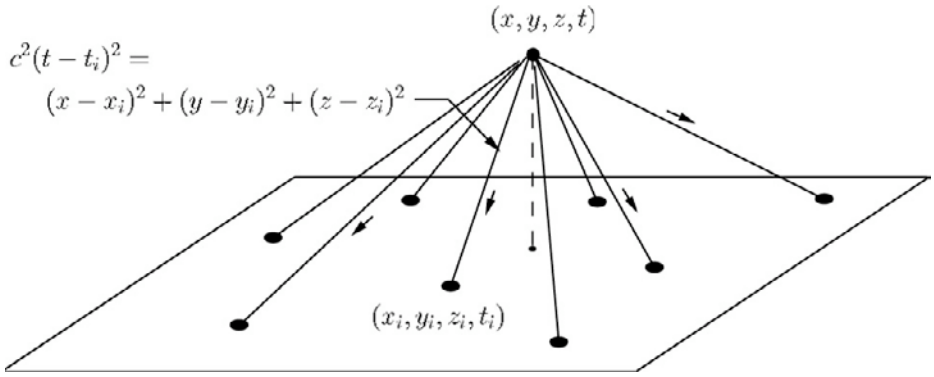

Figure 1.4. Depiction of the time of arrival method of VHF source detection (From Thomas et al. 2004).

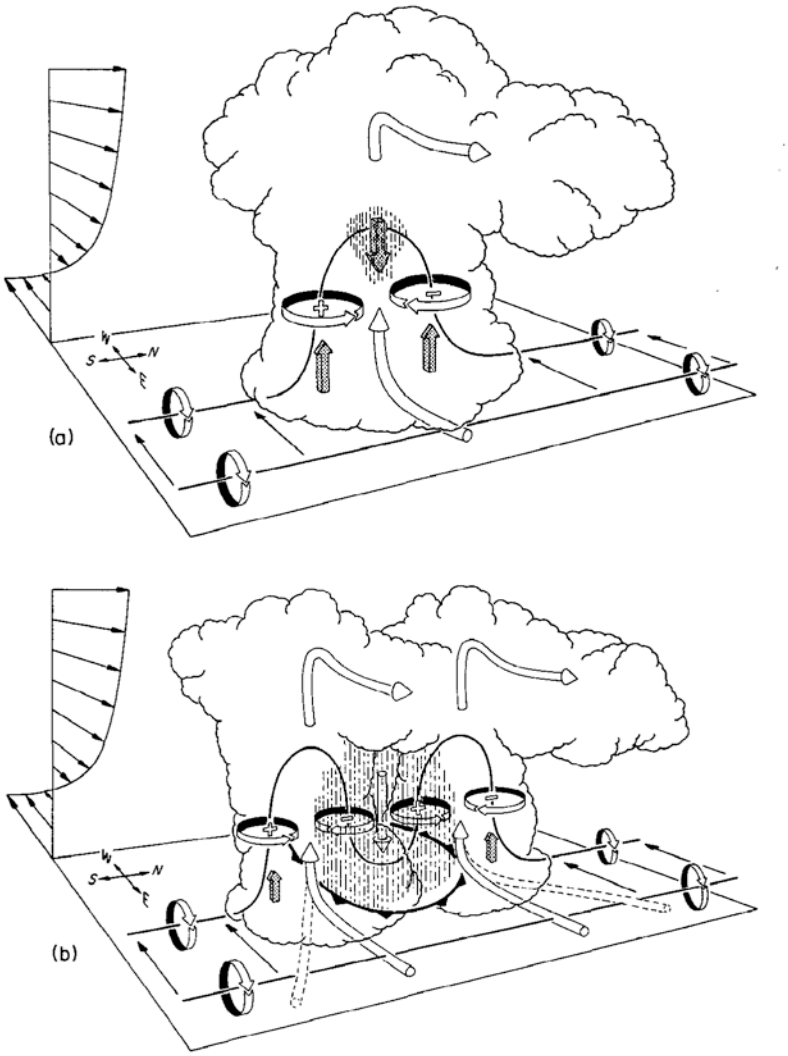

Figure 1.5. Model showing the development of two new rotating updrafts by the tilting of horizontal vorticity into the vertical. Thin solid lines are vortex lines, with arrows depicting their rotation. Cylindrical arrows depict air motions through the cell, while solid arrows depict regions of favorable updraft and downdraft development. (a) Initial thunderstorm updraft tilts local horizontal vortex into the vertical (b) downdraft development between the splitting cells tilts vortex line back downwards, creating two vortex pairs (From Klemp 1987, adapted from Rotunno 1981).

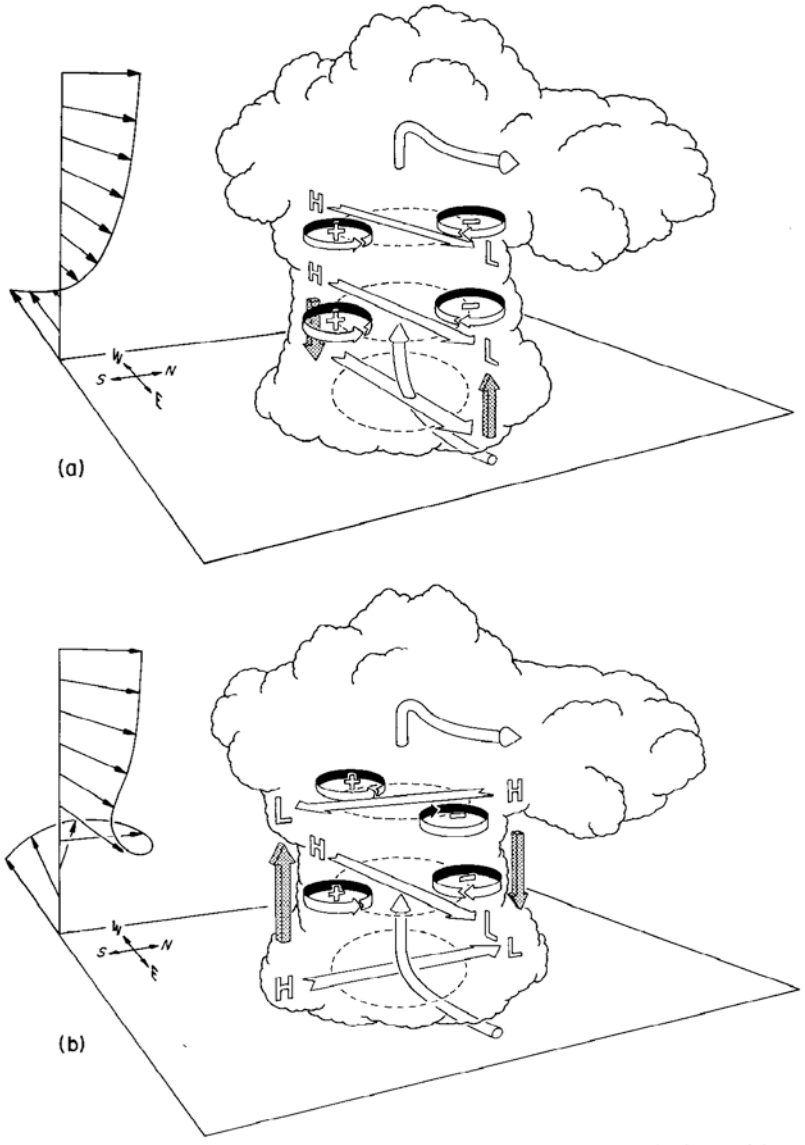

Figure 1.6 Depiction of regions favorable for upward or downward motion (solid arrows) adjacent to a convective updraft in response to atmospheric winds. (a) Directional shear leading to favorable updraft development ahead of the updraft, propagating the cell forwards. (b) Veering wind profile (clockwise turn with increasing height) supporting updraft redevelopment on the right flank of the existing updraft leading to a shift in cell motion to the right of the mean atmospheric flow (From Klemp 1987, adapted from Rotunno and Klemp, 1982).

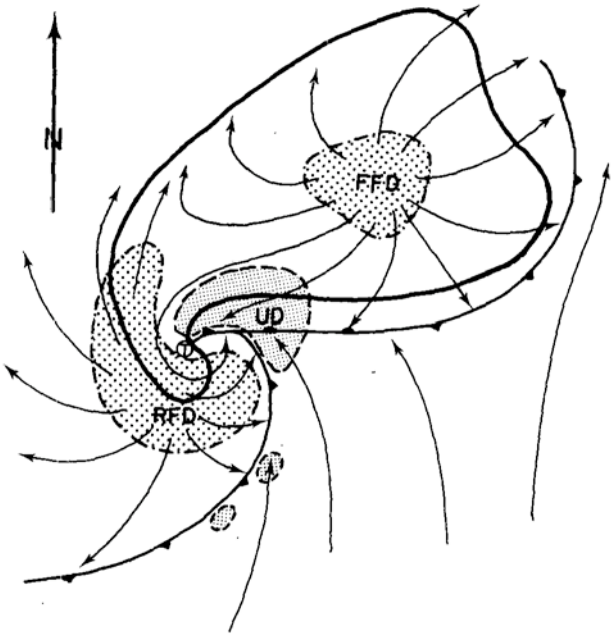

Figure 1.7. Plan view of an idealized supercell thunderstorm. The think black outer line shows the radar reflectivity signature including the "hook echo" present on the southwest side of the cell. The shaded regions are areas of vertical motion within the storm, with the RFD and FFD (rear flank and forward flank downdrafts) being regions of downward vertical motion and the updraft (UP) an area of upward motion. Thin arrows show surface level winds, showing the warm inflow into the updraft from the south and southeast and cooler air spreading out underneath the downdrafts (From Lemon and Doswell 1979).

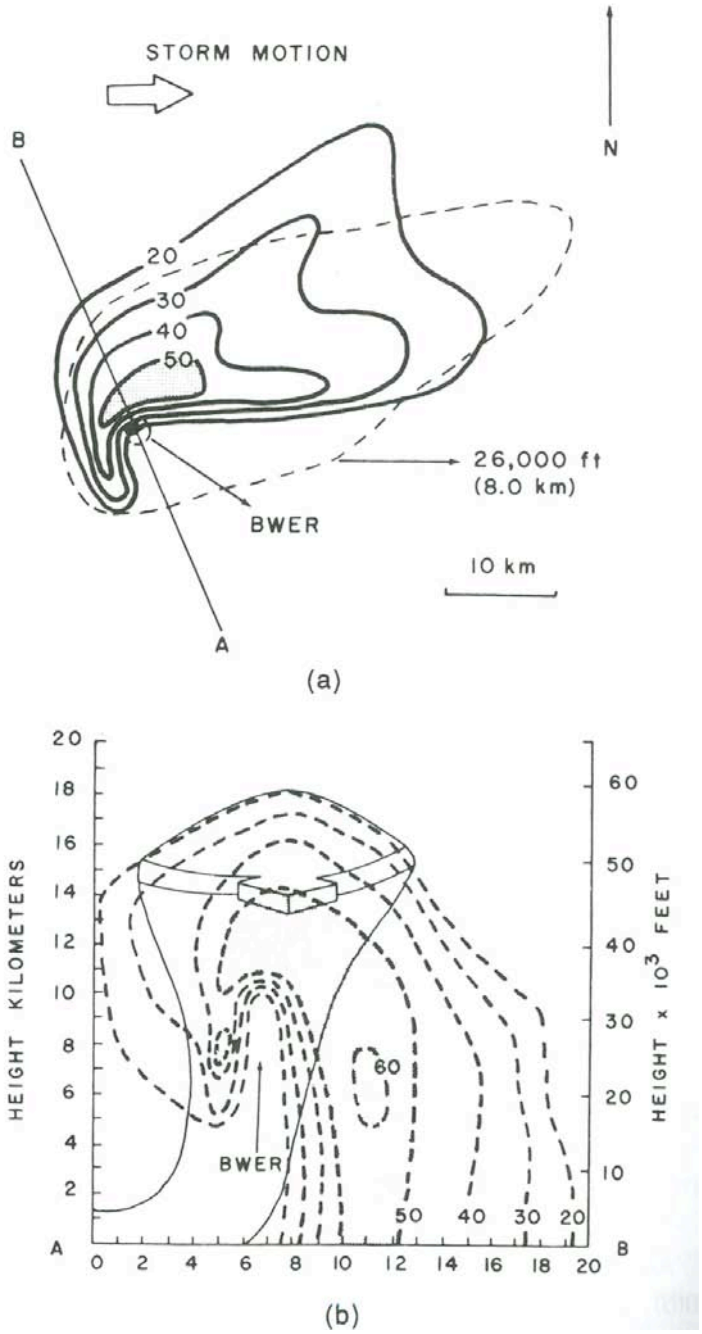

Figure 1.8. Schematic diagram of the bounded weak echo region (BWER) of a supercell with a strong updraft. (a) Plan view showing the BWER location. Solid lines are lines of constant radar reflectivity; note the strong gradient just to the north of the BWER (updraft) location. (b) Vertical cross section along line AB in (a), showing the BWER location. Dotted lines are lines of constant radar reflectivity (again note reflectivity gradient). Solid lines depict air movement within the cell, with a low level inflow entering a nearly vertical updraft (From Bluestein 1993, adapted from Lemon, 1977).

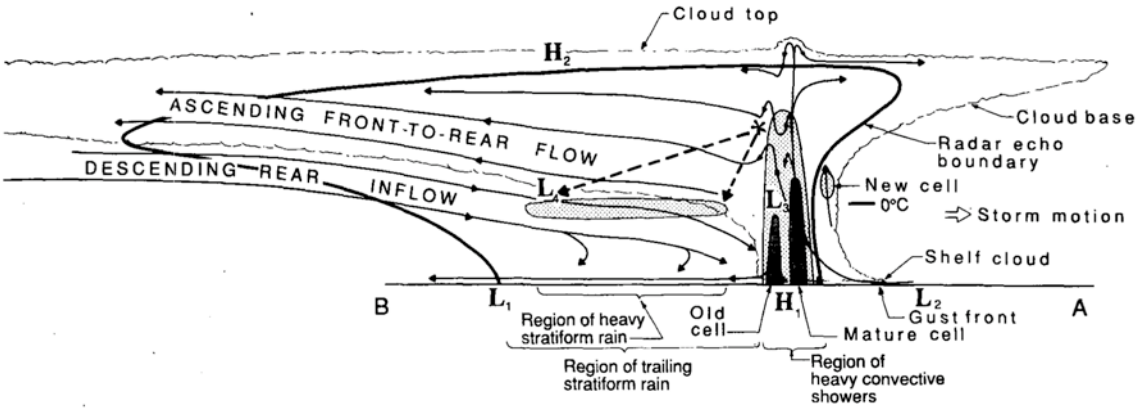

Figure 1.9. Cross section of a linear MCS containing a leading line of intense convection followed by a trailing region of stratiform precipitation. Region of descending rear inflow marks the location of rear inflow jet associated with bowing line segments (From Houze et al.1989).

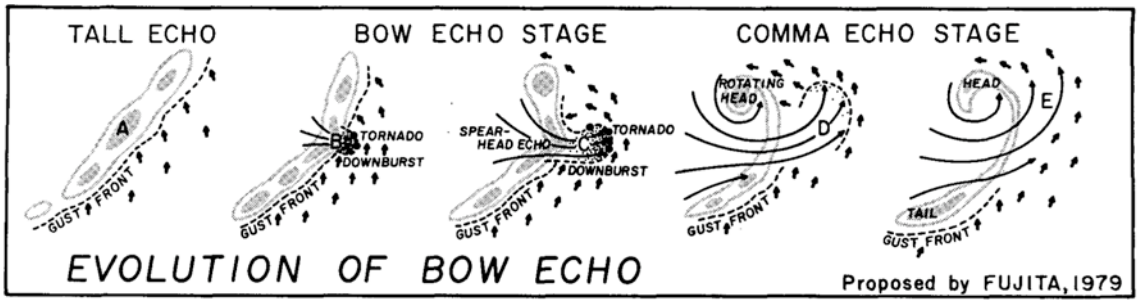

Figure 1.10. Conceptual model of the radar reflectivity structure of an MCS bow echo segment. Also marked are probable locations for the development of a tornado or severe straight-line winds (downburst) (From Fujita 1981).

Figure 2.1. Map of WSR-88D sites within the NEXRAD network (from Serafin and Wilson 2000).

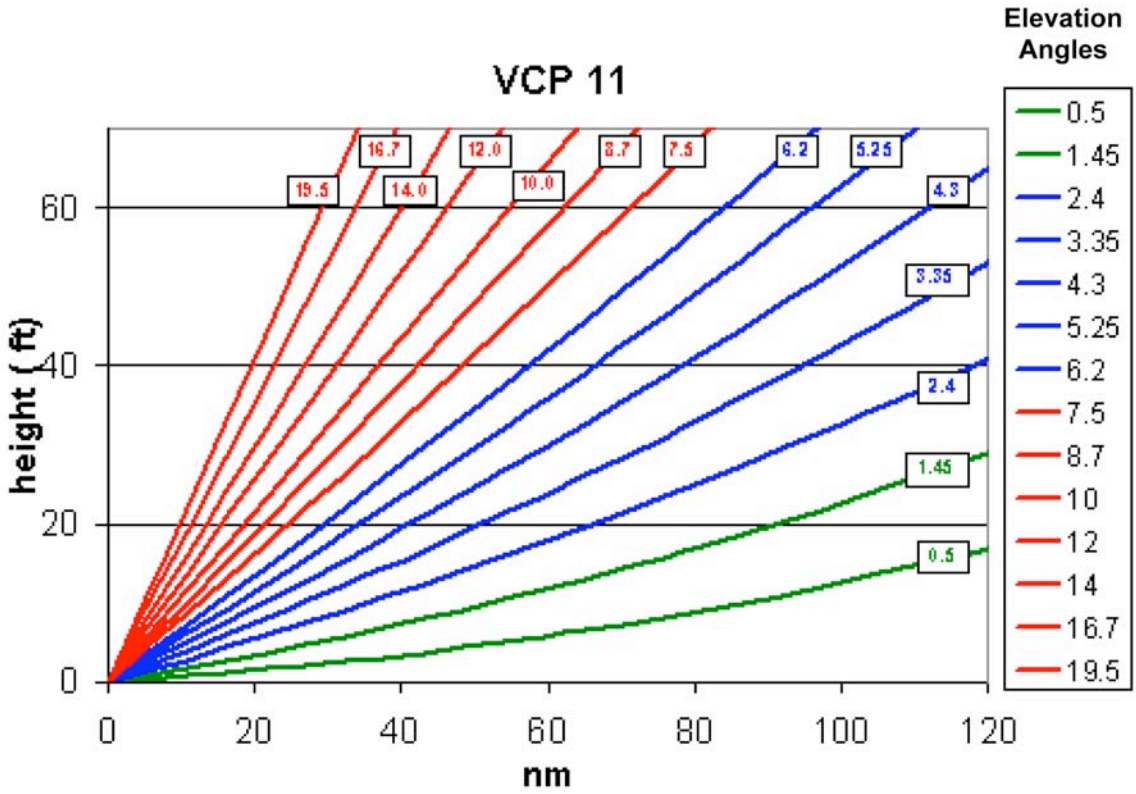

Figure 2.2. Volume Coverage Pattern (VCP) 11 elevation angles. Curves show altitude of radar beam above earth's surface at ranges listed along the x-axis.

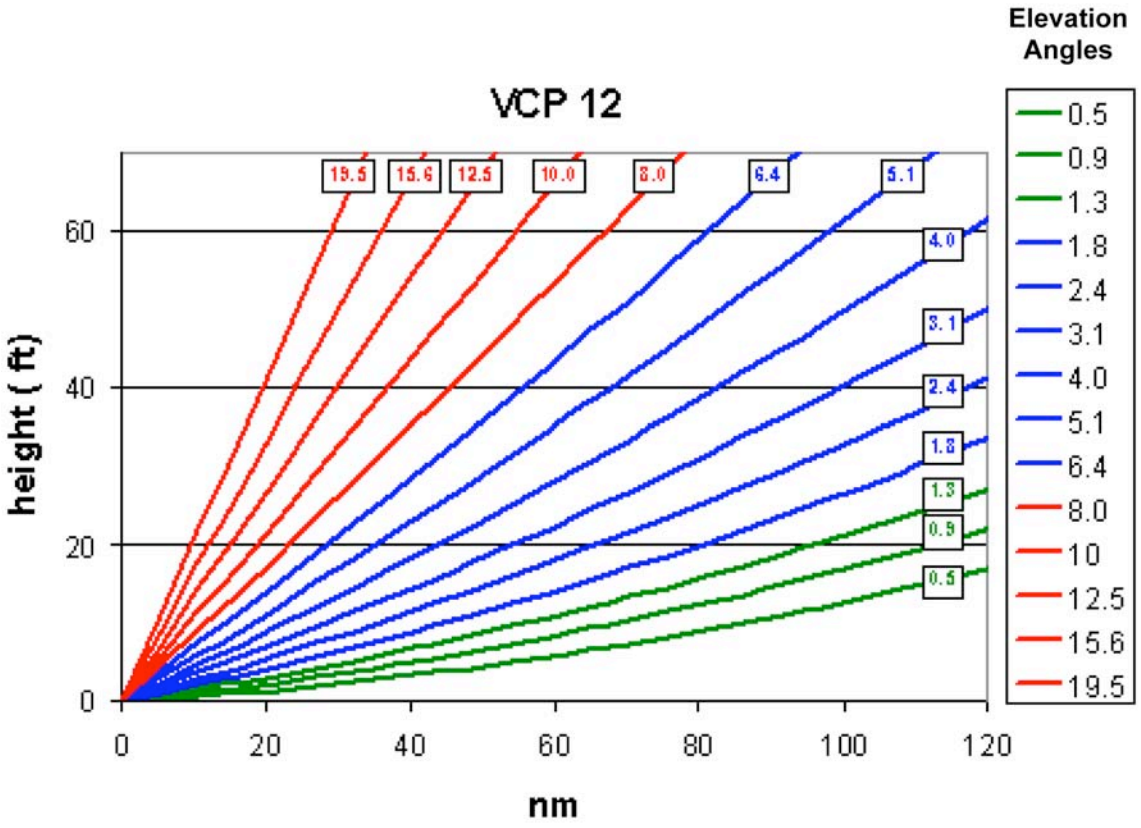

Figure 2.3. Same as Fig. 2.2, but for Volume Coverage Pattern (VCP) 12.

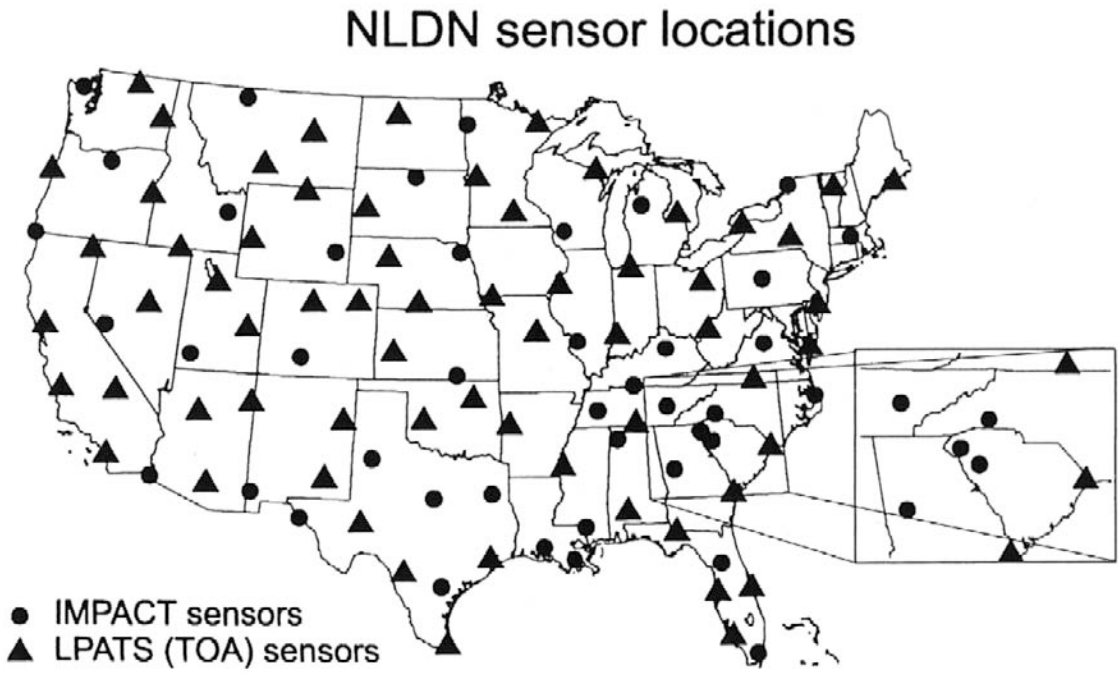

Figure 2.4. Map showing approximate NLDN sensor locations (From Orville and Huffines 1999). Note that all IMPACT and LPATS sensors have subsequently been replaced with IMPACT-ESP sensors.

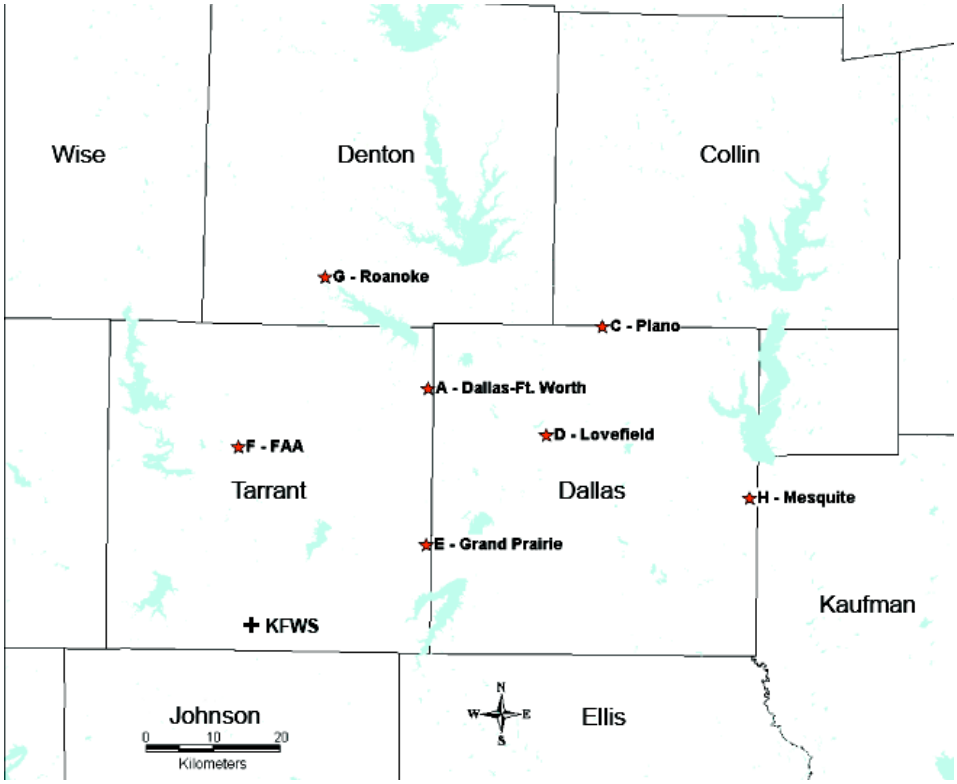

Figure 2.5. Locations of the KFWS WSR-88D site and the D/FW LDAR network sensors that were active on the dates in this study. The center of the LDAR network is at D/FW International Airport (sensor site "A"). Adapted from Patrick and Demetriades (2005).

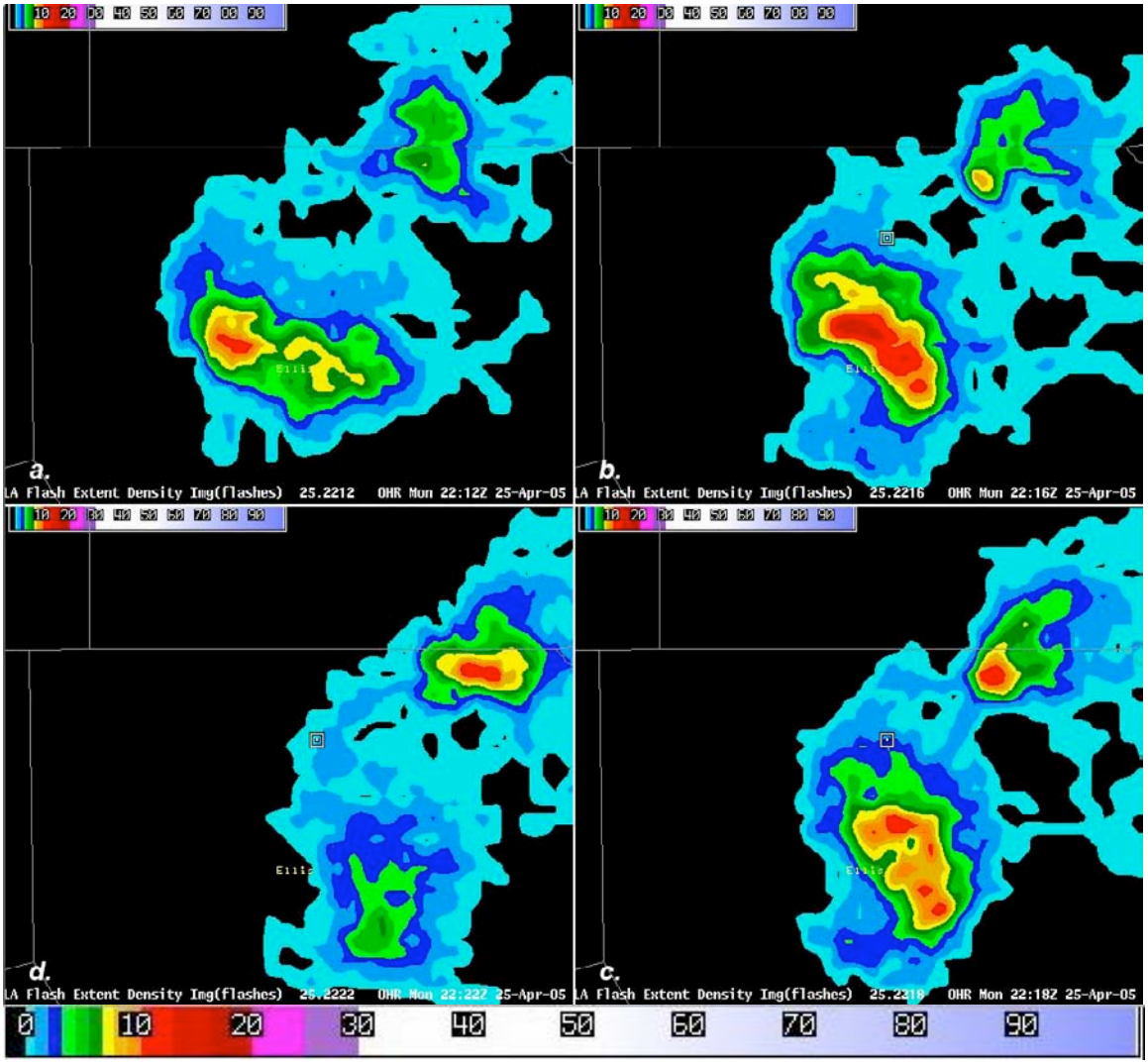

Figure 3.1. Right hand shift in FED (flashes min^{-1} km^{-2}, colors as shown) track for cell two on 25 April 2005. Times are: (a) 2212 UTC, (b) 2216 UTC, (c) 2218 UTC, (d) 2222 UTC.

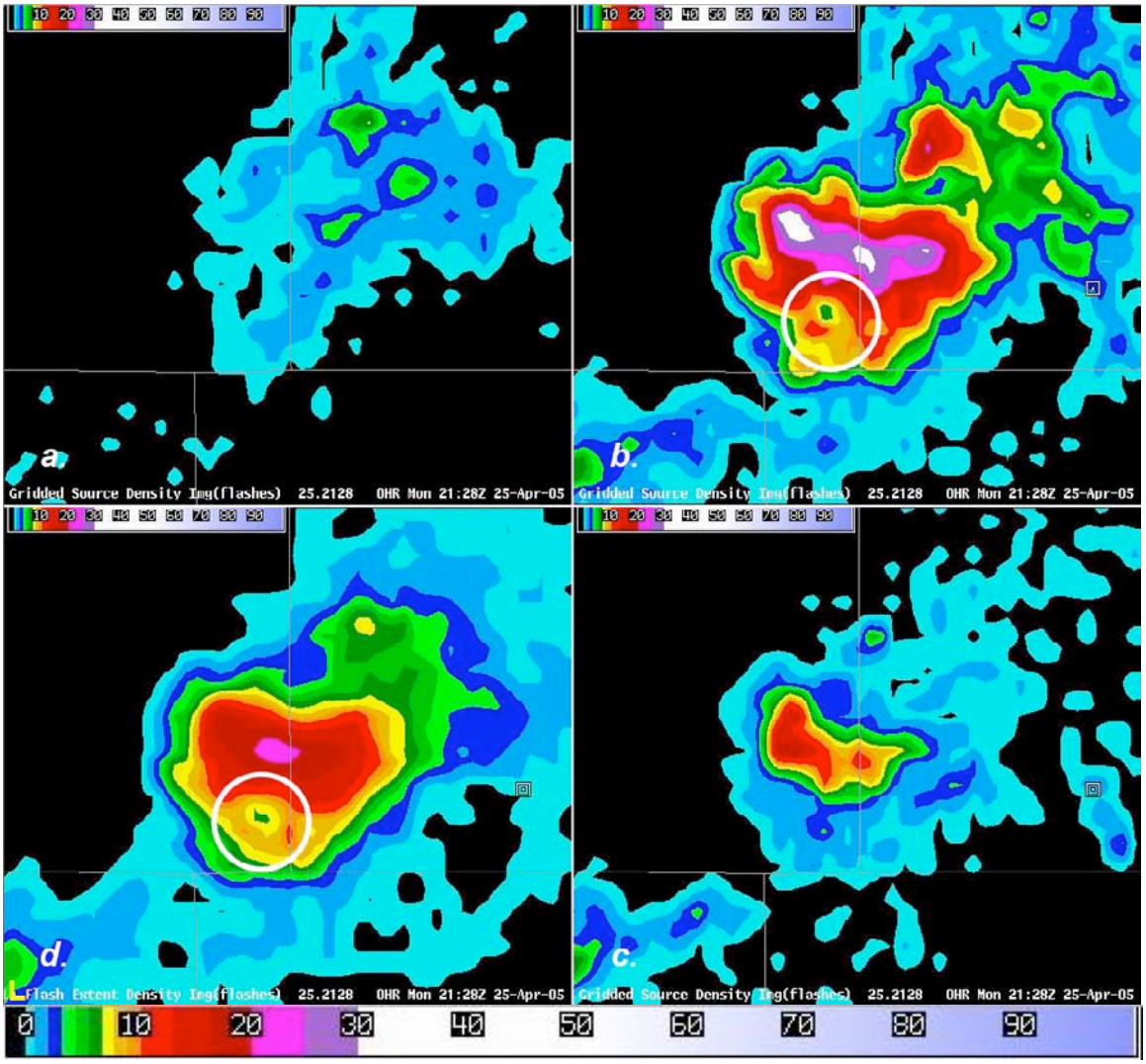

Figure 3.2. FED (flashes min^{-1} km^{-2}, colors as shown) and GSD (sources min^{-1} km^{-2}, colors as shown) images of cell one lightning hole (circled) at 2128 UTC on 25 April 2005. Images are: (a) 0-3 km GSD, (b) 3-6 km GSD, (c) 6-9 km GSD, (d) FED.

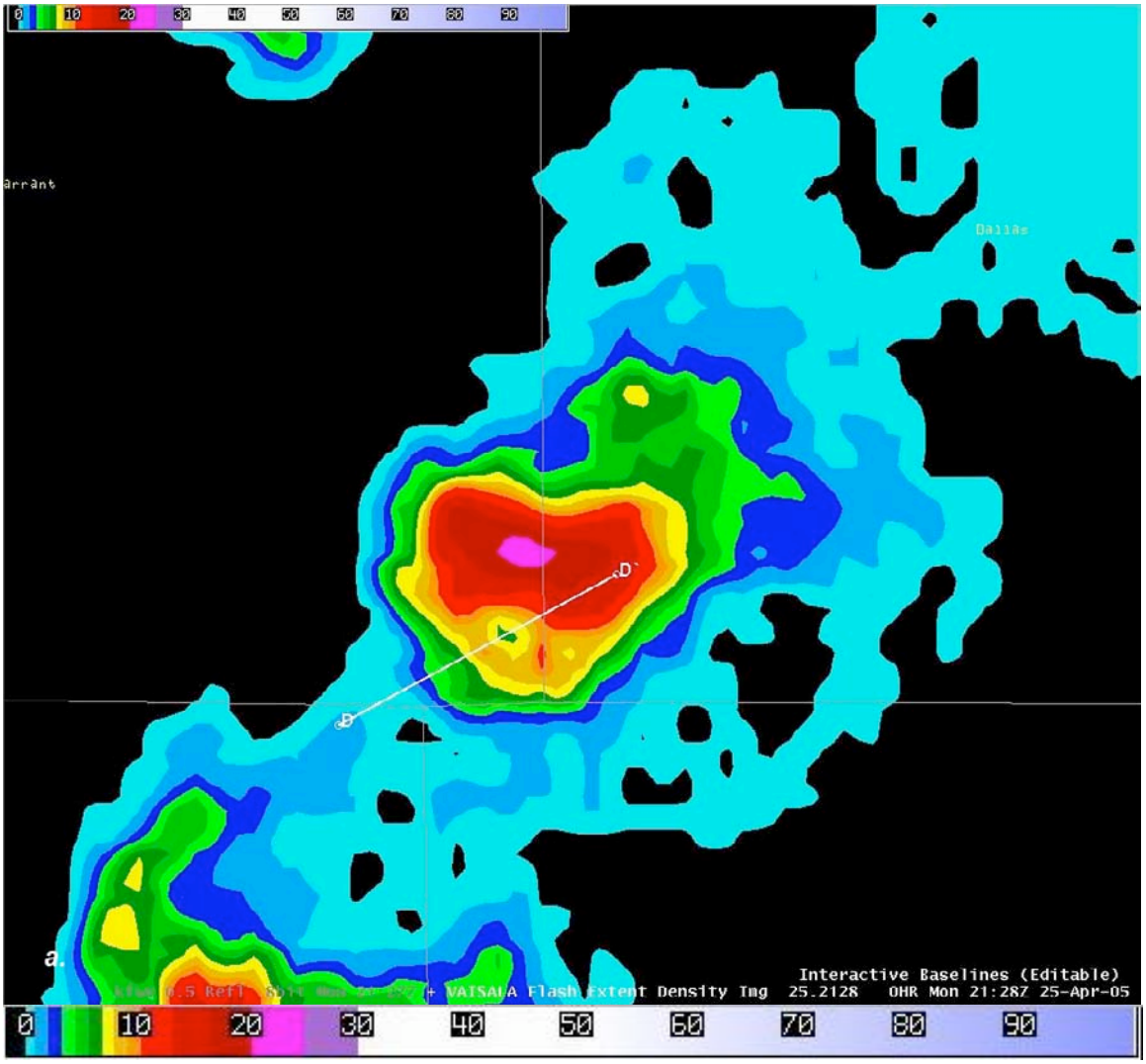

Figure 3.3. FED (flashes min^{-1} km^{-2}, colors as shown) image of cell one lightning hole at 2128 UTC on 25 April 2005. Diagonal line "D" denotes the location of the radar vertical cross section shown in Fig. 3.5.

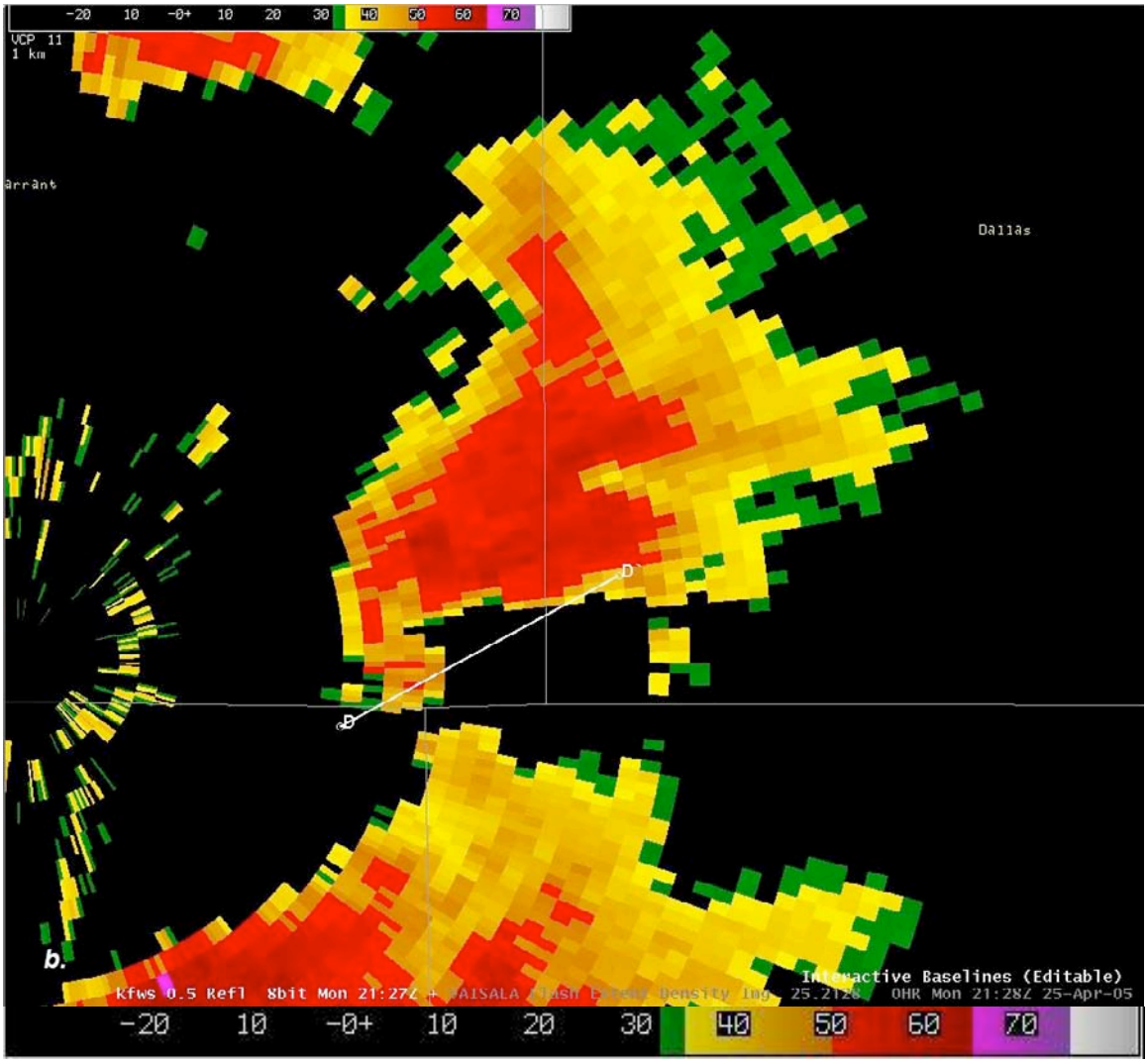

Figure 3.4. 0.5-degree Radar reflectivity (dBZ, colors as shown) image at 2127 UTC on 25 April 2005, corresponding to lightning hole at 2128 UTC. Line "D" denotes the location of the vertical cross section in Fig. 3.5.

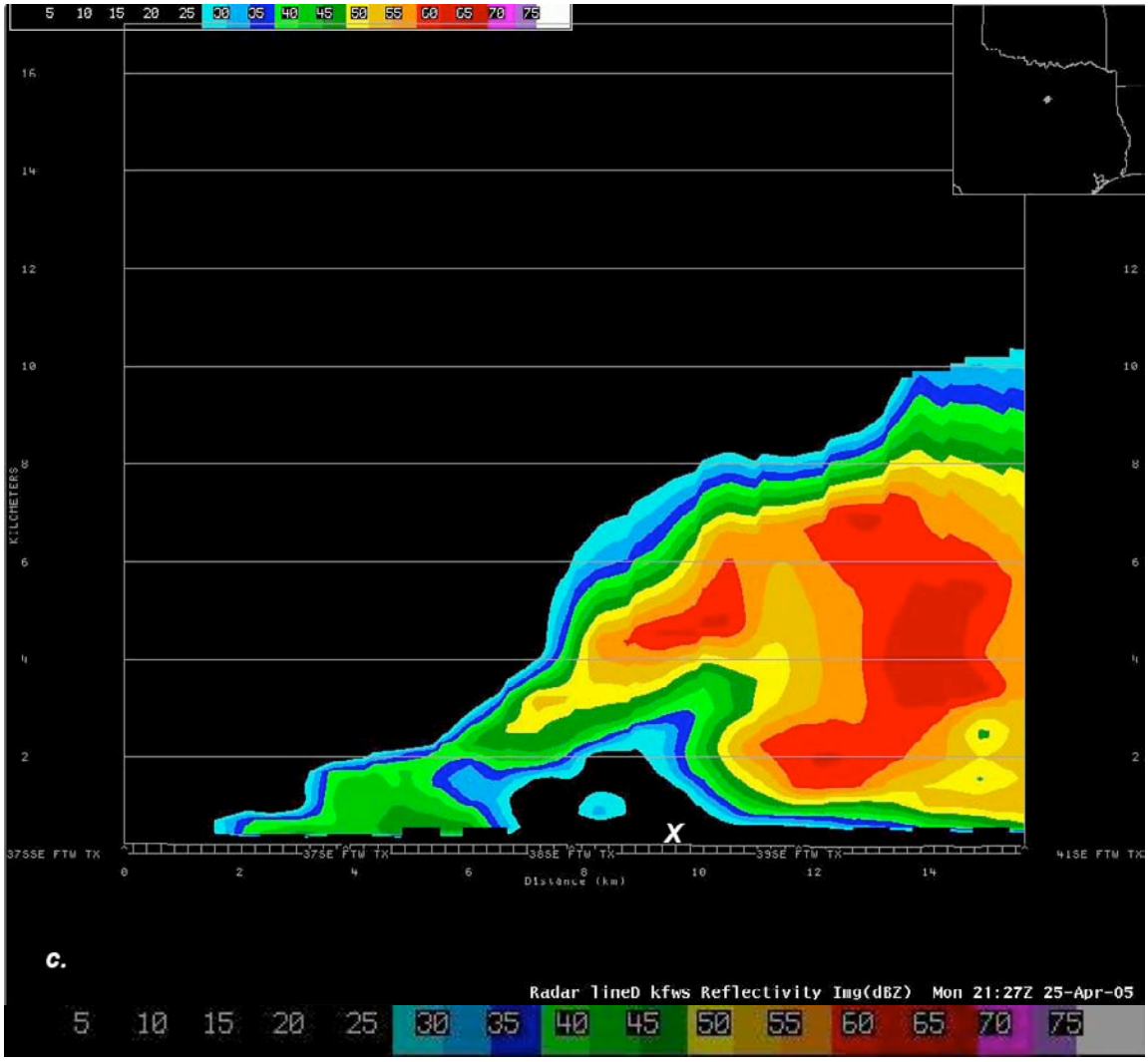

Figure 3.5. Radar reflectivity vertical cross section (line "D") at 2127 UTC on 25 April 2005. The position of the lightning hole from Fig. 3.3 is marked with a white X along the horizontal axis. Note the weak echo region that extends upward 2-3 km in the lightning hole location.

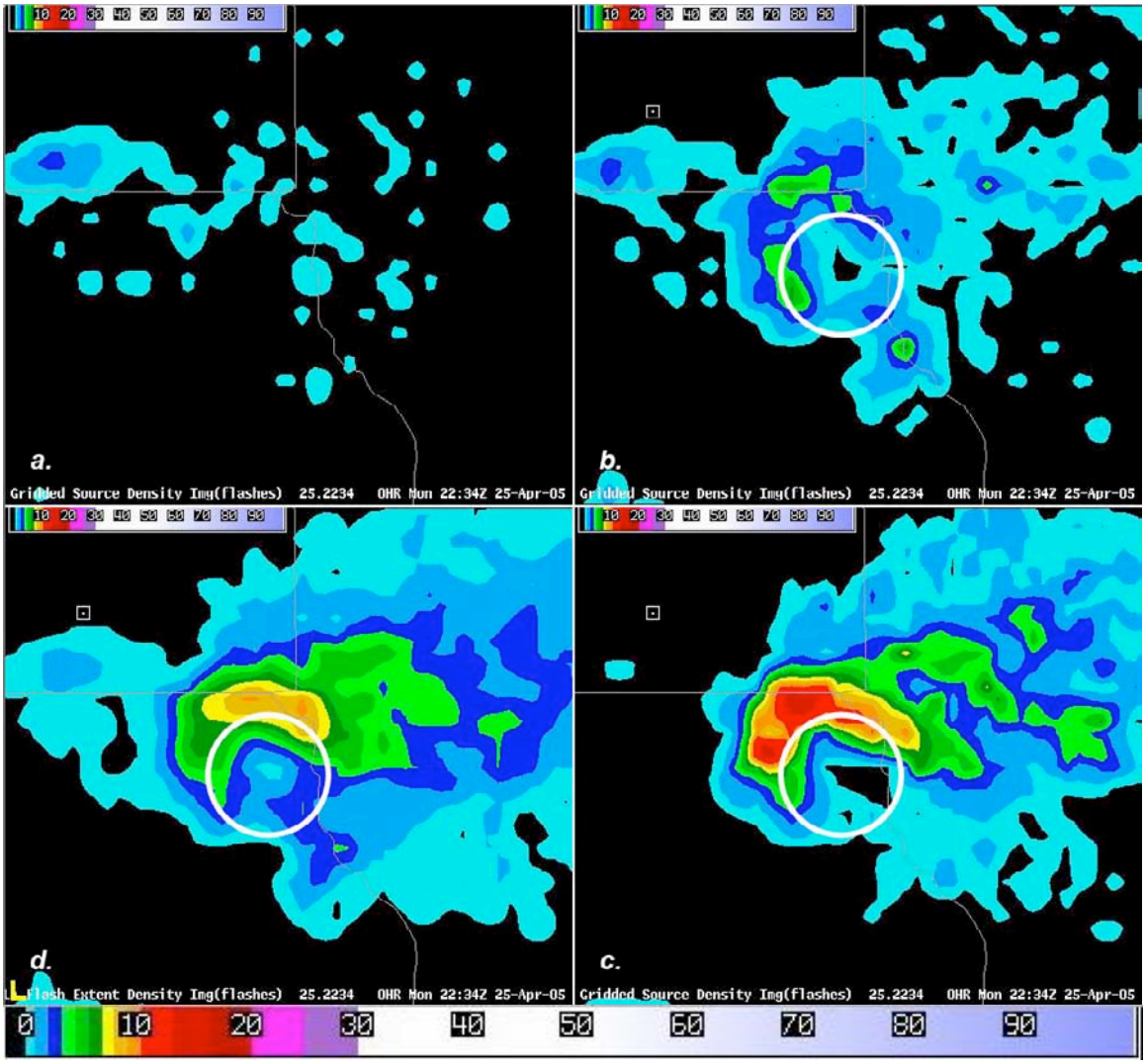

Figure 3.6. GSD (sources min^{-1} km^{-2}, colors as shown) and FED (flashes min^{-1} km^{-2}, colors as shown) images of second cell one lightning hole (circled) at 2234 UTC, 25 April 2005. Images are: (a) 0-3 km GSD, (b) 3-6 km GSD, (c) 6-9 km GSD, (d) FED.

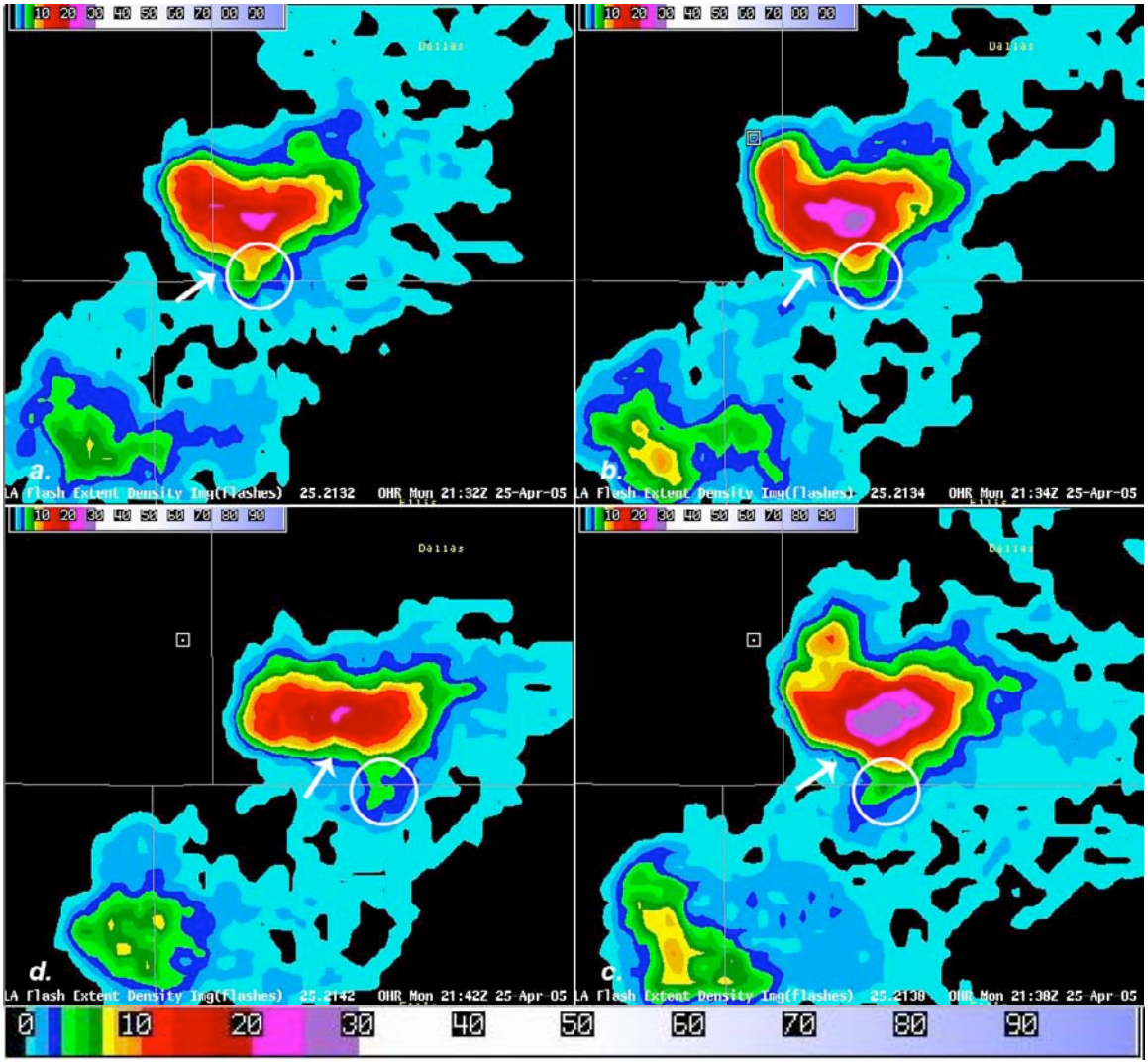

Figure 3.7. FED (flashes min^{-1} km^{-2}, colors as shown) time series of cell one leading appendage (circled) from 25 April 2005. Times are: (a) 2132 UTC, (b) 2134 UTC, (c) 2138 UTC, (d) 2142 UTC. Updraft notches are marked with white arrows.

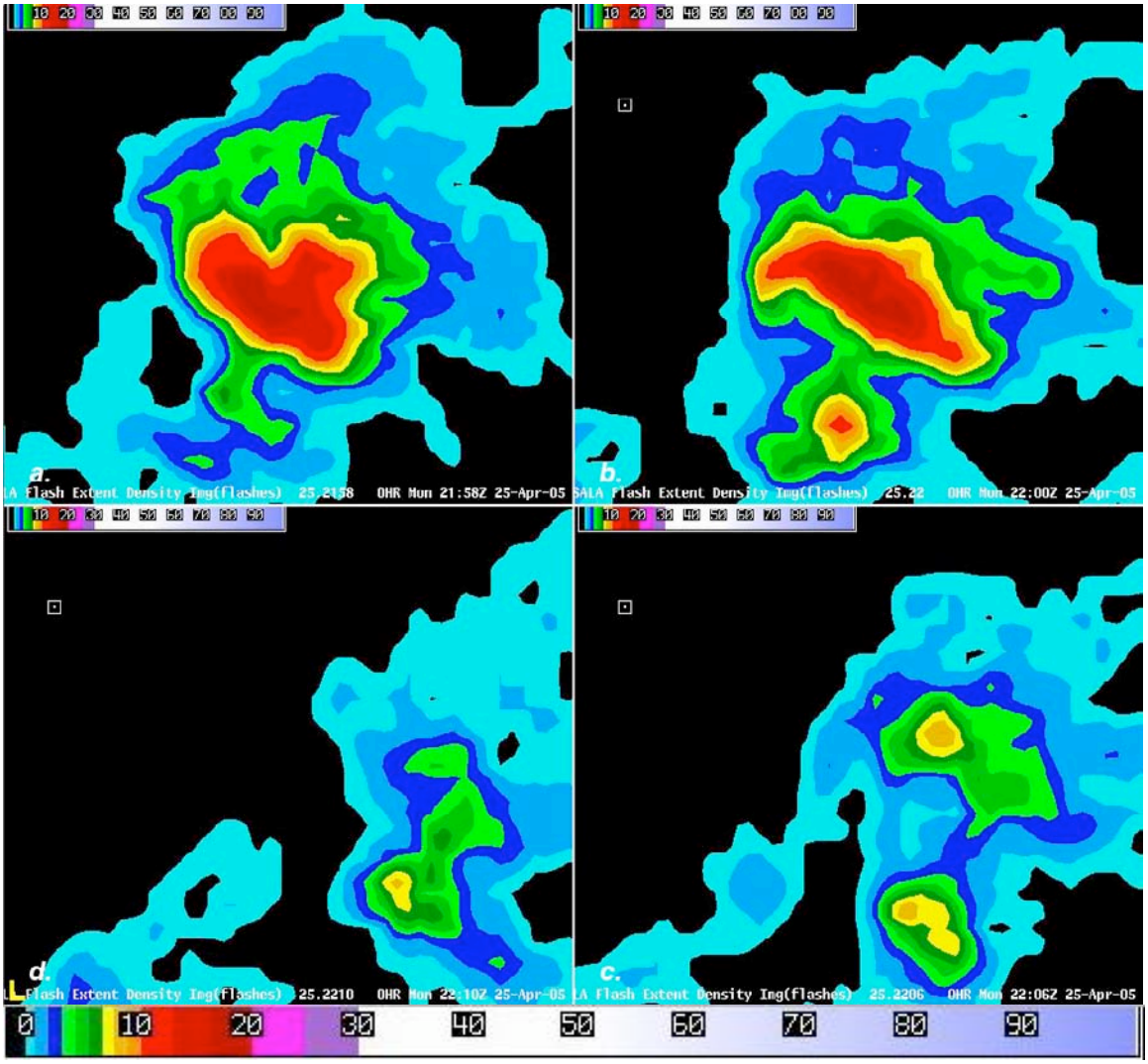

Figure 3.8. New FED (flashes min^{-1} km^{-2}, colors as shown) maximum developing to the south of cell one and then merging with cell one. Times are: (a) 2158 UTC, (b) 2200 UTC, (c) 2206 UTC, and (d) 2210 UTC on 25 April 2005.

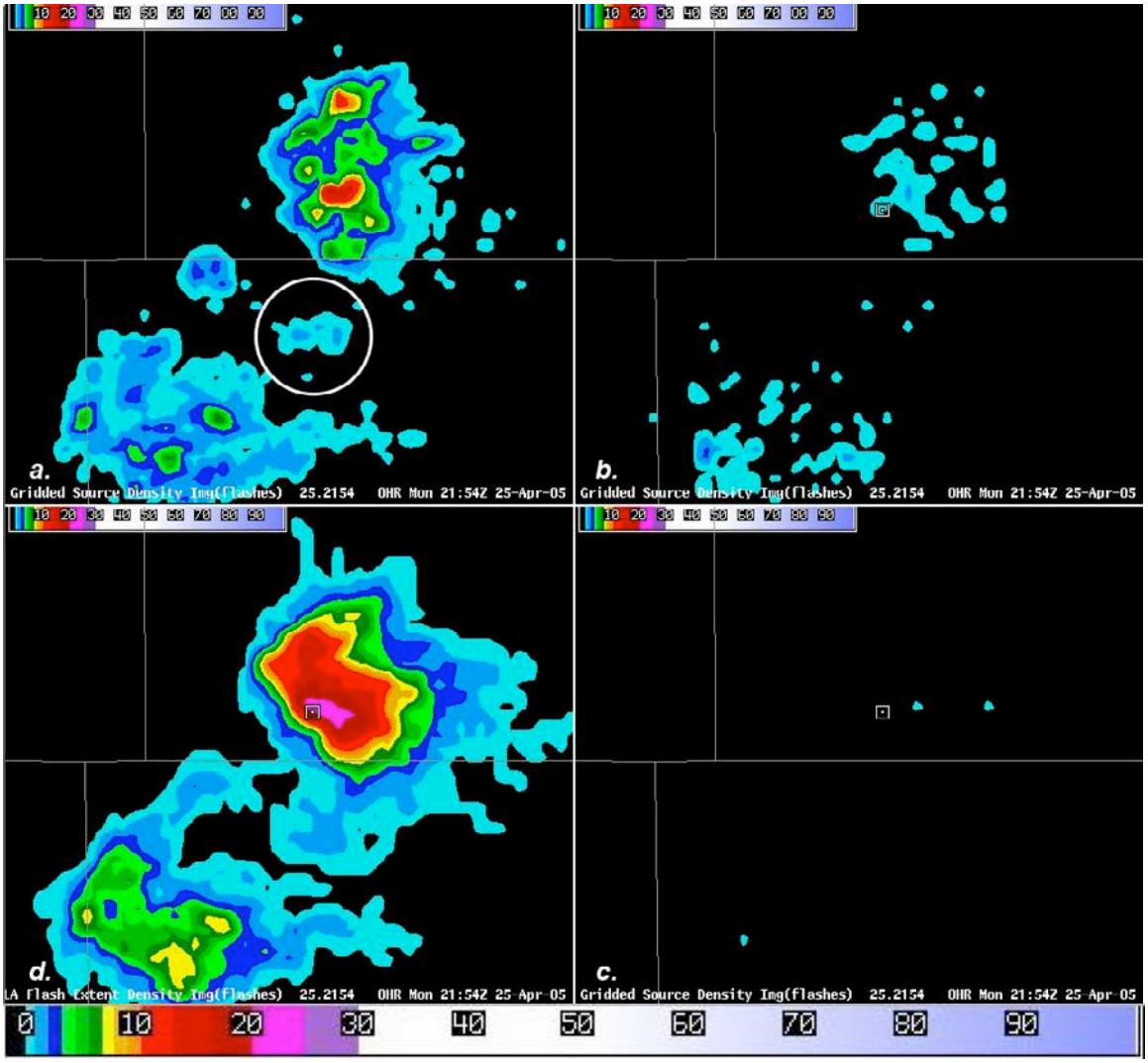

Figure 3.9. Comparison of GSD (sources min^{-1} km^{-2}, colors as shown) and FED (flashes min^{-1} km^{-2}, colors as shown) images at 2154 UTC on 25 April 2005. Images are: (a) 6-9 km GSD, (b) 9-12 km GSD, (c) 12-15 km GSD, (d) FED. Note highlighted region in (a), this feature evolved into the second maximum of FED displayed in Fig. 3.8, although it was not a distinct feature in FED until 2158 UTC, four minutes after appearing on the GSD display.

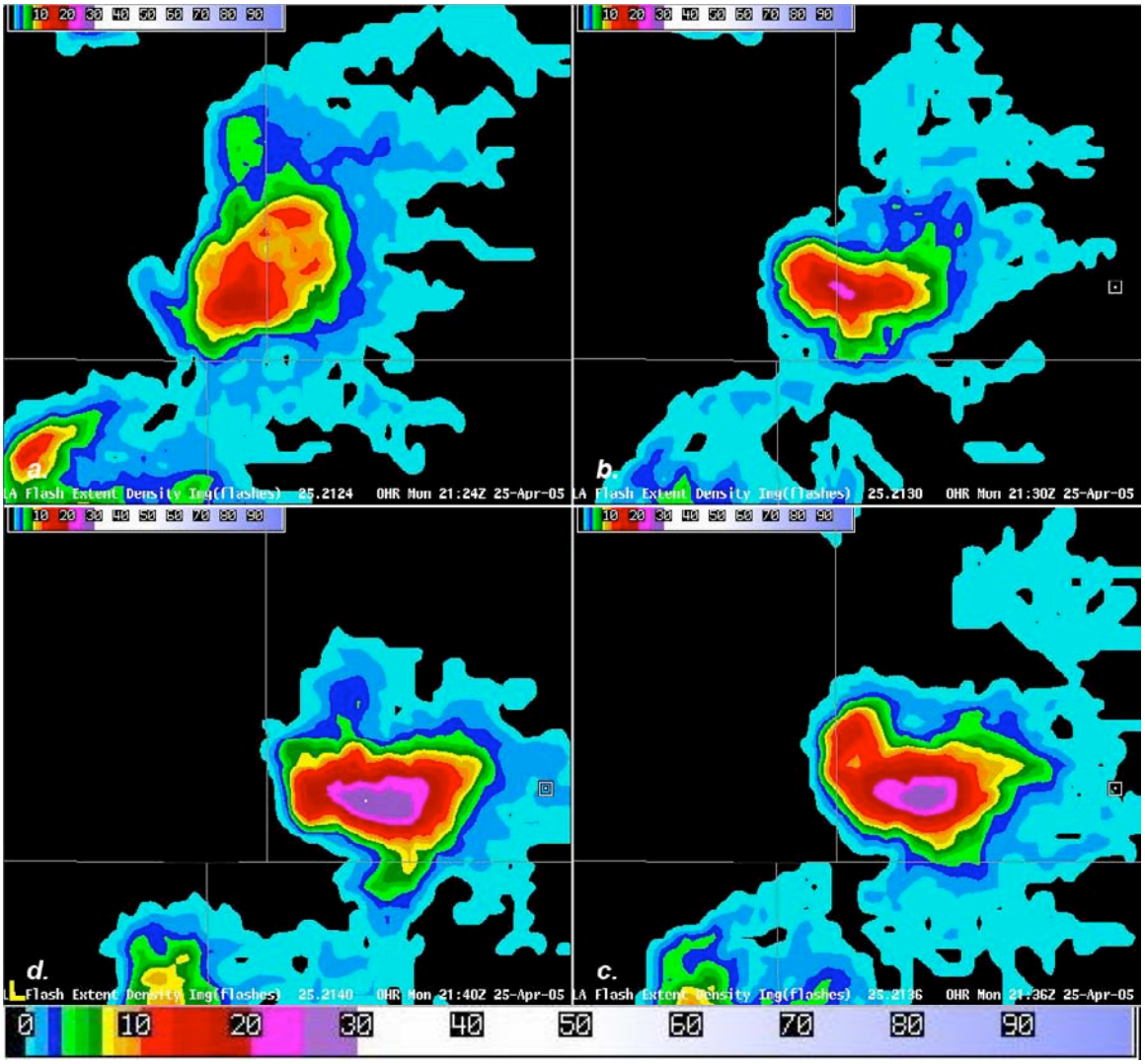

Figure 3.10. Increasing values of FED (flashes min^{-1} km^{-2}, colors as shown) associated with cell one on 25 April 2005. Times are: (a) 2124 UTC, (b) 2130 UTC, (c) 2136 UTC, and (d) 2140 UTC.

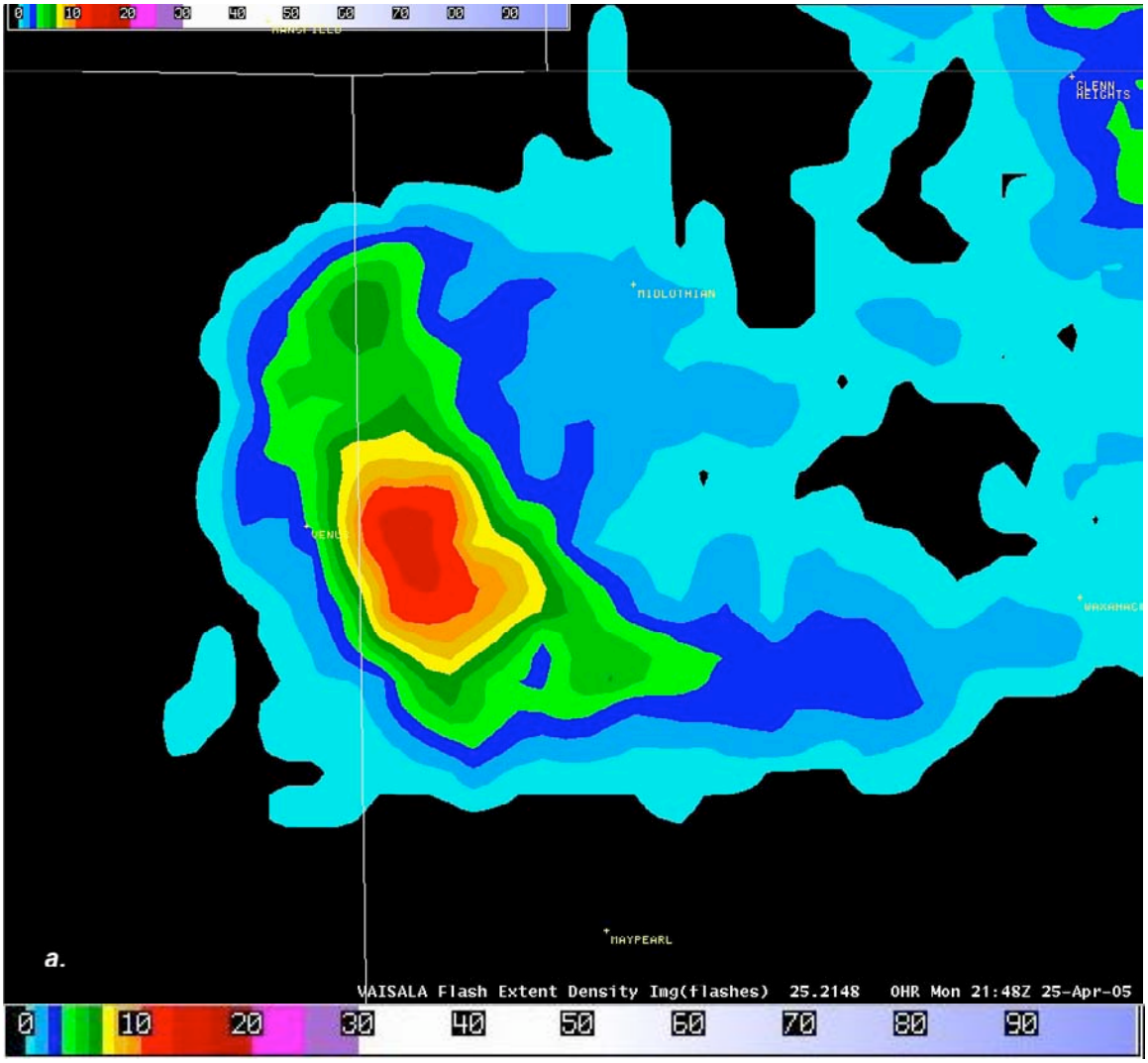

Figure 3.11. FED (flashes min^{-1} km^{-2}, colors as shown) image of cell two at 2148 UTC on 25 April 2005.

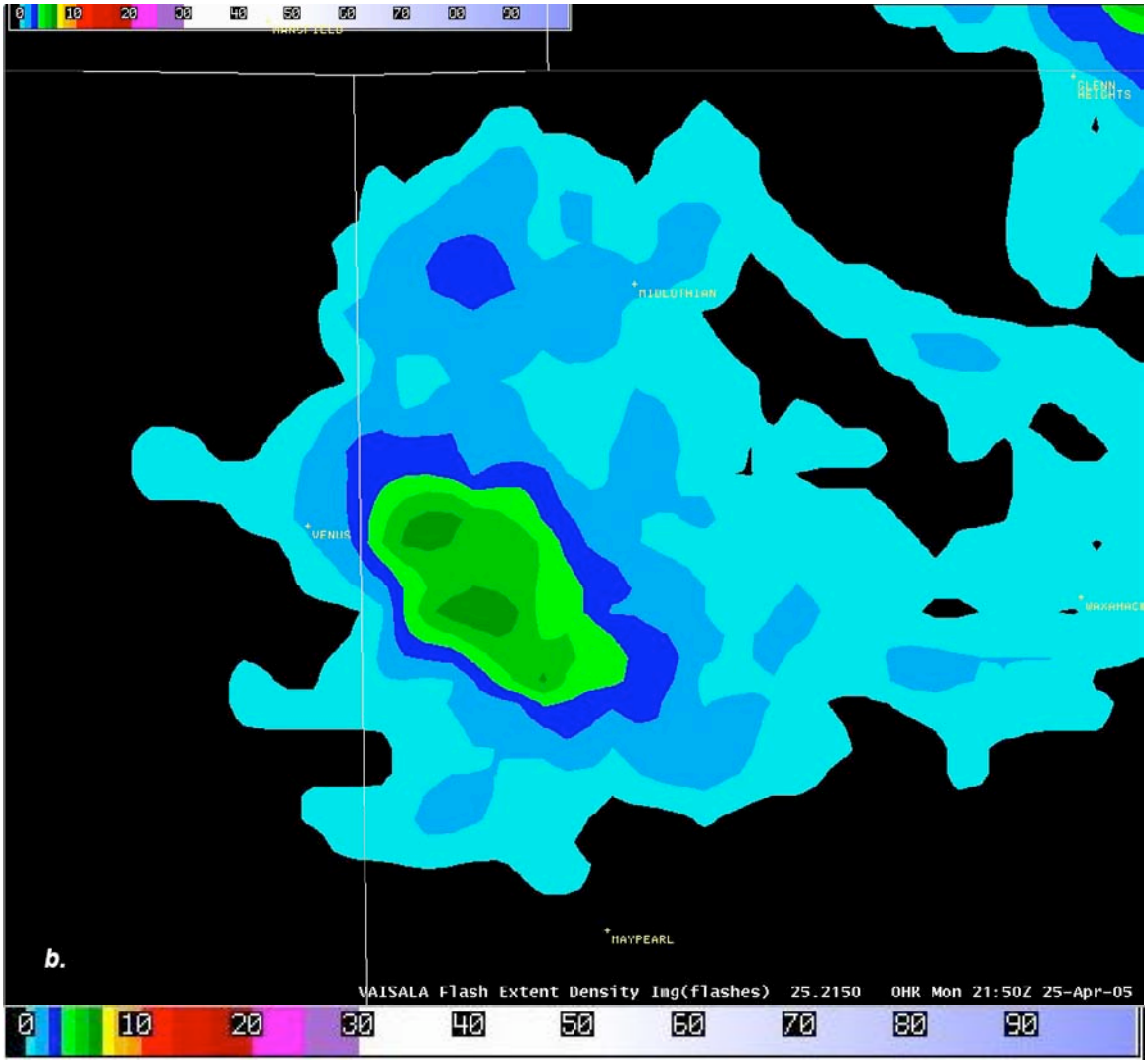

Figure 3.12. FED (min^{-1} km^{-2}, colors as shown) from cell two at 2150 UTC on 25 April 2005. Note the dramatic decrease in FED from the 2148 UTC image (Fig. 3.11).

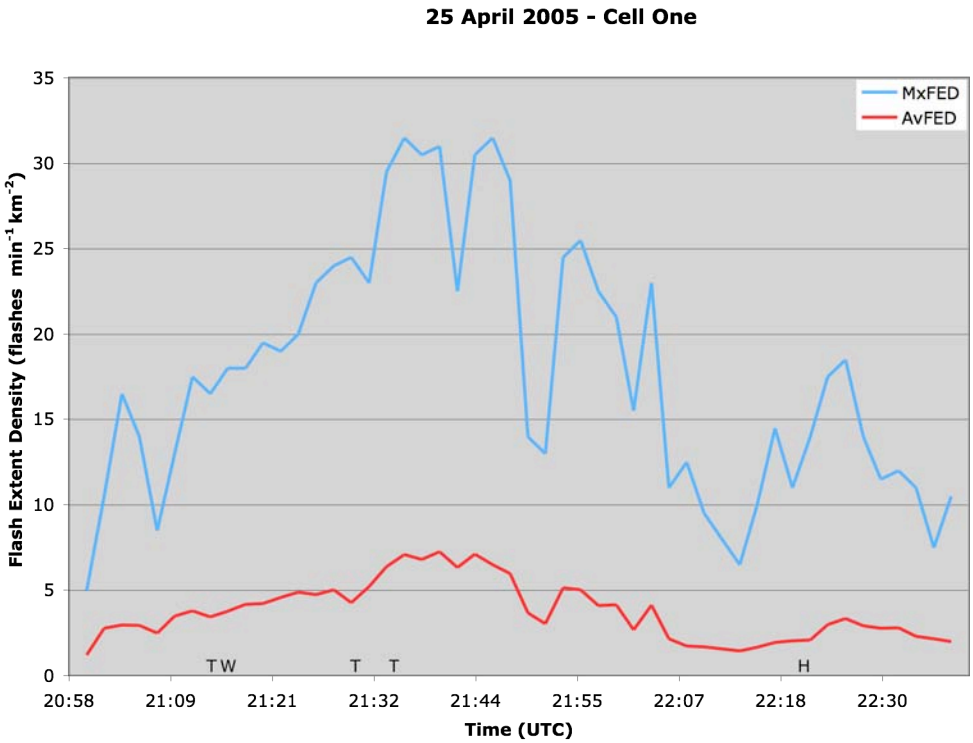

Figure 3.13. Maximum and average flash extent density (flashes min^{-1} km^{-2}) values for cell one on 25 April 2005. Reports of severe weather are noted along the x-axis, with tornadoes labeled as "T", hail reports labeled as "L", and severe wind gusts labeled as "W".

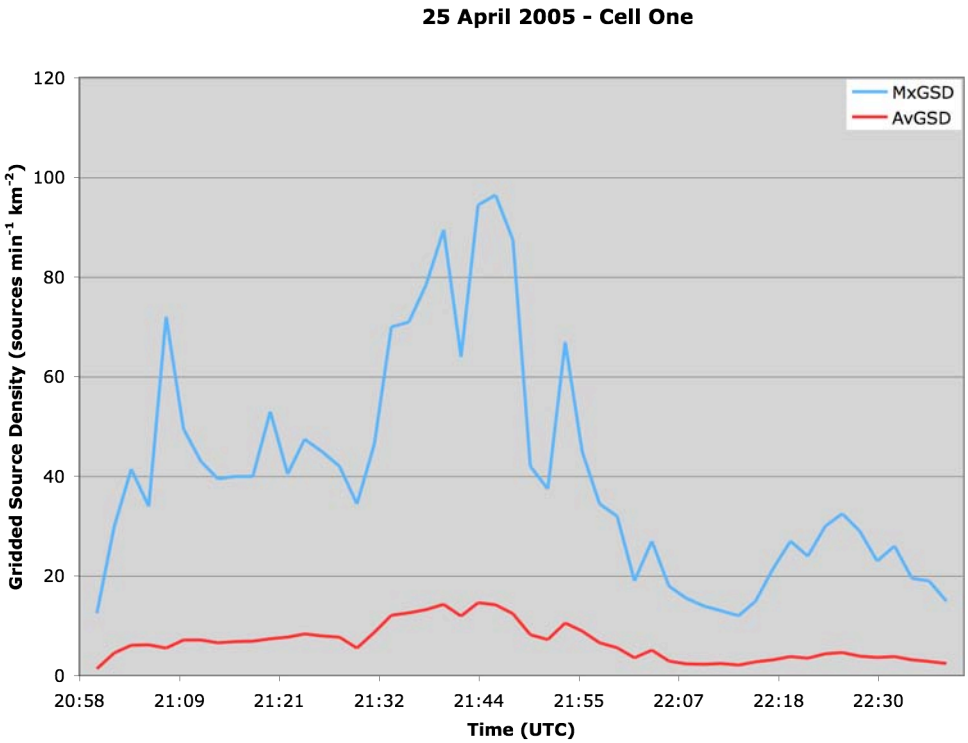

Figure 3.14. Maximum and average gridded source density (sources min^{-1} km^{-2}) values for cell one on 25 April 2005.

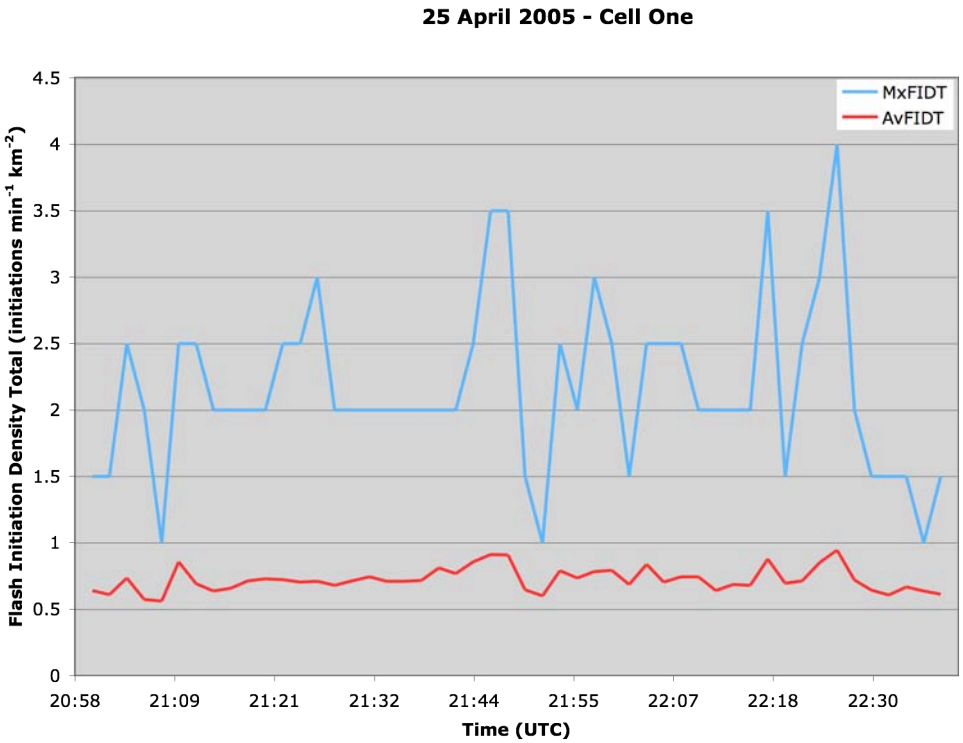

Figure 3.15. Maximum and average flash initiation density total (initiations min^{-1} km^{-2}) values for cell one on 25 April 2005.

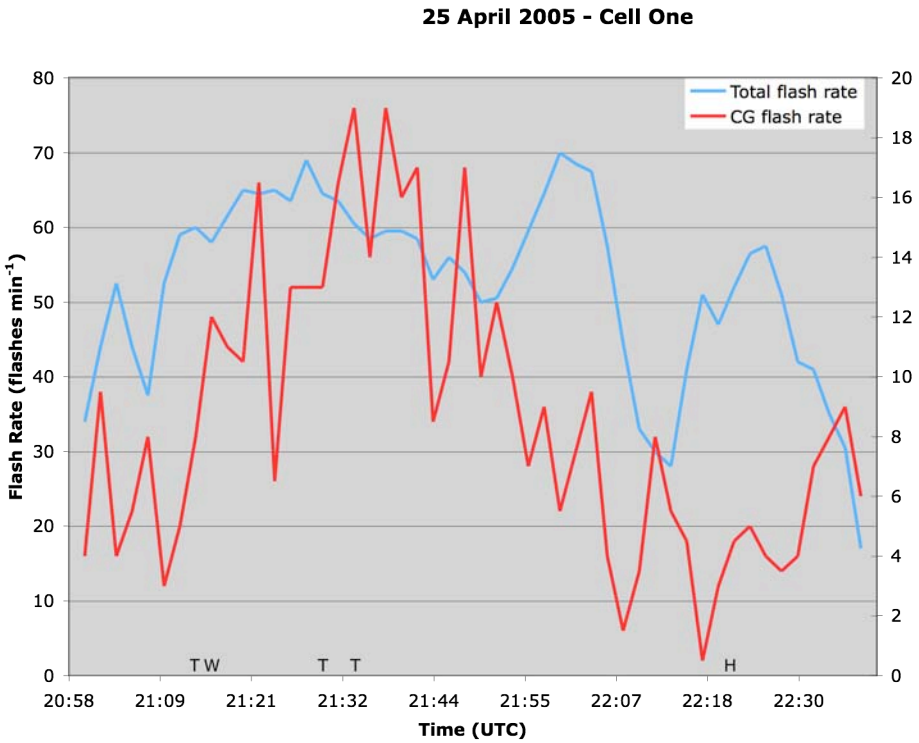

Figure 3.16. Total lightning flash rate (flashes min^{-1}) and CG lightning flash rate (flashes min^{-1}) for cell one on 25 April 2005. Total lightning flash rate values are on the left vertical axis, CG flash rate values are on the right hand vertical axis.

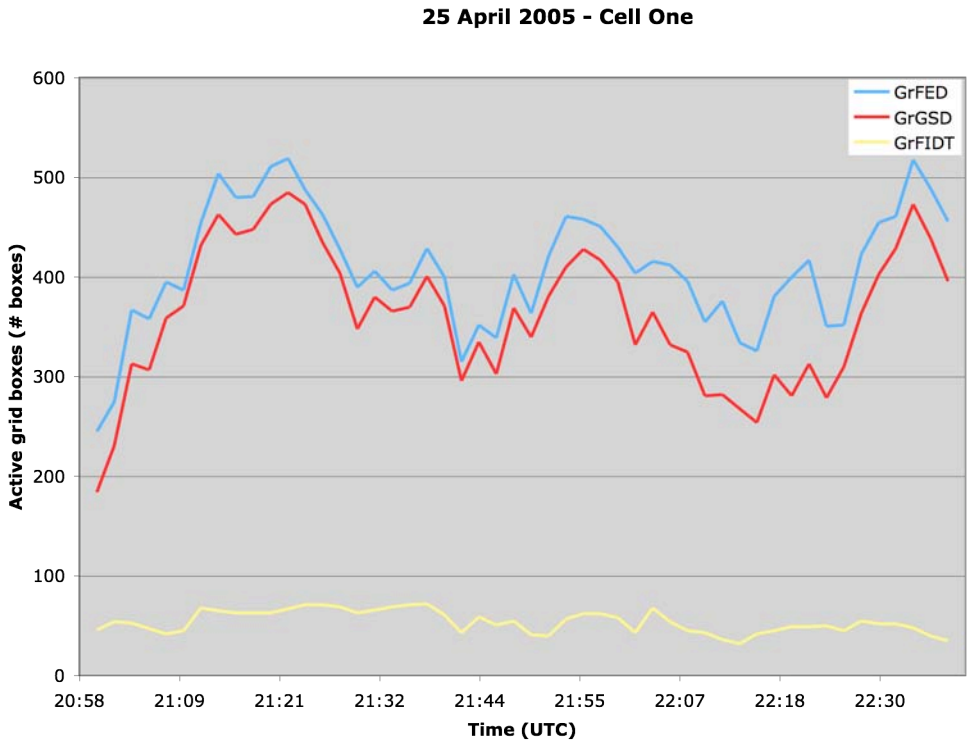

Figure 3.17. Total number of active grid boxes for FED, GSD, and FIDT for cell one on 25 April 2005. Each grid box is a 1km x 1km area.

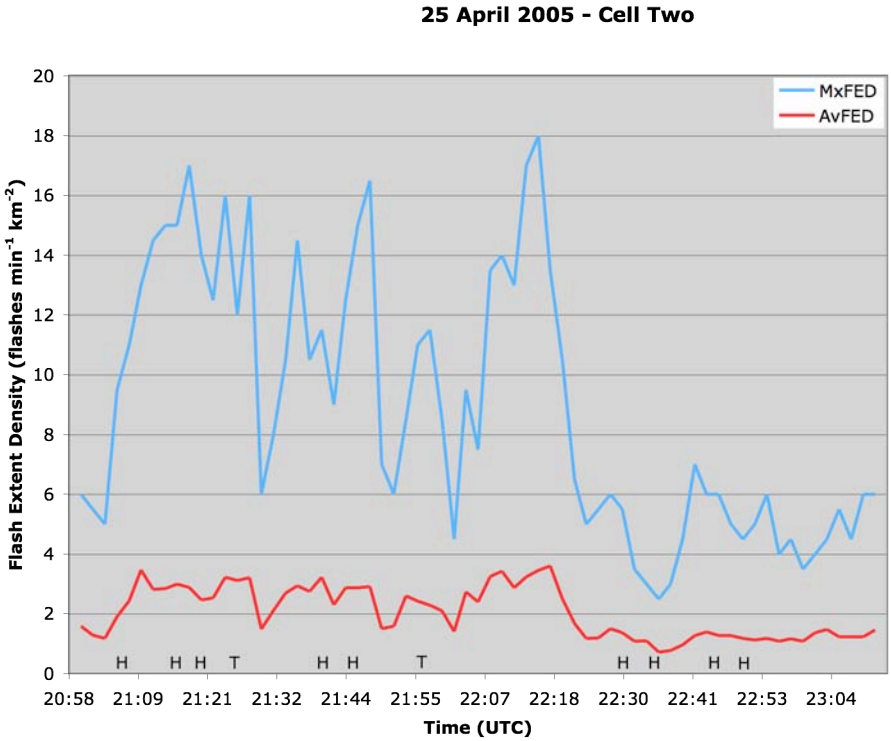

Figure 3.18. Same as Fig. 3.13, except for cell two on 25 April 2005. Storm reports for this cell are marked along the x-axis (labels same as Fig. 3.13).

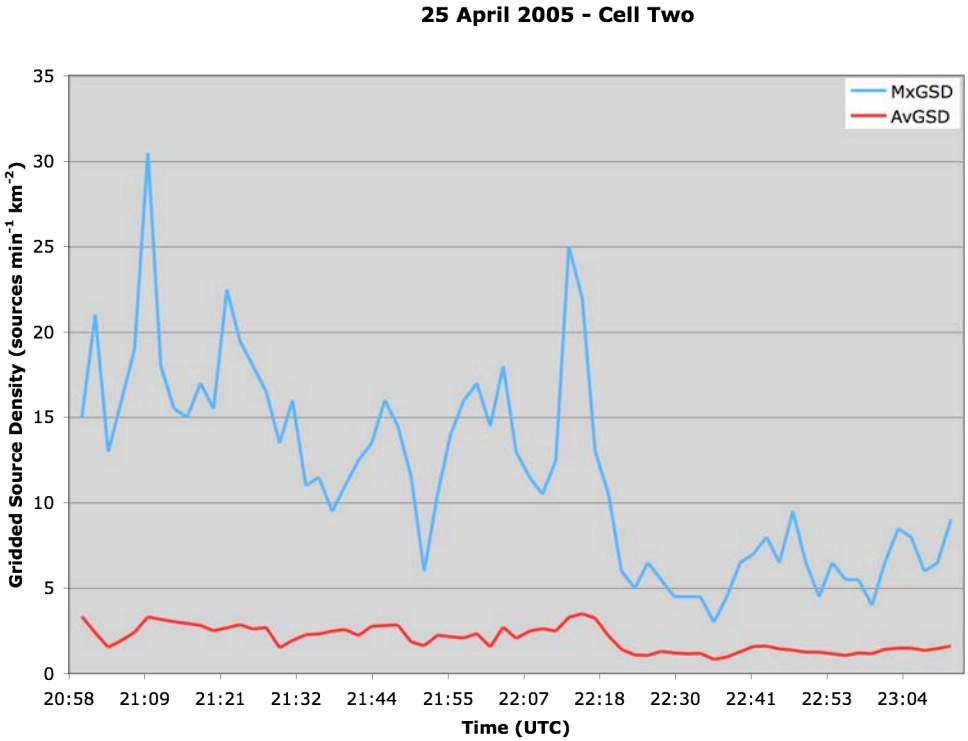

Figure 3.19. Same as Fig. 3.14, except for cell two on 25 April 2005.

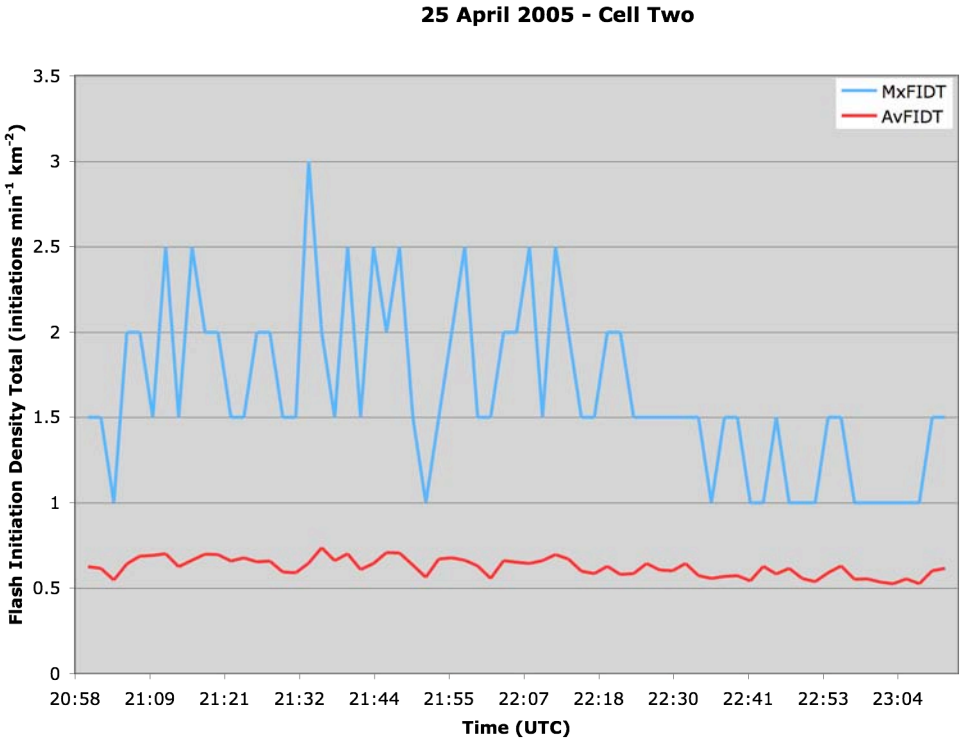

Figure 3.20. Same as Fig. 3.15, except for cell two on 25 April 2005.

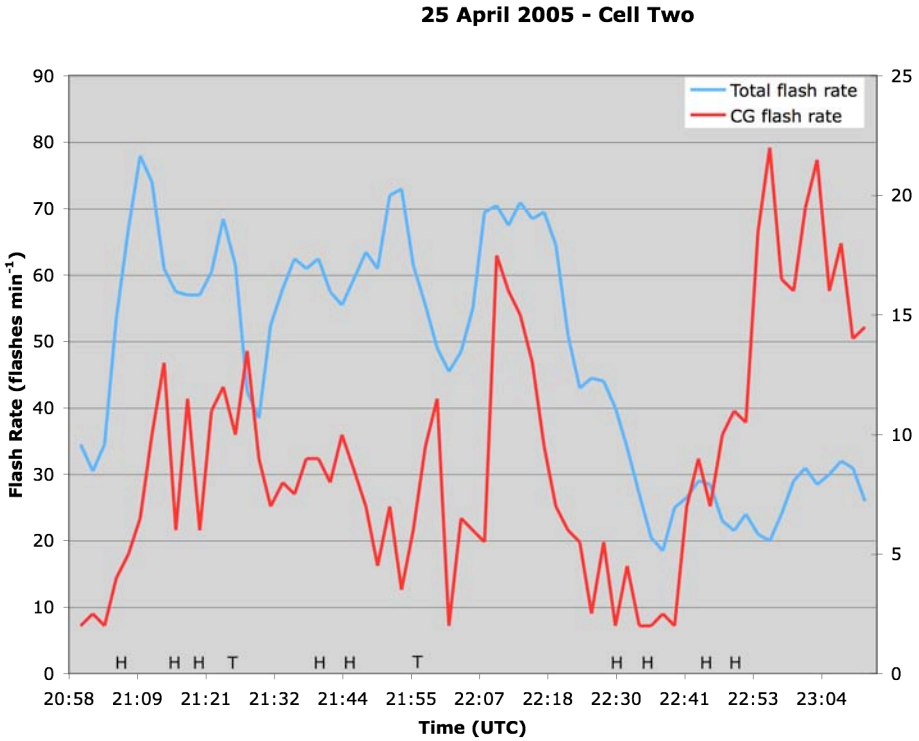

Figure 3.21. Same as Fig. 3.16, except for cell two on 25 April 2005. Total flash rate values are displayed along the left vertical axis, CG flash rate values are on the right hand vertical axis. Storm reports are marked along the x-axis (labels same as Fig. 3.13).

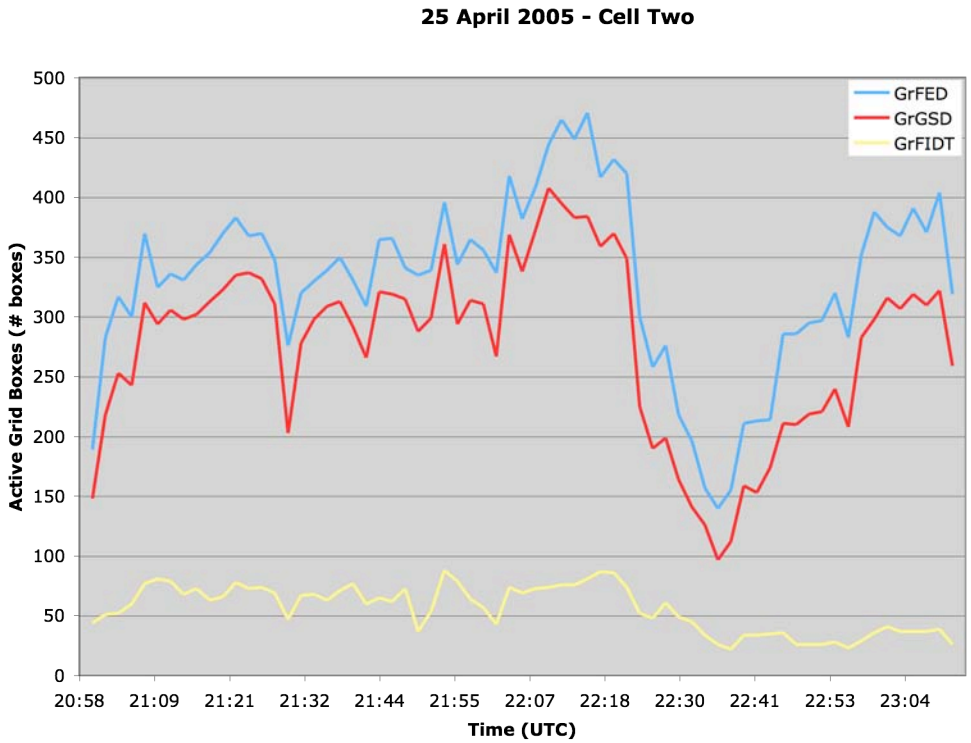

Figure 3.22. Same as Fig. 3.17, except for cell two on 25 April 2005.

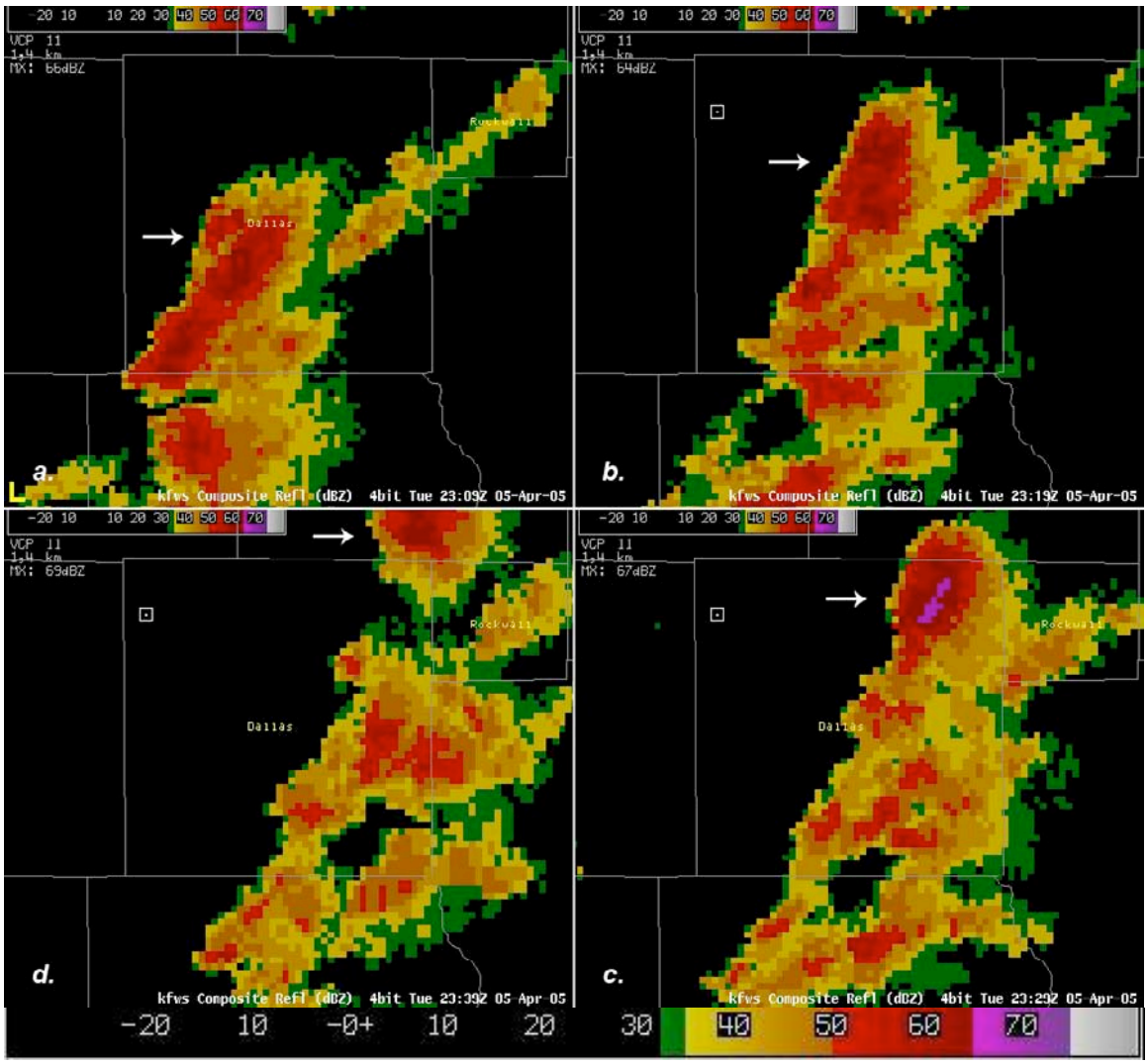

Figure 3.23. Evolution of left moving supercell on 05 April 2005 from KFWS composite reflectivity (dBZ, colors as shown). Position of this cell is displayed at (a) 2309 UTC, (b) 2319 UTC, (c) 2329 UTC, and (d) 2339 UTC.

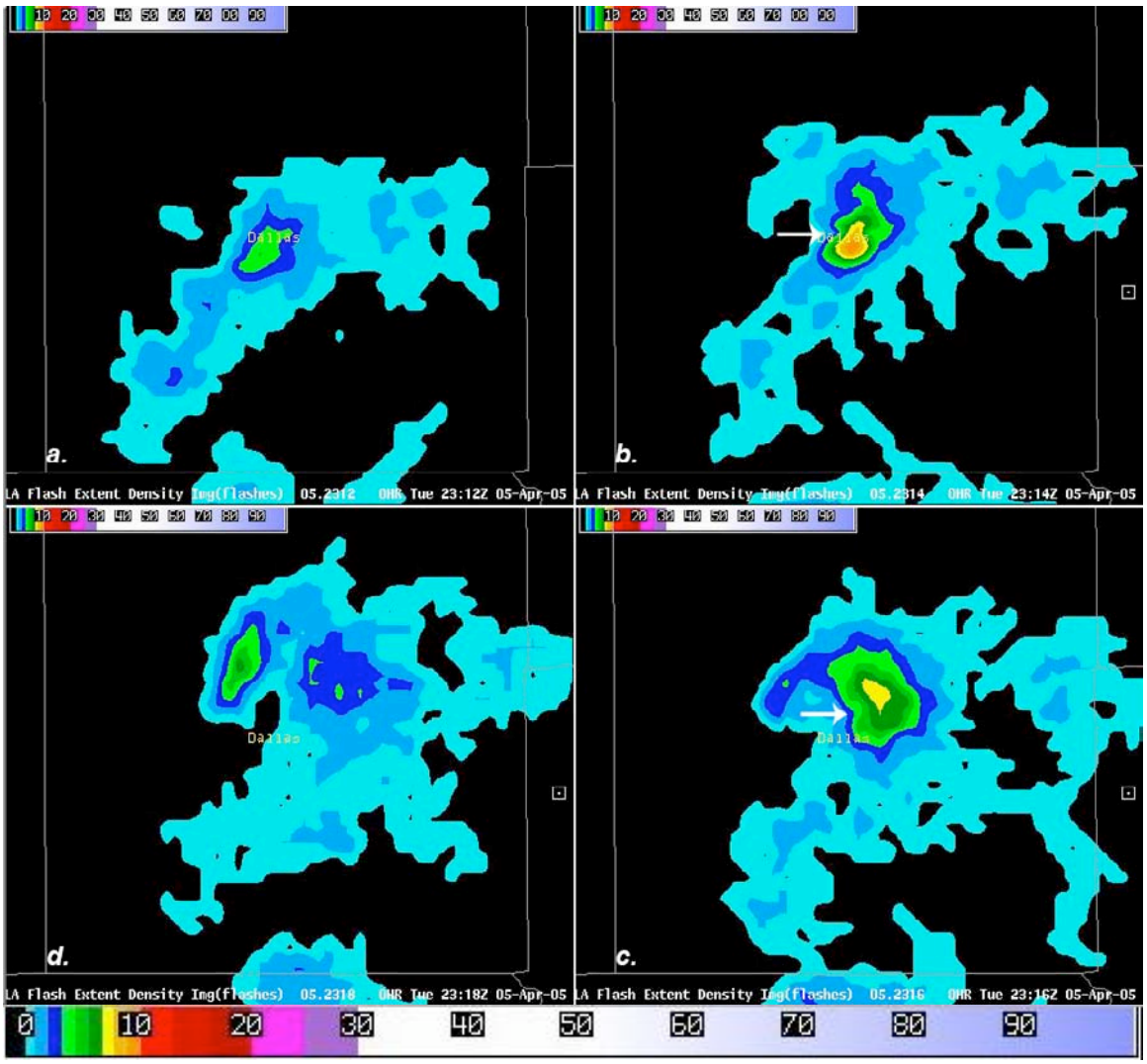

Figure 3.24. Development of leading appendage on the left moving supercell and subsequent shift of FED maximum at (a) 2312 UTC, (b) 2314 UTC, (c) 2316 UTC, and (c) 2318 UTC on 05 April 2005. Updraft notches are marked with white arrows. Units are flashes min^{-1} km^{-2}, colors as shown.

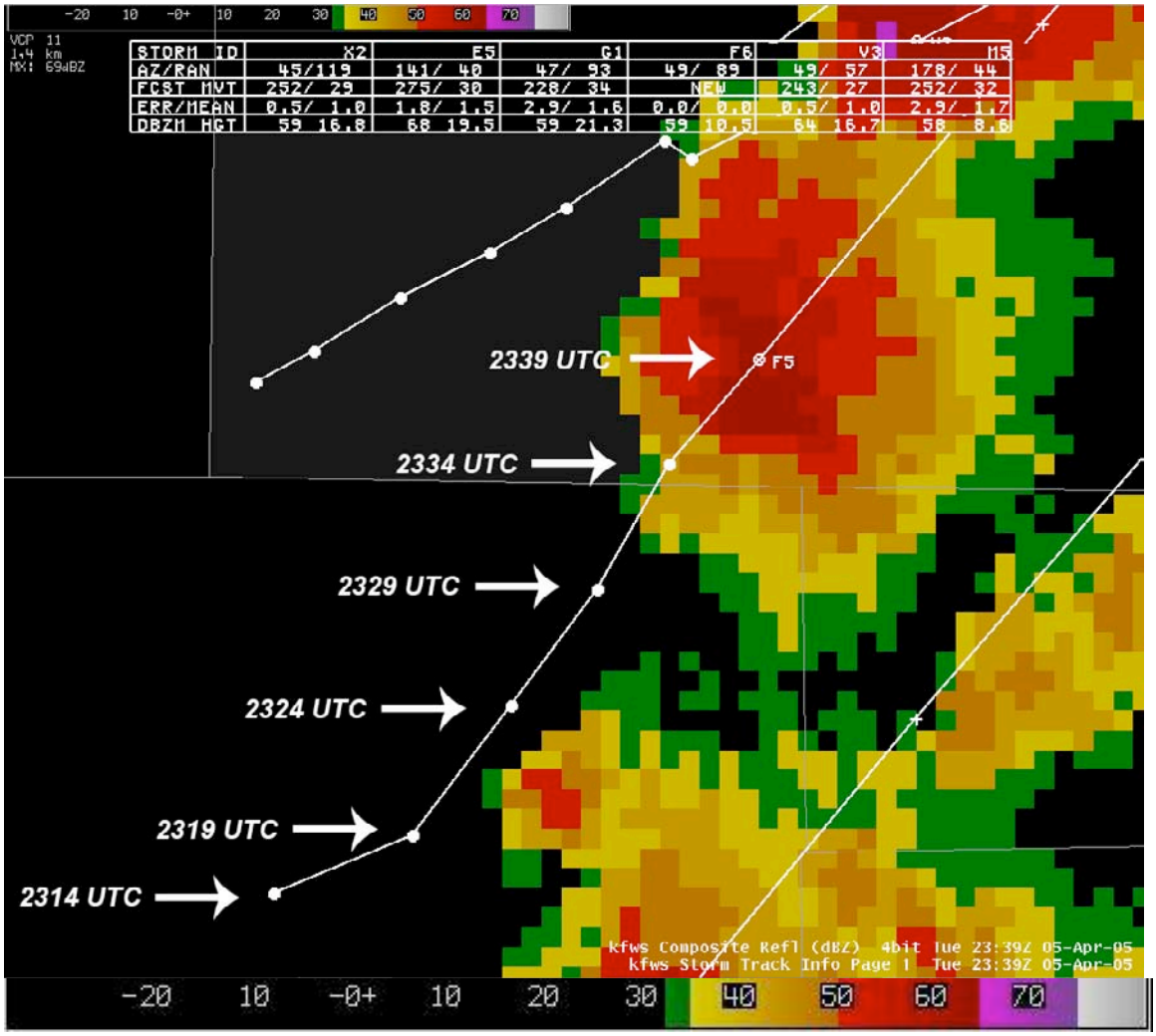

Figure 3.25. KFWS composite reflectivity of cell one (labeled as “F5”) on 05 April 2005 at 2339 UTC. Dots indicate SCIT derived cell locations at each of the times labeled, while the white line denotes the SCIT cell track. Note the turn to the left between 2319 and 2324 UTC, after the development of the FED appendage between 2314 and 2318 UTC (Fig. 3.24).

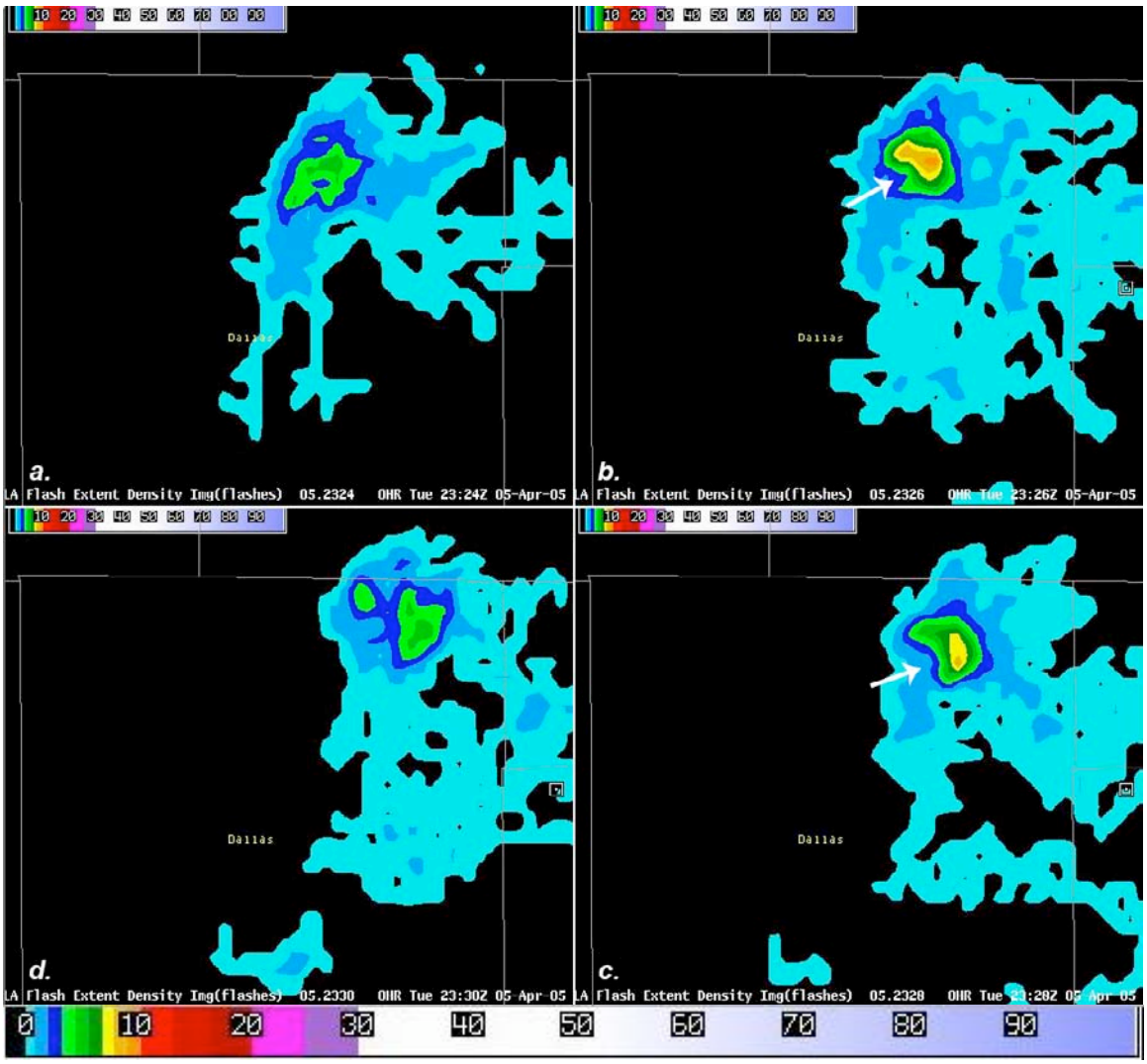

Figure 3.26. Development of second leading appendage associated with the left moving supercell from the 05 April 2005 case. Times are: (a) 2324 UTC, (b) 2326 UTC, (c) 2328 UTC, and (d) 2330 UTC. Updraft notches are marked with arrows. Units are flashes min^{-1} km^{-2}, colors as shown.

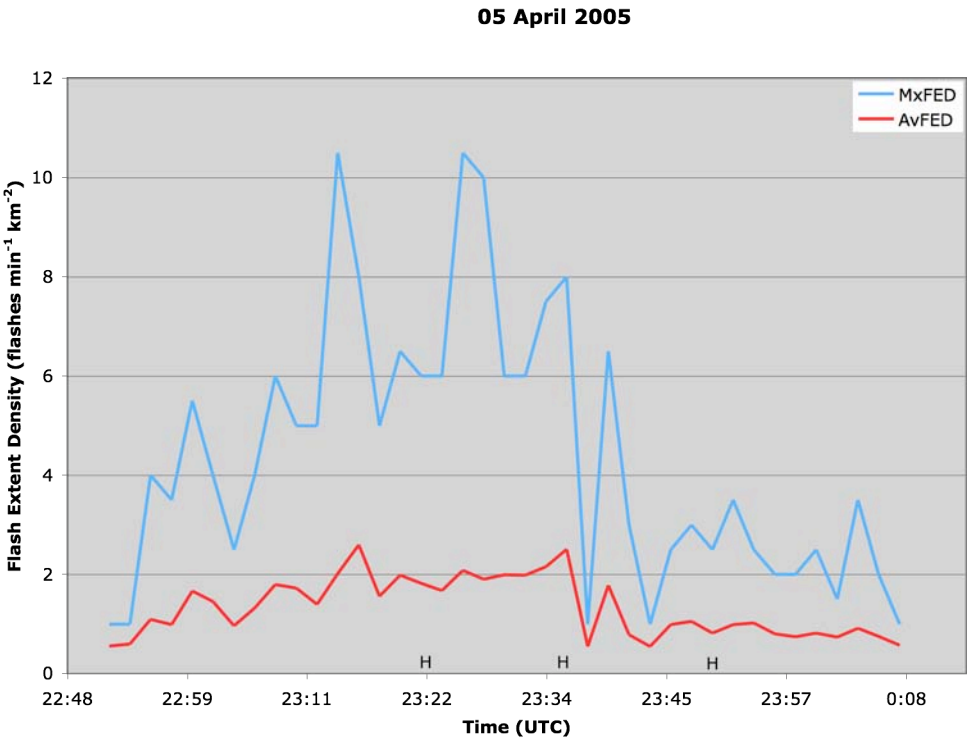

Figure 3.27. Same as Fig. 3.13, except for cell one on 05 April 2005. Reports of severe weather from this date are marked along the x-axis.

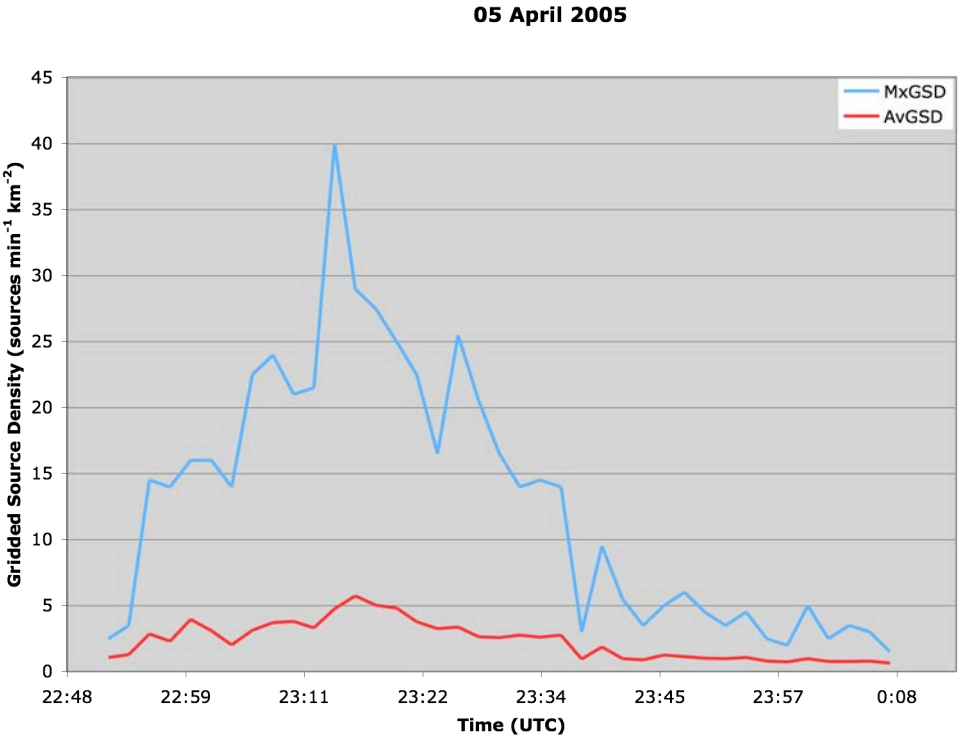

Figure 3.28. Same as Fig. 3.14, except for cell one on 05 April 2005.

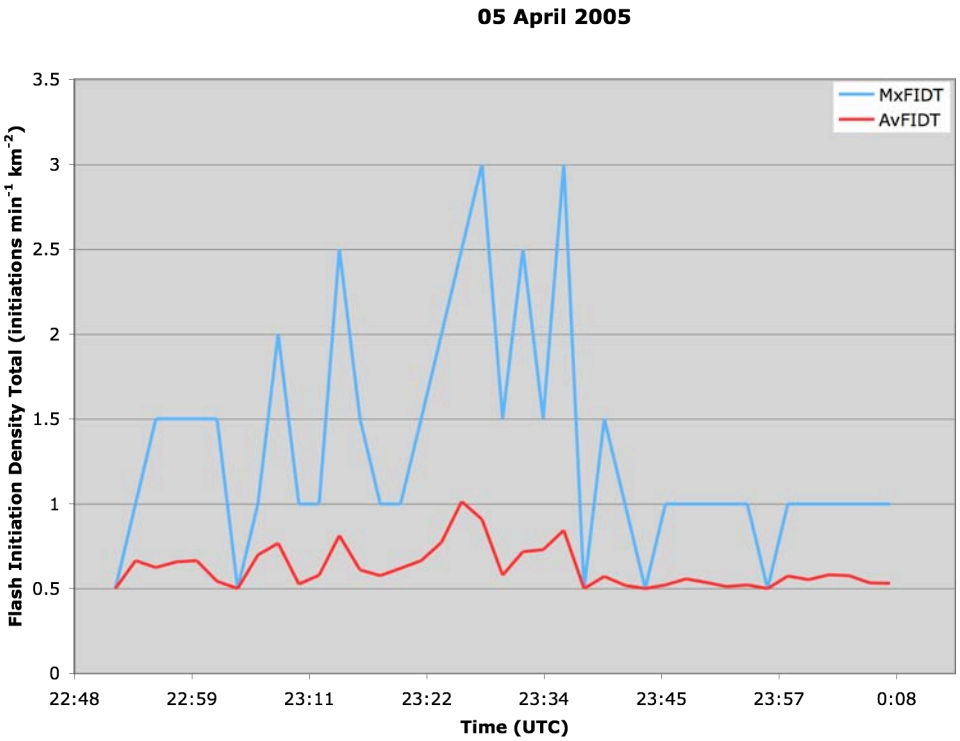

Figure 3.29. Same as Fig. 3.15, except for cell one on 05 April 2005.

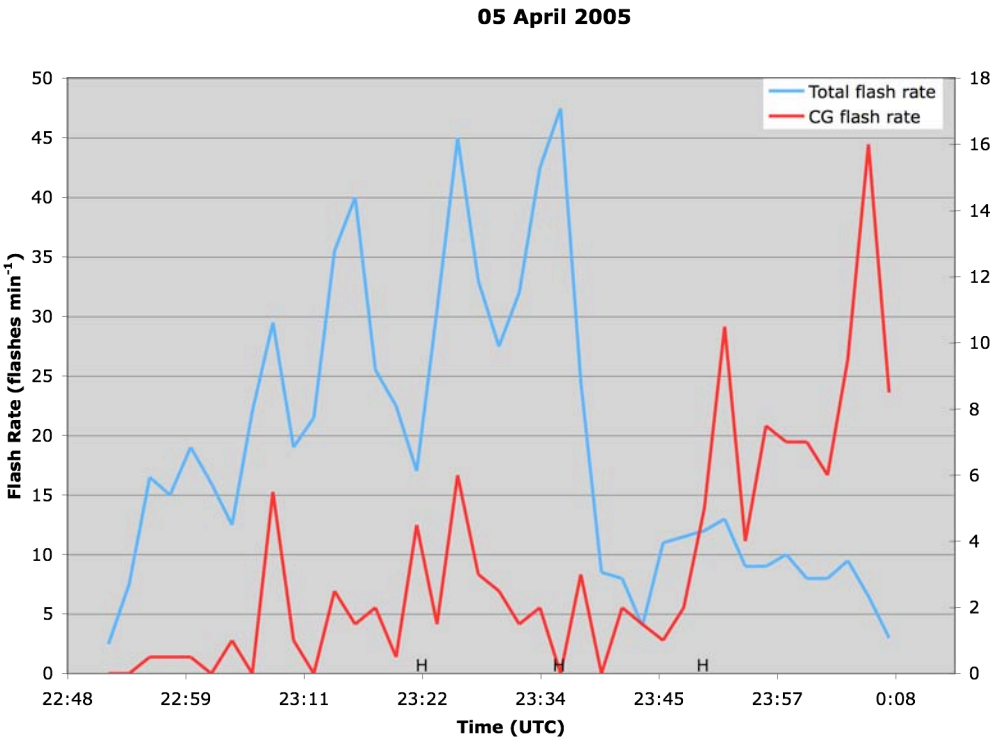

Figure 3.30. Same as Fig. 3.16, except for cell one on 05 April 2005. Total lightning flash rate values are on the left vertical axis, CG flash rate values are displayed on the right hand vertical axis. Severe weather reports are marked along the x-axis.

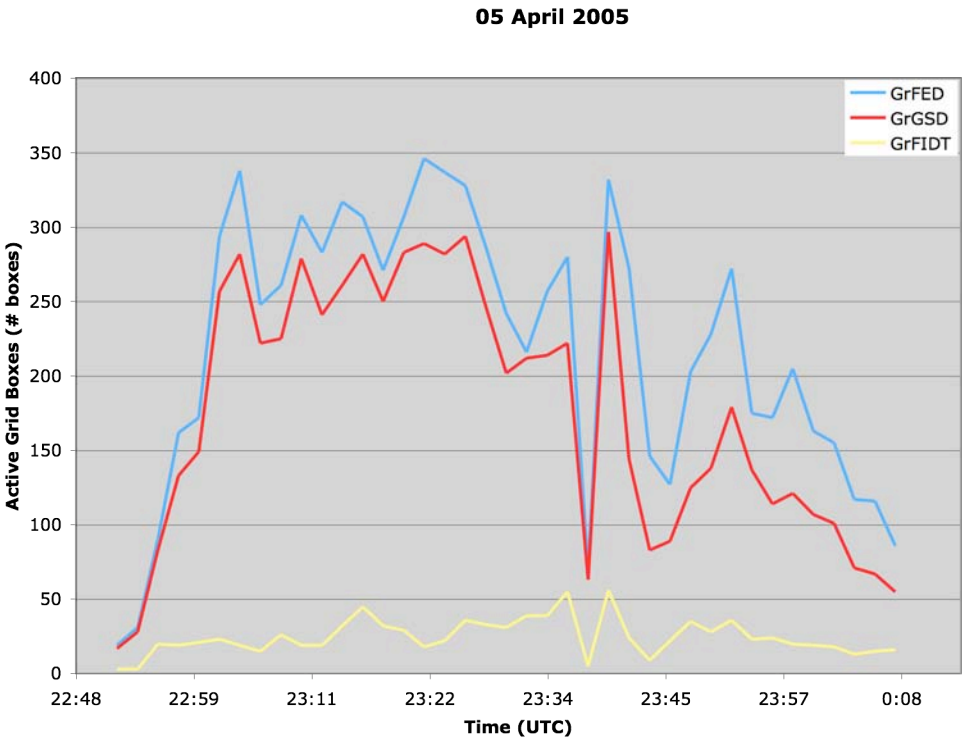

Figure 3.31. Same as Fig. 3.17, except for cell one on 05 April 2005.

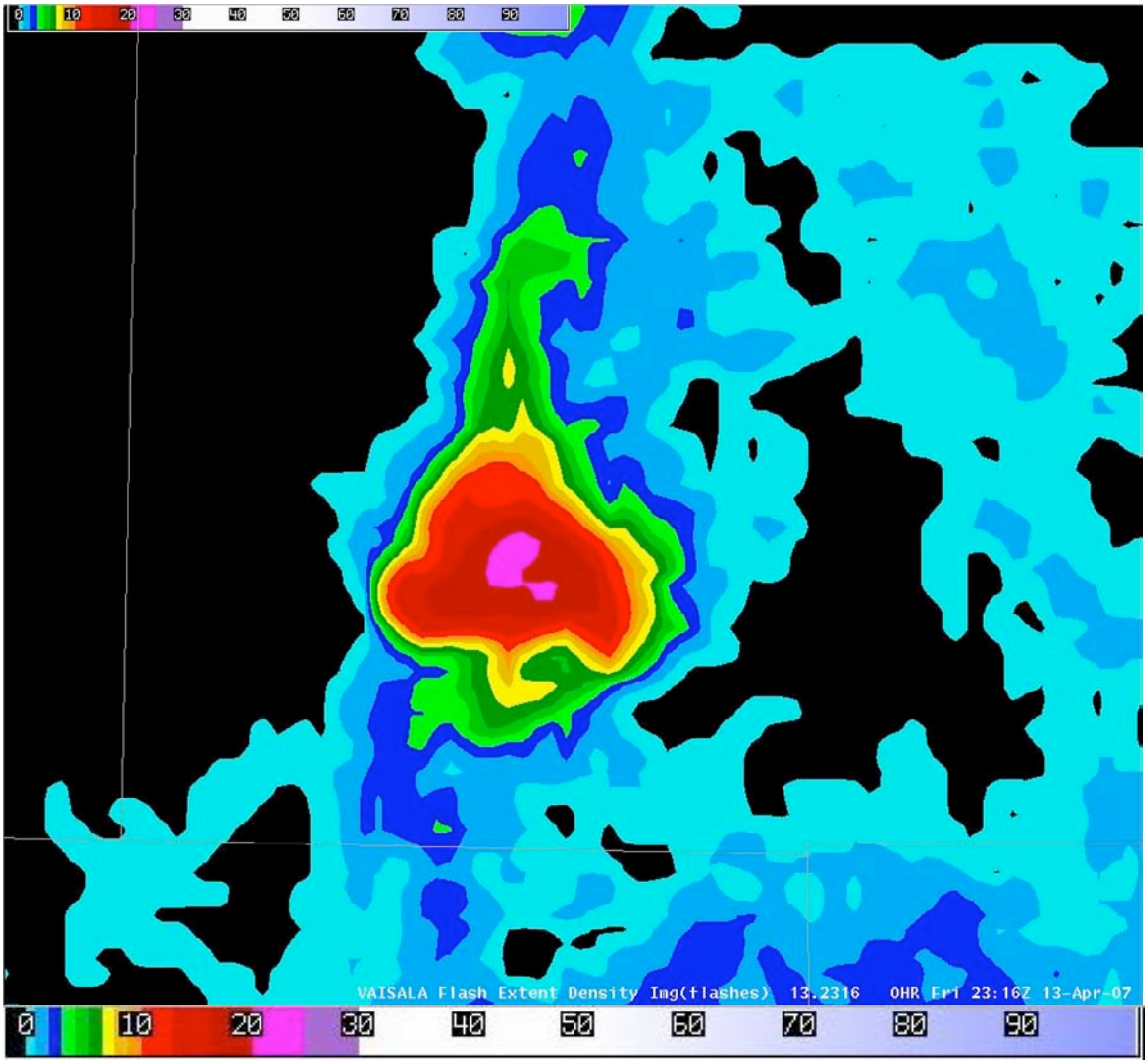

Figure 3.32. Hook shaped FED (flashes min^{-1} km^{-2}, colors as shown) appendage in Denton County at 2316 UTC on 13 April 2007.

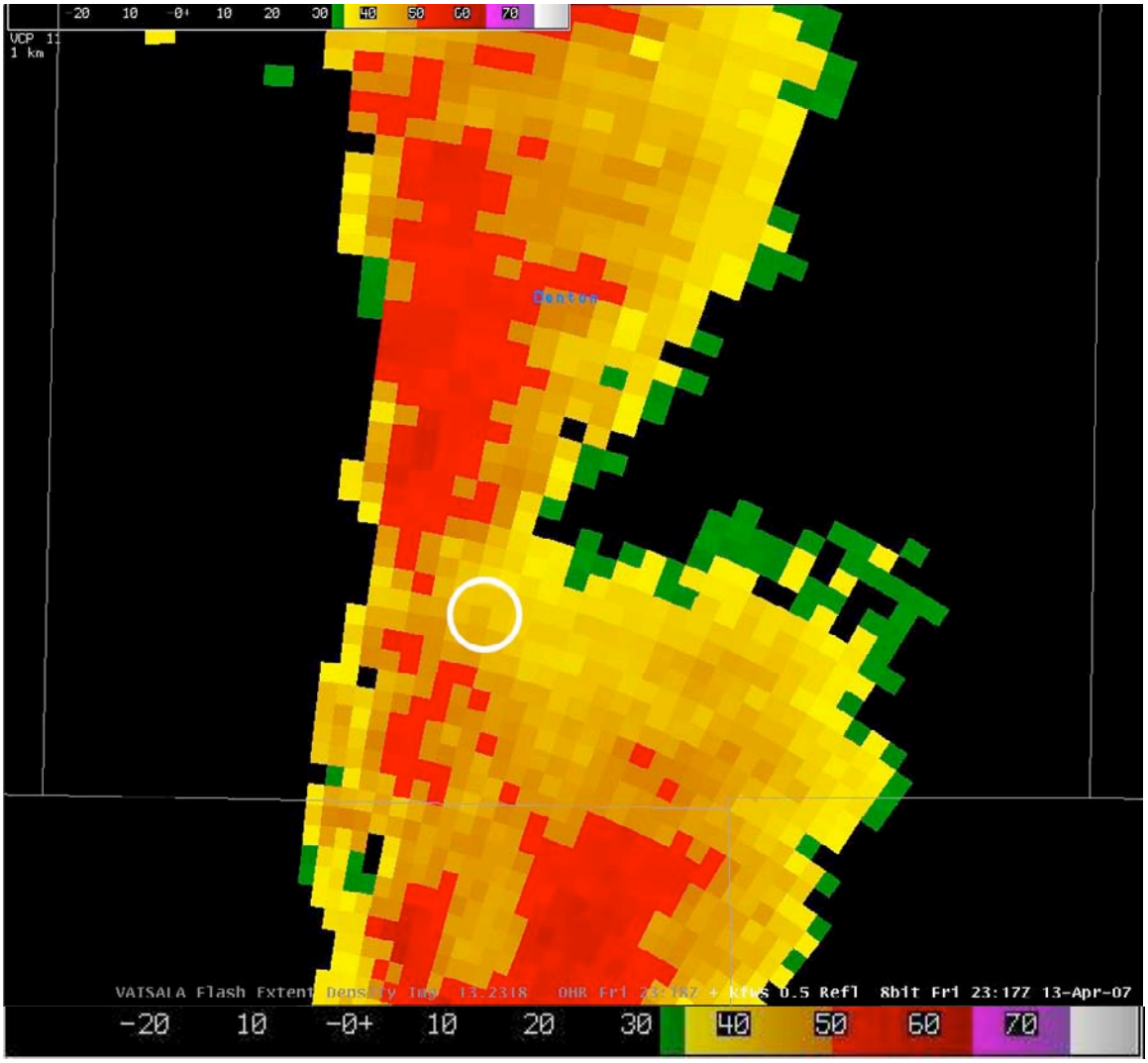

Figure 3.33. KFWS 0.5-degree reflectivity image from 2317 UTC on 13 April 2007 (dBZ, colors as shown). Highlighted area is the area encircled by the FED hook appendage in Fig. 3.32.

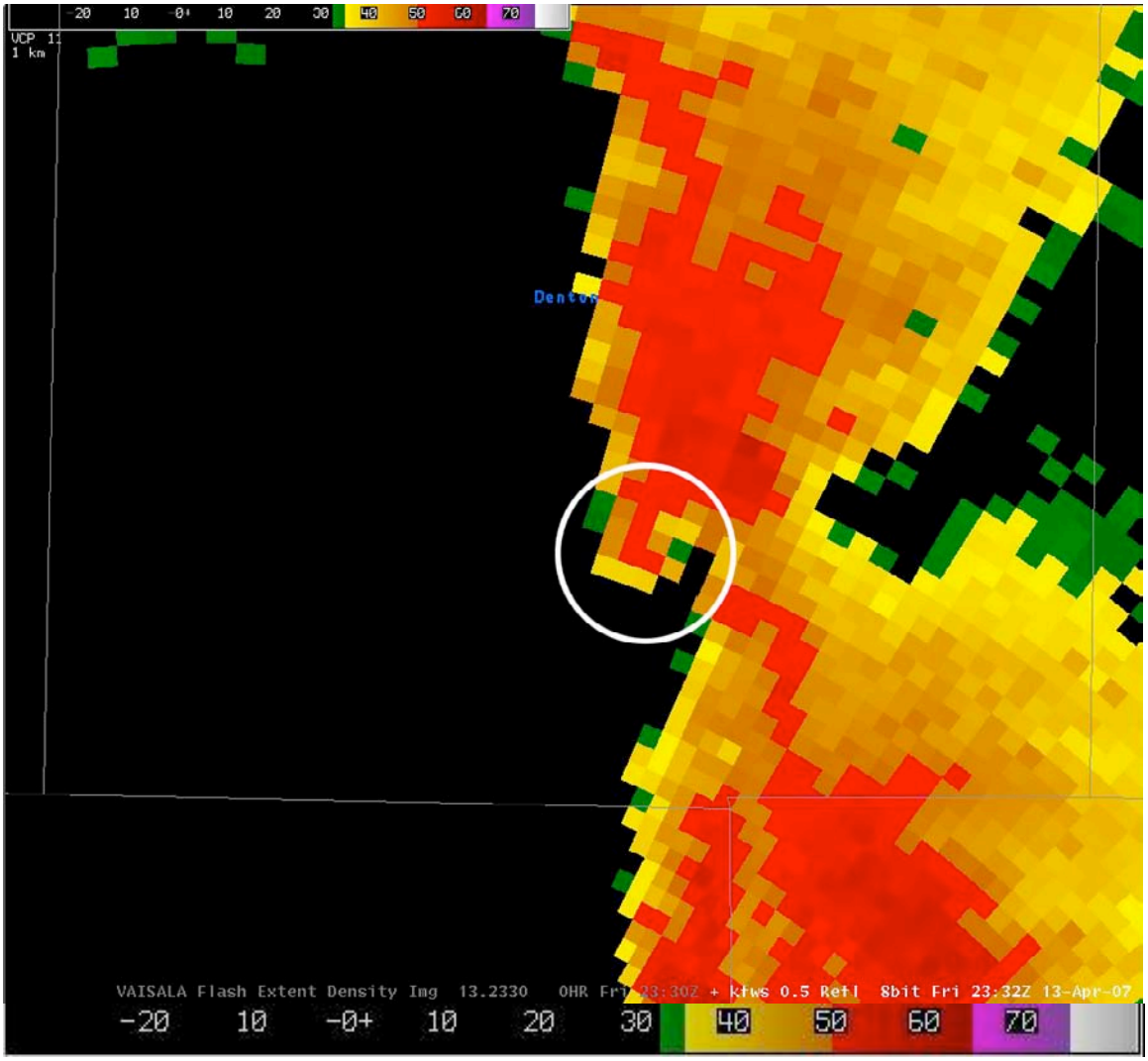

Figure 3.34. 0.5-degree reflectivity image (dBZ, colors as shown) from KFWS radar at 2332 UTC on 13 April 2007 showing a radar hook echo that developed in southern Denton County.

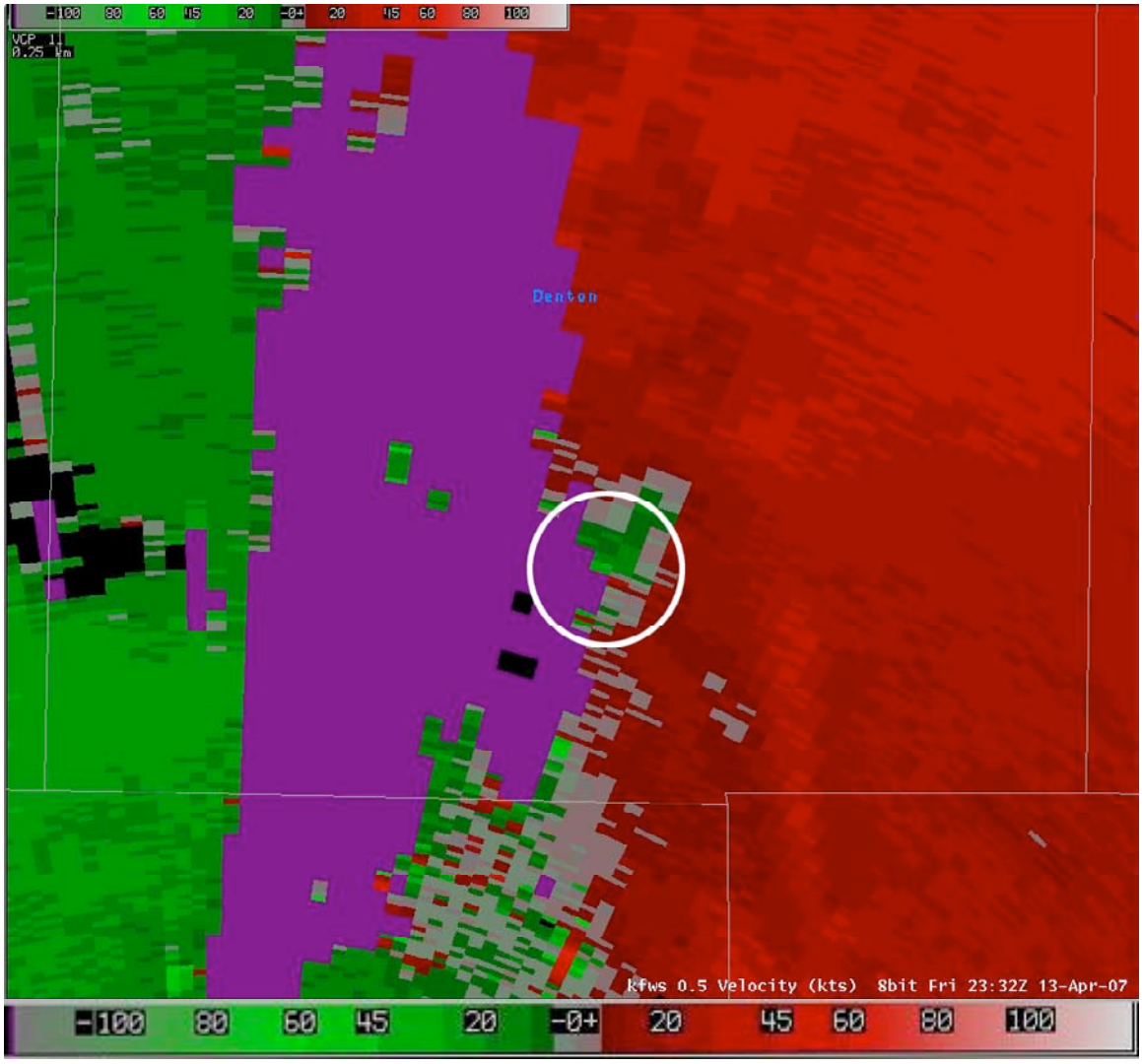

Figure 3.35. KFWS 0.5-degree velocity (ms^{-1}) image from 2332 UTC on 13 April 2007. Highlighted region is the same as that in Fig. 3.34. Note the velocity couplet co-located with the hook echo shown in Fig. 3.34.

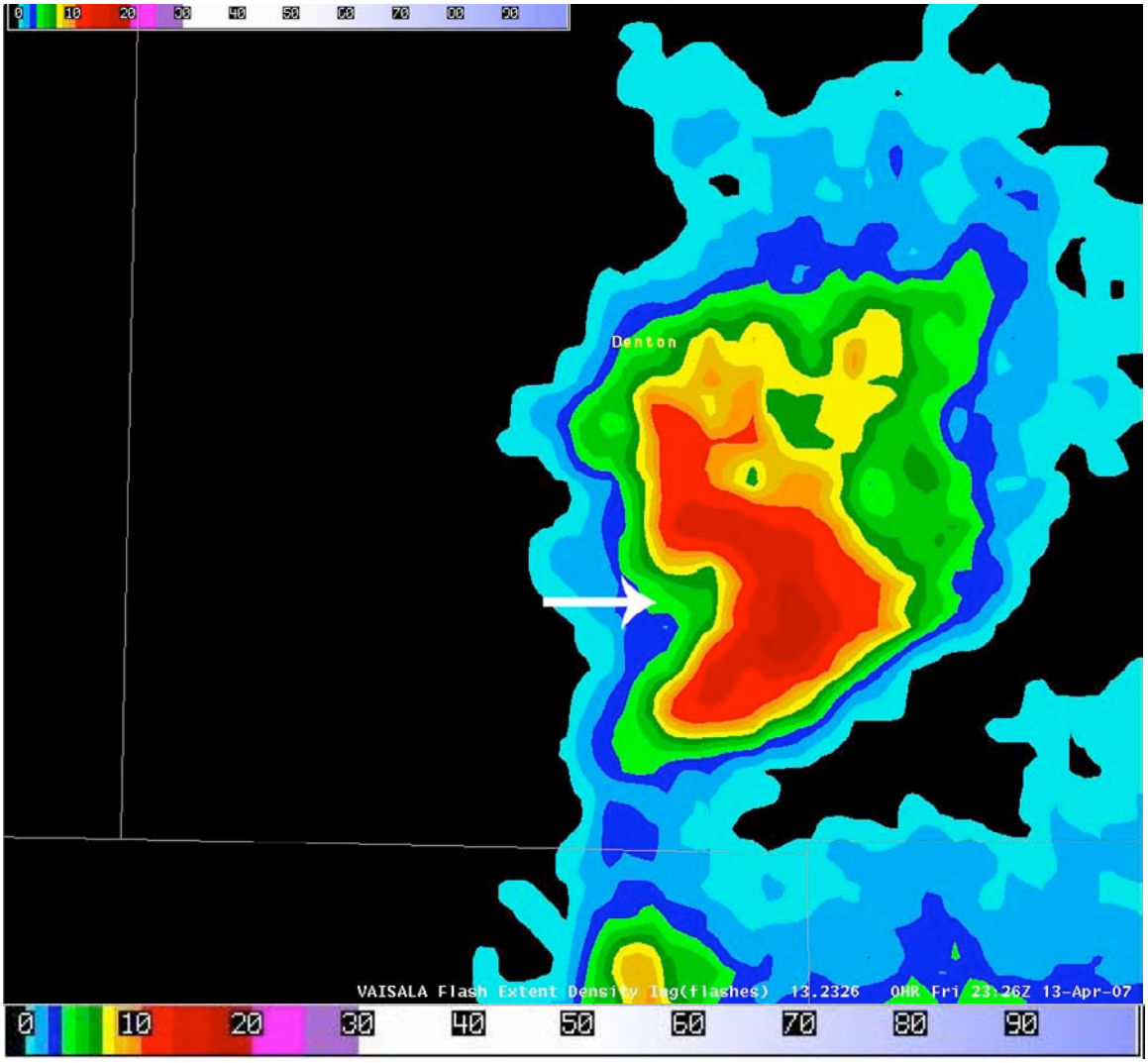

Figure 3.36. FED (flashes min^{-1} km^{-2}, colors as shown) notch developing at 2326 UTC on 13 April 2007 on the rear flank of cell one in Denton County.

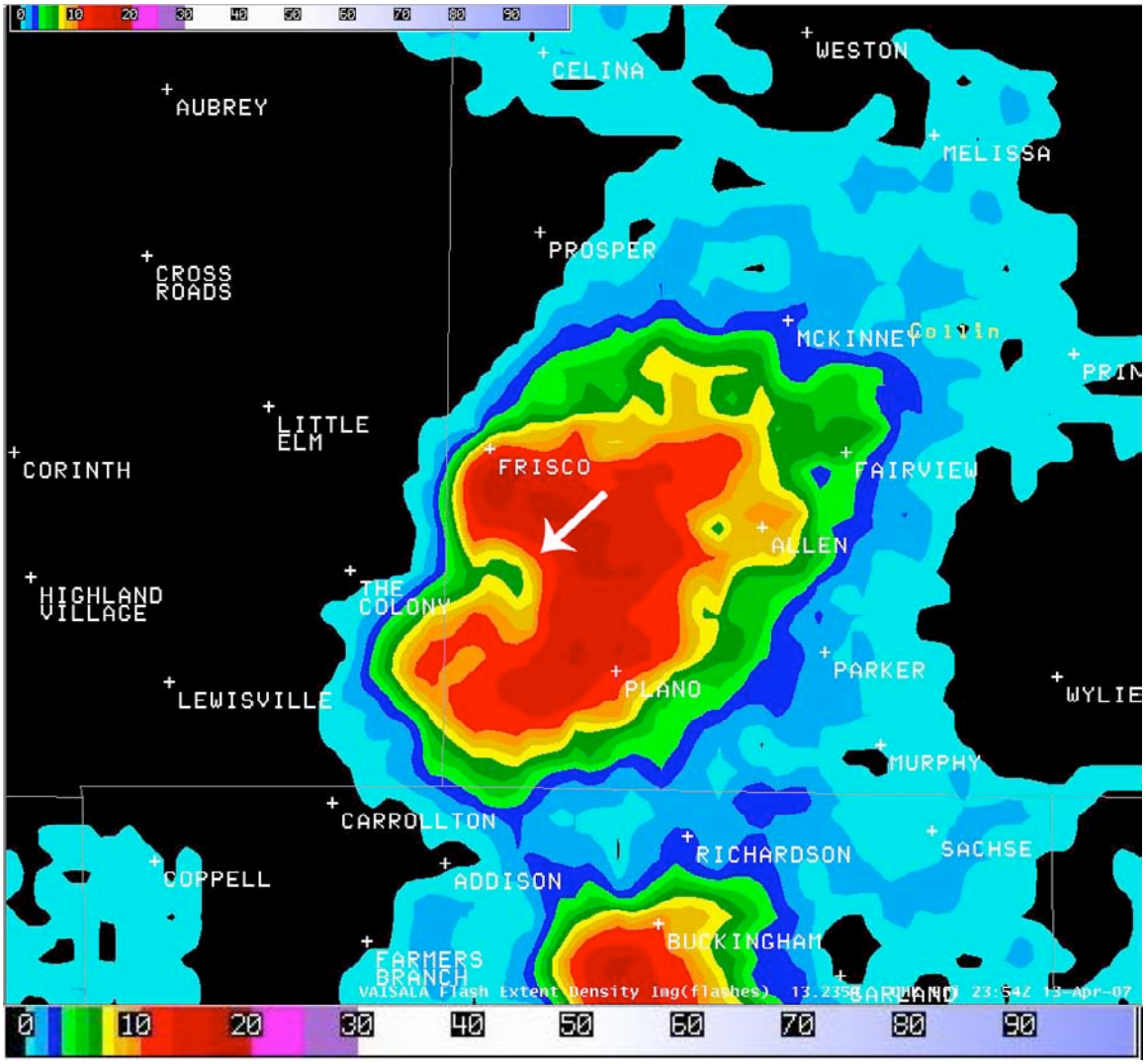

Figure 3.37. FED (flashes min^{-1} km^{-2}, colors as shown) notch from cell one at 2354 UTC on 13 April 2007. A severe wind report was recorded just north of the town of Allen (located on the east side of the FED core) at 0015 UTC.

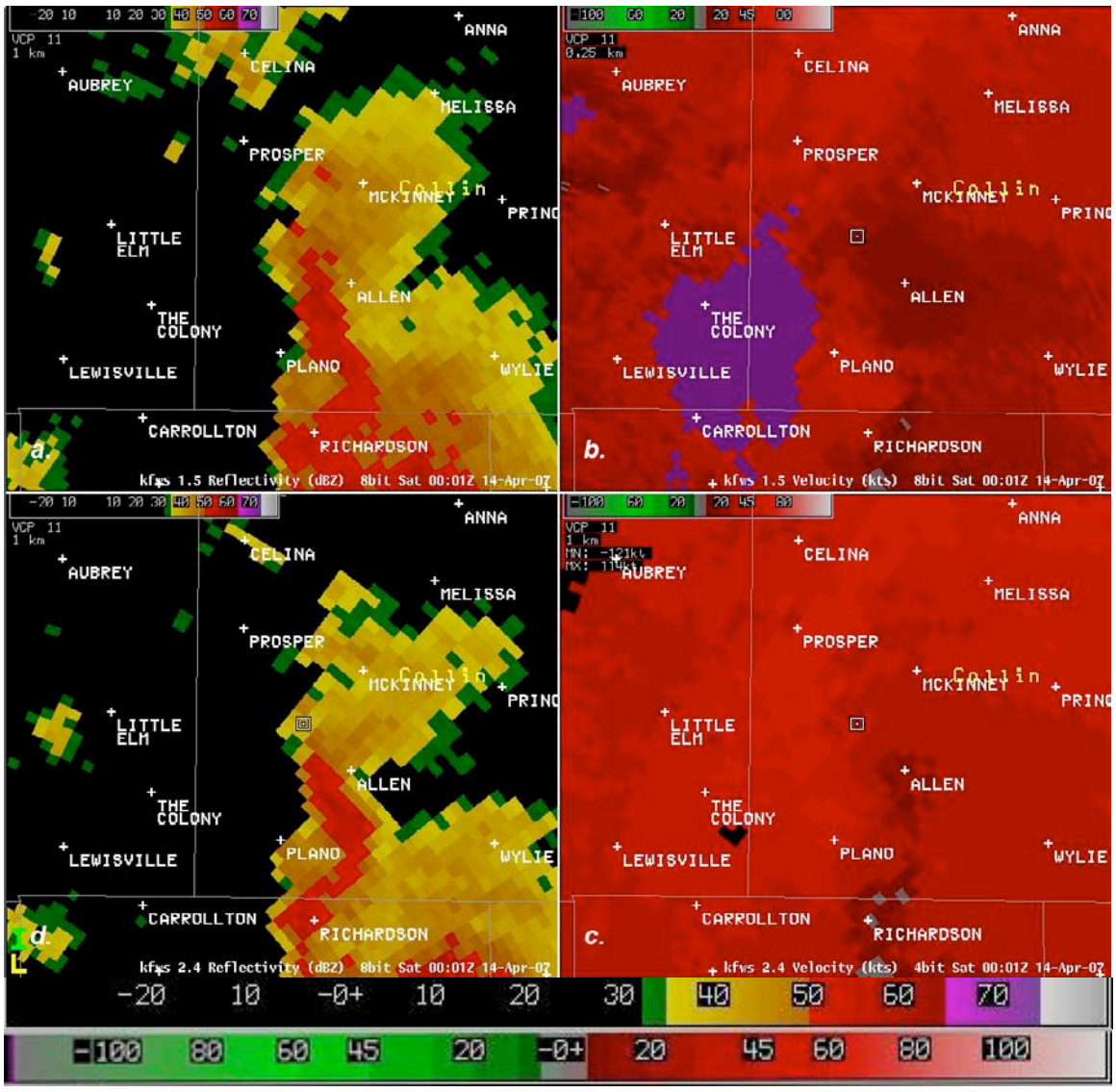

Figure 3.38. KFWS radar reflectivity (dBZ, upper color bar) and velocity (ms^{-1}, lower color bar) images from 0001 UTC 14 April 2007, showing bowing reflectivity and strong straight line winds just to the west of the town of Allen. Images are 0.5 degree: (a) reflectivity and (b) velocity, and 2.4 degree: (c) reflectivity and (d) velocity.

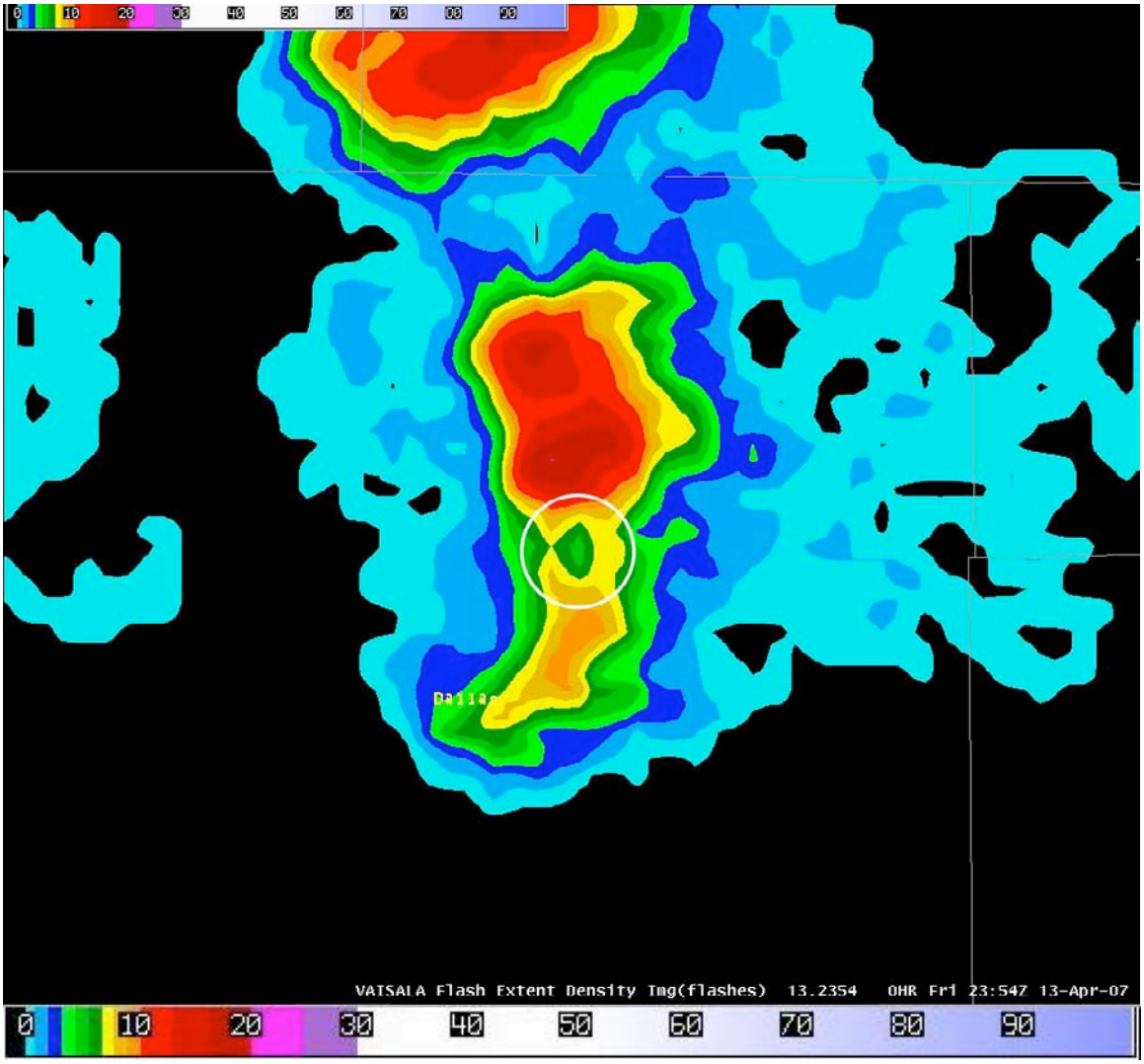

Figure 3.39. FED (flashes min^{-1} km^{-2}, colors as shown) minimum associated with the embedded supercell in Dallas County at 2354 UTC on 13 April 2007.

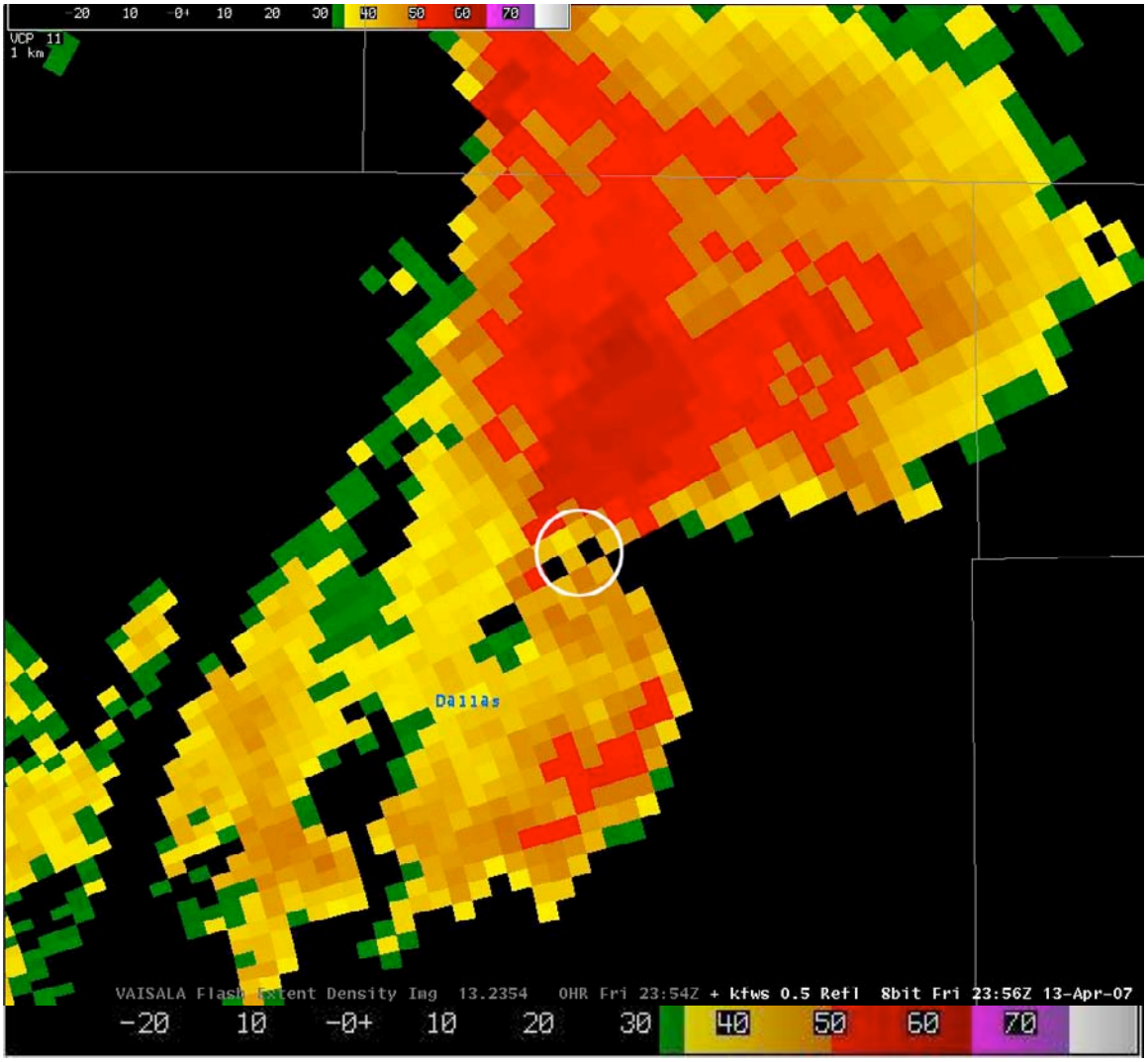

Figure 3.40. KFWS 0.5-degree reflectivity (dBZ, colors as shown) image from 2356 UTC on 13 April 2007. Highlighted location is the position of the FED minimum shown in Fig. 3.39, just to the east of a radar hook echo.

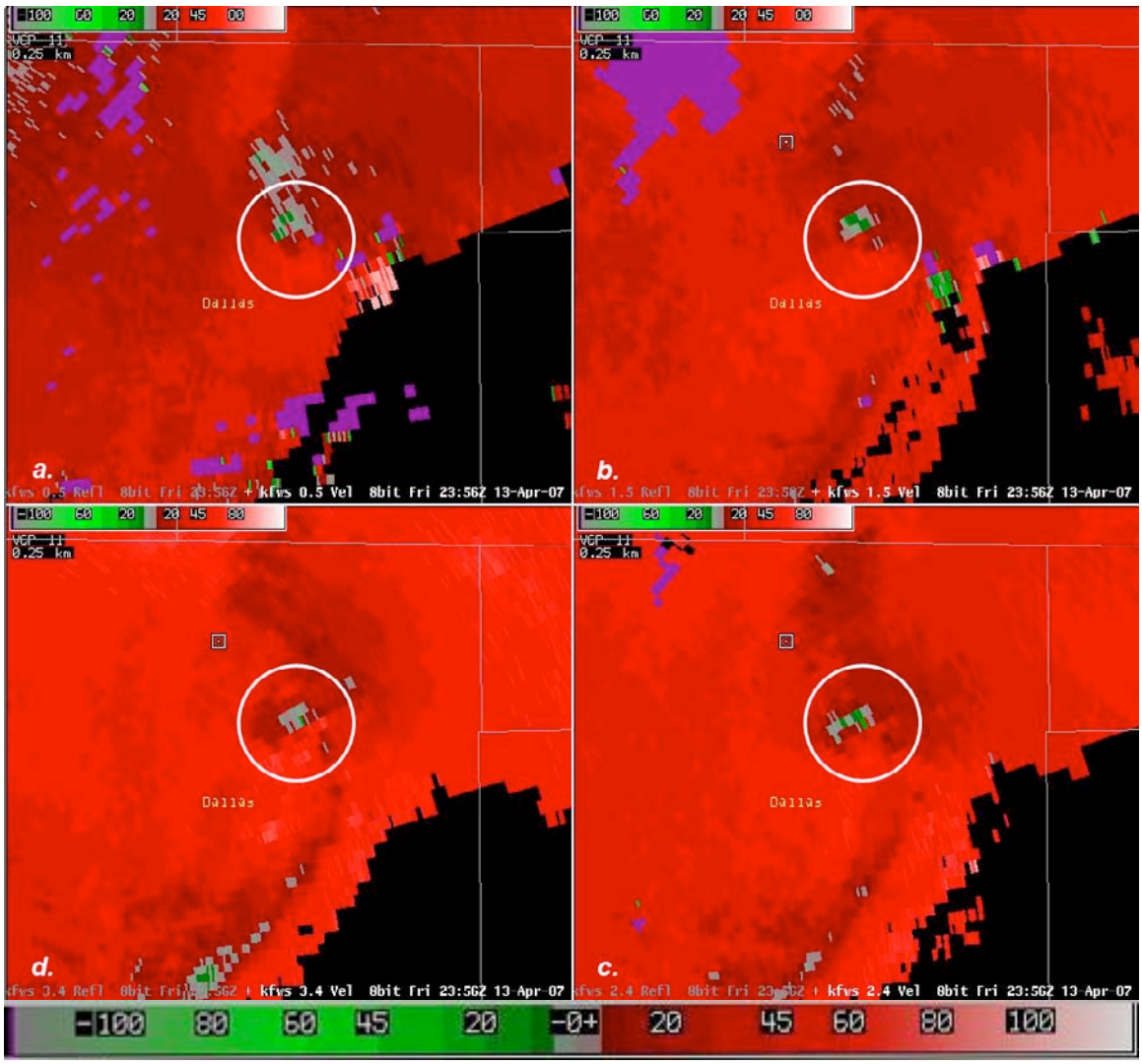

Figure 3.41. Four panel display of low-level velocities (ms^{-1}, colors as shown) over Dallas County at 2356 UTC on 13 April 2007. Images are: (a) 0.5 degree, (b) 1.5 degree, (c) 2.4 degree, and (d) 3.4 degree velocity scans. Encircled region is the location of the FED minimum shown in Fig. 3.39.

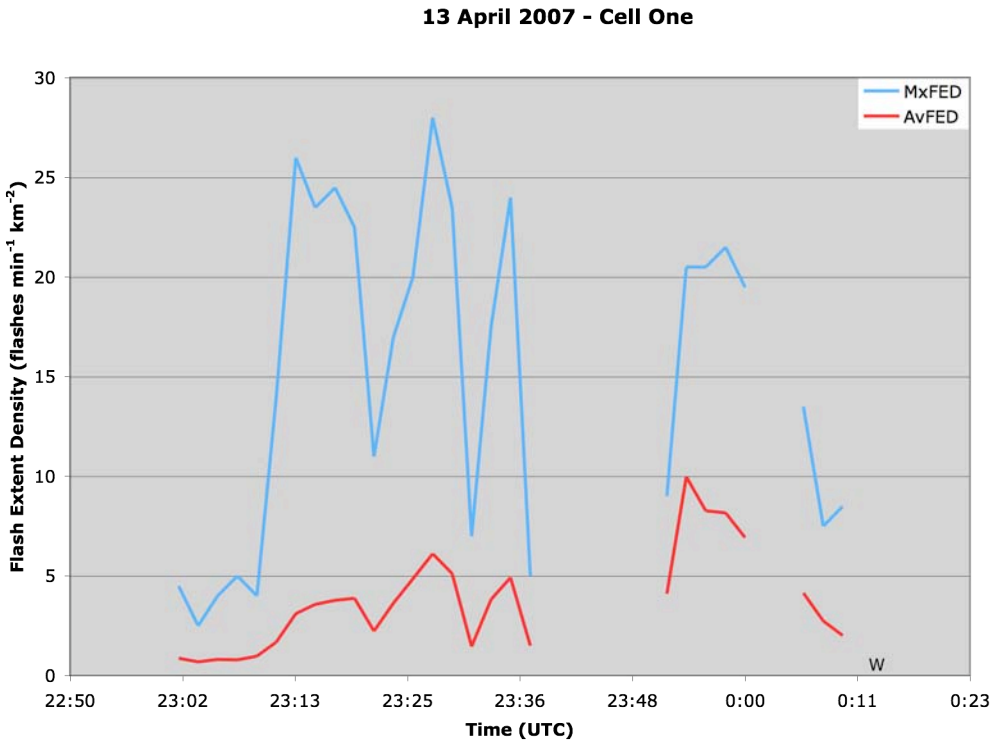

Figure 3.42. Same as Fig. 3.13, except for cell one on 13 April 2007. The time of the severe straight-line wind report in Allen is marked with a "W".

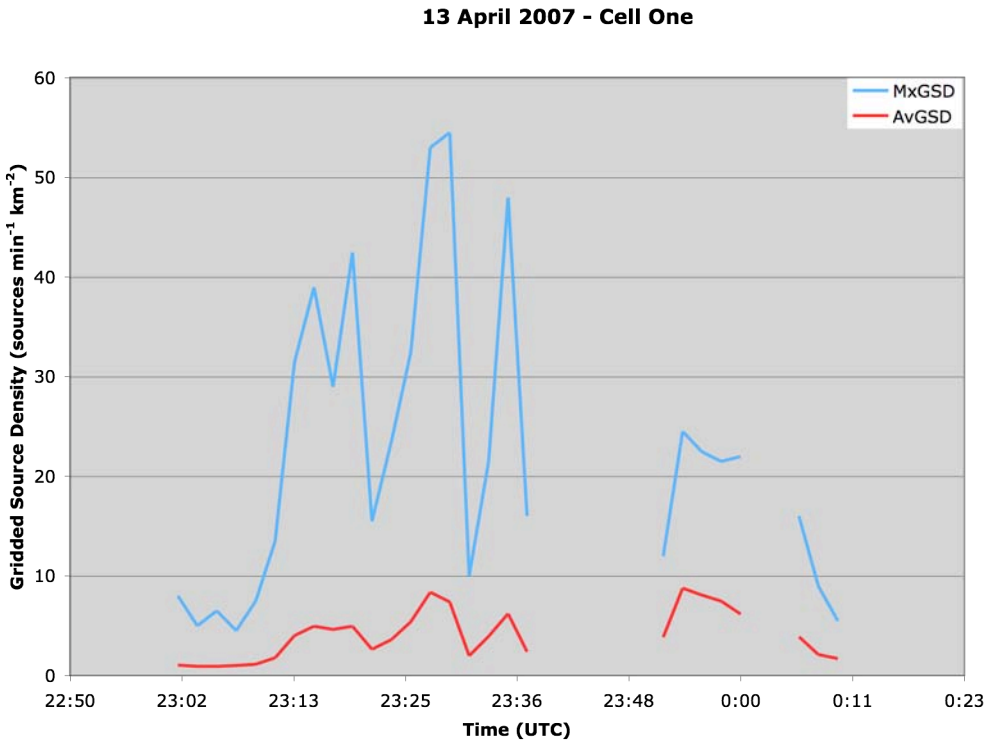

Figure 3.43. Same as Fig. 3.14, except for cell one on 13 April 2007.

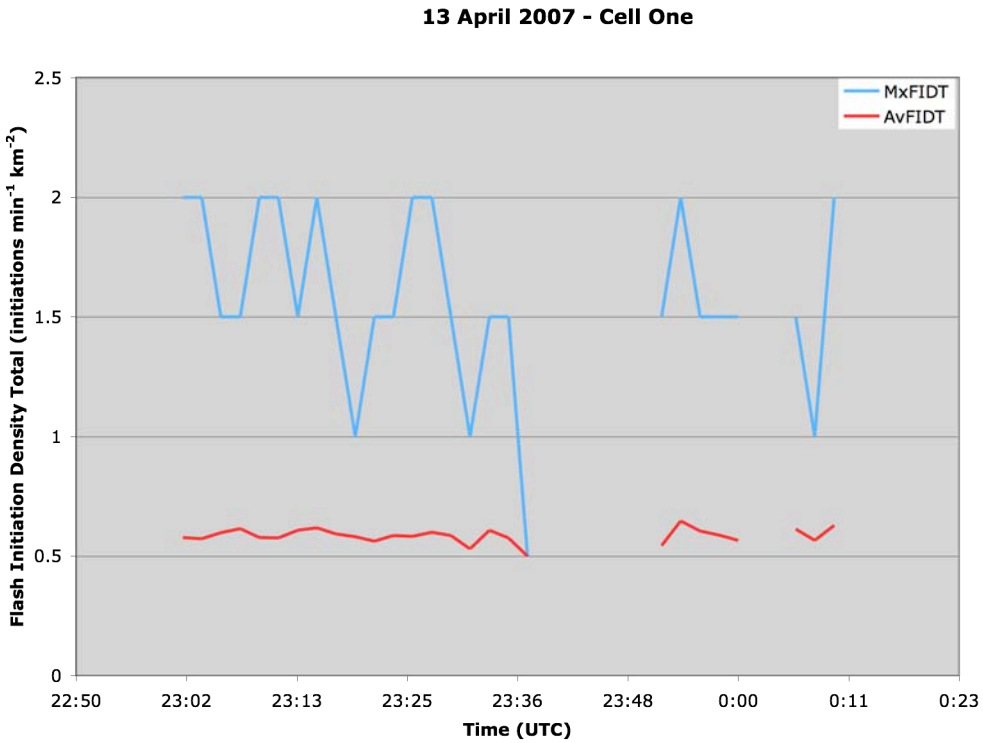

Figure 3.44. Same as Fig. 3.15, except for cell one on 13 April 2007.

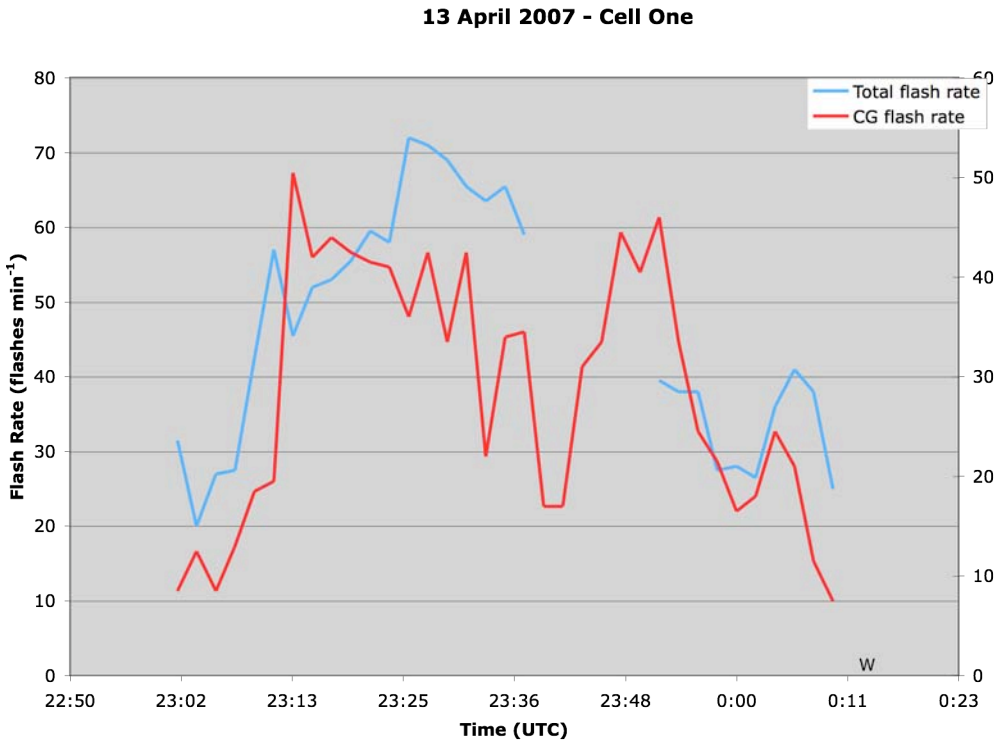

Figure 3.45. Same as Fig. 3.16, except for cell one on 13 April 2007. The straight-line wind report from Allen is marked with a "W" at 0015 UTC. Total lightning flash rate values are on the left vertical axis, CG flash rate values are on the right hand side vertical axis.

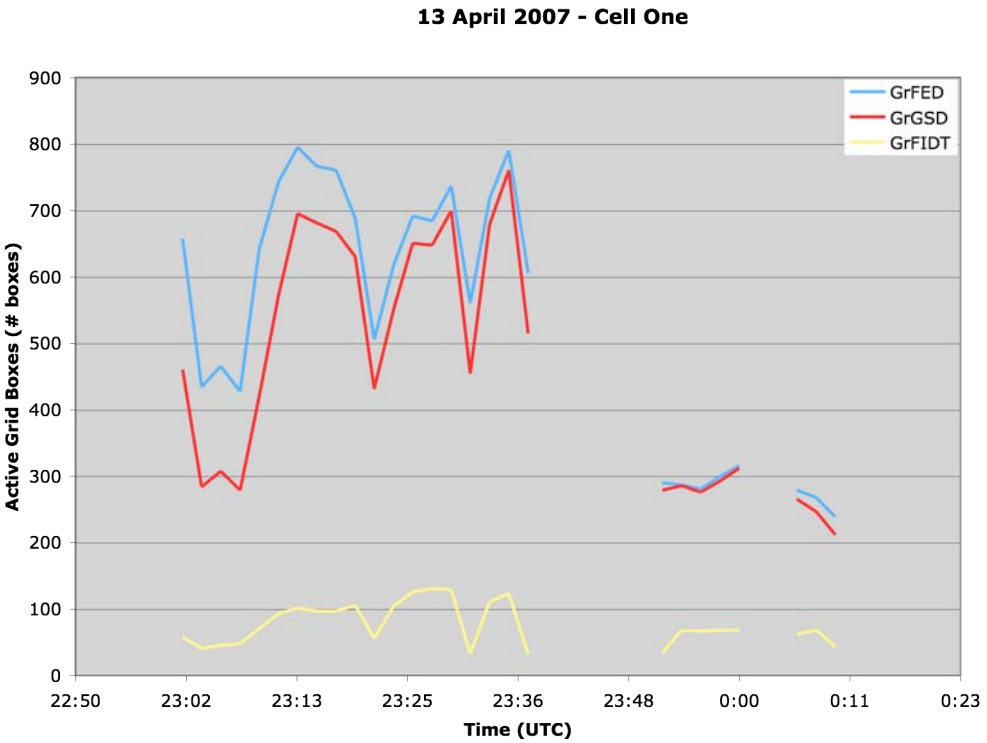

Figure. 3.46. Same as Fig. 3.17, except for cell one on 13 April 2007.

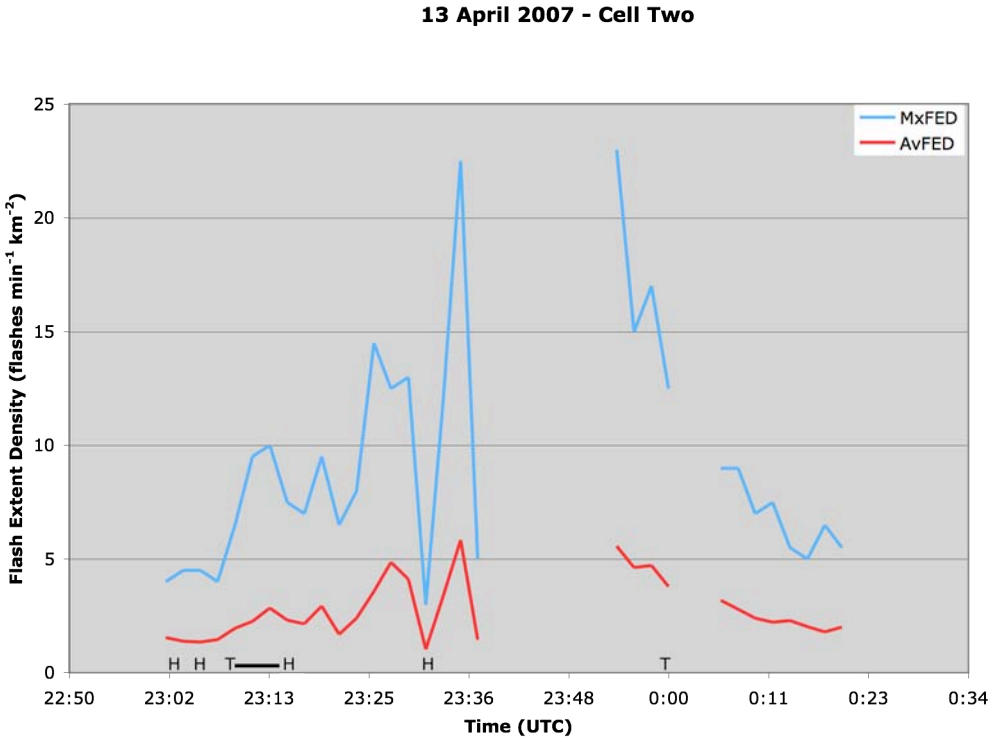

Figure 3.47. Same as Fig. 3.13, except for cell two on 13 April 2007. Storm reports are plotted along the x-axis. The black bar between 2309-2315 UTC represents the length of time that the Haltom City tornado was producing damage. This tornado, rated EF-1, produced one fatality.

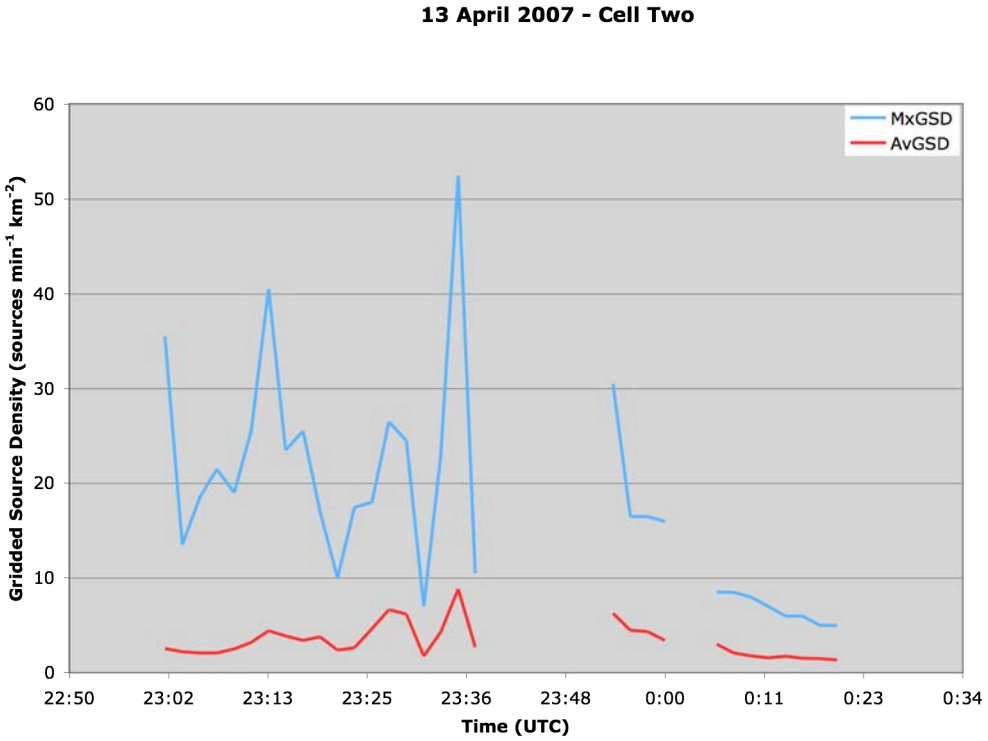

Figure 3.48. Same as Fig. 3.14, except for cell two on 13 April 2007.

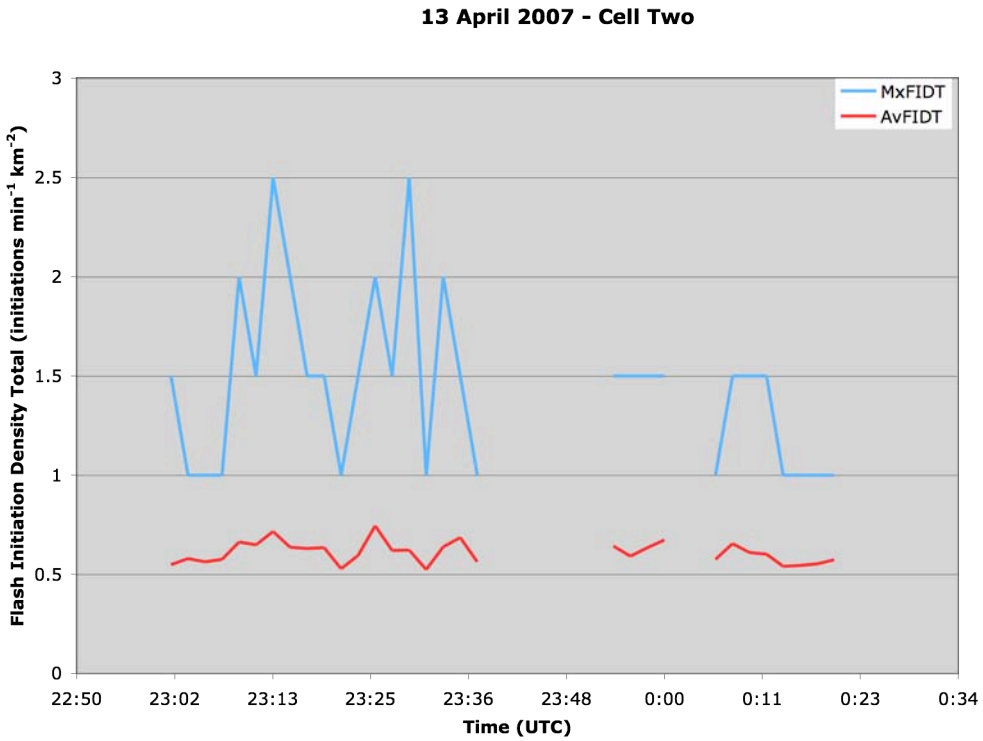

Figure 3.49. Same as Fig. 3.15, except for cell two on 13 April 2007.

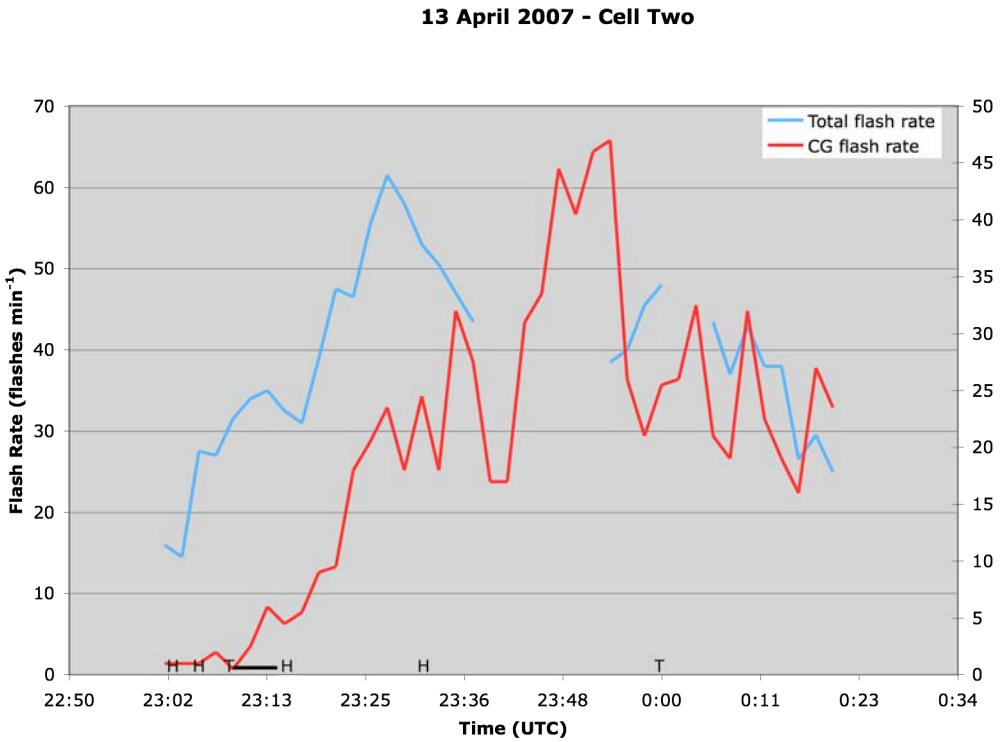

Figure 3.50. Same as Fig. 3.16, except for cell two on 13 April 2007. Severe weather reports are marked, as in Fig. 3.44. The black bar represents the period of time that the Haltom City tornado was producing damage. This tornado was rated EF-1 and caused one fatality.

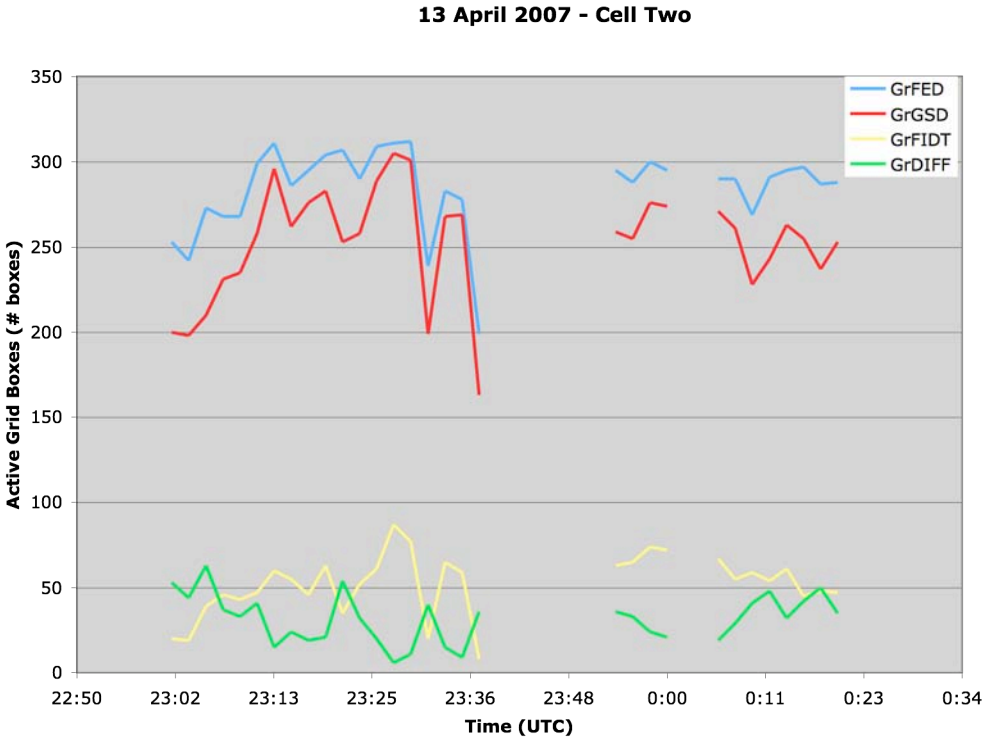

Figure. 3.51. Same as Fig. 3.17, except for cell two on 13 April 2007. Also included is a measure of the difference between GrFED and GrGSD, labeled as GrDIFF.

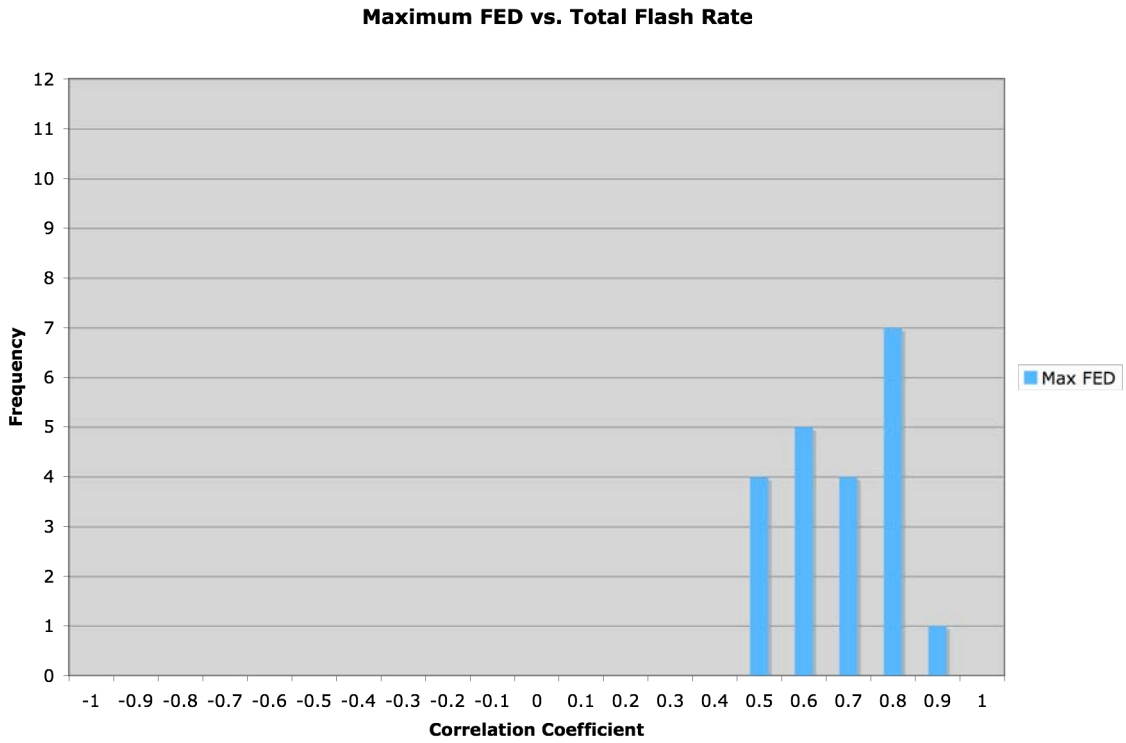

Figure 4.1 Histogram of correlation coefficients between MxFED values and total flash rate for all cells.

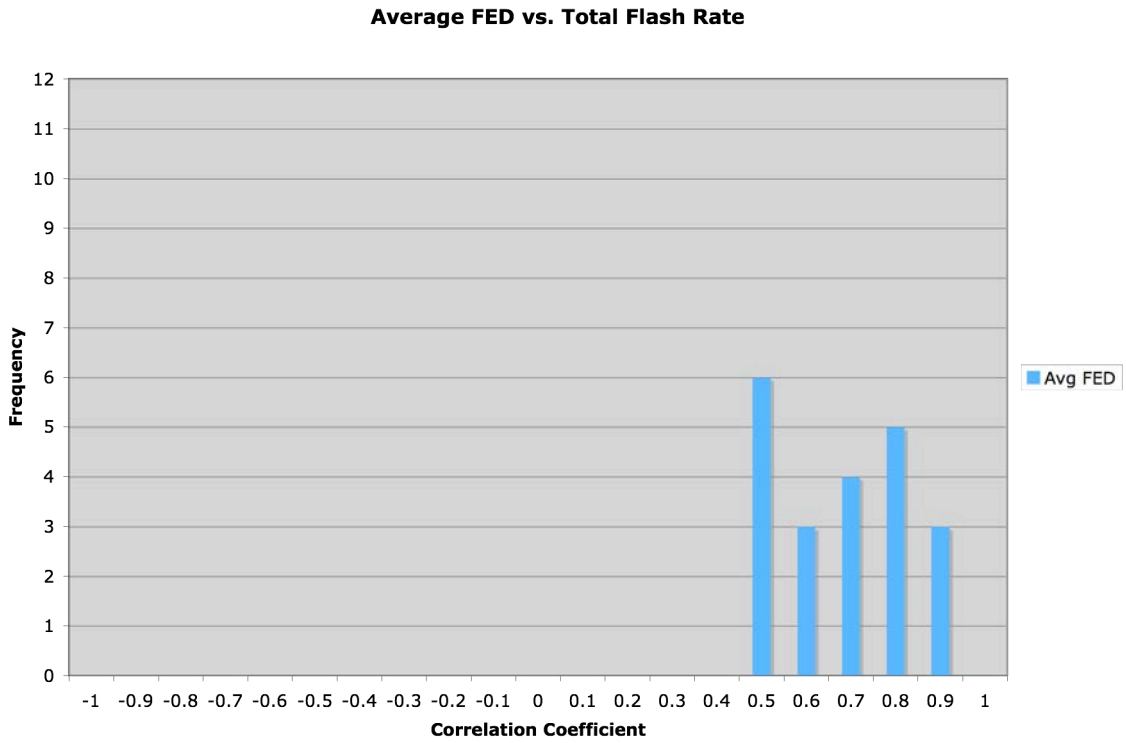

Figure 4.2. Same as Fig. 4.1, except for AvFED and total flash rate.

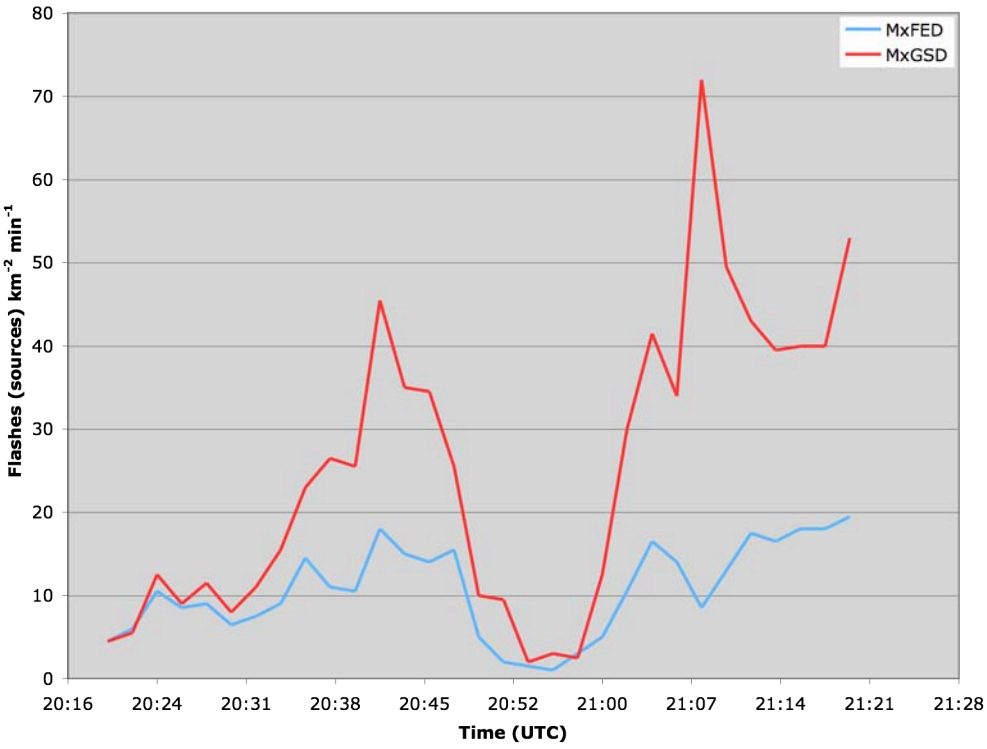

Figure 4.3. Loss of FED (flashes km^{-2} min^{-1}) and GSD (sources km^{-2} min^{-1}) data due to LDAR network "brownout" on 25 April 2005. MxFED and MxGSD data are displayed from cell one.

Table 3.1. Correlation coefficient values for cell one on 25 April 2005.

Correlation Coefficients – 25 April 2005 Cell One					
	Total Flash Rate	CG Flash Rate	VIL	SHI	MSI
MxFED	0.78	0.72	0.40	0.46	-0.66
AvFED	0.73	0.77	0.48	0.48	-0.62
MxGSD	0.62	0.70	0.49	0.46	-0.57
AvGSD	0.65	0.76	0.51	0.47	-0.57
MxFIDT	0.69	0.19	0.15	0.18	-0.71
AvFIDT	0.66	0.26	0.11	0.19	-0.60
GrFED	0.79	0.51	0.14	0.34	-0.86
GrGSD	0.78	0.57	0.19	0.36	-0.86
GrFIDT	0.89	0.52	0.39	0.42	-0.79
Total Flash Rate	--	0.42	0.32	0.30	-0.86
CG Flash Rate	0.42	--	0.51	0.59	-0.36

Table 3.2. Same as Table 3.1, except for cell two on 25 April 2005.

Correlation Coefficients – 25 April 2005 Cell Two					
	Total Flash Rate	CG Flash Rate	VIL	SHI	MSI
MxFED	0.90	0.51	0.40	-0.34	-0.02
AvFED	0.92	0.49	0.47	0.17	-0.03
MxGSD	0.82	0.41	0.51	-0.20	0.10
AvGSD	0.88	0.46	0.49	-0.43	0.01
MxFIDT	0.81	0.36	0.34	0.08	0.02
AvFIDT	0.78	0.34	0.32	-0.03	-0.22
GrFED	0.87	0.72	0.10	0.03	-0.26
GrGSD	0.91	0.71	0.21	-0.0003	-0.30
GrFIDT	0.96	0.44	0.60	-0.21	-0.26
Total Flash Rate	--	0.46	0.60	0.67	-0.35
CG Flash Rate	0.46	--	-0.45	0.50	0.05

Table 3.3. Same as Table 3.1, except for cell one on 05 April 2005.

Correlation Coefficients – 05 April 2005 Cell One					
	Total Flash Rate	CG Flash Rate	VIL	SHI	MSI
MxFED	0.85	-0.23	0.58	0.51	-0.17
AvFED	0.83	-0.38	0.81	0.74	-0.80
MxGSD	0.72	-0.38	0.60	0.59	-0.07
AvGSD	0.69	-0.44	0.65	0.84	-0.07
MxFIDT	0.75	-0.15	0.02	0.23	0.23
AvFIDT	0.77	-0.14	-0.17	-0.39	0.46
GrFED	0.55	-0.20	0.52	0.71	0.27
GrGSD	0.64	-0.32	0.32	0.79	0.48
GrFIDT	0.59	-0.13	0.57	0.78	-0.02
Total Flash Rate	--	-0.27	0.49	0.66	0.02
CG Flash Rate	-0.27	--	-0.05	-0.37	0.43

Table 3.4. Same as Table 3.1, except for cell one on 13 April 2007.

Correlation Coefficients – 13 April 2007 Cell One					
	Total Flash Rate	CG Flash Rate	VIL	SHI	MSI
MxFED	0.64	0.72	-0.05	-0.64	-0.33
AvFED	0.76	0.64	-0.26	-0.80	-0.54
MxGSD	0.67	0.64	-0.28	-0.78	-0.53
AvGSD	0.73	0.64	-0.31	-0.81	-0.57
MxFIDT	-0.21	-0.33	0.22	0.38	0.32
AvFIDT	-0.21	-0.09	-0.09	-0.19	-0.17
GrFED	0.58	0.50	0.13	-0.41	-0.1
GrGSD	0.74	0.65	0.01	-0.57	-0.26
GrFIDT	0.62	0.44	0.04	-0.55	-0.24
Total Flash Rate	--	0.68	0.03	-0.67	-0.26
CG Flash Rate	0.68	--	-0.08	-0.67	-0.36

Table 3.5. Same as Table 3.1, except for cell two on 13 April 2007.

Correlation Coefficients – 13 April 2007 Cell Two					
	Total Flash Rate	CG Flash Rate	VIL	SHI	MSI
MxFED	0.51	0.55	0.08	-0.25	-0.29
AvFED	0.51	0.61	-0.06	-0.33	-0.27
MxGSD	0.18	0.29	-0.15	-0.22	-0.02
AvGSD	0.51	0.61	-0.12	-0.41	-0.26
MxFIDT	0.03	-0.07	0.08	0.14	0.26
AvFIDT	0.00	0.00	-0.08	0.09	0.32
GrFED	-0.24	-0.37	0.01	0.14	0.14
GrGSD	-0.06	-0.16	0.07	0.08	0.23
GrFIDT	0.19	0.07	0.05	-0.02	0.05
Total Flash Rate	--	0.89	0.43	-0.19	-0.60
CG Flash Rate	0.89	--	0.19	-0.41	-0.66

APPENDIX B

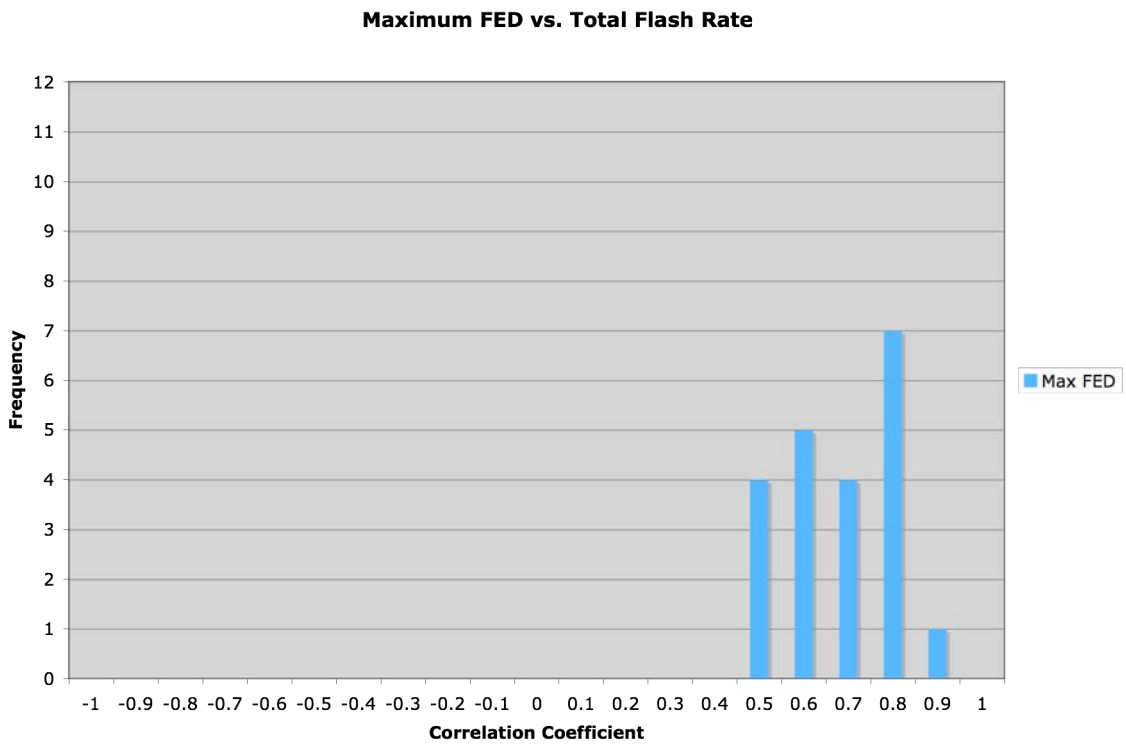

B-1. Histogram of correlation coefficients between total flash rate and MxFED. This figure reproduces Fig. 4-1 in Appendix A.

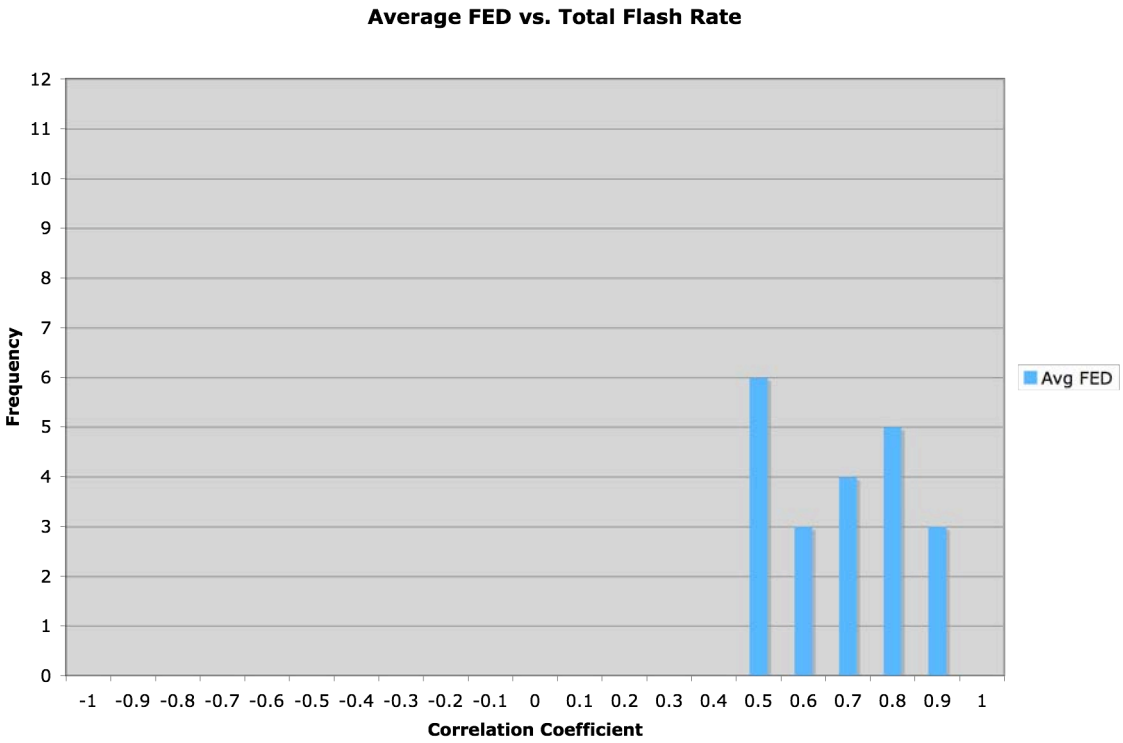

B-2. Histogram of correlation coefficients between total flash rate and AvFED. This figure reproduces Fig. 4-2 in Appendix A.

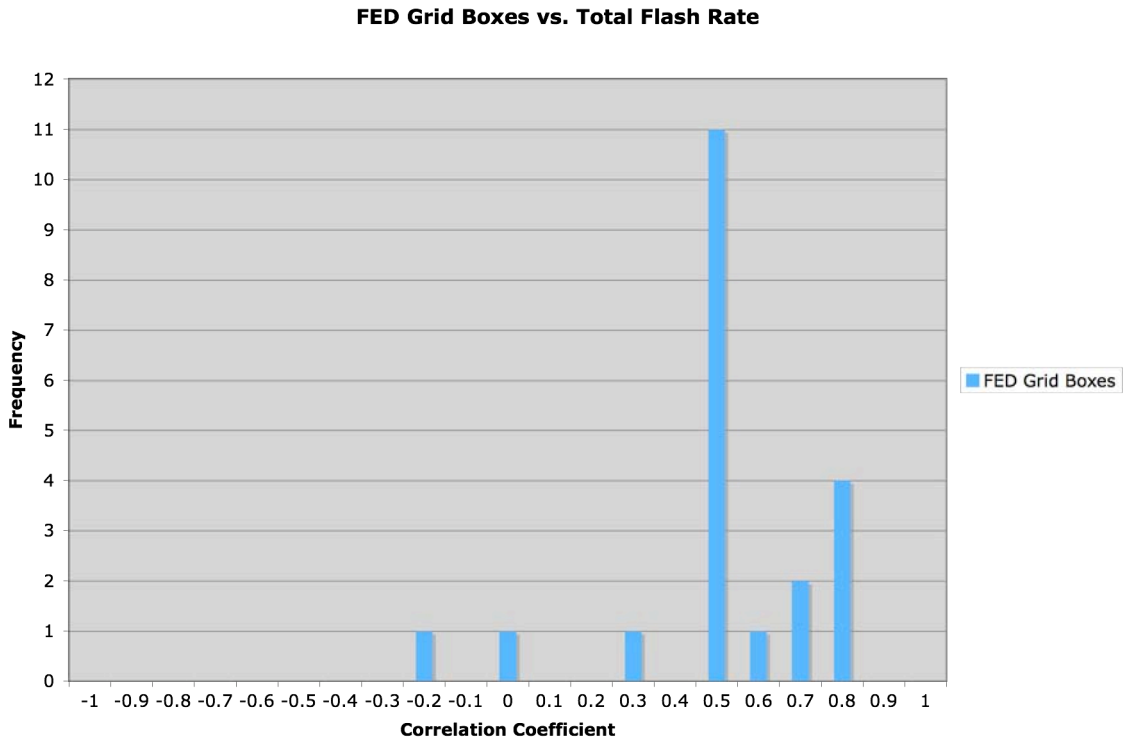

B-3. Histogram of correlation coefficients between total flash rate and GrFED.

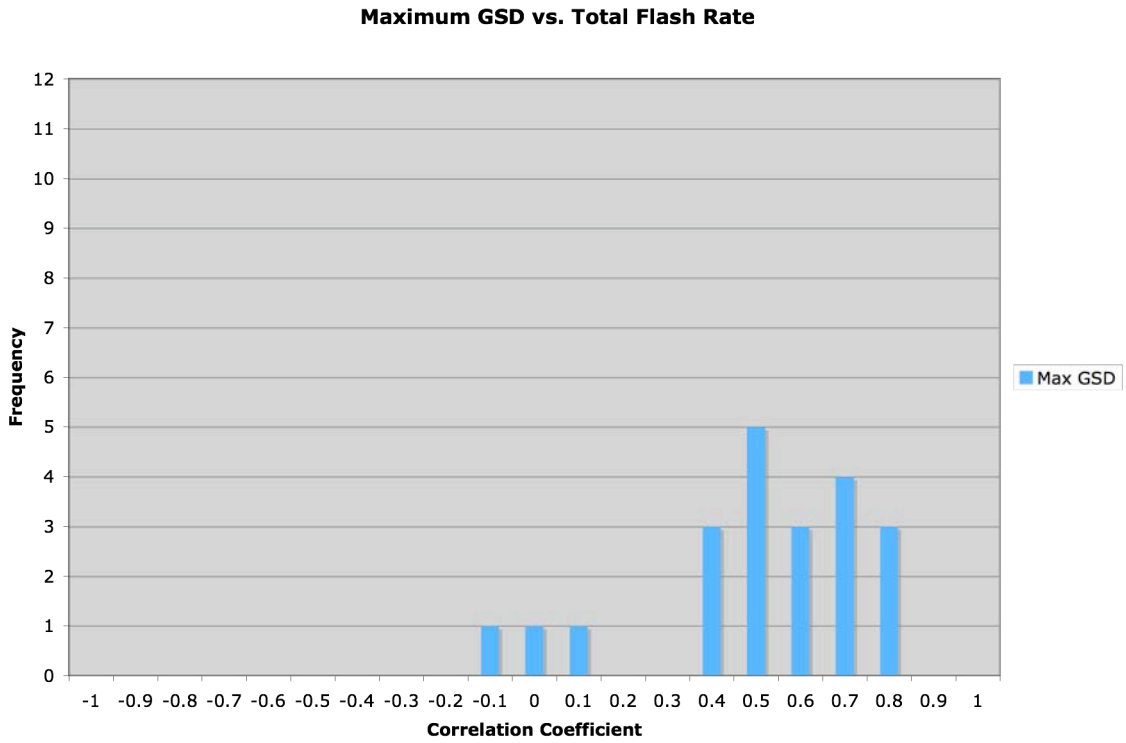

B-4. Histogram of correlation coefficients between total flash rate and MxGSD.

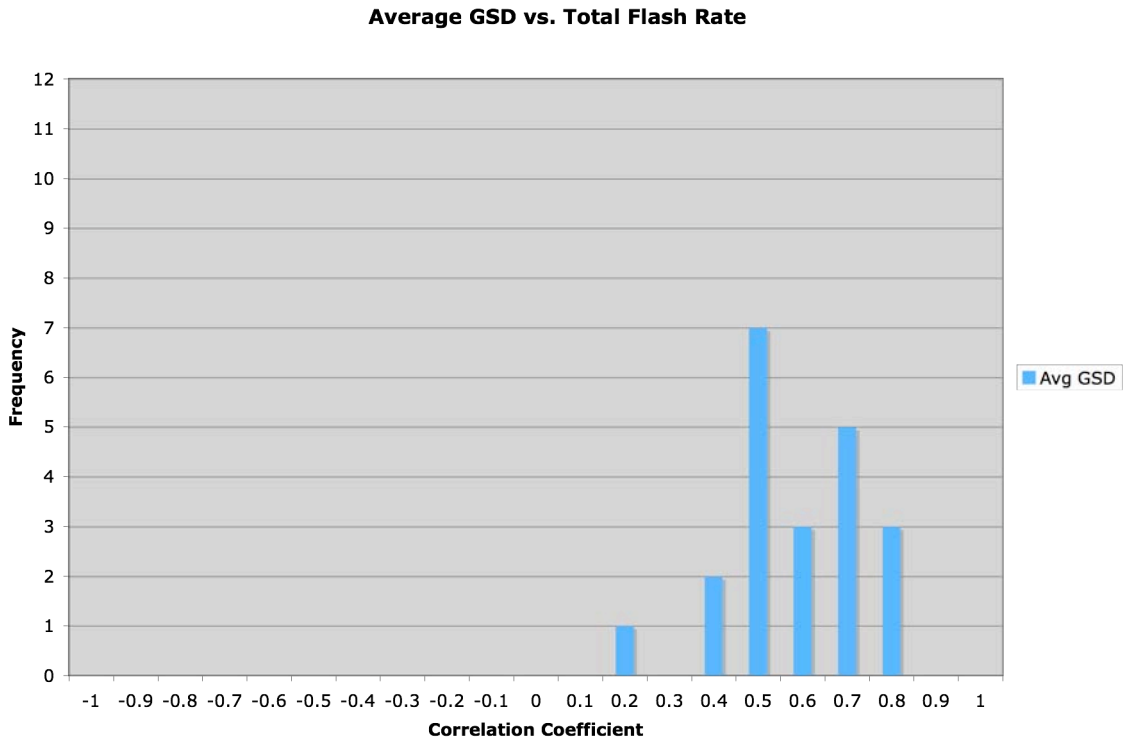

B-5. Histogram of correlation coefficients between total flash rate and AvGSD.

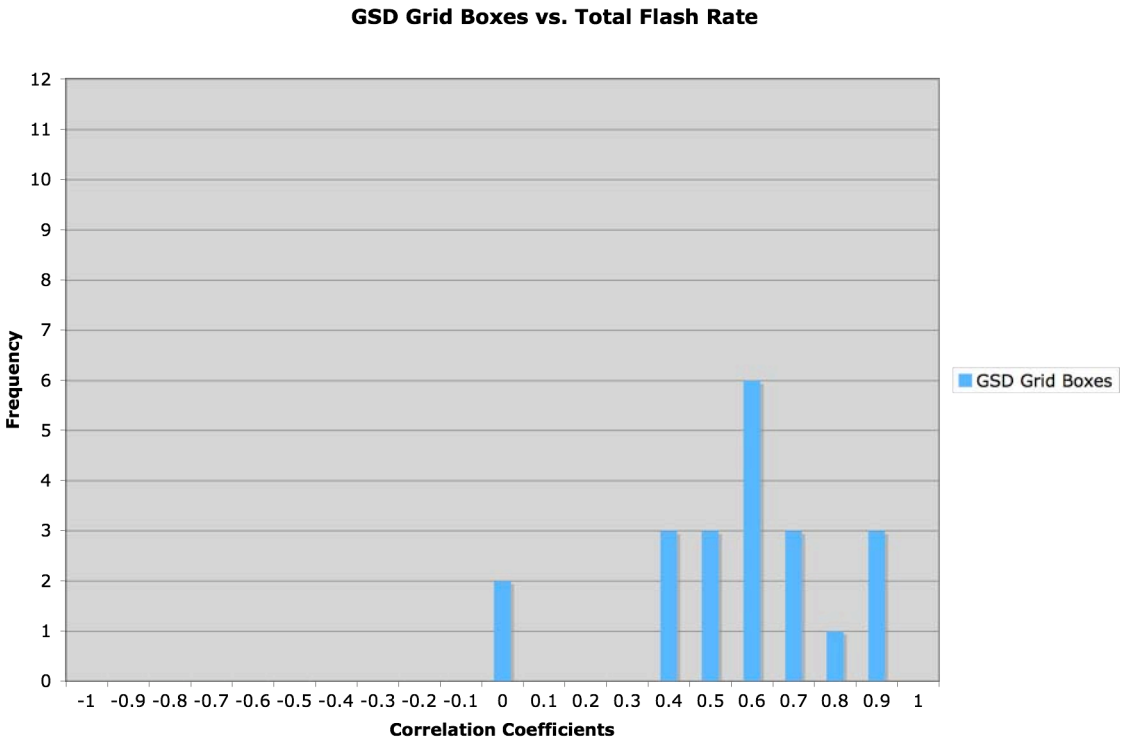

B-6. Histogram of correlation coefficients between total flash rate and GrGSD.

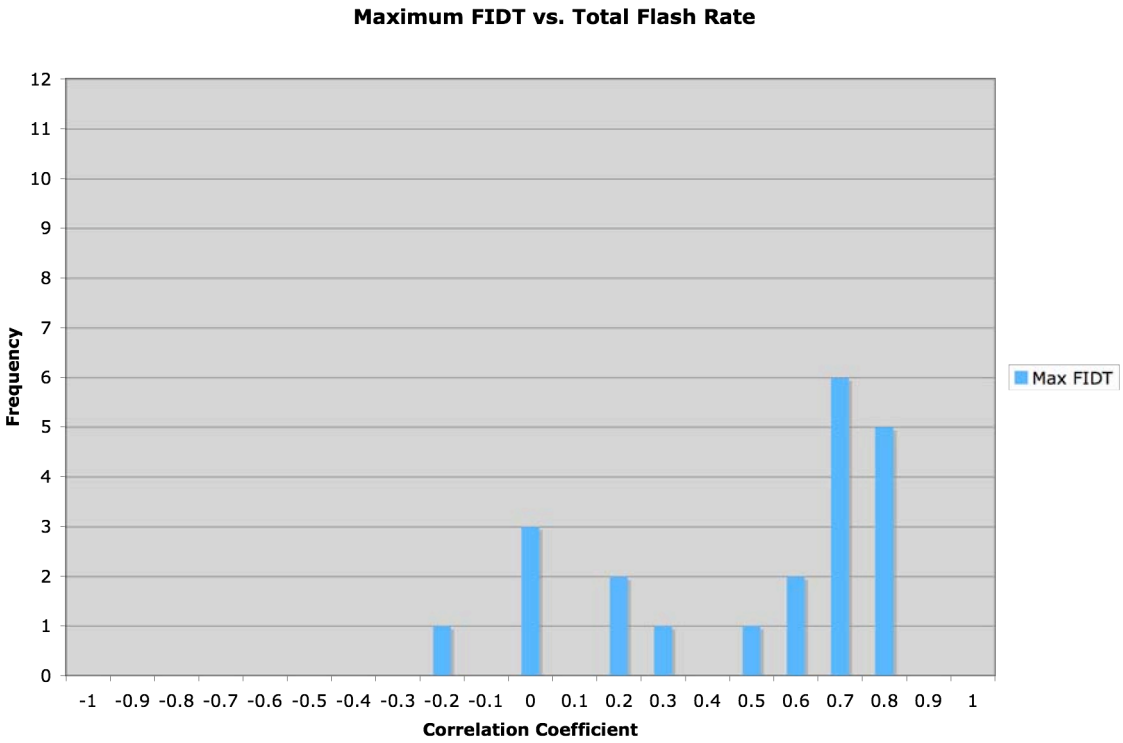

B-7. Histogram of correlation coefficients between total flash rate and MxFIDT.

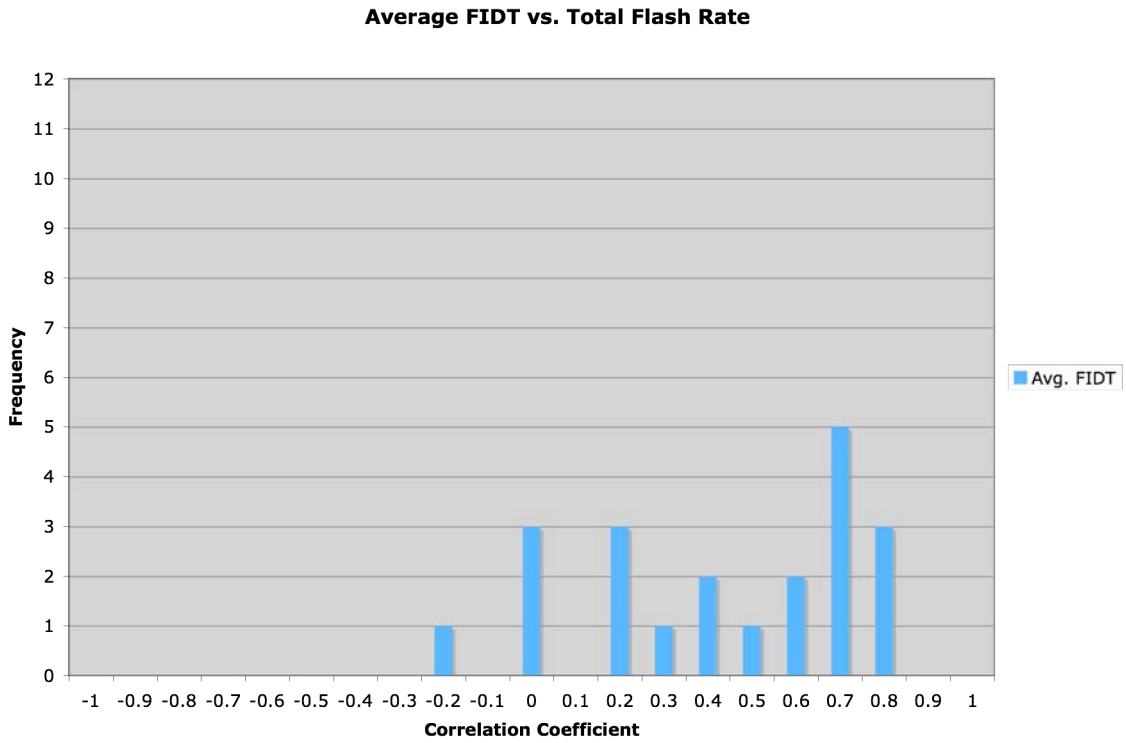

B-8. Histogram of correlation coefficients between total flash rate and AvFIDT.

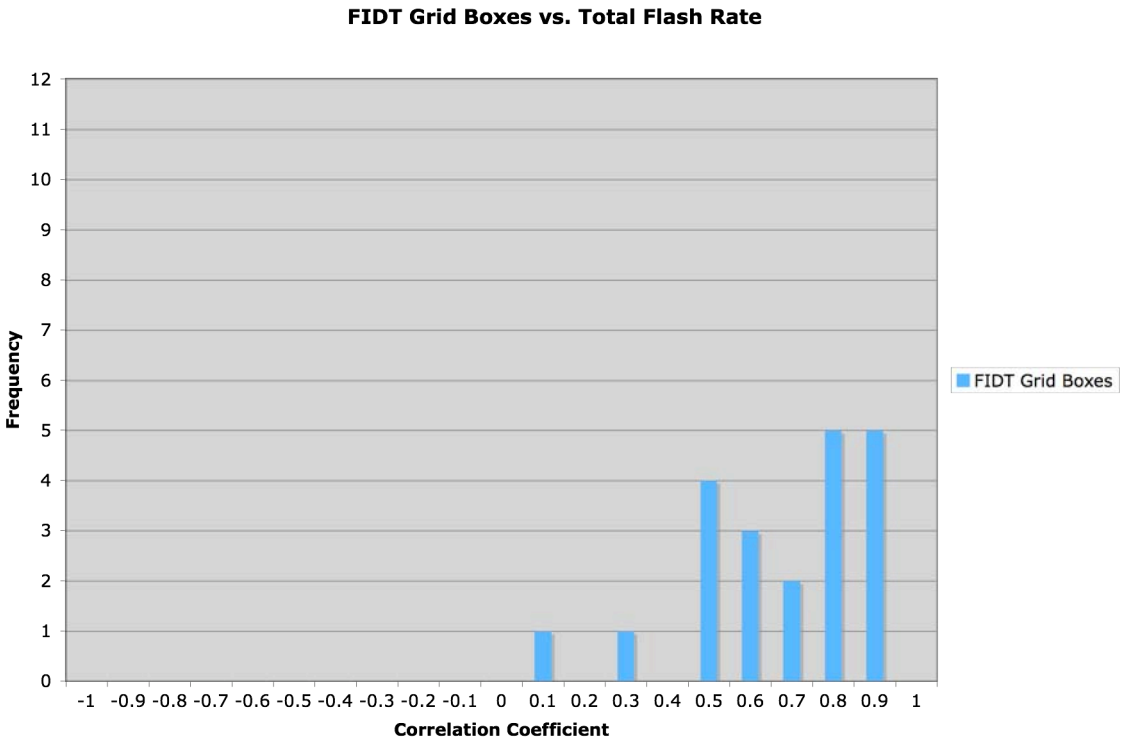

B-9. Histogram of correlation coefficients between total flash rate and GrFIDT.

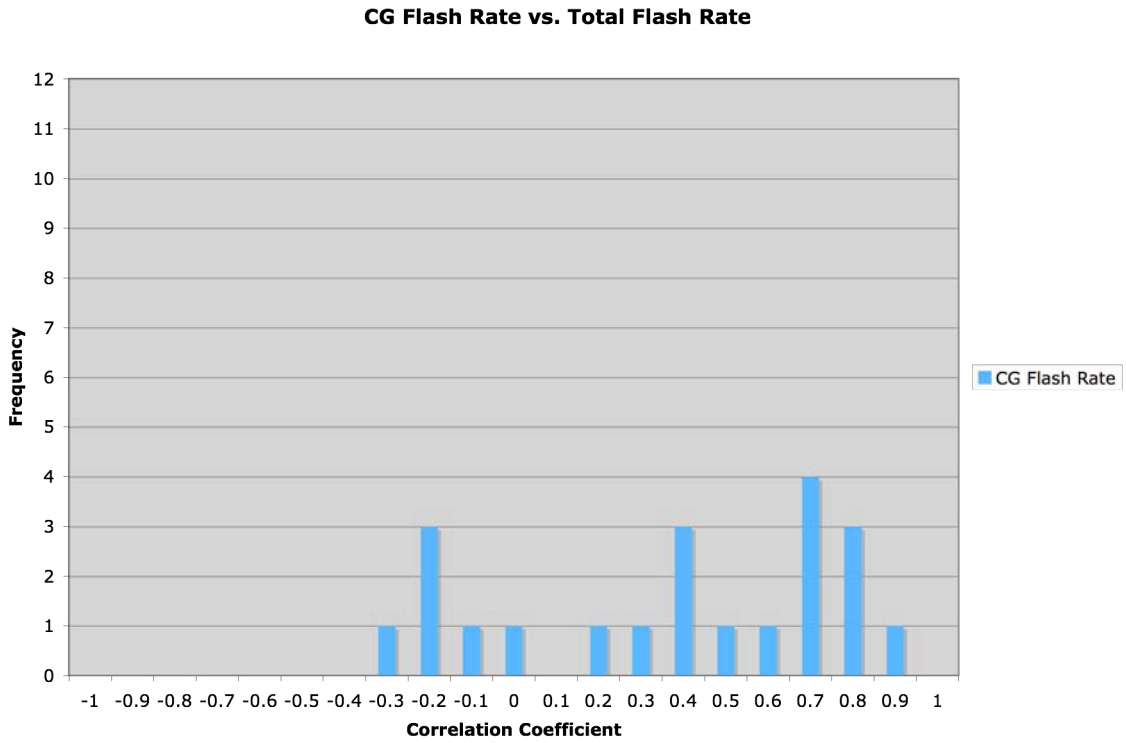

B-10. Histogram of correlation coefficients between total flash rate and CG flash rate.

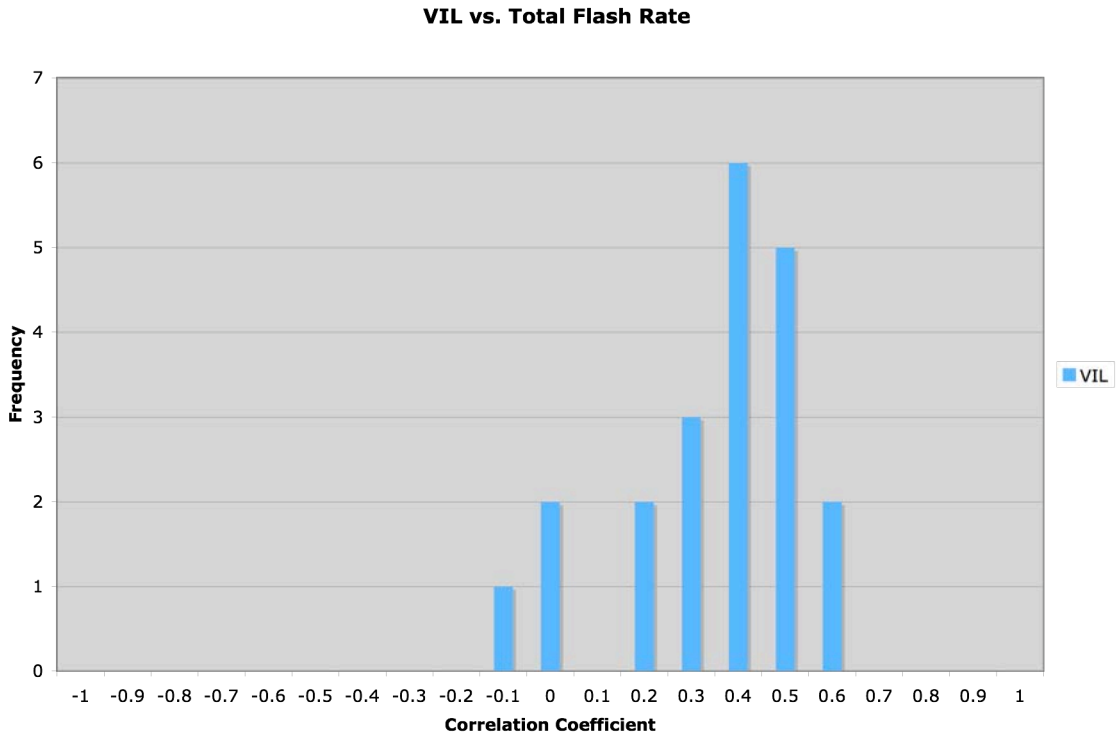

B-11. Histogram of correlation coefficients between total flash rate and VIL.

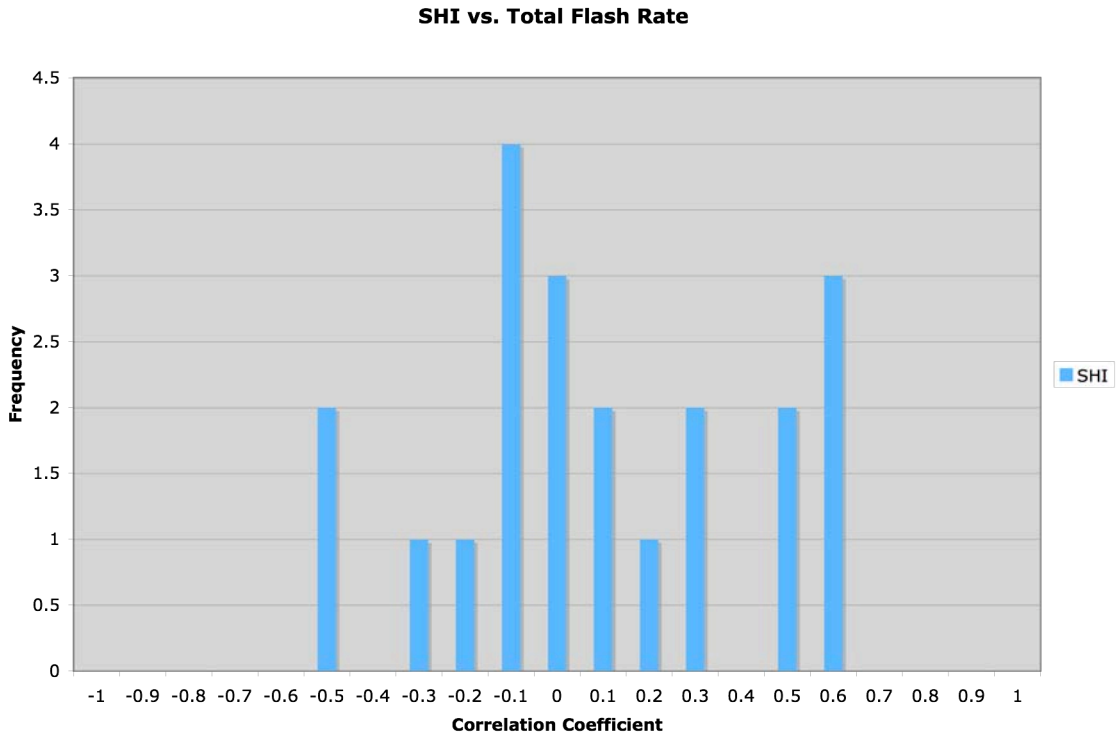

B-12. Histogram of correlation coefficients between total flash rate and SHI.

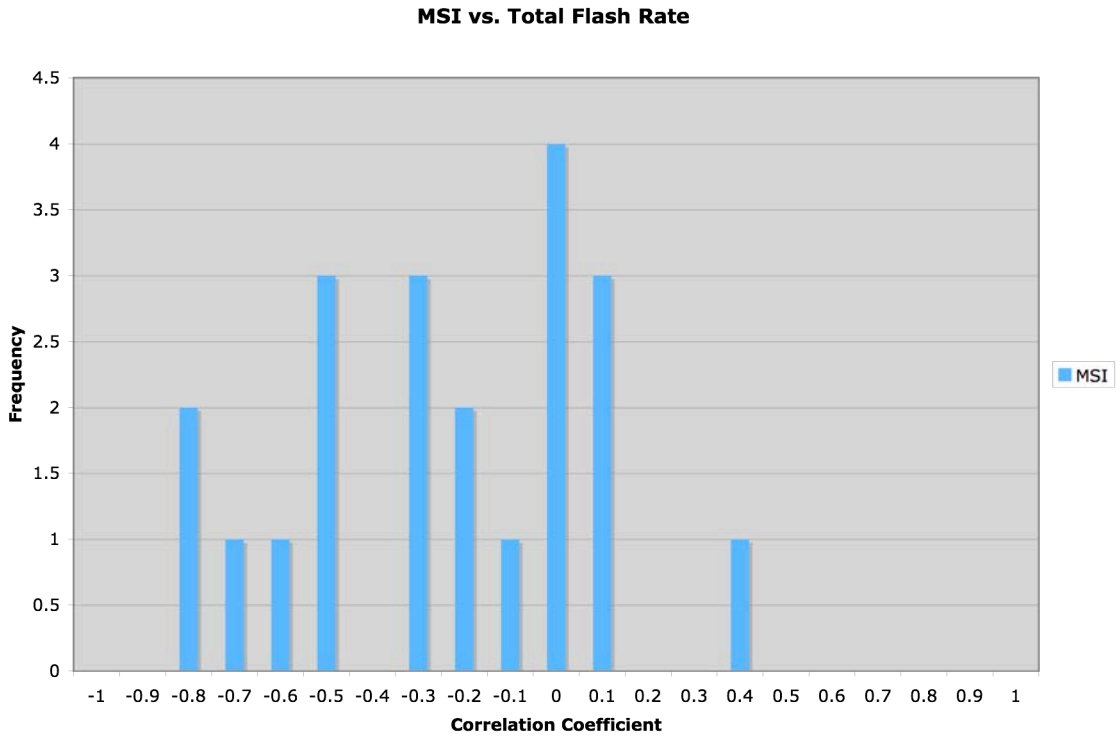

B-13. Histogram of correlation coefficients between total flash rate and MSI.

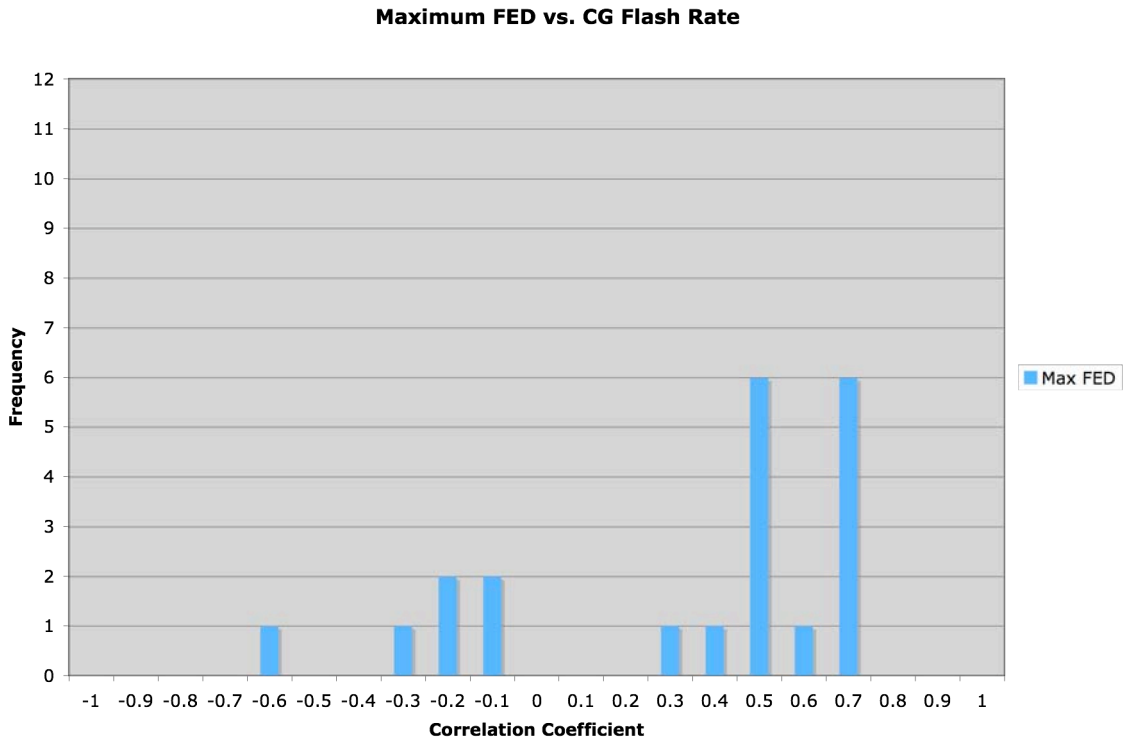

B-14. Histogram of correlation coefficients between CG flash rate and MxFED.

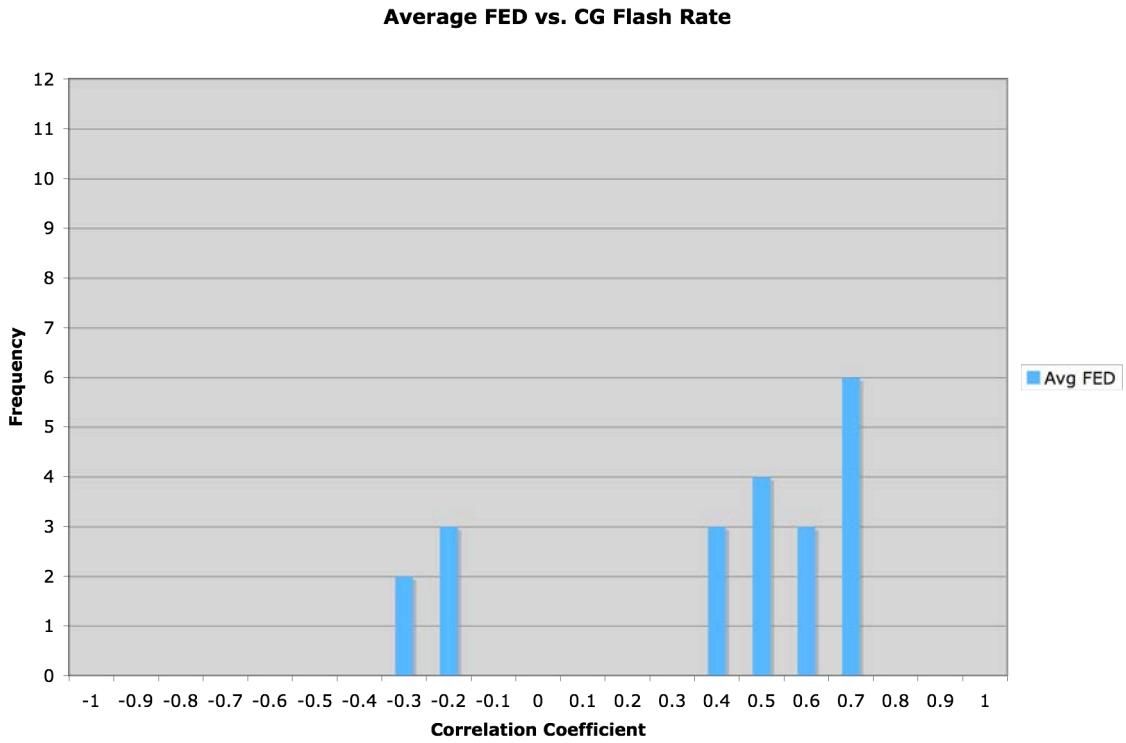

B-15. Histogram of correlation coefficients between CG flash rate and AvFED.

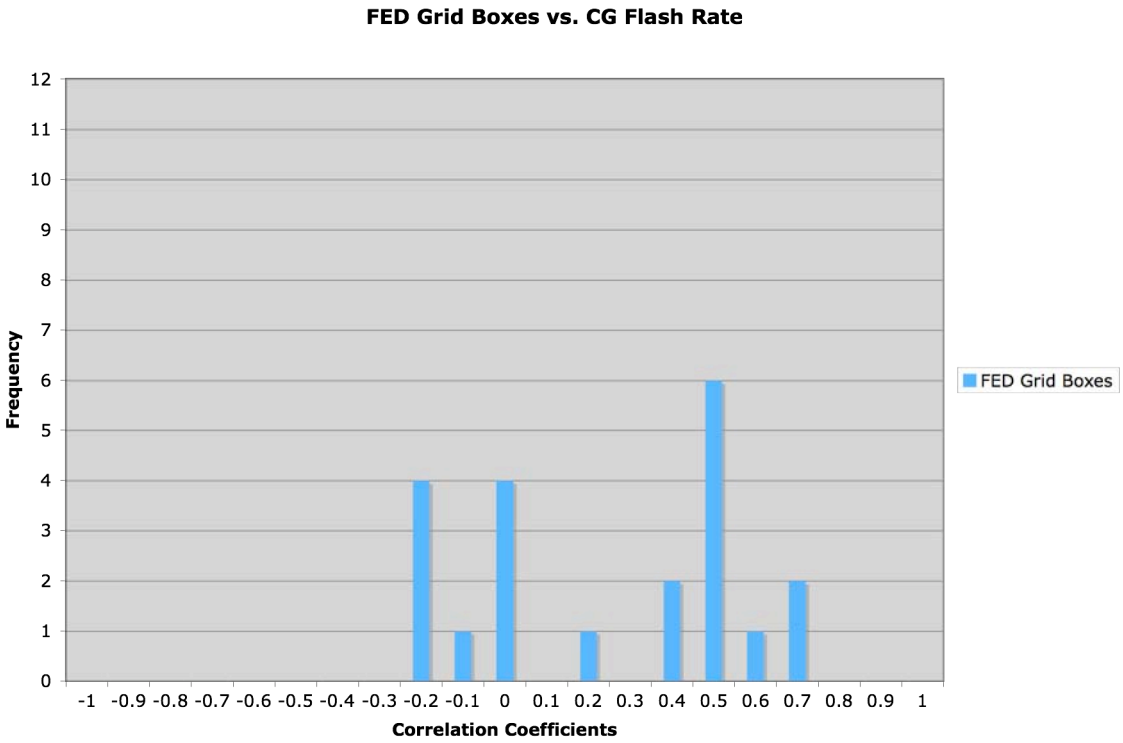

B-16. Histogram of correlation coefficients between CG flash rate and GrFED.

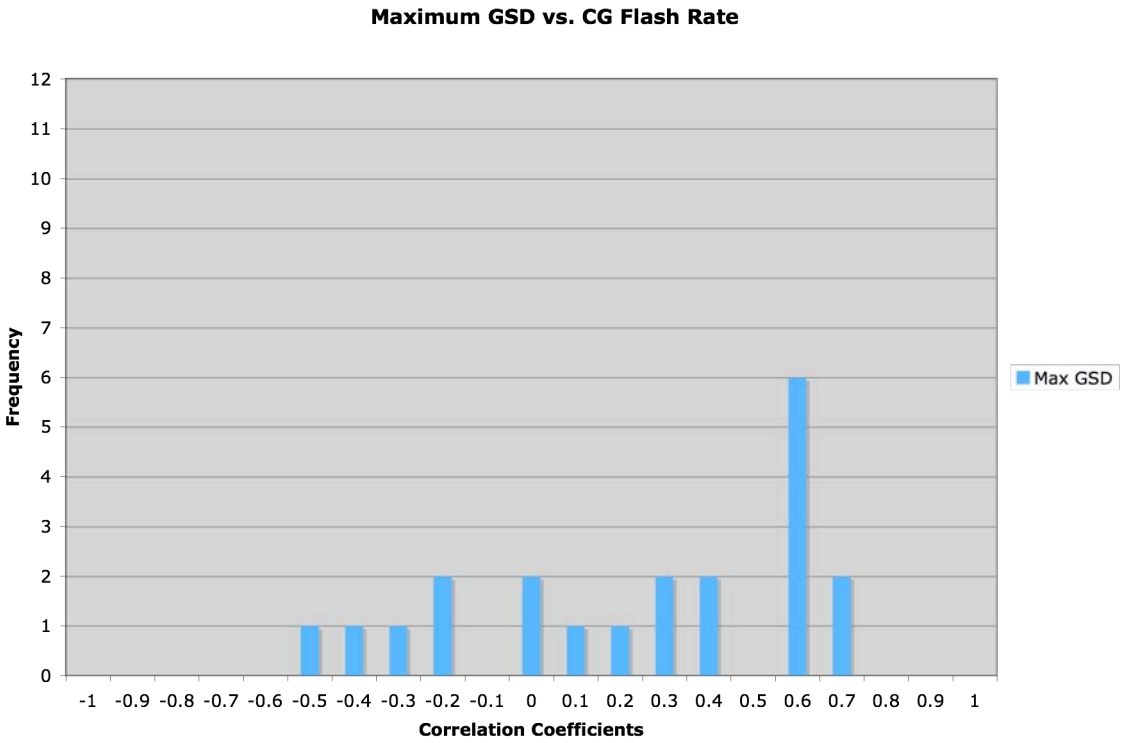

B-17. Histogram of correlation coefficients between CG flash rate and MxGSD.

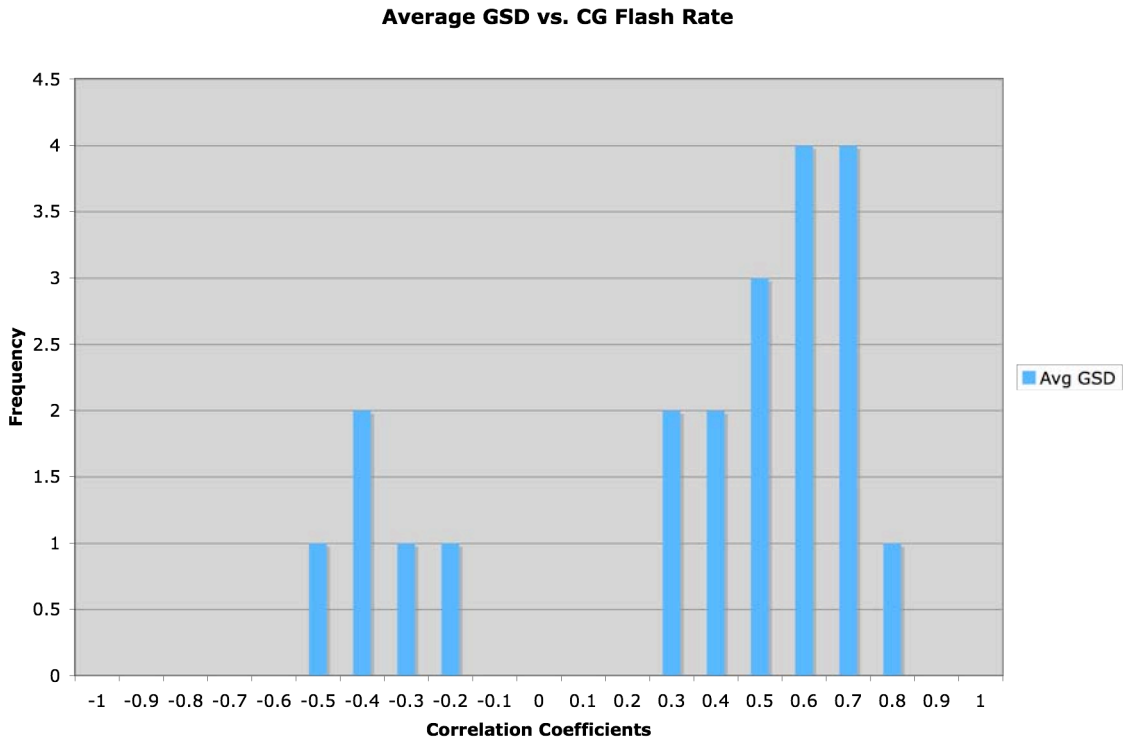

B-18. Histogram of correlation coefficients between CG flash rate and AvGSD.

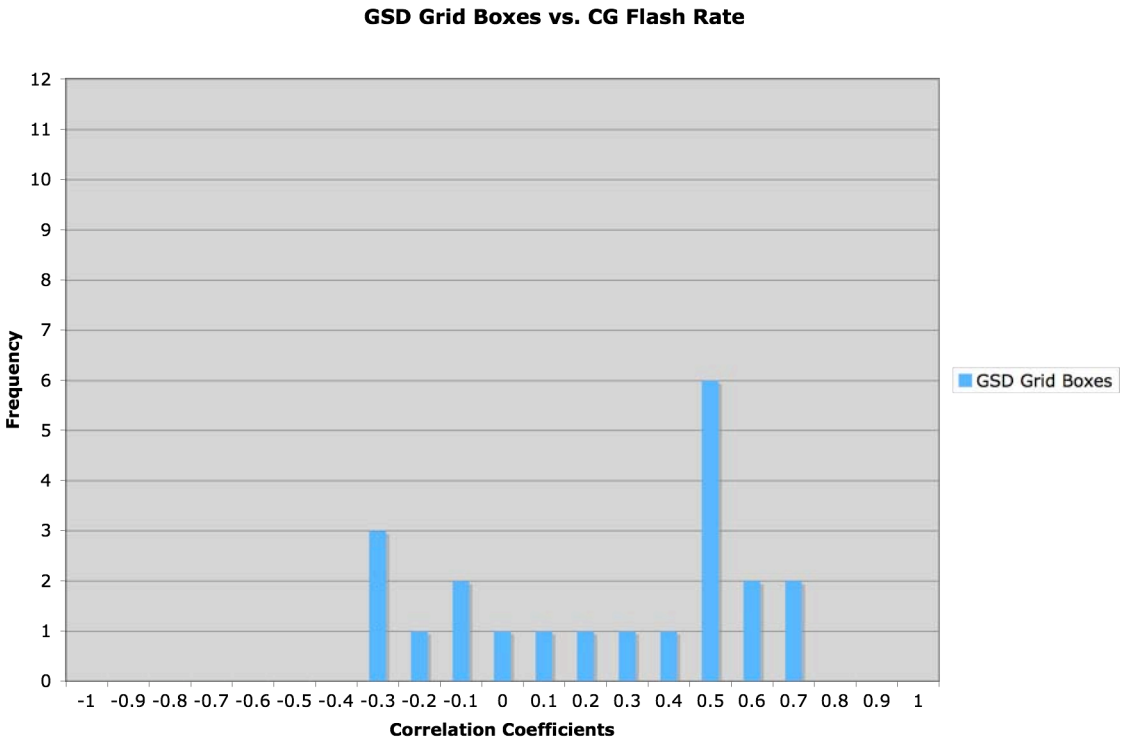

B-19. Histogram of correlation coefficients between CG flash rate and GrGSD.

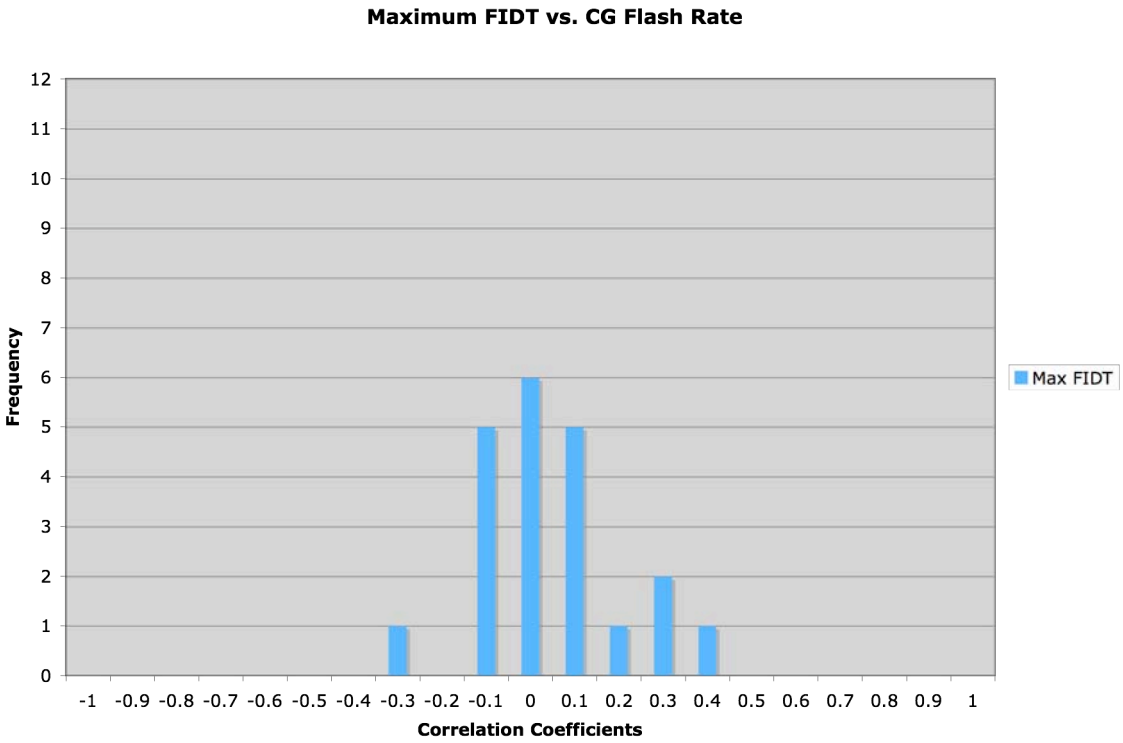

B-20. Histogram of correlation coefficients between CG flash rate and MxFIDT.

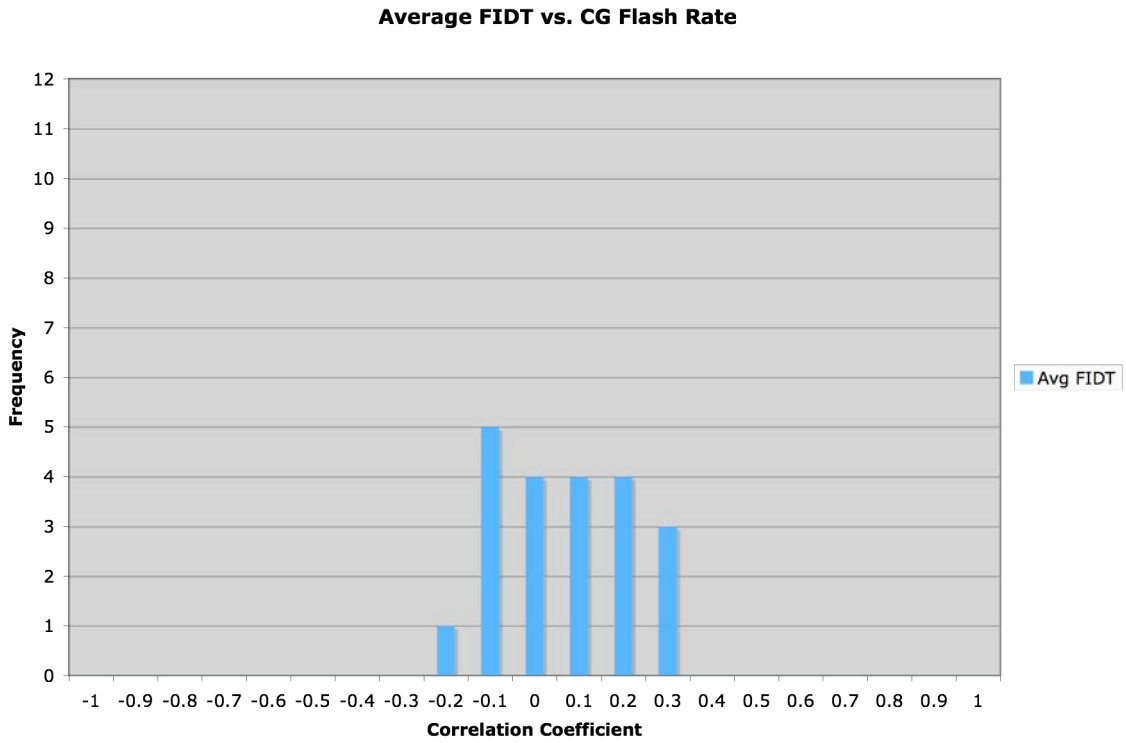

B-21. Histogram of correlation coefficients between CG flash rate and AvFIDT.

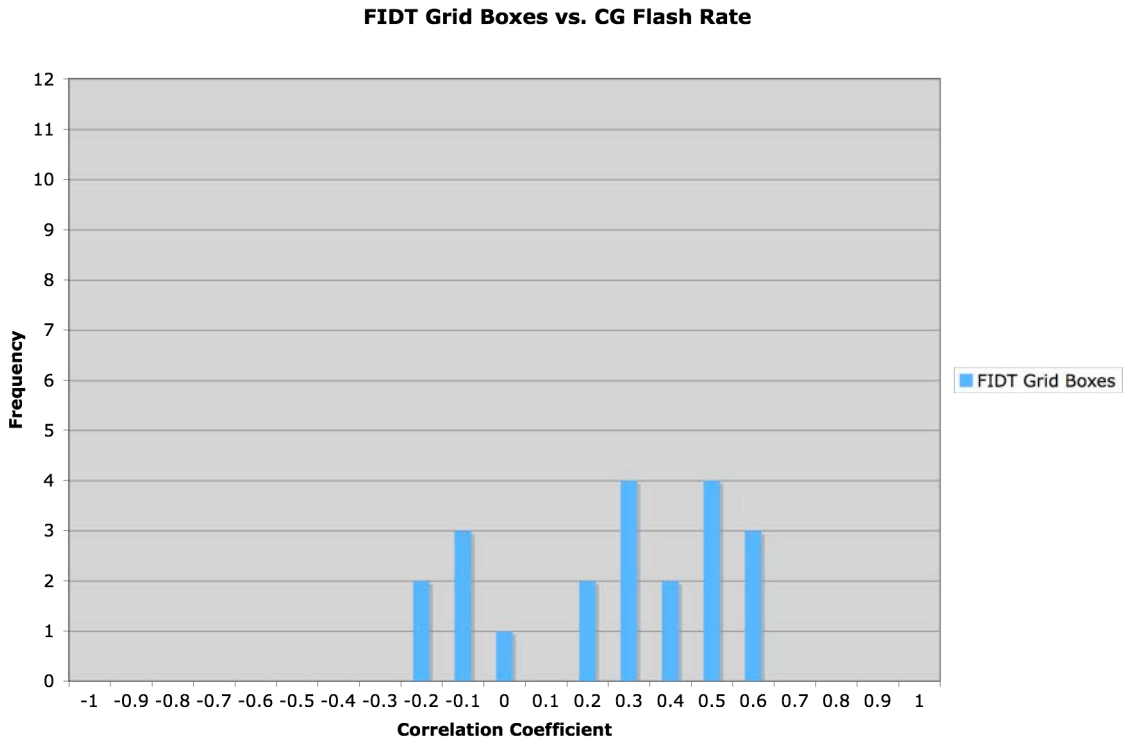

B-22. Histogram of correlation coefficients between CG flash rate and GrFIDT.

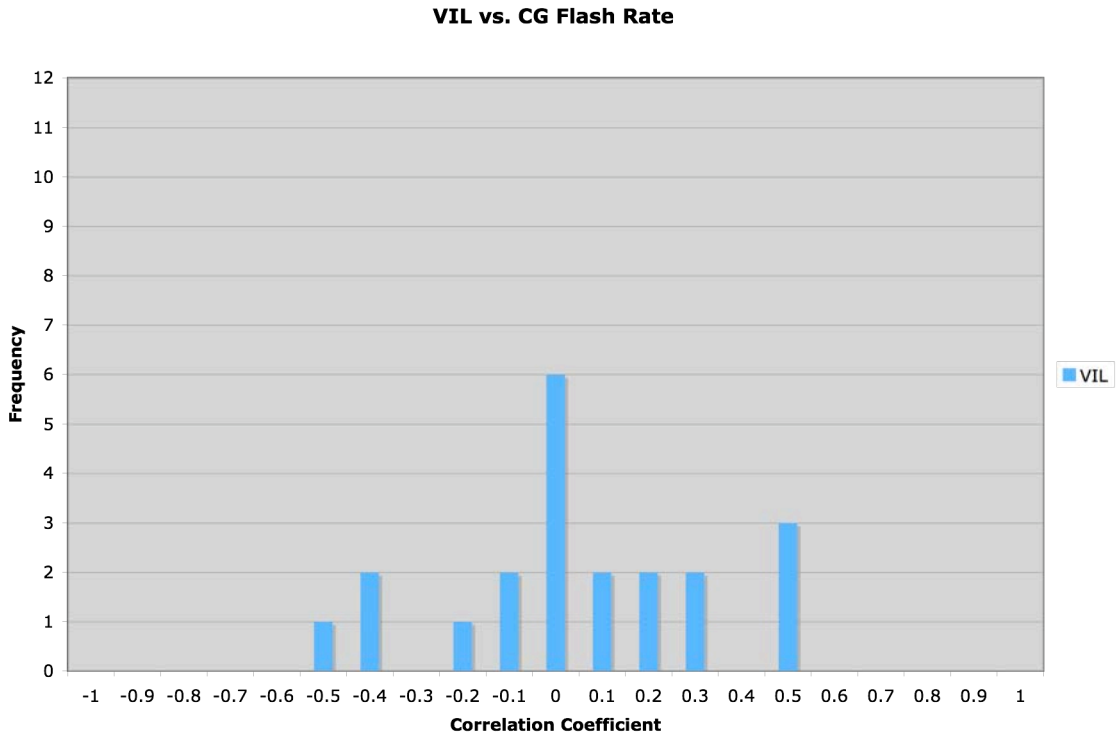

B-23. Histogram of correlation coefficients between CG flash rate and VIL.

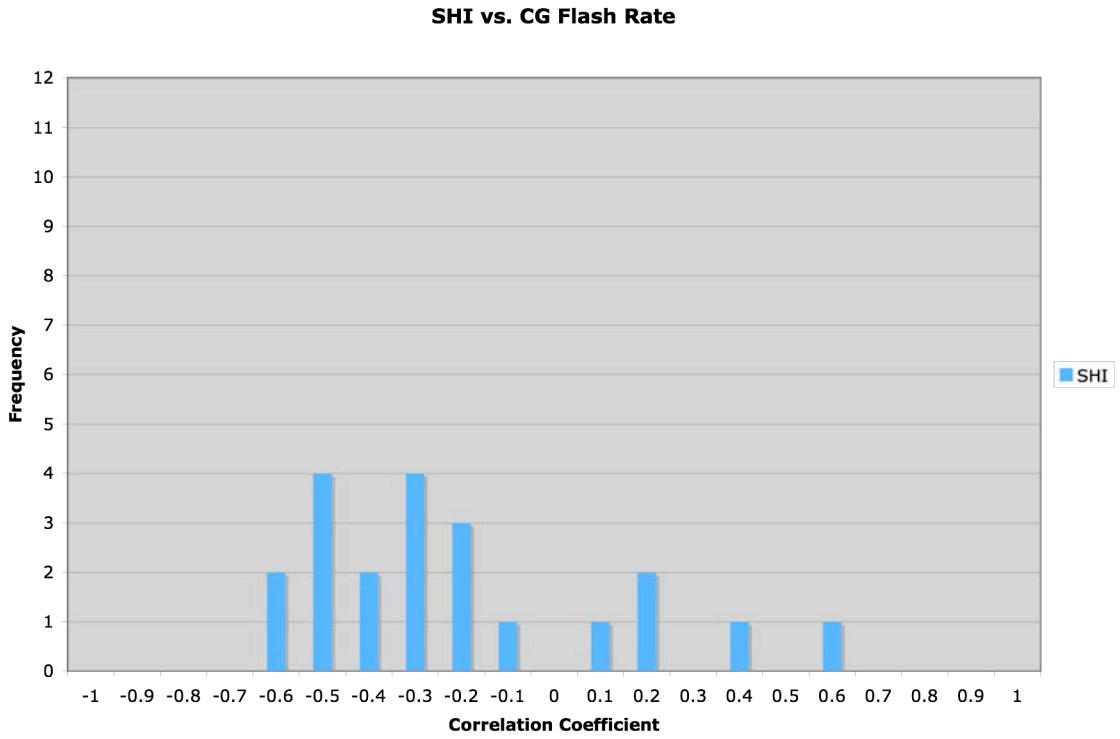

B-24. Histogram of correlation coefficients between CG flash rate and SHI.

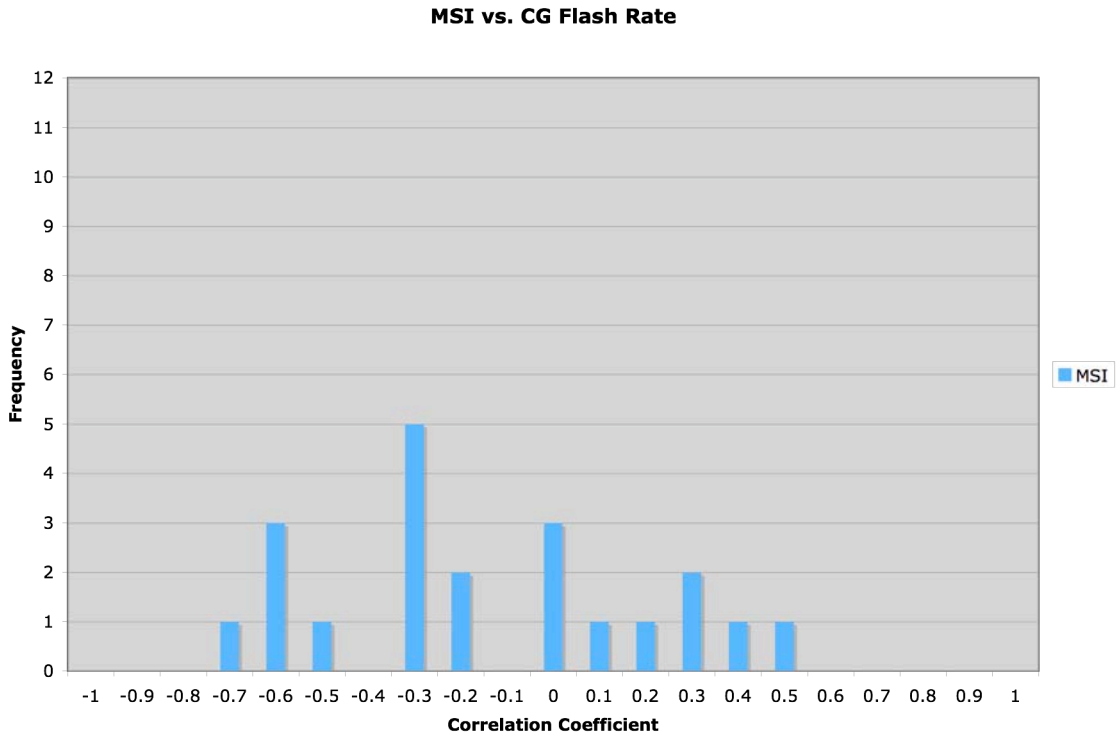

B-25. Histogram of correlation coefficients between CG flash rate and MSI.

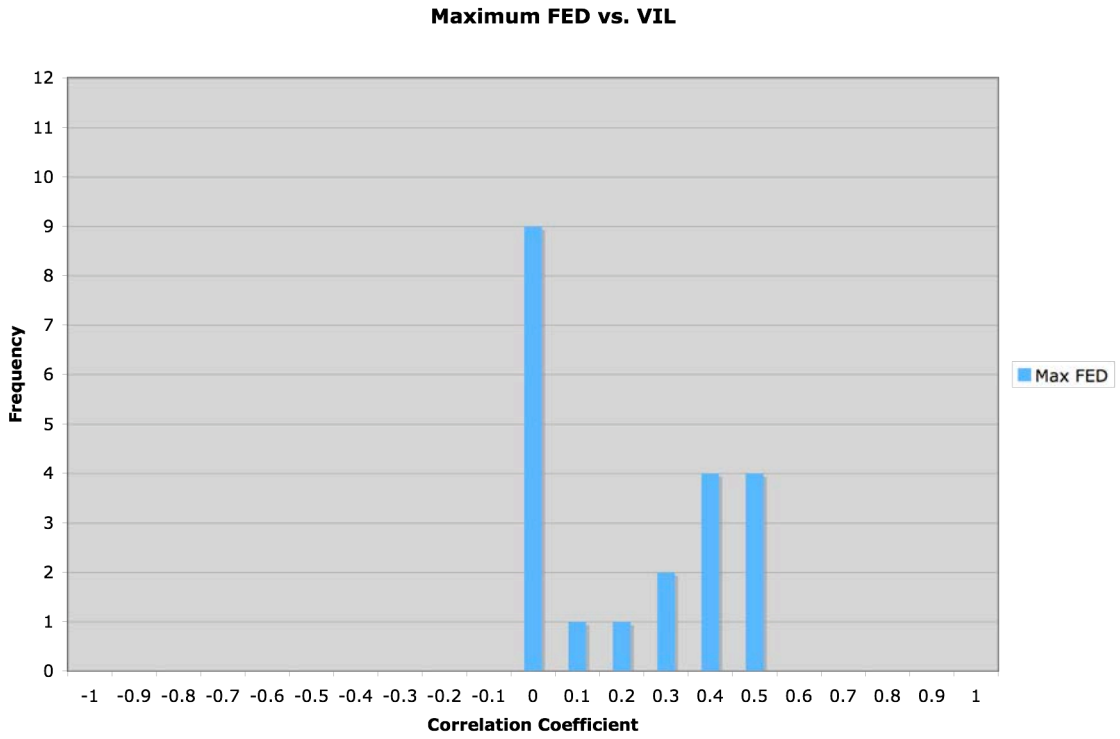

B-26. Histogram of correlation coefficients between VIL and MxFED.

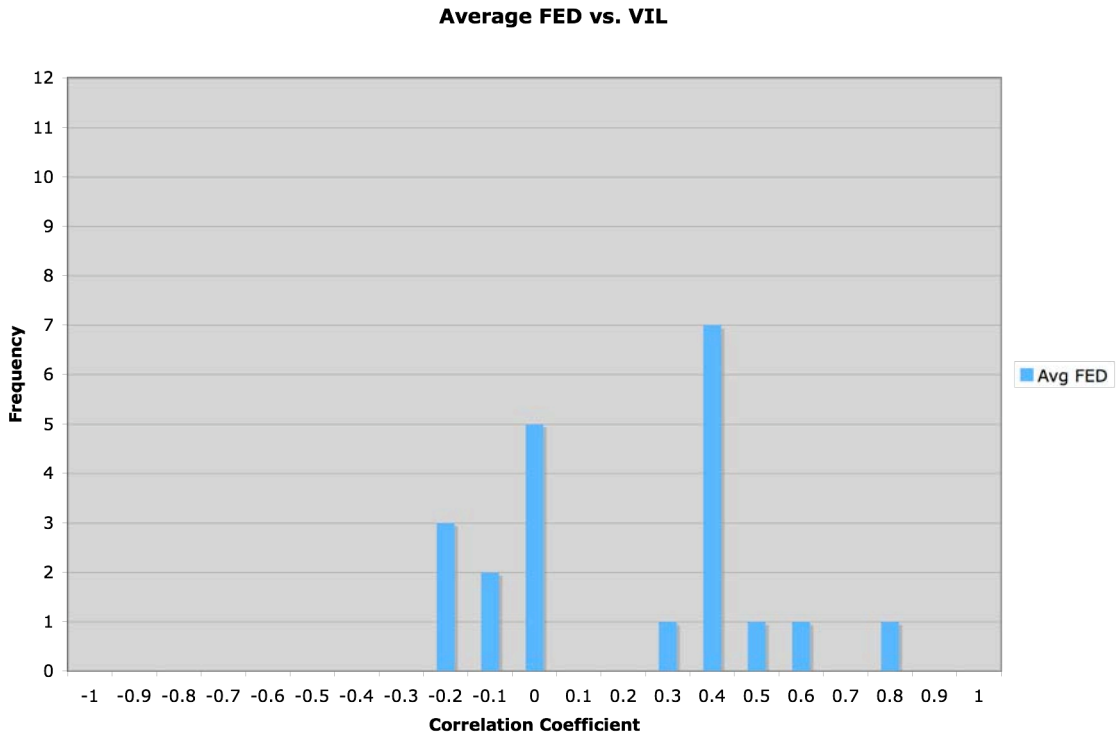

B-27. Histogram of correlation coefficients between VIL and AvFED.

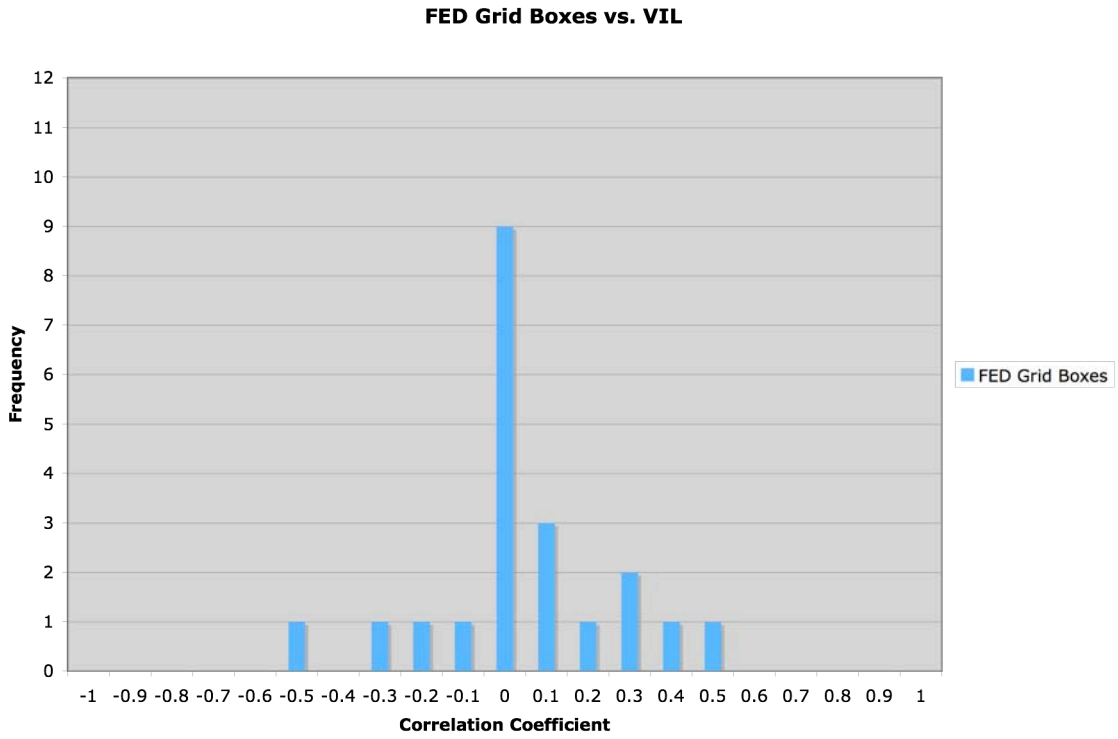

B-28. Histogram of correlation coefficients between VIL and GrFED.

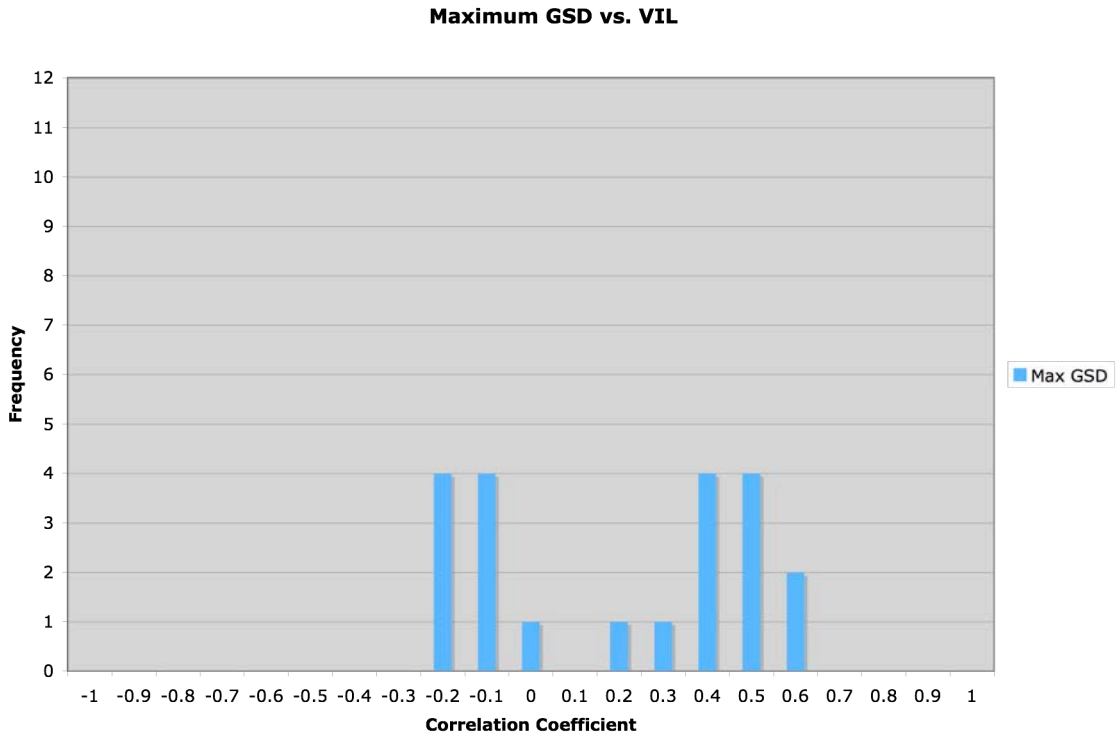

B-29. Histogram of correlation coefficients between VIL and MxGSD.

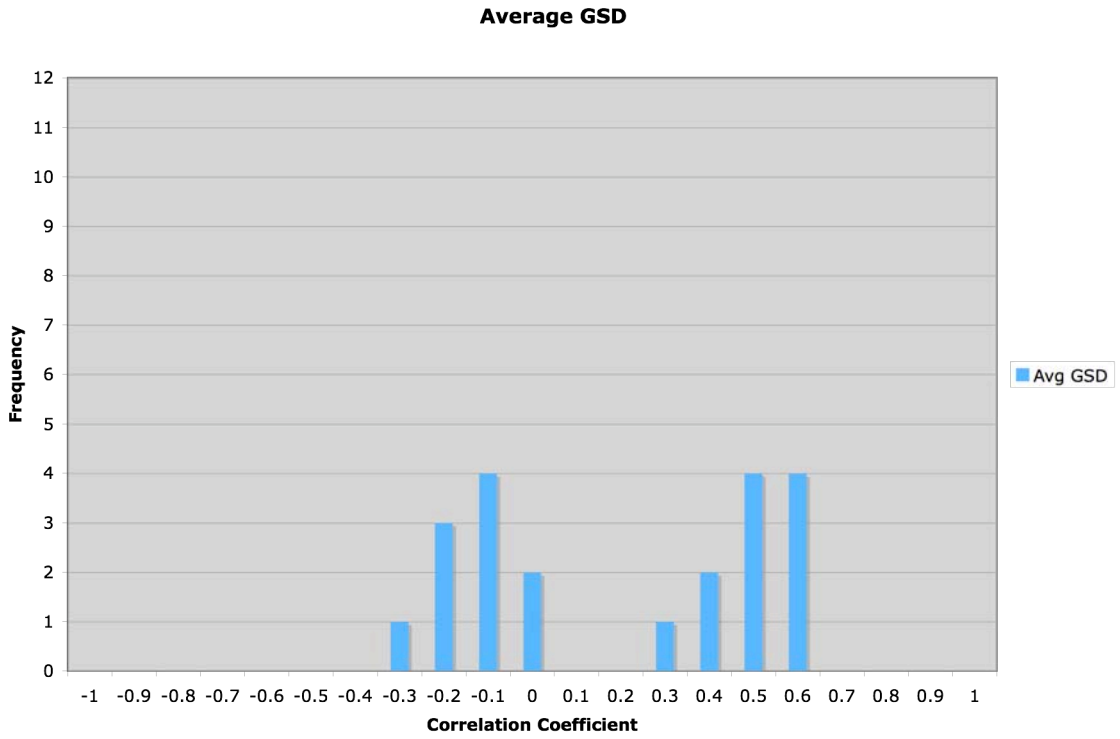

B-30. Histogram of correlation coefficients between VIL and AvGSD.

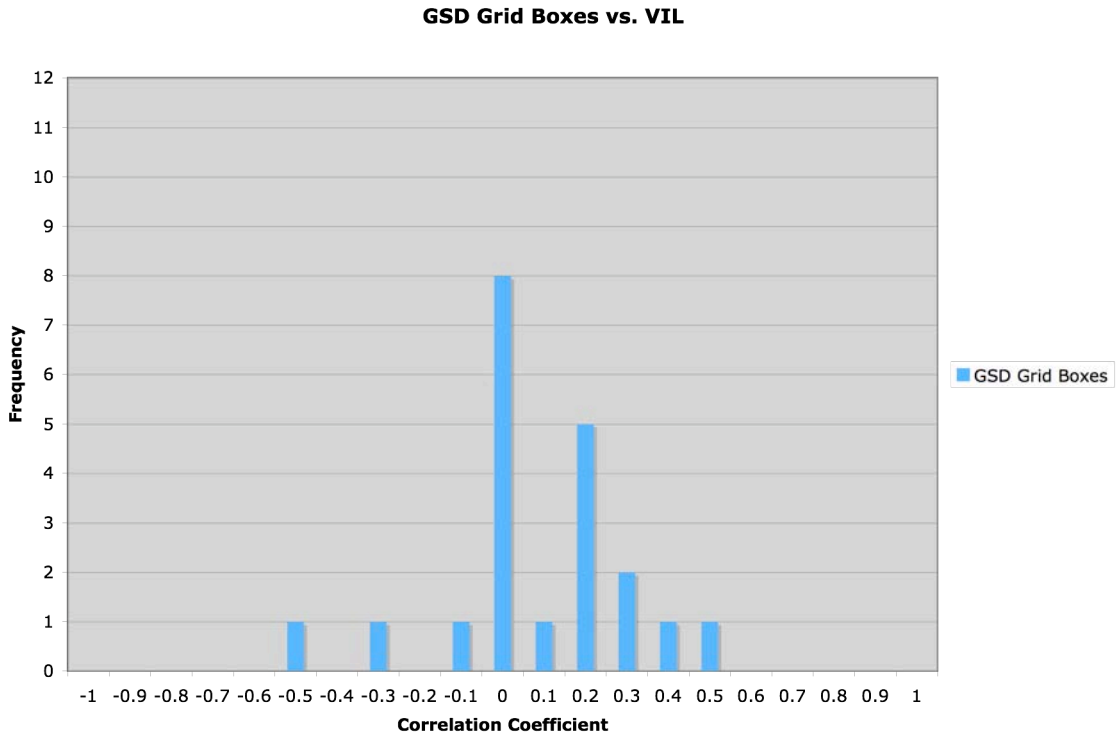

B-31. Histogram of correlation coefficients between VIL and GrGSD.

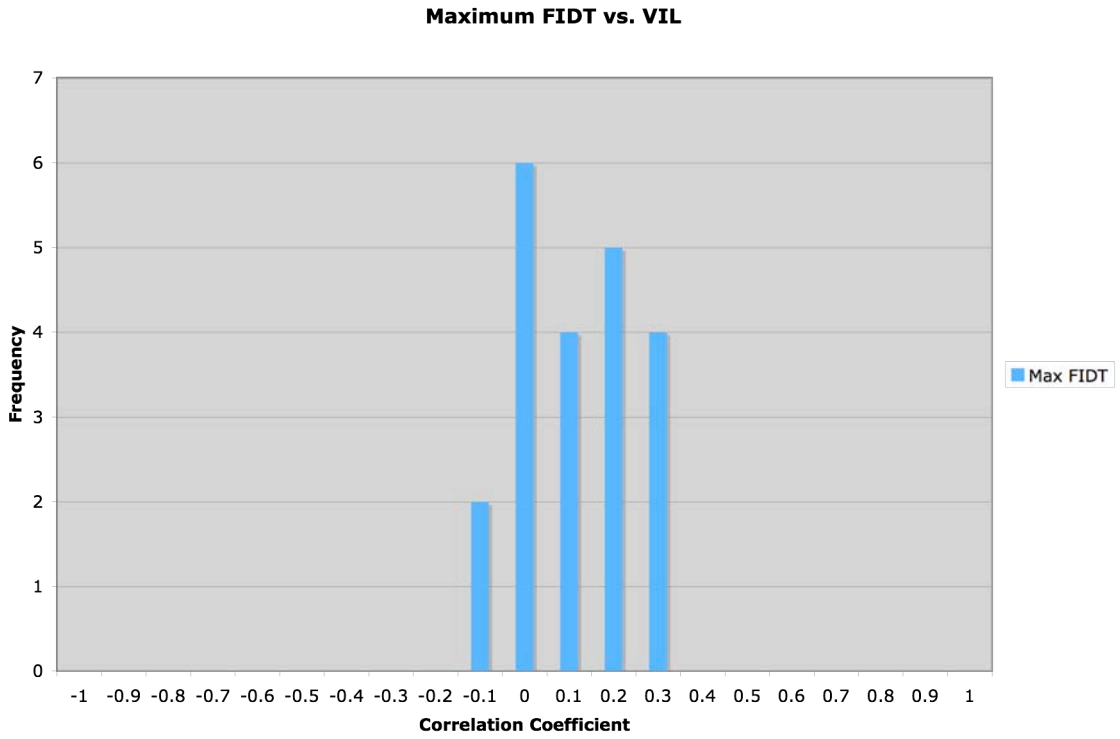

B-32. Histogram of correlation coefficients between VIL and MxFIDT.

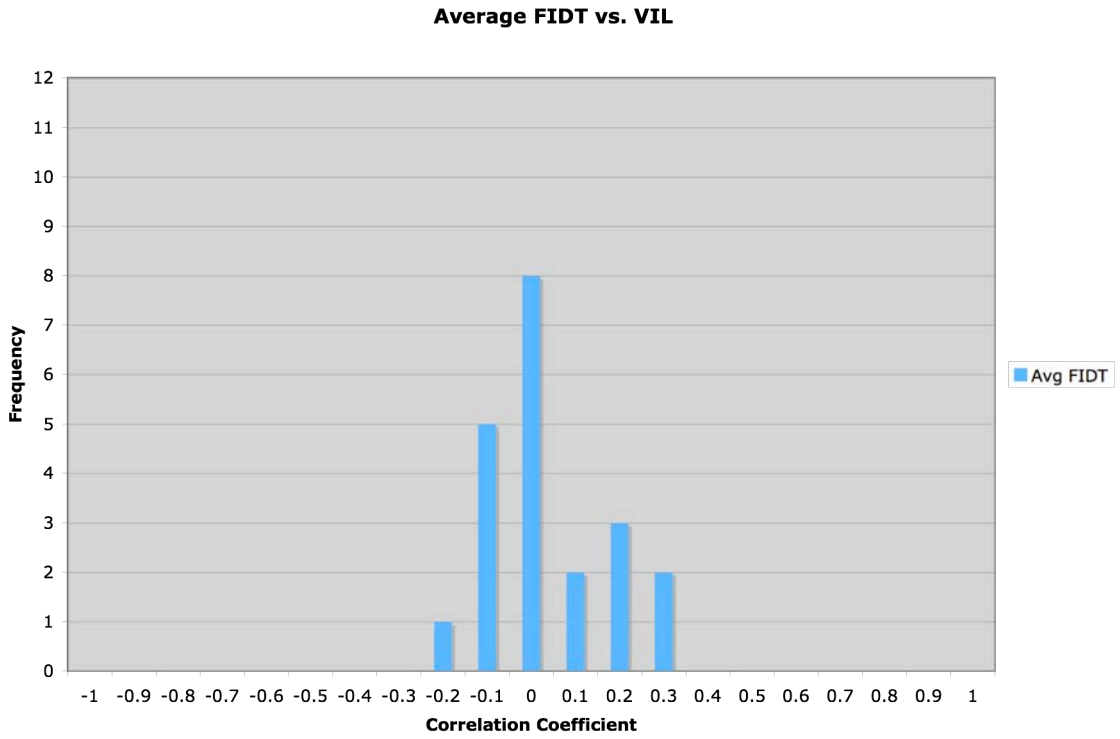

B-33. Histogram of correlation coefficients between VIL and AvFIDT.

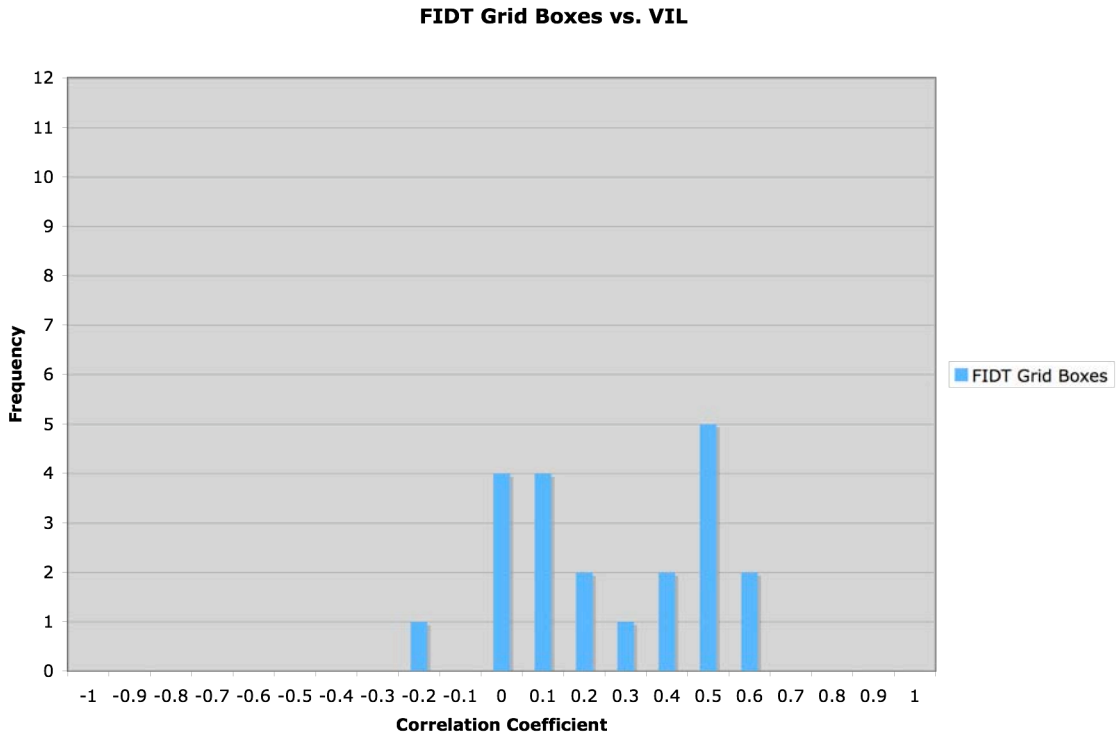

B-34. Histogram of correlation coefficients between VIL and GrFIDT.

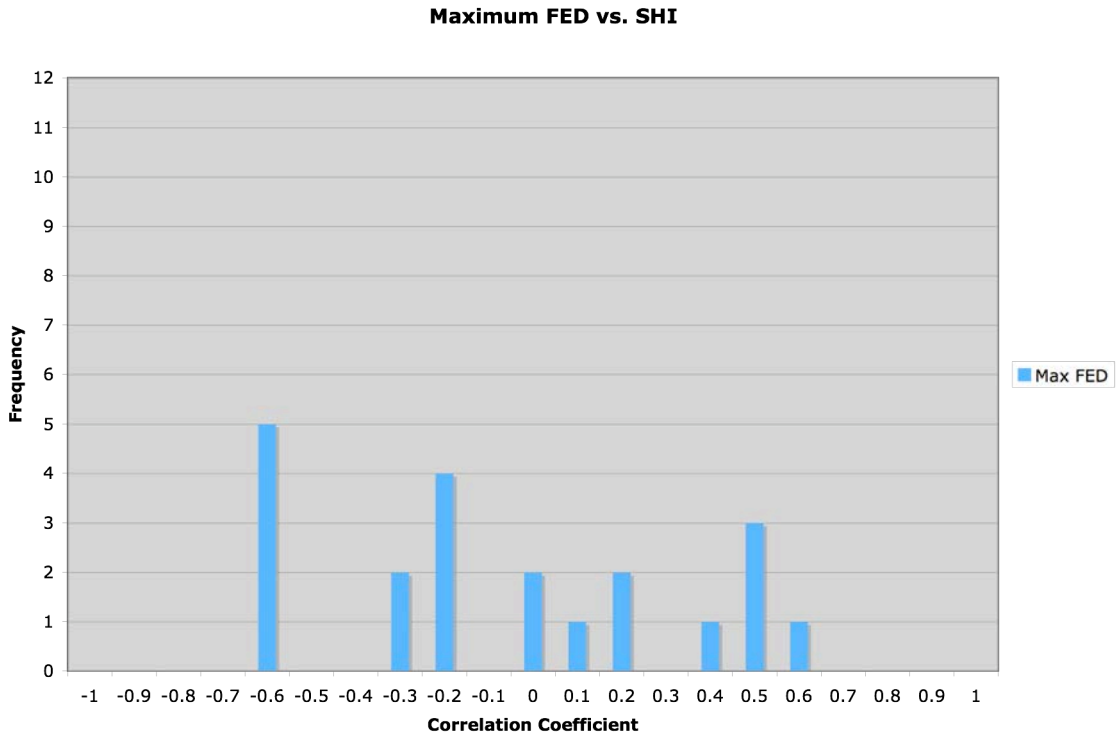

B-35. Histogram of correlation coefficients between SHI and MxFED.

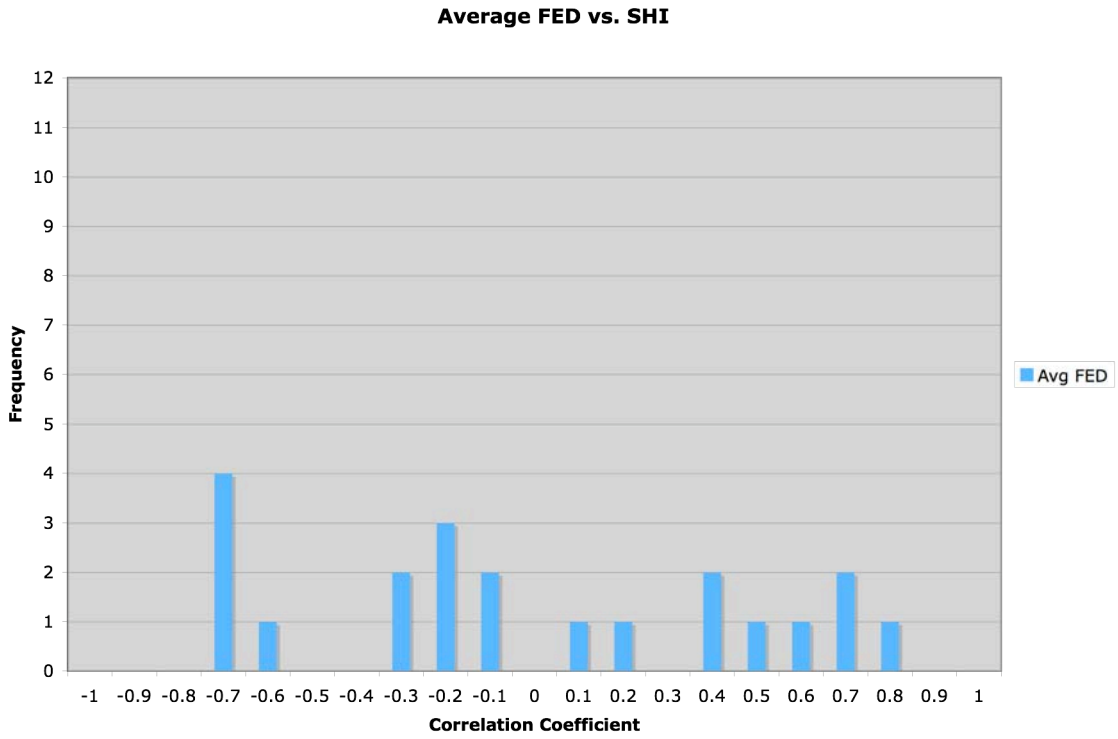

B-36. Histogram of correlation coefficients between SHI and AvFED.

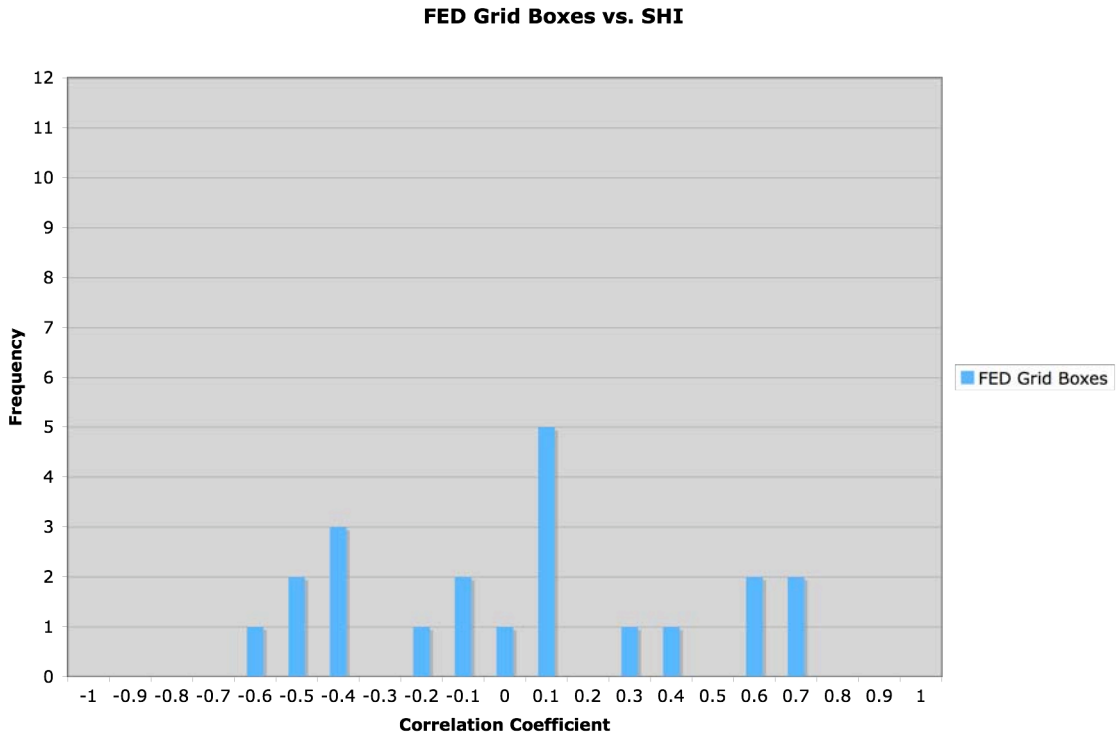

B-37. Histogram of correlation coefficients between SHI and GrFED.

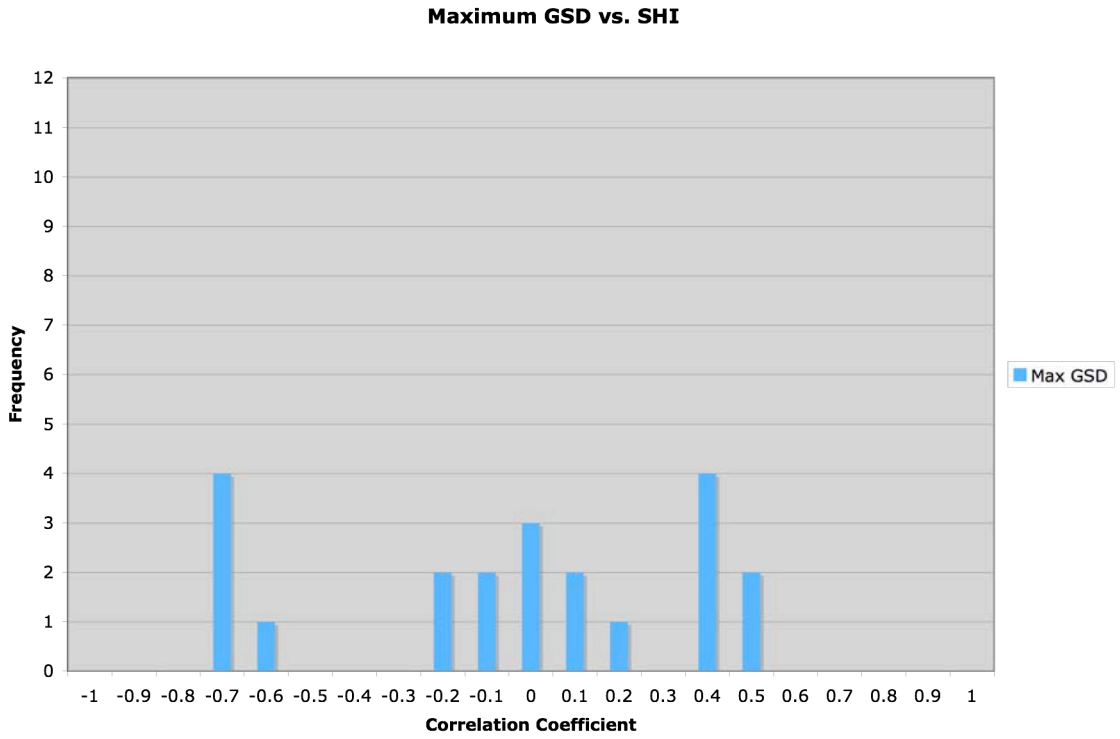

B-38. Histogram of correlation coefficients between SHI and MxGSD.

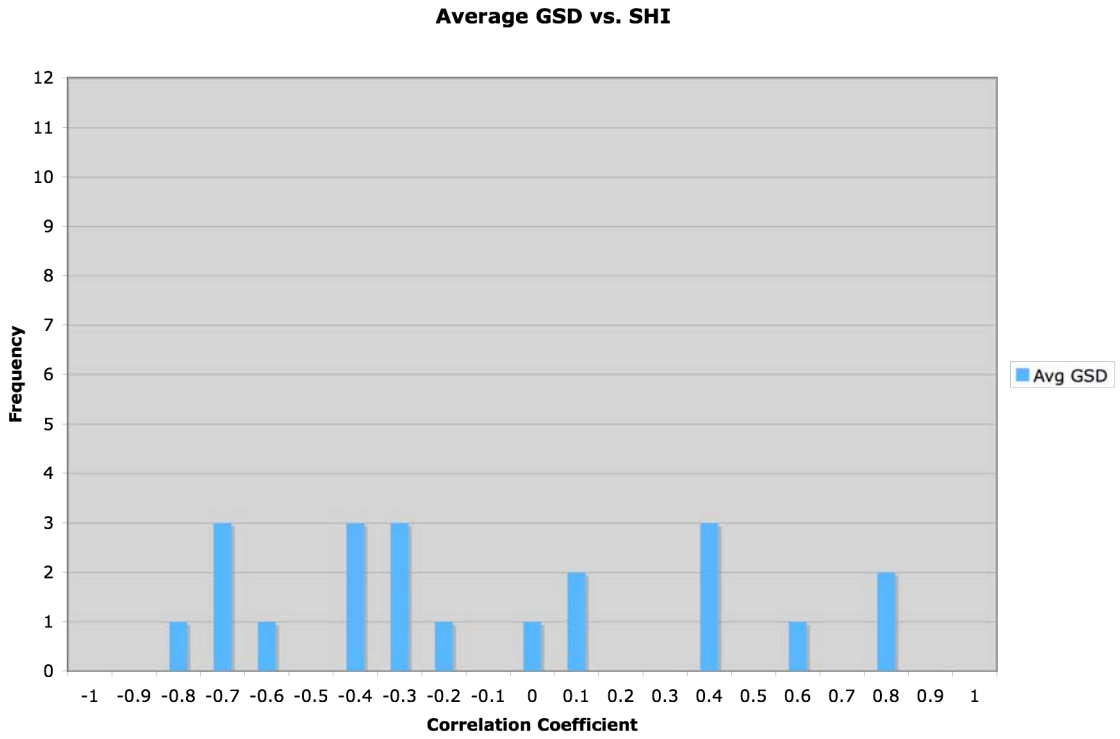

B-39. Histogram of correlation coefficients between SHI and AvGSD.

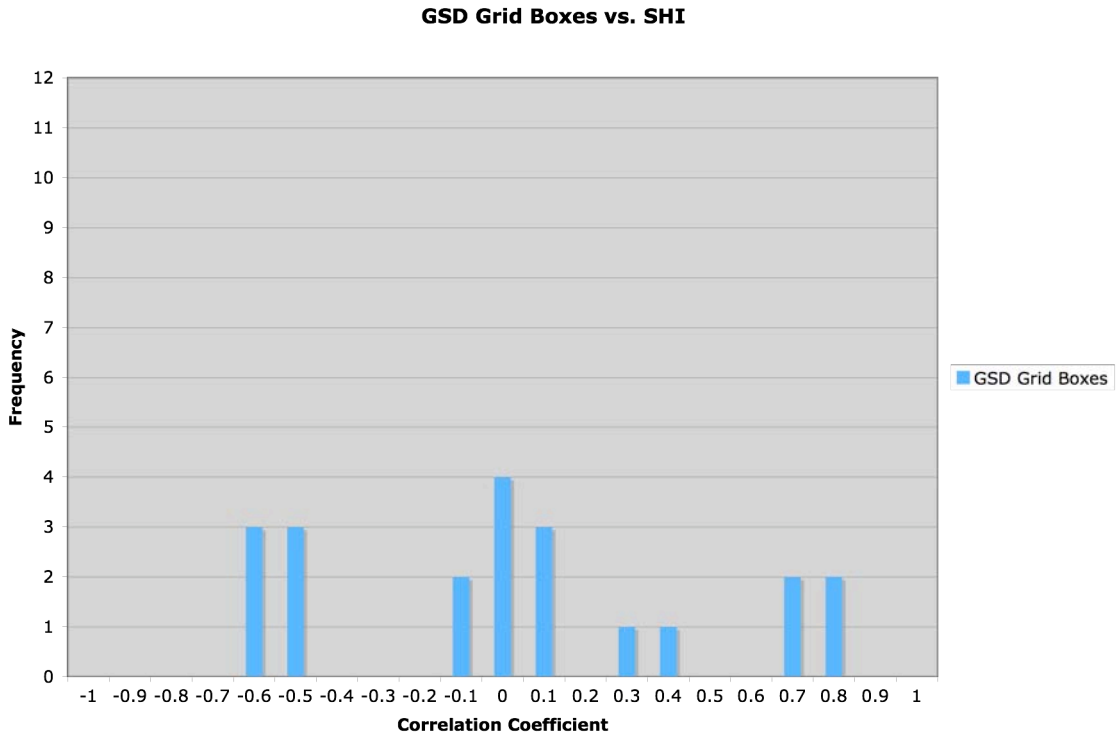

B-40. Histogram of correlation coefficients between SHI and GrGSD.

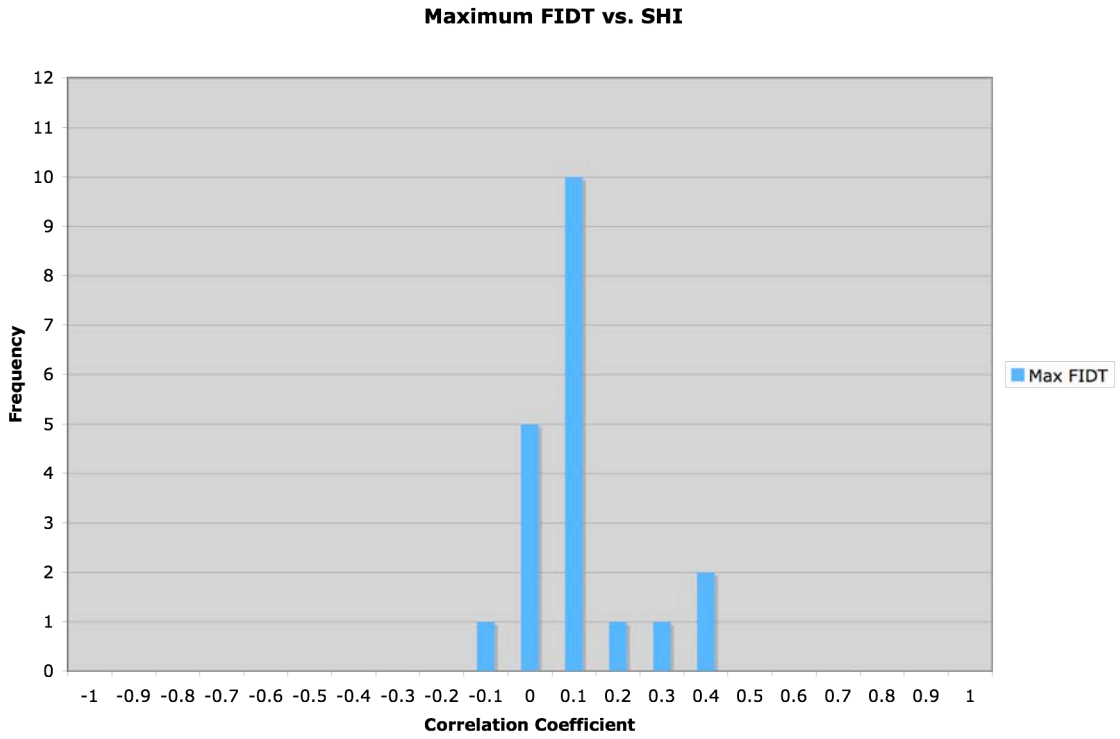

B-41. Histogram of correlation coefficients between SHI and MxFIDT.

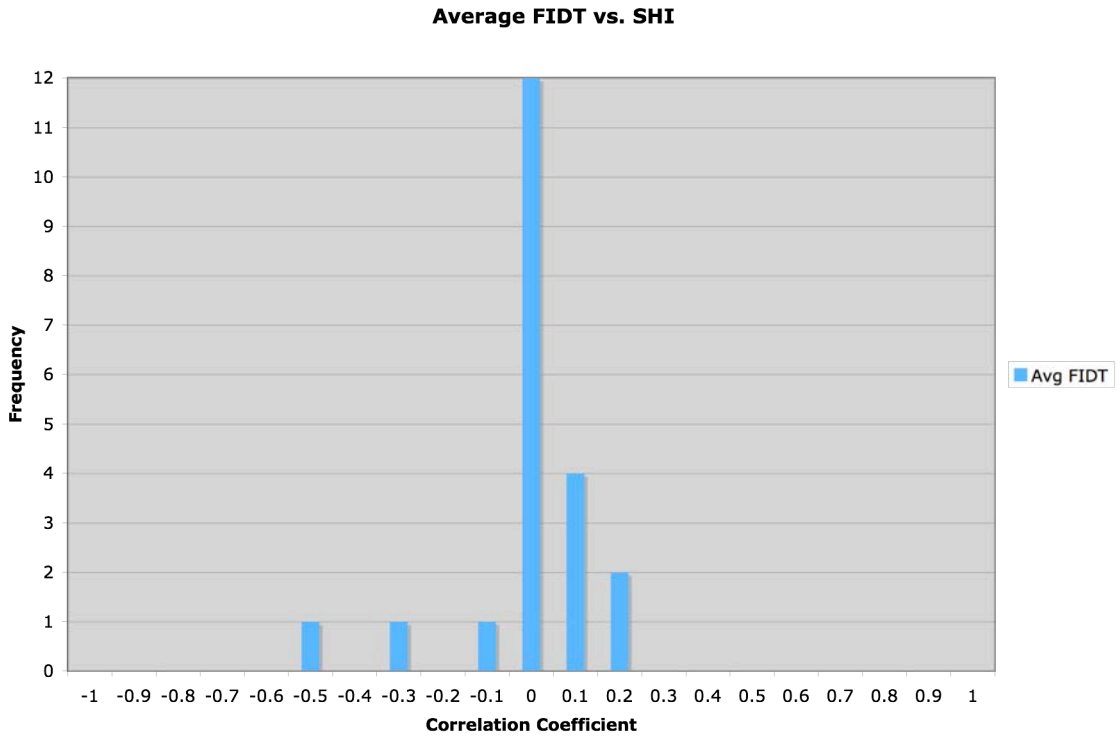

B-42. Histogram of correlation coefficients between SHI and AvFIDT.

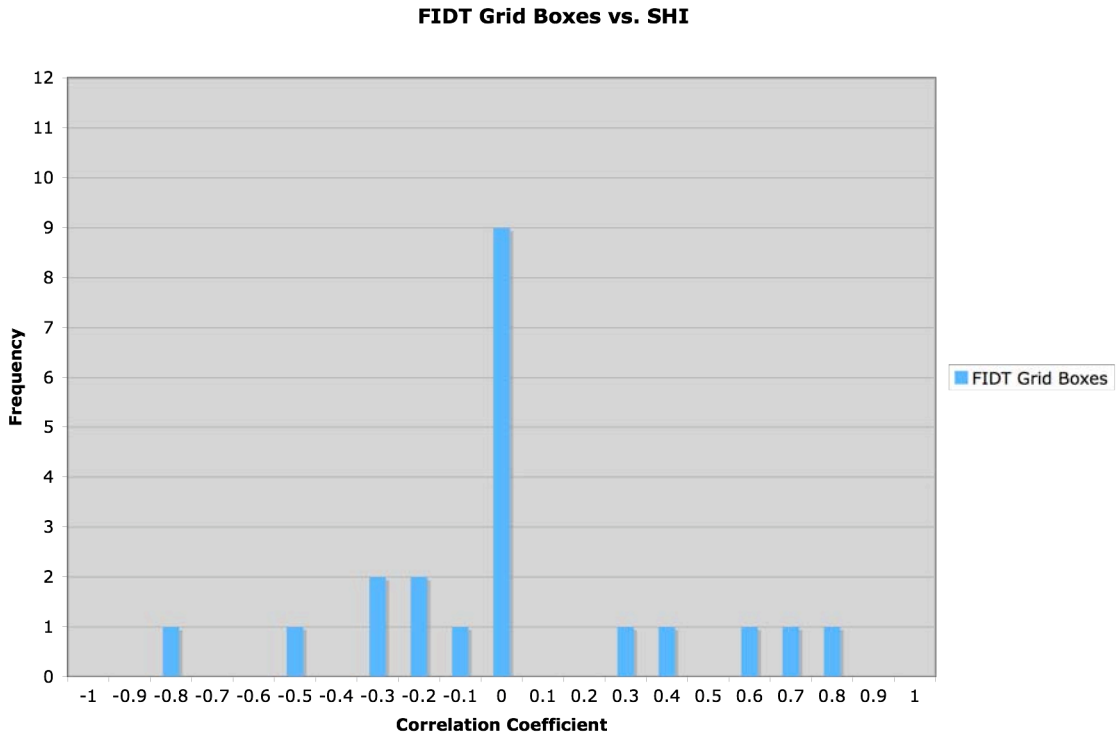

B-43. Histogram of correlation coefficients between SHI and GrFIDT.

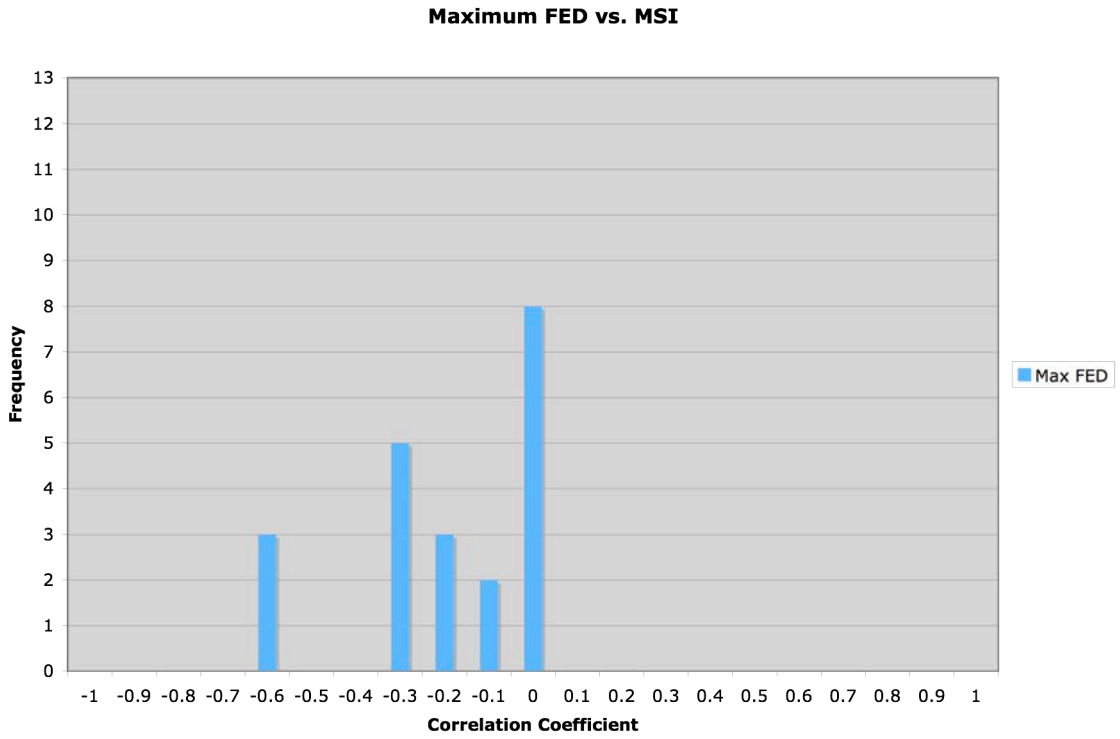

B-44. Histogram of correlation coefficients between MSI and MxFED.

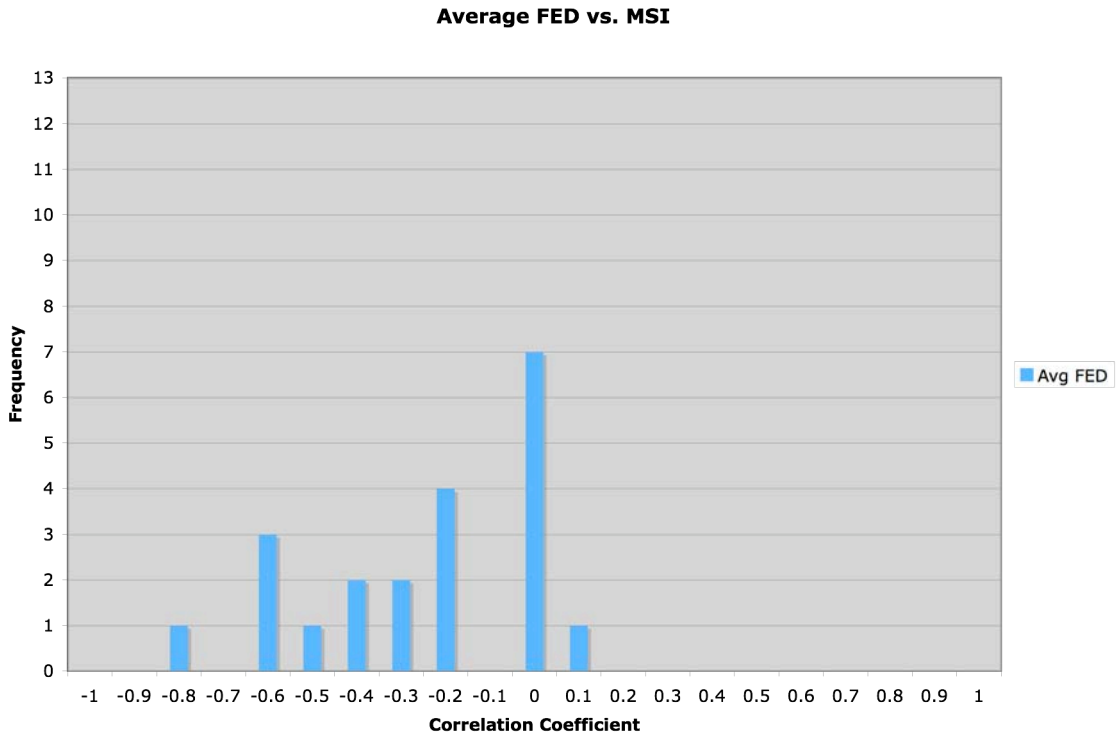

B-45. Histogram of correlation coefficients between MSI and AvFED.

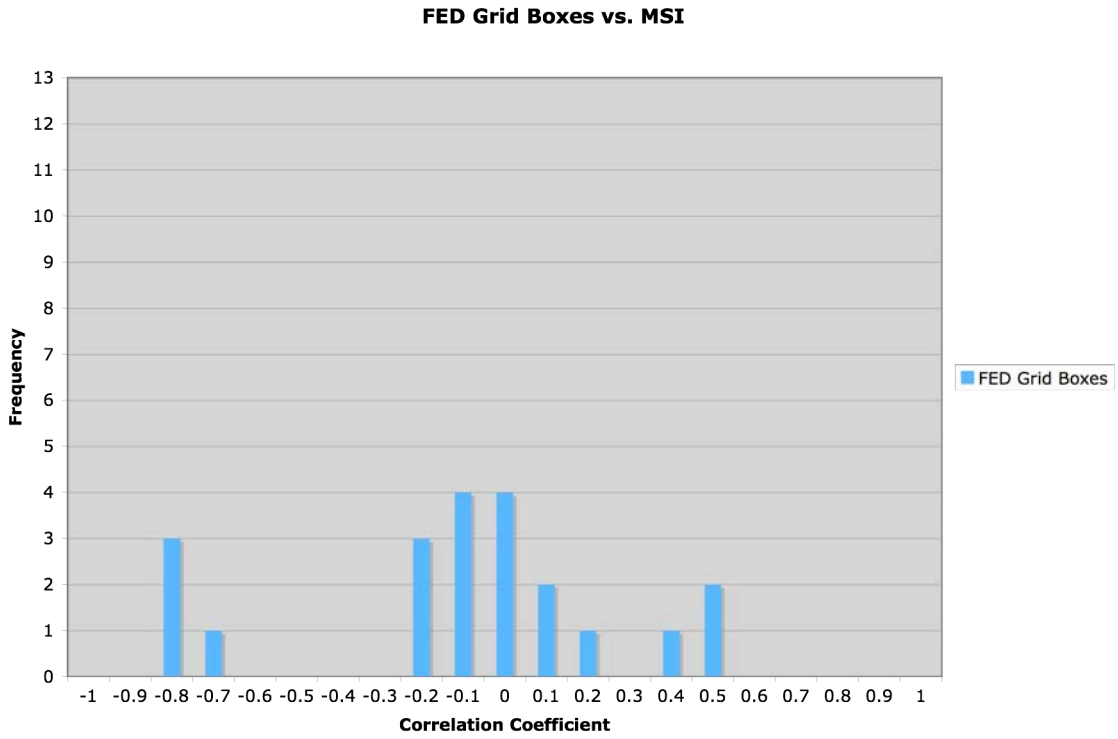

B-46. Histogram of correlation coefficients between MSI and GrFED.

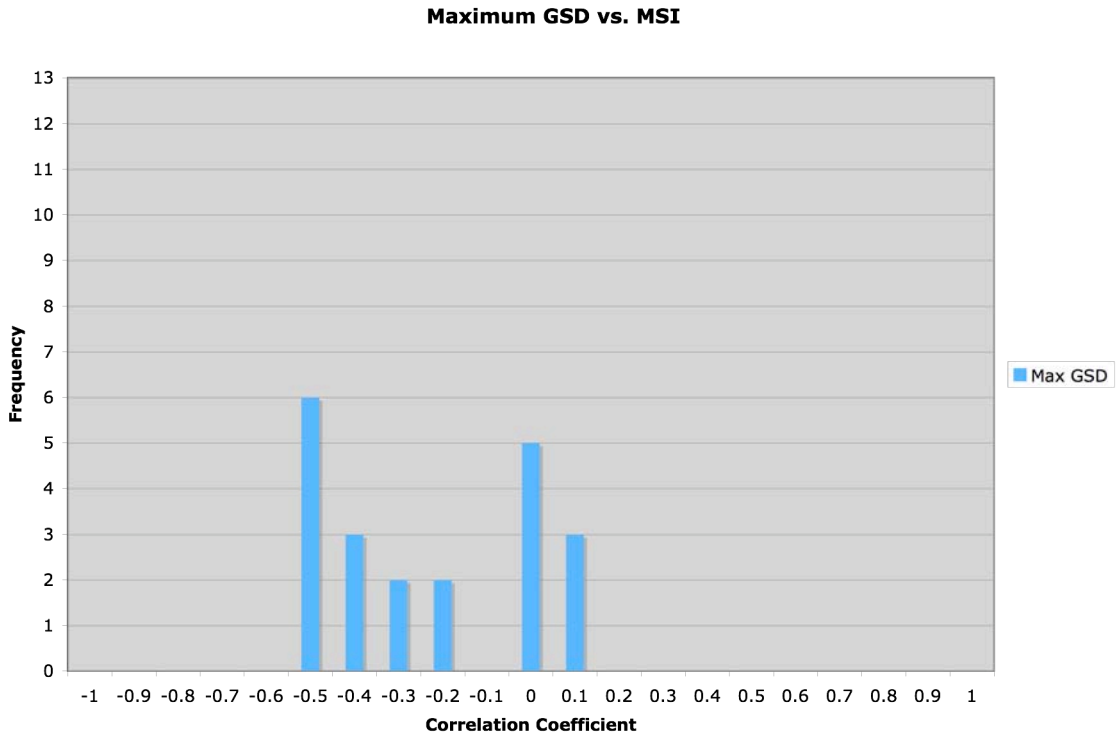

B-47. Histogram of correlation coefficients between MSI and MxGSD.

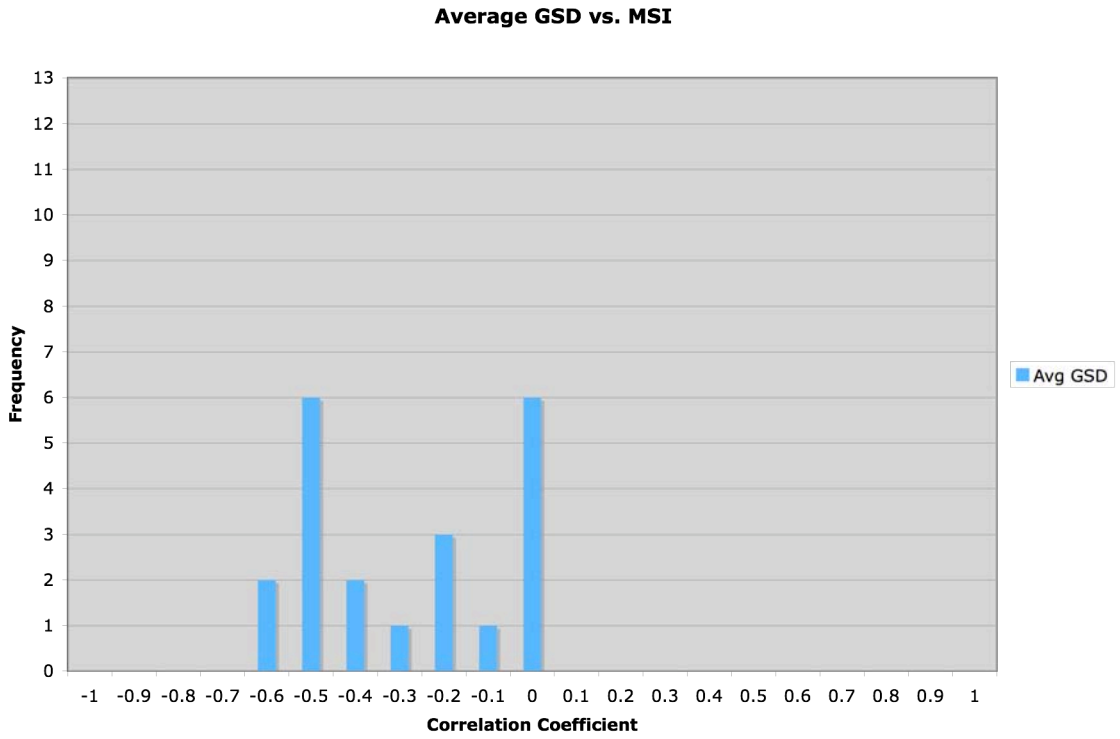

B-48. Histogram of correlation coefficients between MSI and AvGSD.

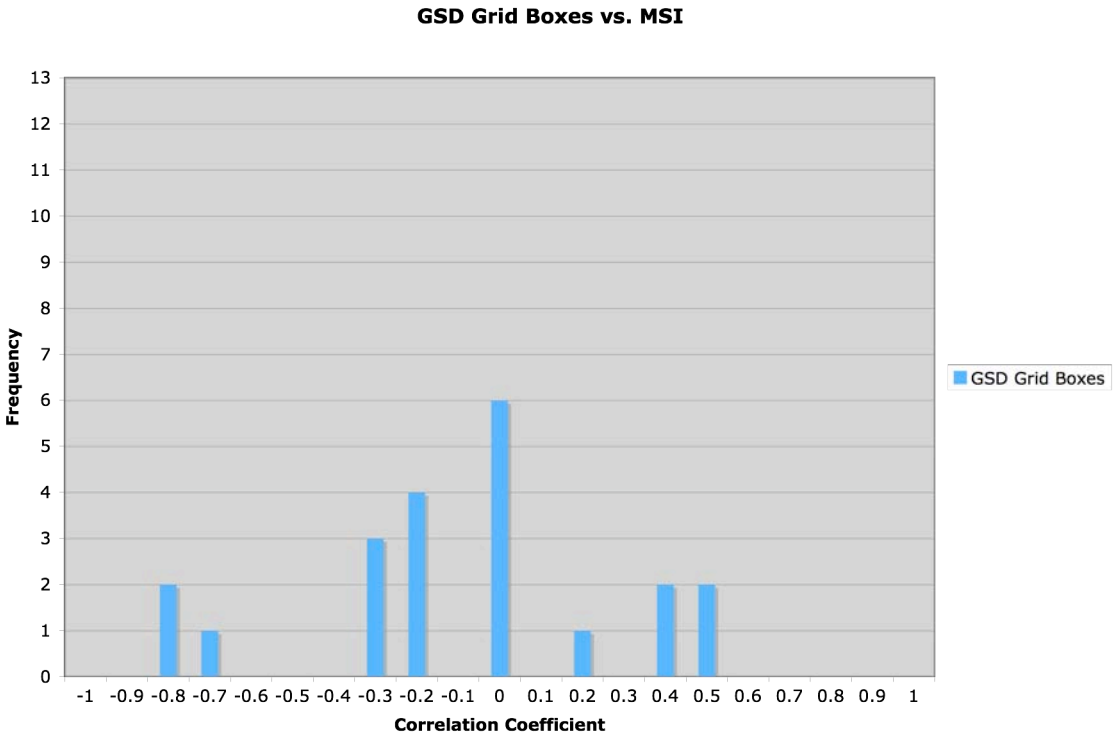

B-49. Histogram of correlation coefficients between MSI and GrGSD.

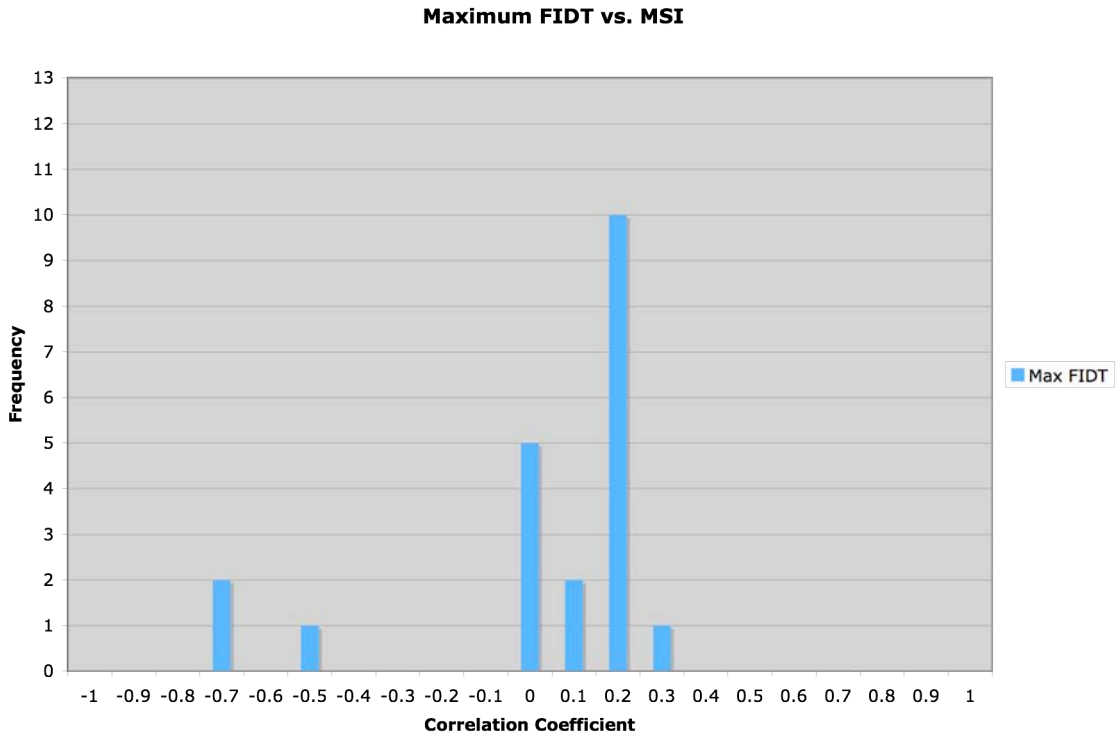

B-50. Histogram of correlation coefficients between MSI and MxFIDT.

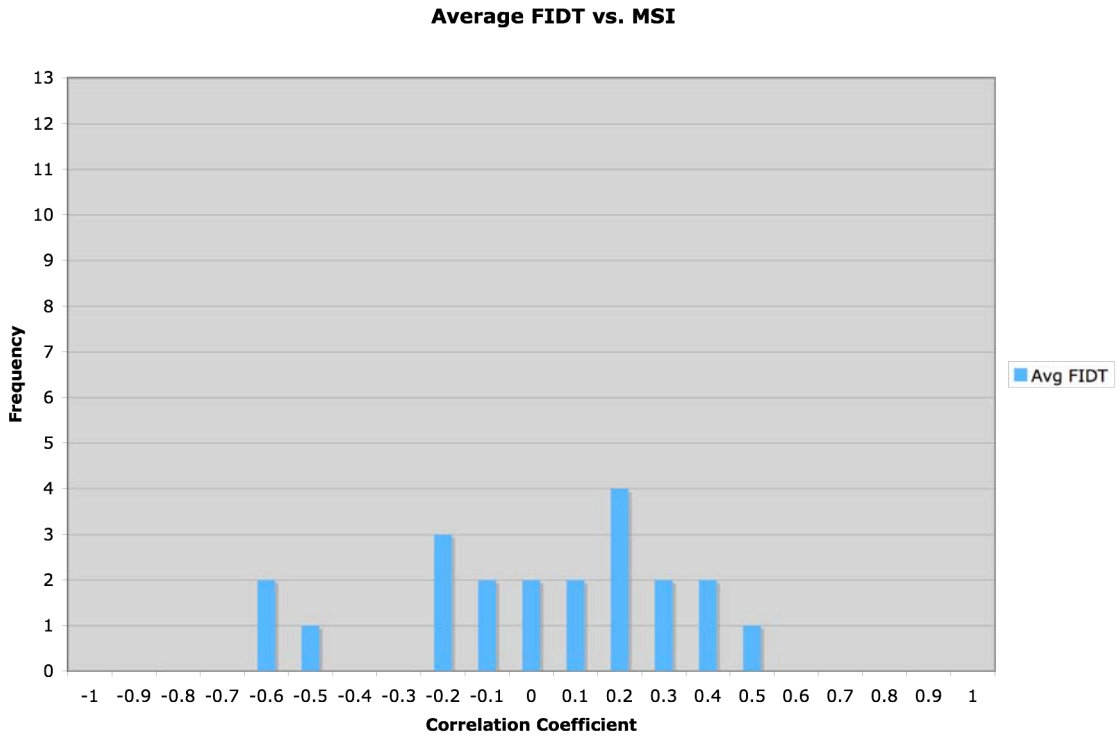

B-51. Histogram of correlation coefficients between MSI and AvFIDT.

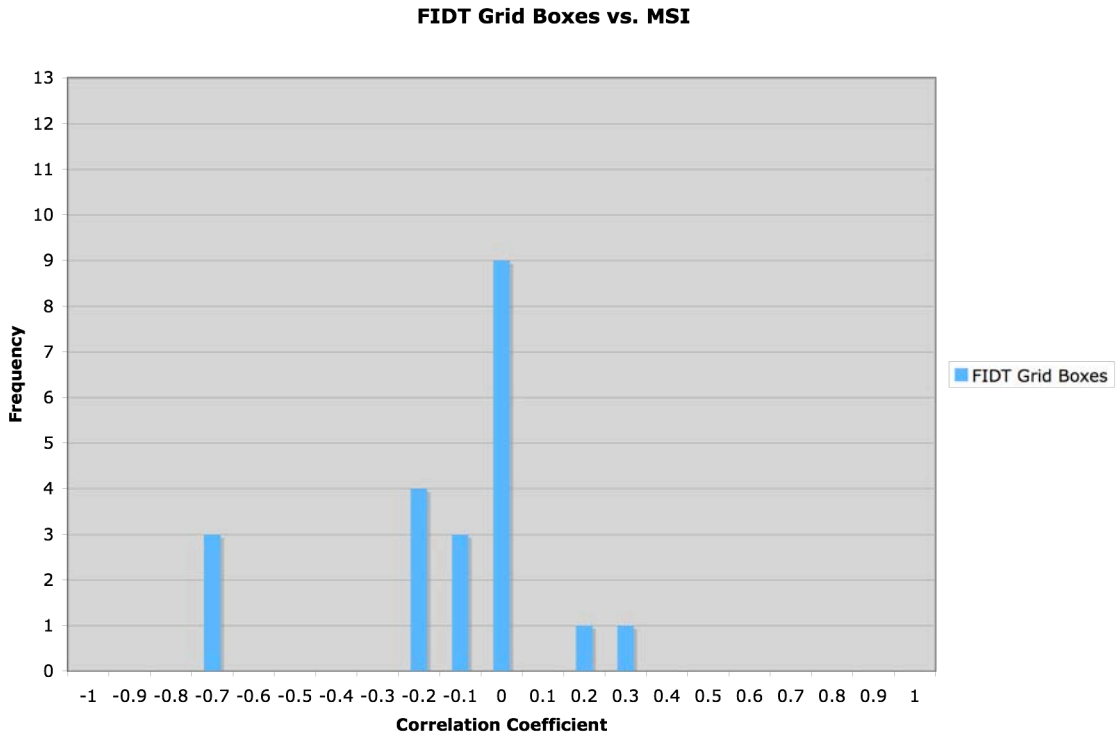

B-52. Histogram of correlation coefficients between MSI and GrFIDT.

VITA

Name:	Christopher Michael McKinney
Address:	NOAA/NWS Weather Forecast Office, Houston/Galveston, Texas 1353 FM 646 Suite 202 Dickinson, TX 77539
Email Address:	chris.mckinney@noaa.gov
Education:	B.S., Meteorology, Texas A&M University, 2006 M.S., Atmospheric Sciences, Texas A&M University, 2008